ADVANCED STEEL CONSTRUCTION

An International Journal

Volume 6 Number 2

June 2010

CONTENTS

Technical Papers

Conference Announcement

Cover: Curved Roof of the New Wuhan Bullet Train Station in China

Editors-in-Chief

S.L. Chan, The Hong Kong Polytechnic University, Hong Kong

W.F. Chen, University of Hawaii at Manoa, USA

R. Zandonini, Trento University, Italy

Cover: Curved Roof of the New Wuhan Bullet Train Station in China

General Information
Advanced Steel Construction, an international journal

Aims and scope

The International Journal of Advanced Steel Construction provides a platform for the publication and rapid dissemination of original and up-to-date research and technological developments in steel construction, design and analysis. Scope of research papers published in this journal includes but is not limited to theoretical and experimental research on elements, assemblages, systems, material, design philosophy and codification, standards, fabrication, projects of innovative nature and computer techniques. The journal is specifically tailored to channel the exchange of technological know-how between researchers and practitioners. Contributions from all aspects related to the recent developments of advanced steel construction are welcome.

Instructions to authors

Submission of the manuscript. Authors may submit double-spaced manuscripts preferably in MS Word by emailing to one of the chief editors as follows for arrangement of review. Alternatively papers can be submitted on a diskette to one of the chief editors.

Asian Pacific, African and organizing editor : Professor S.L. Chan, Email: ceslchan@polyu.edu.hk
American editor : Professor W.F. Chen, Email: waifah@hawaii.edu
European editor : Professor R. Zandonini, Email: riccardo_zandonini@ing.unitn.it

All manuscripts submitted to the journal are recommended to accompany with a list of four potential reviewers suggested by the author(s). This list should include the complete name, address, telephone and fax numbers, email address, and at least five keywords that identify the expertise of each reviewer. This scheme will improve the process of review.

Style of manuscript

General. Author(s) should provide full postal and email addresses and fax number for correspondence. The manuscript including abstract, keywords, references, figures and tables should be in English with pages numbered and typed with double line spacing on single side of A4 or letter-sized paper. The front page of the article should contain:

a) a short title (reflecting the content of the paper);
b) all the name(s) and postal and email addresses of author(s) specifying the author to whom correspondence and proofs should be sent;
c) an abstract of 100-200 words; and
d) 5 to 8 keywords.

The paper must contain an introduction and a conclusion. The length of paper should not exceed 25 journal pages (approximately 15,000 words equivalents).

Tables and figures. Tables and figures including photographs should be typed, numbered consecutively in Arabic numerals and with short titles. They should be referred in the text as Figure 1, Table 2, etc. Originally drawn figures and photographs should be provided in a form suitable for photographic reproduction and reduction in the journal.

Mathematical expressions and units. The Systeme Internationale (SI) should be followed whenever possible. The numbers identifying the displayed mathematical expression should be referred to in the text as Eq. (1), Eq. (2).

References. References to published literature should be referred in the text, in the order of citation with Arabic numerals, by the last name(s) of the author(s) (e.g. Zandonini and Zanon [3]) or if more than three authors (e.g. Zandonini et al. [4]). References should be in English with occasional allowance of 1-2 exceptional references in local languages and reflect the current state-of-technology. Journal titles should be abbreviated in the style of the Word List of Scientific Periodicals. References should be cited in the following style [1, 2, 3].

Journal: [1] Chen, W.F. and Kishi, N., "Semi-rigid Steel Beam-to-column Connections, Data Base and Modelling", Journal of Structural Engineering, ASCE, 1989, Vol. 115, No. 1, pp. 105-119.

Book: [2] Chan, S.L. and Chui, P.P.T., "Non-linear Static and Cyclic Analysis of Semi-rigid Steel Frames", Elsevier Science, 2000.

Proceedings: [3] Zandonini, R. and Zanon, P., "Experimental Analysis of Steel Beams with Semi-rigid Joints", Proceedings of International Conference on Advances in Steel Structures, Hong Kong, 1996, Vol. 1, pp. 356-364.

Proofs. Proof will be sent to the corresponding author to correct any typesetting errors. Alternations to the original manuscript at this stage will not be accepted. Proofs should be returned within 48 hours of receipt by Express Mail, Fax or Email.

Copyright. Submission of an article to "Advanced Steel Construction" implies that it presents the original and unpublished work, and not under consideration for publication nor published elsewhere. On acceptance of a manuscript submitted, the copyright thereof is transferred to the publisher by the Transfer of Copyright Agreement and upon the acceptance of publication for the papers, the corresponding author must sign the form for Transfer of Copyright.

Permission. Quoting from this journal is granted provided that the customary acknowledgement is given to the source.

Page charge and Reprints. There will be no page charges if the length of paper is within the limit of 25 journal pages. A total of 30 free offprints will be supplied free of charge to the corresponding author. Purchasing orders for additional offprints can be made on order forms which will be sent to the authors. These instructions can be obtained at the Hong Kong Institute of Steel Construction, Journal website: http://www.hkisc.org

The International Journal of Advanced Steel Construction is published quarterly by non-profit making learnt society, The Hong Kong Institute of Steel Construction, c/o Department of Civil & Structural Engineering, The Hong Kong Polytechnic University, Hung Hom, Kowloon, Hong Kong.

Advanced Steel Construction
an international journal

VOLUME 6   NUMBER 2   JUNE 2010

Technical Papers

DESIGN OF ECCENTRICALLY CONNECTED CLEAT PLATES IN COMPRESSION

X.E. Khoo [1], M. Perera [2] and F. Albermani [3,*]

[1] Structural Engineer, Bonacci Group
[2] Structural Engineer, Connell Wagner
[3] Associate Professor, School of Civil Engineering, University of Queensland
*(Corresponding author: E-mail: f.albermani@uq.edu.au)

ABSTRACT: The paper presents experimental results from twelve full scale test samples using different CHS member lengths and eccentric cleats combinations. The test results show that the governing connection failure is a sway collapse mechanism. Based on this evidence, a simple design method for eccentric cleat connection in compression is proposed. Results from the proposed design methods are in good agreement with the obtained experimental results and with FE predictions.

Keywords: Eccentric cleat connection, CHS member, design method

1.   INTRODUCTION

Unlike open structural sections where it is possible to connect the structural member directly to a gusset plate, the connection of structural steel hollow sections require certain fabrication such as slotted-end plate, welded-tee and flattened-end connections. This paper deals with slotted-end plate connection type (Figure 1a). The end plate is commonly bolted through a cleat or a gusset plate to a supporting member. This will result in an eccentric connection with unavoidable bending stresses that adversely affect the connection capacity under compression. Although it is possible to eliminate the resulting eccentricity by using a more elaborate slotted-plates detailing (fork type, Figure 1b), this will increase fabrication cost. The slotted-end plate (Figure. 1a) remains the most common type of hollow section connection used in practice.
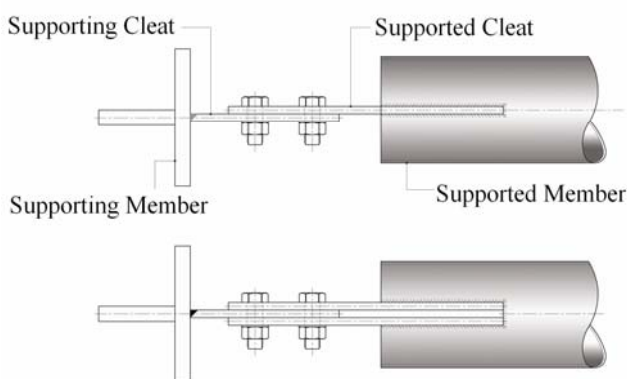
Figure 1a.
Traditional Slotted Cleat Connection

Figure 1b.
Slotted Fork Cleat Connection

The design of eccentric cleats is covered by a number of specifications [1-3] with a wide spectrum of design capacities determined according to these specifications. In Australia, the design of eccentric cleats is covered by the ASI guide [1]. The recommendations in this guide were based on experimental and analytical work presented by Kitipornchai et al. [4]. The work of Kitipornchai et al. identified three possible failure modes for a compression member with eccentrically connected cleat plates at both ends, these are: overall member buckling, connection failure with sway and

connection failure without sway. They had shown that analysis based on the first-yield approach resulted in an overly conservative result while ignoring the eccentric moment generated in the cleat plates would result in unconservative design. Furthermore, they concluded that for most practical applications the relative bending stiffness between the cleat plate and the member to which the cleat is attached will approximate a fully fixed connection. Following this conclusion, they derived six possible plastic collapse mechanisms for the connection that were confirmed by experimental results conducted on isolated cleat plates. Based on this, a design method was proposed that was adopted by the Australian Steel Institute, ASI [1].

This design approach will overestimate the connection capacity if the connection fails in a sway rather than fully fixed mode. This was first recognized during the development of steel connection design software Limcon V3 [5]. In response to this, the ASI issued an advisory note [6] that recommended using the design procedures outlined in the Australian steel structures code [7] taking into account the combined bending and compression actions for designing eccentric cleat connections rather than using the ASI design guide [1].

More recently, New Zealand Heavy Engineering Research Association (HERA) recommended a new step-by-step design method for eccentric cleats [8]. This method suggests that the dominant failure mode of this type of connection is a sway mode. It assumes that at least one end of the overlapping cleat plates is effectively fully fixed while the connection to the end of the supported member can be free to translate. Particular attention is given to identifying the exact type of support conditions at both ends of the cleat plate. A procedure to determine whether a cleat is effectively fixed to the supported member is also outlined in this method.

Experimental study using scaled samples of members connected to eccentric cleats was recently carried out at the University of Sydney [9]. This study showed significant interaction between bending and compression in the cleat plates and the presence of significant sway in the tested samples.

In this paper the results obtained from full-scale experimental program using 12 samples of different member length and eccentric cleats combinations will be presented. The experimental results are compared with available design methods for eccentric cleat connections and with FE predictions and a new design procedure is proposed.

2.   EXPERIMENTAL RESULTS

A total of twelve test specimens were used, three samples of each of the following member lengths (L_b); 3m, 4m, 5m, 6.5m. All the members were Grade 350 hot rolled circular hollow sections CHS with an outside diameter of 139.7mm and a wall thickness of 3.5mm. Different member lengths were used in order to assess the effect of the relative stiffness of the overlapping cleats and the member on the design capacity of the connection.

A constant cleat length Lc = 170mm (Figure 2) was used for the 3m and 6.5m members. For the 4m and 5m length members, three different cleat lengths, Lc, were used. These were; 170mm, 220mm and 270mm. This was done in order to assess the effect of cleat plates' slenderness on the connection capacity while the member slenderness is kept constant. All cleat plates used were 180x10mm Grade 300 steel.
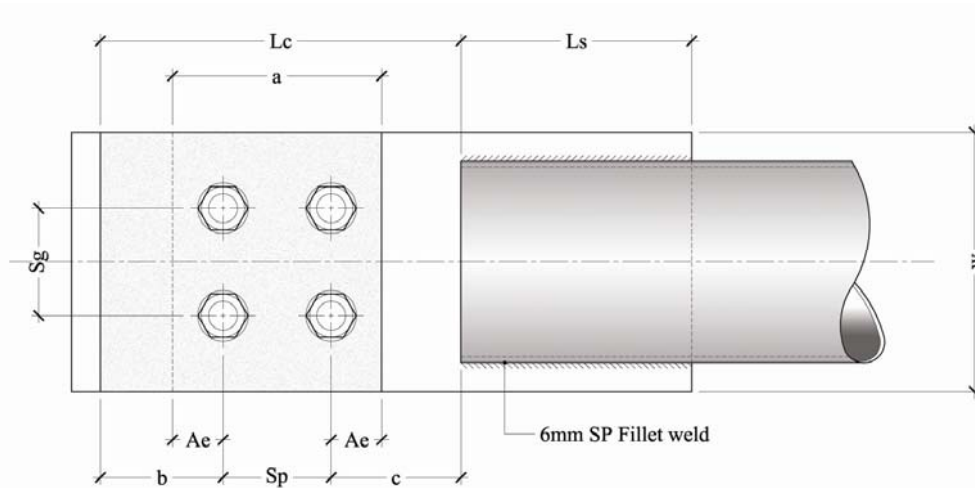
Figure 2. Dimension Nomenclature

Two coupon tests were conducted for the CHS sections and four for cleat plates. These tests indicated an average yield stress of 345MPa for the CHS and 320MPa for the cleats. Cleat connections usually require two weld locations, the first is between the slotted end plate and the supported member (the CHS member) and the second is between the gusset plate and the supporting member. The slotted end plate is usually welded along its entire slot length. For the test specimens a 6mm SP fillet weld with a slotted length, L_s, of 260mm is used (Figure 2). This weld length is adequate for even distribution of shear transfer across the slot length. Bracing members are usually connected to stiffer beams or columns. In the experimental setup used, this is achieved by welding the gusset plate to a thicker square plate (180mmx20mm). The weld used here is a full penetration butt weld as shown in Figure 3. The square plate is attached to a rigid support as shown in Figure 4.
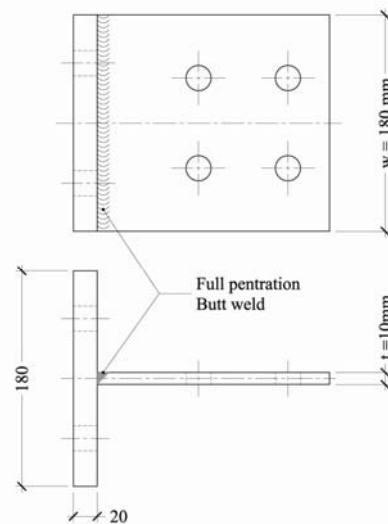
Figure 3. Supporting Cleat Common Dimensions

Good design of bolted connections requires minimizing the length of the cleat assemblies. For cleat assemblies that require two rows of bolts (Figure 2), the minimum length is comprised of the pitch distance, S_p (70mm used in our samples), edge distance, A_e (35mm is used) and clearance to the support (minimum of 15mm is used). The pitch and edge distances are governed by the size of bolt used to connect the plate. All the cleats were assembled using four M20 snug tight bolts (two rows). These length values gave a minimum cleat length, Lc, of 170mm. Table 1 summarizes the details for the 12 samples used in the experiment.

The CHS member was placed horizontally in the test rig with the cleat plates oriented in the vertical plane. Figure 4 is a schematic of the test setup, Figure 5 is a photo of one of the tests and Figure 6 shows the arrangement at the loaded (a) and supported (b) ends of the test sample.
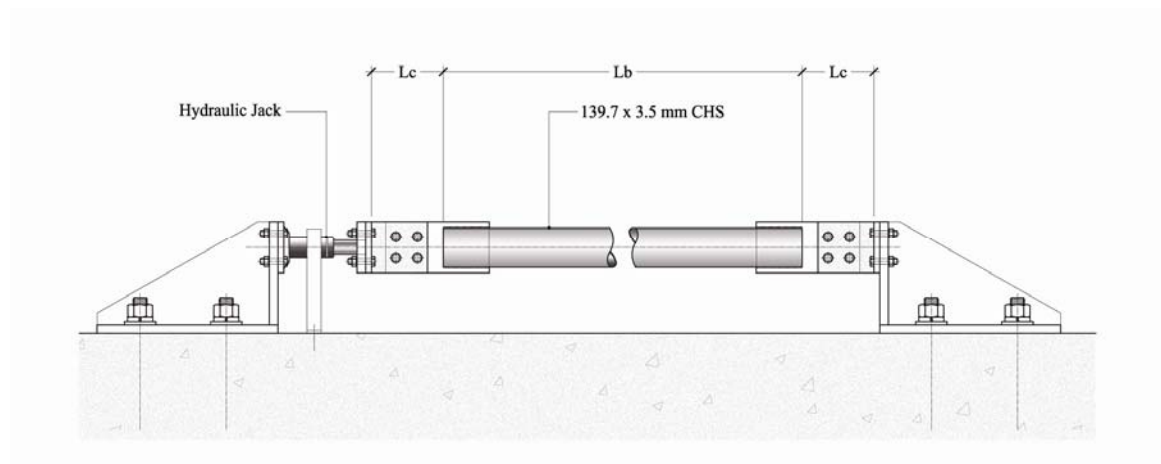
Figure 4. Testing Rig Schematic

Clockwise From Left
Figure 5. Testing Rig; Figure 6. a) Support at Live End; b) Support at Fixed End

Four displacement measurements using LVDTs were recorded for each test. Two of these were placed at the interface between the slotted end plates and the CHS at each end to measure the lateral displacement and the other two at the mid-span of the CHS to measure the lateral and the vertical displacement. Similarly, strain measurements using strain gauges were recorded for four of the test samples (one for each of the 3m, 4m, 5m and 6.5m length samples). Two strain gauges were placed at opposite sides of the CHS at mid-span and the other two on the opposite sides of the slotted end plate at the supported end of the samples.

Table 2 summarizes the test results. Nine test samples (sample A, B and C with 3, 4 and 5m lengths respectively) experienced a sway collapse mechanism at the cleat connection at the supported end of the members. Figure 7 (a, b and c) shows the resulting sway collapse mechanism for L_c 170, 220 and 270mm respectively.

In contrast, samples D1-D3 (6.5m) failed by elastic buckling of the CHS member. When taking the cleat length L_c into account, samples D1-D3 have actual length of 6.84m. Using the experimental failure loads (Table 2) for D1-D3 and a 6.84m length, an effective length factor, k, of 0.98, 1.06 and 0.98 is obtained for D1, D2 and D3 respectively.

a)   b)   c)
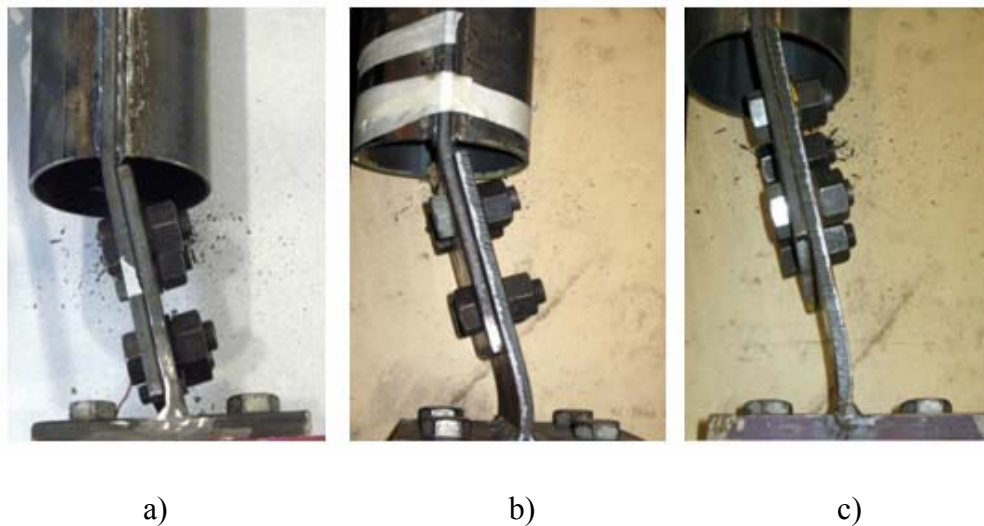
Figure 7. Observed Failure Mode (a) Lc = 170mm (b) Lc = 220mm (c) Lc = 270mm

Figures 8a and 8b show some of the obtained experimental load-lateral deflection curves at mid-span for Samples A1, B1 and C1 (Figure 8a) and Samples B1-B3 (Figure 8b). From these figures, it is clear that the connection capacity is much more sensitive to the slenderness of the cleat plates (Figure 8b) rather than to the member (CHS) slenderness (Figure 8a).

(a)   (b)
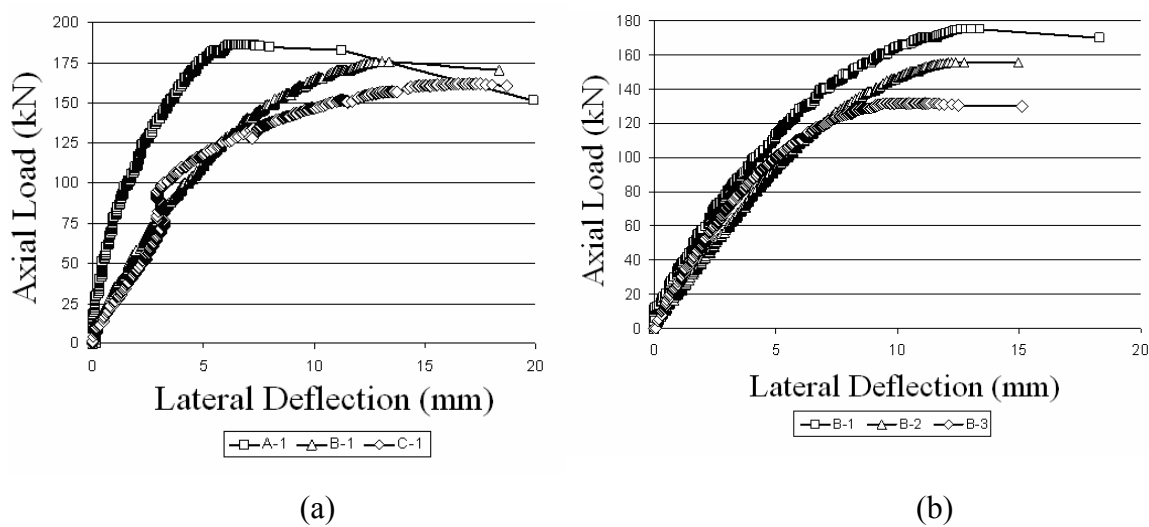
Figure 8. Axial Load Versus Lateral Deflection, (a) Varying Member Slenderness,   (b) Varying Cleat Slenderness

		Brace Length, L_b (mm)	Cleat Assembly Dimensions (mm)									
			L_c	t	w	a	b	c	S_p	S_g	A_e	Ls
Test Specimen	A-1	3000	170	10	180	140	50	50	70	110	35	260
	A-2	3000	170	10	180	140	50	50	70	110	35	260
	A-3	3000	170	10	180	140	50	50	70	110	35	260
	B-1	4000	170	10	180	140	50	50	70	110	35	260
	B-2	4000	220	10	180	140	100	50	70	110	35	260
	B-3	4000	270	10	180	140	150	50	70	110	35	260
	C-1	5000	170	10	180	140	50	50	70	110	35	260
	C-2	5000	220	10	180	140	100	50	70	110	35	260
	C-3	5000	270	10	180	140	150	50	70	110	35	260
	D-1	6500	170	10	180	140	50	50	70	110	35	260
	D-2	6500	170	10	180	140	50	50	70	110	35	260
	D-3	6500	170	10	180	140	50	50	70	110	35	260

Table 1. Test Specimens Dimensions

		Cleat Slenderness (Lc/r)	Brace Slenderness (Lb/r)	Experimental Failure Load (kN)	Proposed Design Method Predicted Failure Load (kN)
Test Specimen	A-1	59	62	158.5	151
	A-2	59	62	186.1	151
	A-3	59	62	159.8	151
	B-1	59	83	175.1	151
	B-2	76	83	155.4	136
	B-3	94	83	131.4	119
	C-1	59	104	165.3	151
	C-2	76	104	153.0	136
	C-3	94	104	115.5	119
	D-1	59	135	141.0	-
	D-2	59	135	131.0	-
	D-3	59	135	140.0	-

Table 2. Test Specimen Experimental and Predicted Failure Loads

3.   COMPARISON OF EXPERIMENTAL RESULTS WITH DESIGN METHODS

The experimental results are compared with the ASI [1] and HERA [8] design methods and with results from connection design software LIMCON V3 [5]. Generally ASI predictions grossly overestimate the connection capacity since it excludes sway failure mechanism.   When comparing the predicted ASI results for the nine samples (A, B and C) that were governed by connection failure, on average the ASI overestimates the capacity by 53%.

When comparing the results for the nine samples (A, B and C) with the design method proposed by HERA [8], it appears that HERA design capacity predictions are on the safe side. The ratios of the predicted capacity using HERA to the experimental results range from 0.48 to 0.70 with an average ratio of 0.56 for the nine samples. The conservatism in HERA approach stems from a number of reasons. For example HERA recommends using an additional 3mm eccentricity for the cleat plates (for the sample tested with 10mm thick cleats, this amount to 30% increase in the resulting moment).   Furthermore, HERA method use the elastic section modulus to evaluate the moment capacity of the cleat plates and HERA approach has been developed with seismic actions in mind.

On the other hand, the correlation between the capacities predicted by LIMCON [5] and the experimental results is very good. The capacity ratios (LIMCON to experiment)   ranged from 0.77 to 0.95 with an average ratio of 0.85. LIMCON method follows the recommendations in AS 4100 [7] for combined actions design where second-order effects are accounted for through moment magnification. It incorporates a design capacity factor φ =0.9. Taking the experimental results as nominal capacities, a more realistic comparison with Limcon can be obtained by dividing Limcon prediction by φ. Accordingly, the average capacity ratio is revised to $0.85/\varphi = 0.94$.

4.   PROPOSED DESIGN METHOD

Based on the experimental observations presented earlier, the sway collapse mechanism (Figure 7) is the governing mechanism that determines the connection capacity. A two steps design method for eccentric cleat connection in compression is proposed in this section. A schematic of the sway mechanism with two plastic hinges is shown in Figure 9, the external work V (ignoring second-order effects) is

$$V= P \, e \, \theta \tag{1}$$

Where P is the applied load, e is the load eccentricity which equals the average thickness of the supported and supporting cleat plates (see Figure 1a) and θ is the rotation as shown in Figure 9.

The internal energy, U, is

$$U= (M_{p1} + M_{p2}) \, \theta \tag{2}$$

Where M_{p1} and M_{p2} are the plastic moments of the supported and supporting cleat plates respectively (for identical cleat plates with σ_y yield stress, $M_{p1} = M_{p2} = M_p = \sigma_y wt^2/4$).
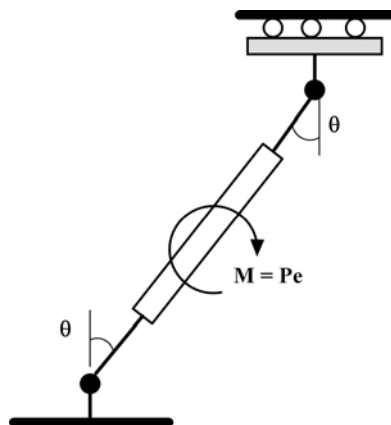
Figure 9. Sway Type Collapse Mechanism

Equating the external and internal energies (Eqs. 1 and 2) and assuming identical supporting and supported cleat plates, the collapse load, P, for the connection can be obtained

$$P = 2M_p/t \tag{3}$$

A non dimensional collapse load, η, is obtained by normalizing the load P from Eq. 3 by P_y (cleat's squash load, $P_y = \sigma_y wt$)

$$\eta = P/P_y \tag{4}$$

The elastic buckling load, P_{EC} of the cleat, assuming sway mode, is calculated

$$P_{EC} = \frac{\pi^2 E I_c}{(1.2L_c)^2} \tag{5}$$

Where E is the elasticity modulus, I_c is the cleat plate moment of inertia ($wt^3/12$) and L_c is the cleat plate length as shown in Figure 2. Depending on slenderness ratio, the critical buckling load P_C is given by [4]

$$\Lambda > \sqrt{2} \quad \rightarrow \quad P_C = P_{EC}$$
$$\Lambda \le \sqrt{2} \quad \rightarrow \quad P_C = P_y(1 - \frac{P_y}{4P_{EC}}) \tag{6}$$

Where,

$$\Lambda = (\frac{P_y}{P_{EC}})^{0.5} \tag{7}$$

The ultimate load P_U of the connection can be obtained from;

$$P_U = \frac{P_C}{1 + \dfrac{P_C}{\eta P_y}} \tag{8}$$

Once the ultimate load is calculated from Eq. 8, a second (and last) step starts by modifying the plastic moment to account for the effect of the axial load P_U in the connection

$$M_p = M_p[1 - (\frac{P_U}{P_C})^2] \tag{9}$$

The revised plastic moment M_p from Eq. 9 is used to obtain a new collapse load P from Eq. 3, a new factor η from Eq. 4 and a revised ultimate load using Eq. 8 (in the 2nd step, P_y, P_{EC}, P_C and Λ remain unchanged from the 1st step).

The ultimate loads predicted by the proposed approach for the test samples used in the current experiment are listed in Table 2. The proposed method gives a good estimate of the connection capacity compared to test results.

5.   PARAMETRIC STUDY OF CLEAT CONNECTIONS

A parametric study for cleat connections using various combinations of cleat length L_c, thickness, t, and width, w, was conducted using three approaches. These are; nonlinear finite element analysis of the cleat using Strand7 software [10], modeling using connection design software LIMCON and the proposed design method. In the nonlinear FE analysis, both the cleat plates and the CHS member are modeled using an assembly of beam elements and an elastic-perfectly plastic material representation is used.

Figure 10 shows the results from the parametric study. The failure load is normalized by the cleat squash load P_y and presented as a function of the cleat slenderness ratio L_c/r. The three points shown in this figure are the experimental results, each point represents the average of three experimental results from specimens A, B and C. Generally a good agreement is obtained between the proposed design method, the experimental results, the numerical (FE) analysis and LIMCON results.   As was explained before, Limcon results shown in Figure 10 were obtained by dividing Limcon predictions by $\varphi=0.9$.
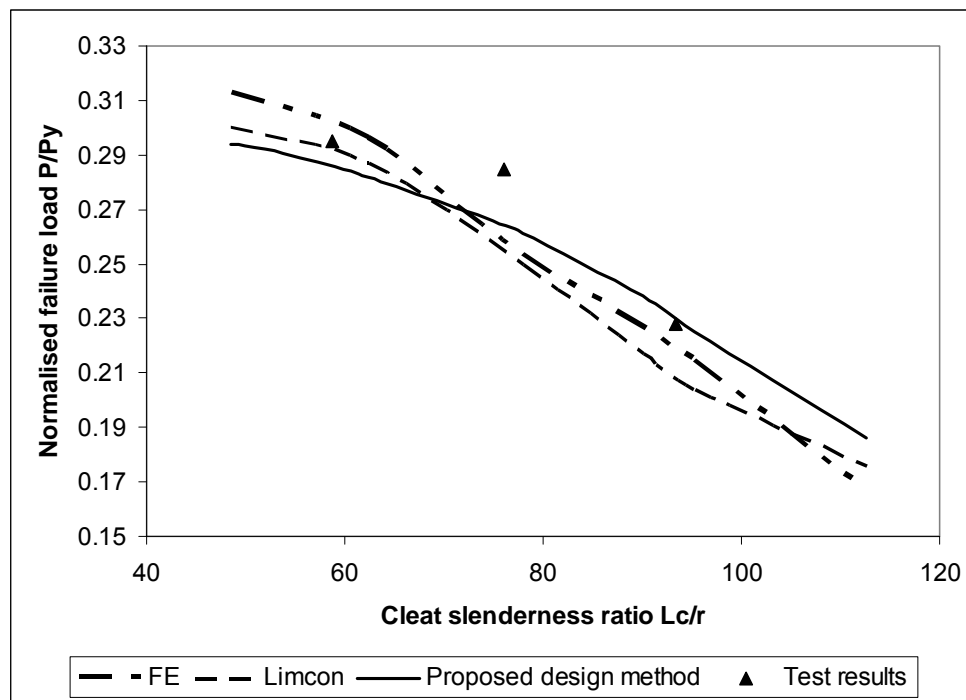
Figure 10. Parametric Study: Variation of Failure Load with Cleat Slenderness Ratio

6.   CONCLUSION

The results from 12 full scale test samples using different member lengths and eccentric cleats combinations were presented in this paper. These results were compared with available design methods and FE results. Based on the experimental observations, the governing connection failure is a sway collapse mechanism. A simple two steps design method for cleat connection design is proposed. A good agreement between results from the proposed design method, experiments and FE predictions is obtained.

ACKNOWLEDGEMENTS

REFERENCES

[1]   Syam, A.A. and Chapman, B.G., "Design of Structural Steel Hollow Section Connections", ASI, 1996.
[2]   AISC, "Hollow Structural Sections Connections Manual", American Institute of Steel Construction, 1997.
[3]   CSA, Canadian Standards Association, CAN/CSA-S16-01, "Limit States Design of Steel Structures", 2003.
[4]   Kitipornchai, S., Albermani, F. and Murray, N., "Eccentrically Connected Cleat Plates in Compression", Journal of Structural Engineering, ASCE, Vol. 119, No. 3, 1993.
[5]   Limcon V3, "Limit State Design of Steel Connections", Engineering Systems Pty Ltd, www.steel-connections.com
[6]   ASI Advisory Note, "Design Method for Eccentrically Connected Cleats Not to be Used", Australian Steel Institute ASI Journal, Vol. 39, No. 2, 2005.
[7]   Standards Australia, AS4100 Steel Structures, 1998.
[8]   Clifton, C. and Sarraf, R. El., "Eccentric Cleats in Compression and Columns in Moment Resisting Connections", New Zealand Heavy Engineering Research Association (HERA, www.hera.org.nz), 2007.
[9]   Stock, D., "Eccentric Cleat Plate Connections in Hollow Section Members in Compression", Department of Civil Engineering, The University of Sydney, 2007.
[10]   G+D Computing, Strand7 Software, www.strand7.com

BEHAVIOR OF L-SHAPED CONCRETE-FILLED STEEL STUB COLUMNS UNDER AXIAL LOADING: EXPERIMENT

Z.Y. Chen[1, 2,*] and Z.Y. Shen[3]

[1] Lecturer, College of Civil Engineering, Tongji University, Shanghai 200092, China
[2] Key Laboratory of Geotechnical and Underground Engineering of Ministry of Education, Shanghai 200092, China
[3] Professor, College of Civil Engineering, Tongji University, Shanghai 200092, China
*(Corresponding author: E-mail: zhiyichen@tongji.edu.cn)

ABSTRACT: Tests were conducted on six L-shaped concrete-filled steel stub columns (CFSSC) and one L-shaped steel hollow column. The nonlinear damage process and the failure mode of the specimens were described. The influences of structural parameters on the axial bearing capacity of L-shaped CFSSCs were investigated. These structural parameters included the width-to-thickness ratio of the steel plate, with or without stiffeners, and the limb length. The experimental results indicated that the confined effect of the steel tube on the infilled concrete was more distinct for an L-shaped CFSSC with a short limb than one with a long limb. For an L-shaped CFSSC with a short limb, the stiffeners may improve the ductility of the specimens to the extent of 1.5 times although they were less effective in improving the bearing capacity. On the other hand, the stiffeners were ineffective in both improving bearing capacity and ductility of the L-shaped CFSSC with a long limb.

Keywords: L-shaped concrete-filled steel column; stub column; axial loading; ultimate bearing capacity; ductility

1.   INTRODUCTION

L-shaped columns are commonly used as corner columns in structural buildings. For instance, the wall thickness in a medium-rise building is relative thin. As a result, the cross-section of beams and columns are usually larger than the wall thickness in a common frame structure. This phenomenon weakens the integrity of the overall space and brings inconvenience to decoration as well. Limb width of a special shaped column (e.g. T-shaped and L-shaped columns) is within 100 to 300 mm, resolving the problem of column projection. Because of asymmetry of two principal axes, the calculation is complicated for an L-shaped column. Besides, additional moment of torsion follows horizontal forces (e.g. wind forces or earthquake actions) due to non-coincidence of torsional center and mass center. In addition, uncertainty of the direction of horizontal forces imposed results in the difficulty of determining orientation of the applied forces in a test. This leads to different properties in terms of bearing capacity, ductility and stiffness for special shaped columns according to different loading directions subjected. Therefore behavior of special shaped column is a difficult issue.

So far, a comprehensive research is carried out for structures with special shaped reinforced concrete columns. Some cities in China, e.g. Tianjin and Guangzhou, have issued local specifications for special shaped reinforced concrete columns[1,2]. The national standard "Technical specification for concrete structures with specially shaped columns" (JGJ149-2006)[3] has also been issued and implemented based on the local specifications. However it is still lack of basic theoretical research on special shaped concrete-filled steel columns (CFSCs). The research results reported are also limited in the world. Of those, Tongji University performed experimental and theoretical research on the seismic behavior of L-shaped CFSCs[4]. However, this kind of members took no consideration of effective confinement of in-filled concrete. In addition to the rectangular ones[5], South China University of Technology carried out experimental study on axial behavior of L-shaped and T-shaped concrete-filled steel tubular stub columns with binding

bars[6-8]. The current application of special shaped concrete-filled steel structures is known as New China Building in Guangzhou[9,10]. L-shaped and T-shaped concrete-filled steel tubular stub columns with binding bars are adopted for part of columns in the underground structures. In view of the distinguished efficiency of concrete-filled steel structures in economic and social aspects, it is necessary to carry out further research on force and deformation capacities of special shaped CFSCs.

2.   TEST PROGRAM

2.1   Test Specimens

In medium- and high-rise buildings, the story height is generally 2.8m. The limb width of special shaped columns is taken as the wall thickness, generally 200mm. A scaling factor of 1:2 was considered. The total clear lengths of specimens were 800mm and 1200mm; the limb width was 100mm; the limb lengths were 200mm and 300mm. In previous concrete-filled stub column experiments, swelling of the outer steel plate was a common failure mode of specimens. It indicates that the outer steel plates are buckled as two sides of the steel plate are fixed-supported and the others are simply- or fixed-supported according to the actual condition. In the national code for design of steel structures [11], the steel plate width-to-thickness ratio under such condition is limited as 60. Hence designed width-to-thickness ratios of 50 ($t = 4$ mm) and 60 ($t = 5$ mm) were adopted, for L(R)2 series and L(R)3 series. The dimension and the cross section of the specimens are summarized in Figure 1 (only those with 200mm limb length are presented as space is limited). Detailed parameters are listed in Table 1.
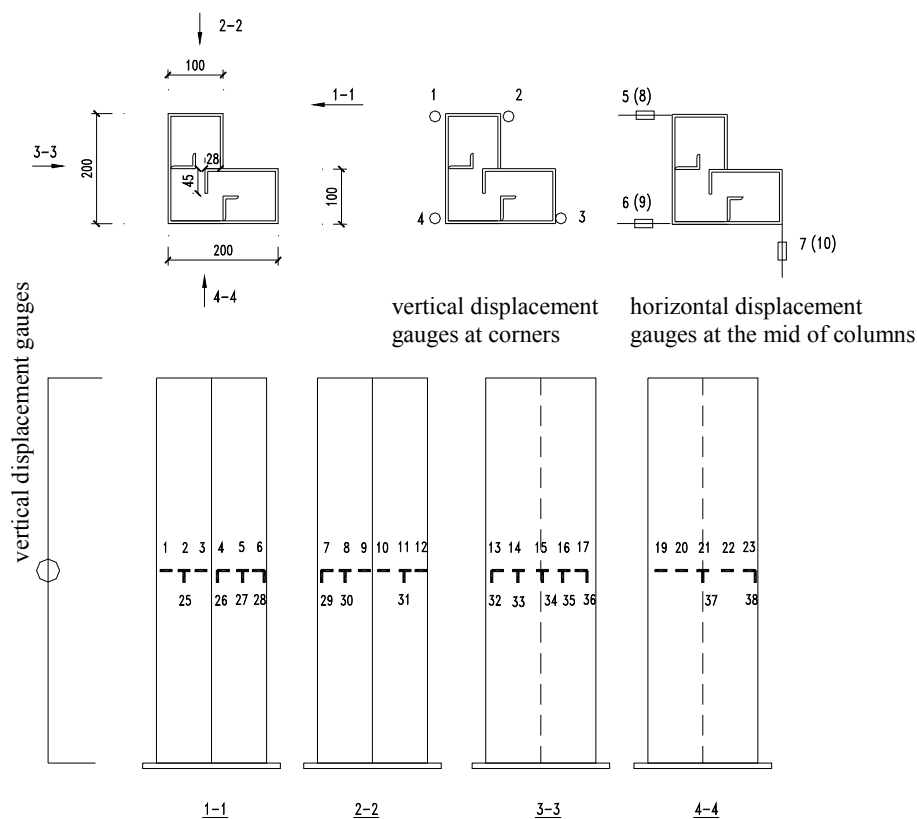
Note: the gauge arrangement is similar for the specimens with limb length of 300mm.

Figure 1. Specimen Dimensions and Gauge Arrangement

Table 1. Summary of Specimens

No.	Limb length, B (mm)	Total length, L (mm)	Steel plate thickness, t (mm)	Concrete grade
LR2-a	200	800	4(3.62)	C40
LR2-b	200	800	4(3.62)	C40
L2	200	800	4(3.62)	C40
LR3-a	300	1200	5(4.62)	C40
LR3-b	300	1200	5(4.62)	C40
L3	300	1200	5(4.62)	C40
LR3-H	300	1200	5(4.62)	–

Note: L represents L-shaped column; R represents stiffened rib in steel tubes; H represents hollow steel column; the numbers in parentheses are the measured values of steel plate thickness.

2.2   Material Properties

1) Steel plate properties

The plates for L-shaped concrete-filled steel stub columns were Q235 steel. According to the national standard "Metallic materials-test pieces for tensile testing" (GB6397-86)[12], three test pieces were taken from each steel plate of different plate thickness along and perpendicular to the rolling direction. Tensile test was performed in the lab of material mechanics, Tongji University. The obtained results are listed in Table 2.

Table 2. Tensile Test Results

Coupon	Yield strength MPa	Tensile strength MPa	Elastic modulus $\times 10^5$ MPa	Elongation %
4mm	310	465	2.030	24
5mm	295	442	2.117	37

2) Concrete properties

The concrete grade was C40 in the test. The ordinary portland cement was used; the maximum grain size of crushed stones was 20mm; common medium sand was used. All the specimens were casted in one day. At the same time, three 150×150×150mm cubic coupons were fabricated and were cured under the same conditions of the specimens. After curing period of 28 days, cube compressive strength tests were conducted according to the national standard "Standard for test method of mechanical properties on ordinary concrete"(GB/T 50081-2002)[13]. The average cube compressive strength, f_{cu}, was 60.1 MPa as obtained from the tests. The axial compressive strength, f_{ck}, which was converted from f_{cu} was 45.7 MPa.

2.3   Test Setup and Gauge Arrangement

Axial compressive tests were conducted by a 500 ton test machine in the static experimental laboratory, Tongji University. The gauge arrangement was shown in Figure 1. At the four corners of each specimen, four vertical displacement gauges were installed to record the total vertical deformation of the column. Three horizontal displacement gauges were installed at the middle and top of the column, respectively, to measure the torsion angle of the cross sections. Strain gauges numbered from 1 to 23 (18 was not present) were used to inspect circumferential strain of the steel tube while strain gauges numbered from 25 to 38 were used to inspect its longitudinal strain.

2.4   Loading Sequence

Prior to imposing axial compressive force, the specimen was aligned to the geometrical center. Then, it was aligned physically according to the values of vertical displacement and longitudinal strain. Loading should not be formally imposed until instruments worked normally under the preloading (about 40 percent of the ultimate load estimated). Stepped loading was performed based on the estimated ultimate load. Before 50 to 60 percent of the estimated ultimate load, the stepped loading imposed was 1/15 of the estimated ultimate load. An interval time of two minutes was taken at every two loading levels in order to let deformation fully developed. After that, the nonlinear behavior of specimens was distinct. Consequently, a data acquisition system was used for digital signal acquiring and processing until specimen failure.

3.   TEST PROCESS AND ANALYSIS OF TEST RESULTS

3.1   Test Damage Process and Failure Mode

The damage process were almost analogous for all specimens, basically experiencing several phases such as elastic phase, small swelling at steel plate of the limb, obvious swelling at steel plate of the limb, and remarkable strength deterioration. The failure mode of the specimens is related to the limb length, with or without stiffeners and with or without infilled concrete.

For L-shaped CFSC with limb length of 200mm, limb width of 100mm, and relative small plate width-to-thickness (LR2-a and LR2-b), minor flaking of the mill scale was visually identifiable, which was accompanied by a continuous noise, when the imposed load is about 90 percent of the estimated ultimate load. As the imposed load was increased, the onset of web buckling was evident. As the imposed load was increased toward the ultimate load, two to four buckling waves occurred. The deformation increased sharply. The test was then stopped.

For L-shaped CFSC with limb length of 300mm, limb width of 100mm, and relative large plate width-to-thickness (LR3-a and LR3-b), the test process was similar to the L(R)2 series specimens during the elastic phase. As the imposed load was increased toward the ultimate load, the first occurrence of the swelling was locally at the concave face. Then swelling occurred at every faces. The deformation increased sharply, especially at the convex face. However no buckling was observed at the ends of the limbs.

On the counterpart, local buckling occurred for the L-shaped CFSC without stiffeners (L2 and L3). With the increase of the applied load, buckling phenomenon became more and more obvious. The specimen failed when the out plane deformation reached some extent.

The failure mode of the L-shaped hollow steel column possessed the following features: (1) if a half wave occurred in one of the two big faces, then a total wave must occur in the other big face, where nodal line was formed in the position of the stiffener; (2) at the bottom of the column, two limbs, which were combined as a plate member, formed one half wave in the longitudinal direction; and (3) at the top and the medium of the column, the failure mode was analogous to the rectangular hollow steel tubes. That is, two counter plates swelled, and the other two counter plates sunk. Therefore, it can be concluded that due to the lack of the lateral supporting of concrete the hollow steel tube tends to local buckling and the ultimate force decreased sharply despite the small width-to-thickness ratio resulted by the stiffeners.

Figure 2 plots the typical failure modes for L-shaped CFSCs. The ultimate bearing capacities, N_u^{exp}, are listed in Table 3, where f_y represents yield strength of steel plate, A_c and A_s represent the cross section area of concrete and steel, respectively.

Table 3. Ultimate Bearing Capacities of L-shaped CFSCs

No.	f_{ck} MPa	A_c mm^2	f_y MPa	A_s mm^2	N_u^{exp} kN
LR2-a	45.7	26087	310	3913	2568
LR2-b	45.7	26087	310	3913	2892
L2	45.7	26836	310	3164	2460
LR3-a	45.7	43190	295	6810	4024
LR3-b	45.7	43190	295	6810	3908
L3	45.7	44133	295	5867	3708
LR3-H	--	--	295	6810	1604

(a)   (b)

Figure 2. Failure Modes: (a) LR2-a; (b)LR3-a

3.2   Analysis and Discussion of Test Results

1) Force versus vertical displacement ratio curves (No.1~4 vertical displacement gauges)

The forces versus vertical displacement ratio relationships are shown in Figure 3. From Figure 3(a), it is found that ultimate bearing capacity differs in LR2-a and LR2-b due to the loading eccentricity. The force verses vertical displacement ratio curves indicate that: (1) prior to the 70 percent ultimate force, all curves were closely analogous with each other and almost kept straight (in an elastic state); (2) the first inclination occurred due to the development of plastic region; (3) as the imposed load reached 90 percent of the ultimate load, plastic flow occurred. Slight swelling of steel plates was visually observed due to the compressing of the concrete. Vertical deformation increased severely, and the second inclination occurred; (4) as vertical displacement ratios of LR2-a and LR2-b approximated 4312×10^{-6} and 4676×10^{-6} respectively, peak values of the specimens were reached; (5) from then on, concrete cracked and expanded and steel tub bulged. The relationships of L(R)2 specimens fell gradually and formed a relative long horizontal segment at 68 to 78 percent of ultimate force due to the bonding effect of the stiffener.

L2 reached the ultimate force when vertical displacement ratio was 3892×10^{-6}. Without stiffeners, partly due to the small flexural rigidity of the steel plates, it was difficult to control concrete plastic flow. Thus the curve started to ramp when the peak value was reached. With the increase of the deflection of the steel tube, lateral stress increased rapidly. This meant the constrained effect on the concrete core was enhanced. As a result, the slope of the curve decreased when imposed load was 1744kN. It showed good ductility of the specimen.
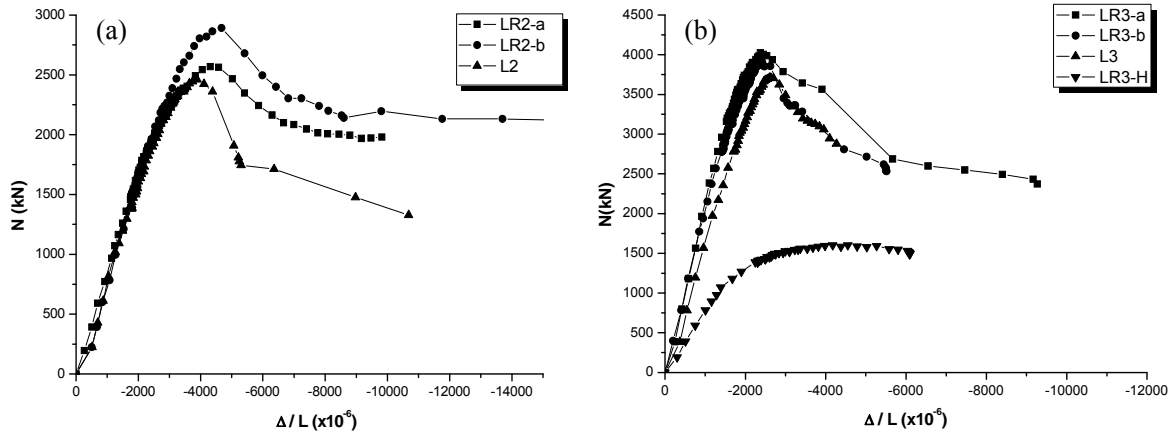
Figure 3. Force Versus Average Vertical Displacement Ratio Curves:
(a) L(R)2 Series; (b) L(R)3 Series

It can be concluded that for an L-shaped CFSSC with a short limb, the stiffeners may improve the ductility of the specimens although they are less effective in improving the force capacity.

As seen from Figure 3(b), it is found that the force-average vertical displacement ratio curves of LR3-a and LR3-b were almost analogous. The relationships indicated that: (1) prior to the 80 percent ultimate force, all curves almost kept straight. The slope and ultimate force of L3 were relative smaller than those of LR3-a and LR3-b; (2) local buckling of the steel plate occurred since the plate width-to-thickness ratio was large. Especially for L3, its maximum value of the width-to-thickness ratio was 65, exceeding the limit value of 60 for uniaxial compressive plate with two edges fixed. The ultimate force was reached as the displacement ratio was 2500×10^{-6}; (3) the relationships of three specimens were almost analogous and forms a relative long horizontal segment at 60 to 70 percent of the ultimate force. It showed good ductility of the specimen.

It can be concluded that the stiffeners are ineffective in both force capacity and ductility of the L-shaped CFSC with a long limb.

Comparison of force verses vertical displacement ratio curves between the hollow steel tube and concrete-filled steel columns indicated that the latter present better stiffness, strength and stability.

2) Longitudinal strain of steel tube (No.25~38 strain gauges)

To study the longitudinal strain and development of plastic region on the cross section, force-average longitudinal strain curves are plotted in Figure 4. As seen from two plots, it is found that the average longitudinal strain of L(R)2 specimens was about 2500µε as the imposed load reached the ultimate force. For LR2-b, it was 4000µε. The descending branch of the force-average longitudinal strain curves were gradually. As the imposed load reached ultimate force of L(R)3, the average longitudinal strain was about 2000µε. Passing over the peak value, slopes of the curves decreased sharply without the horizontal segment. This indicated that the stress distributed uniformly in L(R)2 specimens. Deformation fully developed. However the stress was distributed non-uniformly in L(R)3 specimens. Limb ends sustained most of the external force. At the ultimate force, part of the cross section of these specimens did not yield or just reached the yield region.
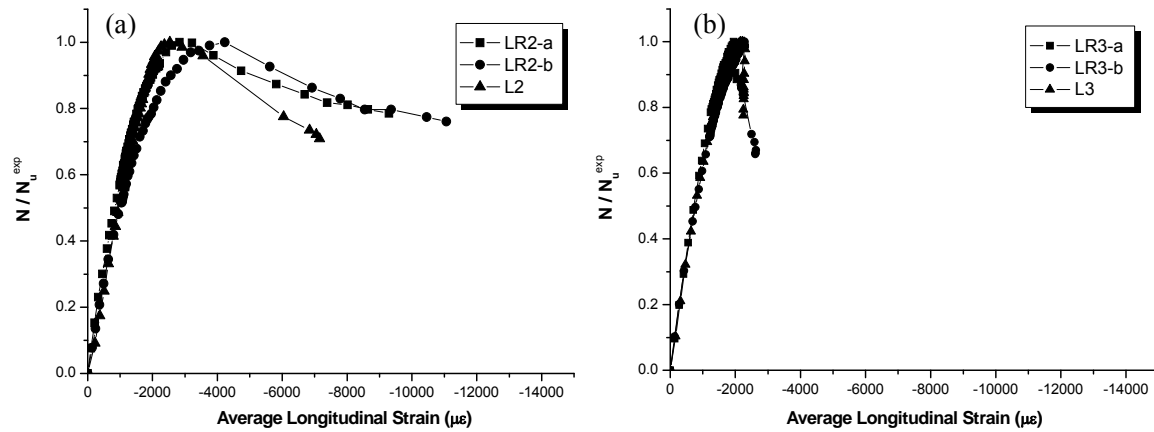
Figure 4. Force Versus Average Longitudinal Strain Curves: (a) L(R)2 series; (b) L(R)3 series

3) Lateral strain of steel tube (No.1~23 strain gauges)

In order to investigate the restrained effect of the steel tube on the concrete during different loading phase, experimental results are organized in the manner of Figures 5-7. Lateral strains of steel tubes were plotted against 0.2, 0.4, 0.6, 0.8, and $1.0N_u$. The number in the abscissa represents the serial number of strain gauges.
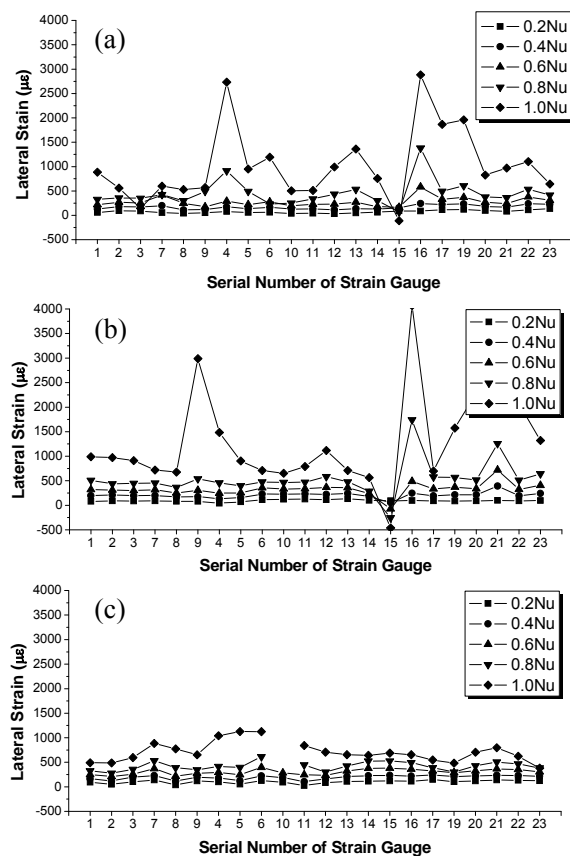
Figure 5. Lateral Strain of Steel Tubes for
L(R)2 Series: (a) LR2-a; (b) LR2-b; (c) L2
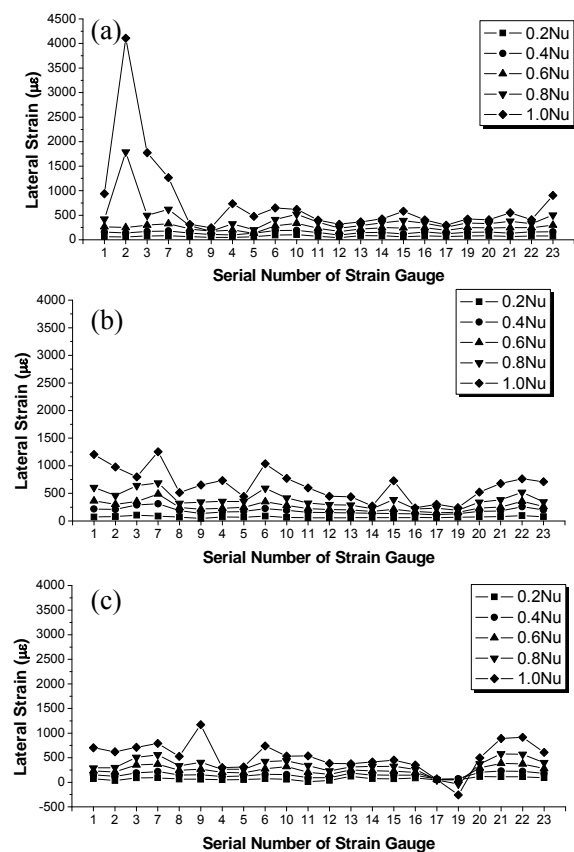
Figure 6. Lateral Strain of Steel Tubes for
L(R)3 Series:(a) LR3-a; (b) LR3-b; (c) L3

The stress distributed uniformly on the cross section prior to 0.8 N_u. At final loading phase, lateral stresses in the steel tube increased due to the occurrence of the concrete plastic flow as well as the compressive effect on the steel tube. The restrained force developed, which was one of the factors that increased the concrete strength.

4) Torsion of the cross section (No.5~10 lateral displacement gauges)

Due to non-coincidence of torsional center and mass center, additional moment of torsion was evidently yielded by the secondary moment resulted from a vertical force and initial defects and initial eccentricities.

Figure 7. Lateral Strain of Steel Tubes for LR3-H

To investigate the torsional parameters of L-shaped CFSCs, horizontal displacement gauges were placed at the middle and the top of the specimens to record horizontal displacement. Then the torsional angle of the limb in Figure 8 was calculated as: displacement difference between horizontal displacement gauges at the same horizontal plane was divided by the length of the section side.

From Figure 8, it can be seen that the torsional angles of L-shaped CFSCs were small, within the range of 1 to 2×10^{-3} radian. The torsional directions of the cross sections at the top and the middle of the column were basically reverse.

Figure 8. Torsional Angles of the Cross Section: (a) LR2-b; (b) LR3-b

4.   CONCLUSIONS

Based on the failure process and analysis of the experimental results, the following conclusions are drawn:

(1) In view of the failure mode, the stiffened specimens with short limbs failed in the manner of compressive fracture. Several buckling waves occurred in the middle of the column along the longitudinal direction. As seen from the longitudinal strain curves of the steel tube, the cross section sustained external forces uniformly. Full cross section yielded at the ultimate load. Thus force capacity was improved greatly. For the specimens with long limbs, local buckling only occurred at the top of the column. Parts of steel tube yielded at the ultimate load. In view of this, it is suggested that the limb length-to-width ratio should not be larger than 2.0 in practices for CFSSC with different configurations in order to obtain full bearing capacity.

(2) As seen from the force versus average vertical displacement ratio curves, curves kept straight prior to 70 to 80 percent of the ultimate load. For an L-shaped CFSSC with a short limb (LR2-a, b), the stiffeners may improve the ductility of the specimens although they are less effective in improving the force capacity. On the other hand, the stiffeners are ineffective in both force capacity and ductility of the L-shaped CFSSC with a long limb (LR3-a, b).

(3) Compared to L(R)2 specimens, local buckling concentrated in the middle and the top of L(R)3 specimens due to the large width-to-thickness ratio. Stress in the middle of the column plate was lower than the yield strength. Material strength could not fully used. This was also one of the main factors that increased the force capacity of the specimens.

(4) The lateral stress curves had several peaks, i.e. buckling waves, for specimens with short limbs. For specimens with long limbs and without stiffeners, the lateral stress was relatively distributed uniformly. This test phenomenon indicated confined effect of the steel tube on the infilled concrete was more distinct for an L-shaped CFSSC with a short limb than one with a long limb, and with stiffeners than without stiffeners.

(5) The torsional angles of L-shaped CFSSCs are small, within the range of 1 to 2×10^{-3} radian.

ACKNOWLEDGMENTS

REFERENCES

[1]   Committee of Urban-rural Development of Tianjin, "Technical Specification for Lightweight Framed Structures with Special-shaped Reinforced Concrete Columns of Large Bay Dwelling House (DB29-16-98)", China Architecture & Building Press, 1998.

[2]   Guangdong Association for Engineering Construction Standardization, "Design Specification for Special-shaped Reinforced Concrete Columns (DBJ/T15-15-95)", Technology and Standardization, 1995.

[3]   Ministry of Housing and Urban-Rural Development of the People's Republic of China, "Technical Specification for Concrete Structures with Specially Shaped Columns (JGJ 149-2006)", China Architecture & Building Press, 2006.

[4]   Wang, D. and Lv, X.L., "Experimental Study on Seismic Behavior of Concrete-filled Steel T-section and L-section Columns", Journal of Building Structures, 2005, Vol. 26, No. 4, pp. 39-106.

[5]   Cai, J. and He, Z.Q., "Axial Load Behavior of Square CFT Stub Columns with Binding Bars", Journal of Constructional Steel Research, 2006, Vol. 62, No. 5, pp. 472- 483.

[6]   Chen, D.M., "Basic Mechanics Study on Behavior of Special-shaped Concrete-filled Steel Tubular Columns with Binding Bars", South China University of Technology, 2000.

[7]   Li, Z.J., Cai, J., Tan, Z.D. and Chen, D.M., "Experimental Research on Behavior of Special-shaped Concrete-filled Steel Tubular Columns with Binding Bars", Engineering Mechanics, 2001, Vol. A02, pp. 124-129.

[8]   Long, Y.L. and Cai, J., "Experimental Investigation into Axial Compressive Behavior of L-shaped Concrete-filled Steel Tubular Stub Columns with Binding Bars", Journal of South China University of Technology (Natural Science Edition), 2006, Vol. 34, No.11, pp.87-92.

[9]   Chen, Z.J. and Lin, Z.F., "Dynamic Analyses of Test Model for New China Building in Guangzhou", World Information On Earthquake Engineering, 2002, Vol. 18, No. 3, pp.102-105.

[10]   Chen, Z.B., Chen, X., Ye, Q.Y. and Luo, C., "Structural Design of Guangzhou New China Mansion", Journal of Building Structures, 2000, Vol. 21, No. 3, pp. 2-9.

[11]   Ministry of Housing and Urban-Rural Development of the People's Republic of China, "Code for Design of Steel Structures (GB 50017-2003)", China Architecture & Building Press, 2003.

[12]   China State Bureau of Standards, "Metallic Materials-test Pieces for Tensile Testing (GB6397-86)", China Architecture & Building Press, 1998.

[13]   Ministry of Housing and Urban-Rural Development of the People's Republic of China, "Standard for Test Method of Mechanical Properties on Ordinary Concrete (GB/T 50081-2002)", China Architecture & Building Press, 2003.

EXPERIMENTAL STUDIES OF LOAD CAPACITIES OF DOUBLE-LAYER SHORING SYSTEMS

Jui-Lin Peng[1,*], Pao-Li Wang[2], Ying-Hua Huang[3] and Tsung-Chieh Tsai[3]

[1] *Prof., Dept. of Constr. Engrg.,*
Yunlin Univ. of Sci. and Technol., Douliu, Yunlin, 64002 Taiwan, ROC.
[2] *Ph.D. Student, Dept. of Graduate School of Eng. & Tech.,*
Yunlin Univ. of Sci. and Technol., Douliu, Yunlin, 64002 Taiwan, ROC.
[3] *Assistant Prof., Dept. of Constr. Engrg.,*
Yunlin Univ. of Sci. and Technol., Douliu, Yunlin, 64002 Taiwan, ROC.
*(Corresponding author: E-mail: pengjl@yuntech.edu.tw)

ABSTRACT: The most common shoring system used in mid-headroom buildings in Taiwan is the double-layer shoring system made of wooden shores or adjustable steel-tube shores or a combination of both. This study identifies the causes of shoring system collapse and proposes solutions that ensure the safety and stability of double-layer shoring systems. The test results show that the load capacity is the largest for a double-layer shoring system set by the lateral supports along the four sides. In terms of connections of horizontal stringers, the failure models of "single overlap" and "double overlap" are extremely similar. The shoring members in the system tend to move toward the overlap position after loading. The single butt connection is recommended to replace these two overlapping connections in construction sites since the former provides higher load capacity in shoring systems. In terms of the eccentric load, load capacity when shoring arrangements of the top and bottom stories are not directly symmetrical is lower than that of the top and bottom stories with a directly symmetrical arrangement. The load capacity is increased considerably when a shoring system is reinforced with V-shaped inclined braces. The load capacity of a shoring system with a setup combining wooden shores and adjustable steel-tube shores is higher than that of a system reinforced with wooden shores only.

Keywords: Adjustable steel tube shore; collapse; double-layer shoring system; load capacity; shoring; wooden shore

1. INTRODUCTION

During construction, various temporary shoring structures are utilized to support construction loads on formwork before fresh concrete reaches its designed strength. Such falsework frequently adopts different shoring systems based on different construction site conditions. Construction sites in Taiwan are typically one of three types—low headroom, medium headroom and high headroom—based on different internal clearance heights of buildings. In Taiwan, low, medium and high headroom is defined as headroom smaller then 4 m, between 4 m and 7 m and greater than 7 m respectively.

Two types of shores (Figure 1), wooden shores and adjustable steel-tube shores, are often used at mid-clearance construction sites in Taiwan, mainly because of cost considerations. Double-layer shoring systems made of wooden shores, adjustable steel-tube shores or a combination of both are employed depending on different internal headroom heights of buildings. To construct a double-layer shoring system, horizontal stringers are first laid on vertical shores in a side-by-side manner, and then more vertical shores are installed on horizontal stringers to form a double-layer system (Figure 2). This support structure is nicknamed, "Snake-Melon Shed" in Taiwan; in this study, this system is called, "Double-layer Shoring System."

Cross section	d$_1$ (mm)	d$_2$ (mm)	D(mm)	T(mm)
A-A	58.82	56.295	-	-
B-B	-	-	60.14	2.21
C-C	-	-	48.04	2.31
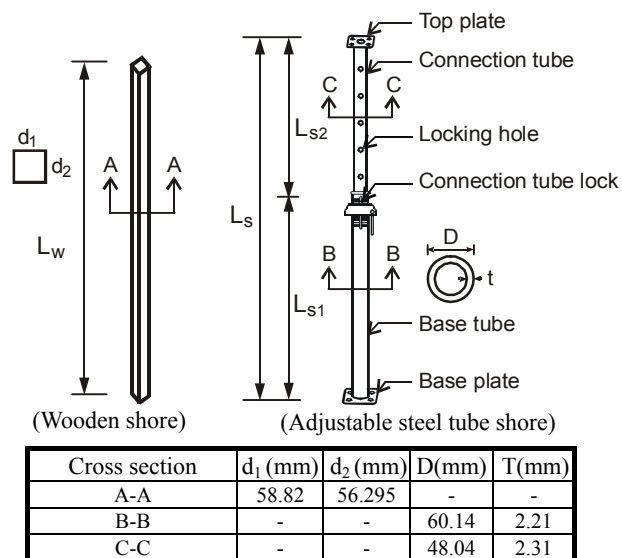
Figure 1. Dimensions of Wooden Shore and Adjustable Steel Tube Shore
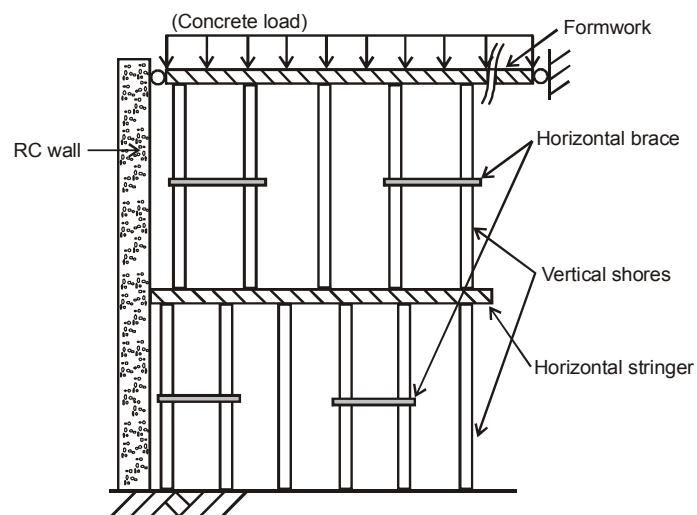
Figure 2. Setup of a Double-layer Shoring System with Horizontal Stringers and Braces

Figure 3. Collapse Scene at Construction Site of
Xinzhu Chemical Engineering Warehouse Mall, Taiwan

Since design specifications in Taiwan do not cover this type of temporary shoring system, workers rely on their experience when setting up such shores. Due to budget constraint, constructors usually use a relatively low-cost double-layer shoring system as falsework, instead of the more expensive steel-tube scaffolding structure. However, the failure of double-layer shoring systems frequently results in collapse, causing casualties and enormous loss of life and property. For example[1] (Figure 3), the collapse of a double-layer shoring system at the Xinzhu Chemical Engineering Warehouse Mall, Taiwan, killed one worker and seriously injured seven others.

Many studies have investigated the structural behaviors of steel-tube scaffolds as falsework. Hadipriono and Wang [2] examined failure causes of temporary shoring systems and concluded that failures usually occurred during concreting. Kao [3] conducted an experimental study on modular units of steel-tube scaffolds using reduced models. Leu et al. [4] calculated the critical loads of shoring systems based on structural dynamic features and the natural frequencies of steel-tube scaffolding structures. Chan et al. [5,6,7,8] proposed a non-linear analysis method for checking of stability. Peng et al. [9,10,11] analyzed construction safety and failure models of scaffolding falsework for high-clearance floors with a headroom exceeding 7 m.

In a study of falsework for multi-story buildings, Mosallam and Chen [12] and El-shahhat et al. [13] obtained notable analytical results regarding shoring and re-shoring. In a study on the effects of wooden shores and adjustable steel-tube shores used in one-layer shoring systems, Peng [14] concluded that the leaning column effect has significant impact on load capacity of one-layer shoring systems. In the study of double-layer shoring systems, Peng [15] numerically analyzed the critical loads and failure behaviors of various shoring systems and established a simplified analytical model. Lemessurier formula [16] was used to calculate system critical load in the study [15].

In the past, studies of falsework generally investigated system critical load and the failure model of steel-tube scaffolding structures, whereas studies of double-layer shoring systems were conducted only for the purpose of analyses. The analytical results obtained required verified via further tests. This study conducts loading tests for double-layer shoring systems in mid-clearance structures to identify the failure models of double-layer shoring systems. Solutions for improving the safety of double-layer shoring systems are based on research results.

2.   RESEARCH OBJECTIVES AND SIGNIFICANCE

This study explores the load capacities of double-layer shoring systems via experimental tests to identify collapse causes and provide improvement solutions to ensure construction safety. Test configurations of double-layer shoring systems are based on actual setups at construction sites in Taiwan. The highlights of this study are as follows.

2.1   Effect of Lateral Supports

Buildings typically have openings such as entrances, windowsills or courtyards. During construction, horizontal stringers of double-layer shoring systems often cannot be linked by supports connected to reinforced concrete walls or columns. Additionally, when constructing such structures as gas stations and pavilions, the shoring systems are normally either laterally supported only on one side or unsupported. This study explores the effects of lateral supports on load capacity of double-layer shoring systems.

2.2   Effect of Joint Forms of Horizontal Stringers

When a building construction area is large, a method of connection to install an entire shoring system is needed. When setting up double-layer shoring systems on construction sites, workers often mount horizontal stringers on the top of bottom-story shores and do not pin the joint layer of horizontal stringers with nails for the sake of convenience. This study explores the effects of different joint forms of horizontal stringers in double-layer shoring systems.

2.3   Effect of Horizontal Braces

This study explores the effects of horizontal braces on load capacity of shoring systems by simulating practical bracing reinforcement on actual construction sites. From the viewpoint of structural stability, the collapse of entire double-layer shoring systems is commonly caused by lateral movement of horizontal stringers. The "leaning column effect" is likely when horizontal stringers move laterally [16]. At most construction sites, double-layer shoring systems are reinforced with "lateral braces." Whether or not this bracing reinforcement enhances the stiffness of wooden shores is worthy of investigation.

2.4   Effect of Eccentric Loads on Shores

Axial force transfer will be interrupted in double-layer shoring systems that have vertical shores for the top and bottom stories that are not directly symmetrical. Thus, horizontal stringers between the top and bottom stories bear the vertical force directly transferred from top-story shores, resulting in bending failure of horizontal stringers and likely leading to failure of the overall shoring system.

When shores are set up in a double-layer shoring system on construction sites, workers are not expected to set the top- and bottom-story shores on the same axial line. This study investigates the load capacities and failure models of double-layer shoring systems with eccentric loads and analyzes whether axial force indirectly transferred significantly impacts load capacity.

2.5   Effect of Inclined Boundaries

Designers in some cases use slant planes for esthetic considerations (e.g., car ramp lanes and auditoriums). In this case, the boundaries of a double-layer shoring system may be planes inclined at various angles. This study explores the effects of inclined boundaries on the load capacity of double-layer shoring system via laboratory tests.

2.6   Effect of Combined Shores

Due to budget constraints and the available length of shores, many double-layer shoring systems are set up in such a manner that the bottom story is made of adjustable steel-tube shores, while the top story is made of wooden shores. Through testing, this study investigates the difference in load capacity between double-layer shoring systems using both wooden shores with adjustable steel-tube shores and those using wooden shores only.

2.7   Effect of Different Reinforcements

Most workers strengthen shoring systems on construction sites based on experience; but they may not know the load capacity after reinforcement. This study explores the effects of various reinforcements for double-layer shoring system based on a comparison with existing reinforcements on construction sites.

3.   MATERIAL PROPERTY AND TEST PLAN

3.1   Material Property

The wooden shores and adjustable steel-tube shores selected for this study are commonly used in Taiwan. The material properties of the shores are as follows. (1) The wooden shores are made of Kapur. Their average cross section is 5.6295×5.882 cm; average static bending elastic modulus (equivalent to Young's modulus of elasticity) is $1.247×10^6$ N/cm^2 (127,163 kgf/cm^2). (2) The properties of the adjustable steel-tube shores are as follows. The average diameter and thickness of the base tube are 60.14 mm and 2.21 mm, respectively. The average diameter and thickness of connecting tubes are 48.04 mm and 2.31 mm, respectively (Figure 1). Young's modulus of elasticity is $2.11×10^7$ N/cm^2 (2,150,000 kgf/cm^2).

3.2   Test Plan

Figure 4 shows the definition of in-plane and out-of-plane adopted in this study. The tubes are numbered clockwise as tube 1, tube 2… to tube 6 (Figure 4). Failure of the double-layer shoring system involves problems of structural stability. To investigate the failure behavior of a shoring system, axial force and lateral displacement are considered two key measurements. The axial force is measured using load cells placed in the fillister between the load holder and oil-pressure piston. Lateral displacement is measured using two rulers set on the horizontal stringers and two theodolites are used to measure the lateral displacements of systems in two directions. Test configurations of this study are as follows.
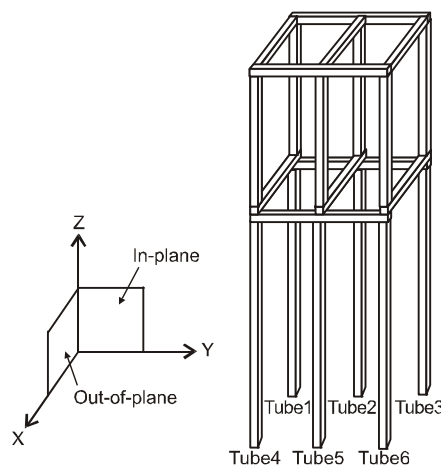
Figure 4. Definition of In-plane and Out-of-plane of Double-layer Shoring Systems

3.2.1   Isolated wooden shore

This study investigates the load capacity of isolated wooden shores as a basis for comparisons and for subsequent bearing-capacity tests on double-layer shoring systems. The wooden shores are 3.0 m long. Load capacity is measured via loading tests that meet the CNS-453 code [17]. However, the top-end boundary conditions of bottom-story shores in a double-layer shoring system are horizontal stringers. This boundary condition likely affects the load capacity of wooden shores. Therefore, the top-end boundary condition is used as horizontal stringers to minimize the real construction conditions.

3.2.2 Shoring systems reinforced with lateral supports

This study conducts tests with various support conditions to identify the effects of lateral supports on load capacity of double-layer shoring systems. Three cases are tested: (A) Double-layer shoring systems with no lateral supports: the double-layer shoring system is set up with 6 wooden shores on both the top and bottom stories. The top shores are 1.8 m long and the bottom shores are 3 m long (Figure 5(a)). The shores for the top and bottom stories are placed 60 cm apart. Horizontal stringers are placed at the joints of the top and bottom stories. Without any lateral supports, the shoring system alone bears vertical loads. The bottom end of the shoring system is placed on concrete floor and the top end is fastened with a horizontal wooden frame to simulate the most common scenario on construction sites. (B) Double-layer shoring systems with lateral supports on two sides: the basic double-layer shoring system is reinforced with lateral supports on the weak axial direction, allowing the system to have lateral displacement in one direction only (Figure 5(b)). (C) Double-layer shoring systems with lateral supports on four sides: the basic double-layer shoring system is reinforced with longitudinal supports and lateral supports on four sides, such that the system bears lateral forces in both directions from supports (Figure 5(c)). To avoid horizontal movement, lateral supports, 60-cm adjustable steel tubes, were connected to the horizontal stringers in the basic shoring system (Figure 5(c)).

(a) unsupported   (b) supported on two sides   (c) supported on four sides
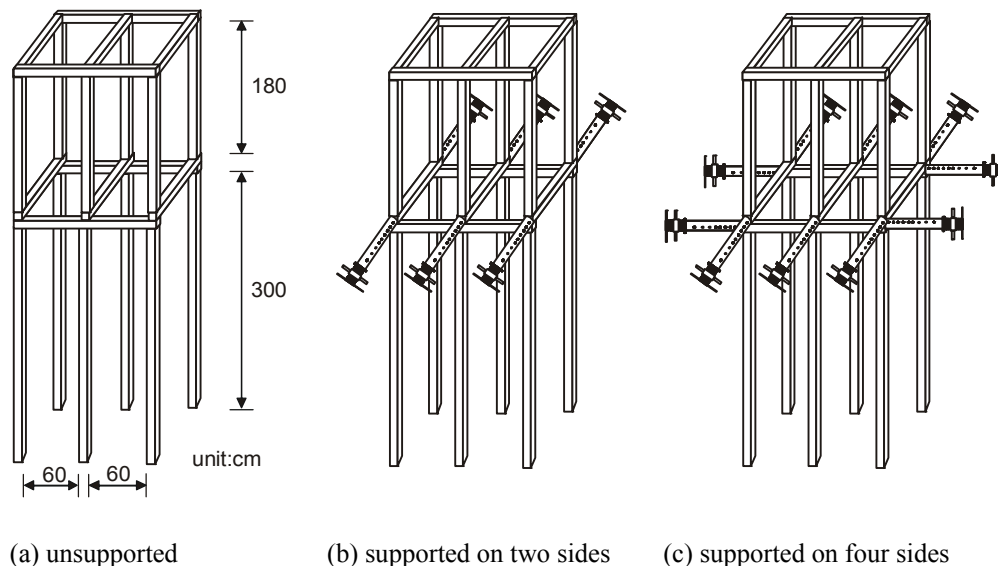
Figure 5. Arrangements of Double-layer Shoring Systems with Varied Lateral Supports

3.2.3 Varied connection forms of horizontal stringers

This study explores the effects of various joint forms for horizontal stringers in double-layer shoring systems. The connection at the joint layer of horizontal stringers can be of two types—"butt connections" and "overlap connections." Three connection configurations for double-layer shoring systems are considered based on typical conditions on construction sites: (A) a single butt fastened with a 30-cm board connected to horizontal stringers (Figure 6(a)); (B) a single overlap without any fastening form connects horizontal stringers (Figure 6(b)); and, (C) double overlaps without any fastening form connecting horizontal stringers (Figure 6(c))—this is a common joint used for horizontal stringers on construction sites in Taiwan. These three tests are all conducted with lateral supports on four sides.

(a) single butt   (b) single overlap   (c) double overlaps
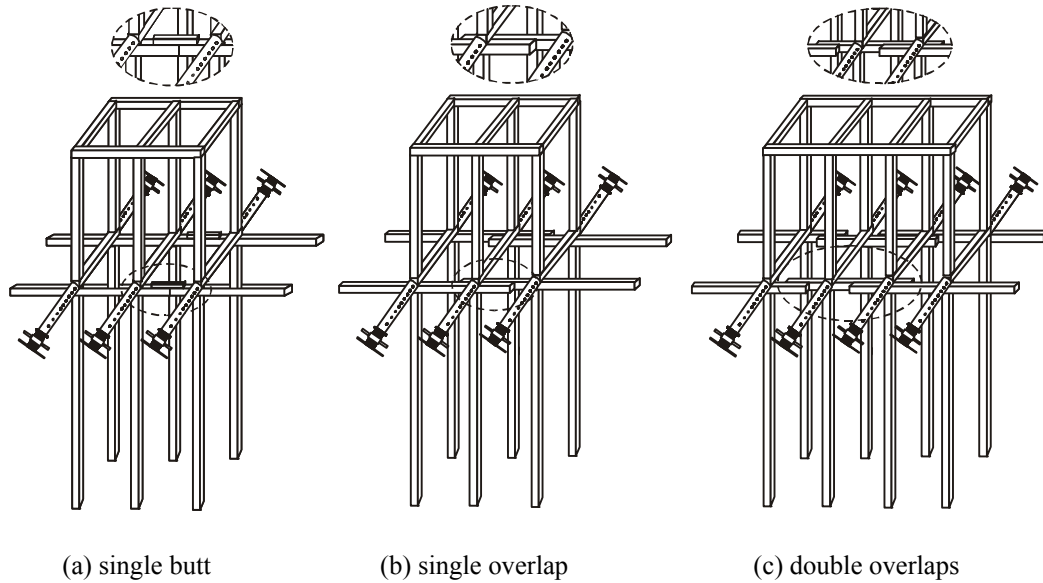
Figure 6. Arrangements of Double-layer Shoring Systems with Varied Connection Forms
for Horizontal Stringers

3.2.4 Shoring systems reinforced with closed-form horizontal braces

Four horizontal braces form the rectangular hollow to simulate the longitudinal and lateral braces used on construction sites. These horizontal braces are only tied to vertical shores without objects to resist lateral forces. This test investigates reinforcement effects of these horizontal braces. The test is configured by tying horizontal braces to tubes 1, 2, 4 and 5 of the bottom-story wooden shores with wires at a height of 1.5 m above the ground, and setting up lateral supports on the weak plane (Figure 7). The horizontal wooden braces are 80 cm long, 6 cm wide and 3 cm thick.
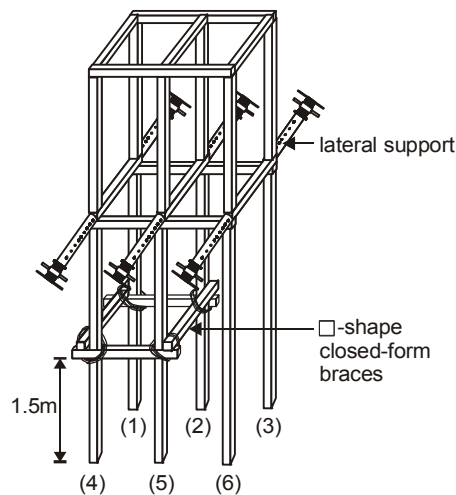
Figure 7. Arrangements of Double-layer Shoring Systems with Horizontal Braces

3.2.5   *Effect of eccentric loads on shores*

On construction sites, one commonly encounters a situation in which the top- and bottom-story shores are not aligned in double-layer shoring systems. This test is designed to determine whether the load capacities and mechanical behavior of the shoring system are affected when axial force is transferred indirectly. In the test configuration, the top shores of the double-layer shoring system displaced 20 cm inward and lateral supports are set up along four sides (Figure 8).
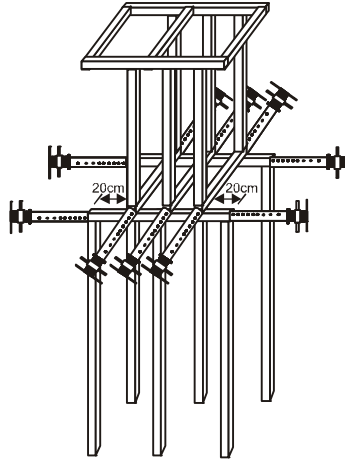
Figure 8. Arrangements of Double-layer Shoring Systems with Indirect Transfer of Axial Forces

3.2.6   *Inclined boundary conditions*

This test examines the effects of inclined boundary conditions on the load capacity of a double-layer shoring system. Two boundary conditions are compared. (A) The top and bottom boundaries of the double-layer shoring system are both plane surfaces (Figure 5(c)). (B) The bottom boundary of the double-layer shoring system is an inclined surface (Figure 9). The inclination angle α of the base is 20°. These two test setups have lateral supports on four sides.
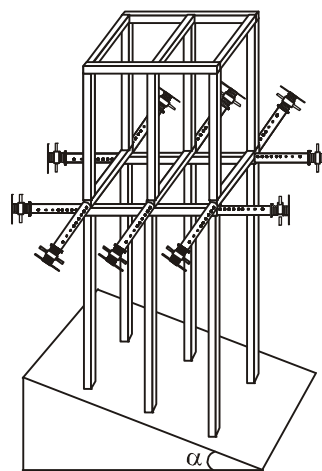
Figure 9. Arrangements of Double-layer Shoring Systems with Inclined 20° to Ground

3.2.7   Combination of wooden and steel-tube shores

This test assesses the load capacity of wooden shores in a double-layer shoring system (Figure 5(c)). Furthermore, the load capacity of wooden shores and adjustable steel-tube shores combined (Figure 10) is investigated. These tests are conducted with lateral supports on four sides (Figures 5(c) and 10).
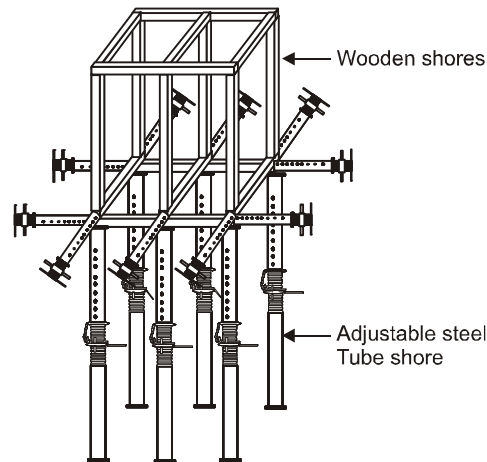
Figure 10. Combination of Wooden & Adjustable Steel Tube Shores
in Double-layer Shoring Systems

3.2.8   Effect of different reinforced types

This test compares the effects of various reinforcements on double-layer shoring systems. The following configurations were tested:

(A) Large inclined reinforcement braces were installed on the top and bottom stories. Four wooden shores, two for 3.0 m and 1.9 m in length respectively, were used as diagonal braces in the double-layer shoring system (Figure 11(a)). Small woodblocks were inserted into the gap such that the diagonal braces are tight when the length of the wooden shores is inadequate.

(B) Small inclined braces were installed on the top and bottom stories. Four inclined wooden shores, each 72 cm long, were used to reinforce the double-layer shoring system (Figure 11(b)). The reinforced wooden shores were setup diagonally with an inclination angle θ of 30° and were pinned with nails on the stringers and vertical shores.

(C) Small and large inclined braces were installed under horizontal stringers with closed-form horizontal braces (Figure 11(c)). The small inclined brace was made of wood planks (50 cm × 6 cm) installed under the horizontal stringers. These two wooden planks were fixed by nails to the horizontal stringers and vertical wooden shores at an angle of 45°. The large inclined brace was a wooden shore setup diagonally between the horizontal stringers and vertical shores. The setup of the closed-form horizontal braces was the same as that for (Figure 7).

(D) A V-shaped large inclined brace structure was considered. These reinforced V-shaped inclined braces were installed between tubes 1, 2, and 3 and tubes 5, 6, and 7 of the double-layer shoring system (Figure 11(d)). The lateral supports were setup on two sides of the system.

(a) Large inclined braces   (b) Small inclined braces   (c) Small & large inclined braces   (d)V-shaped reinforcement
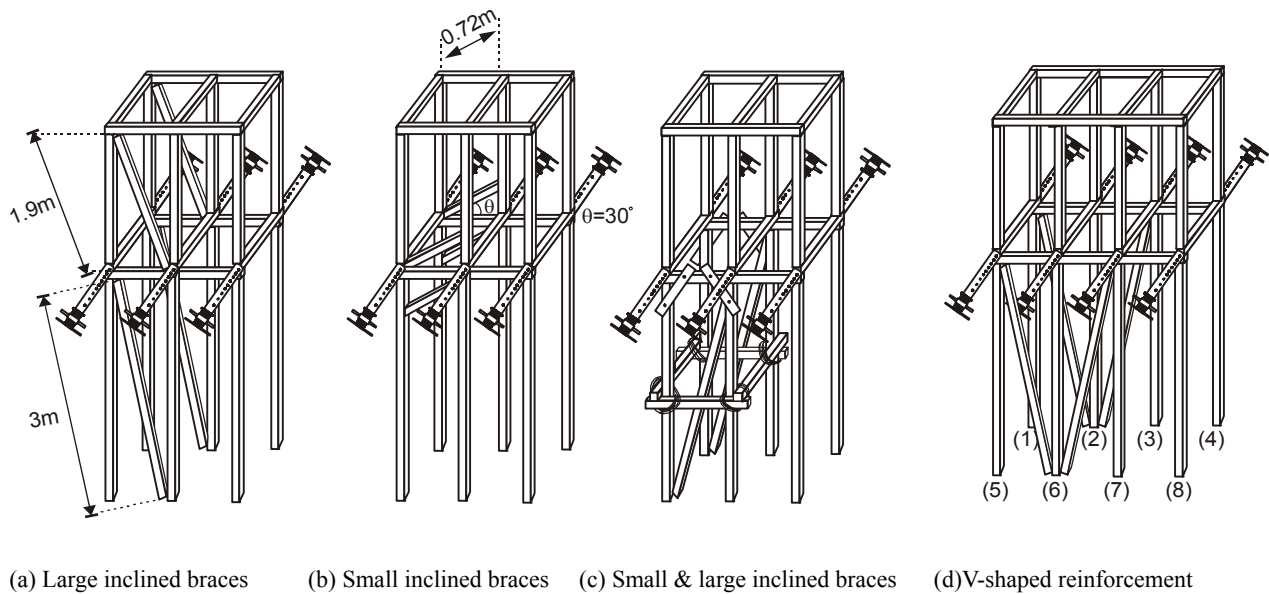
Figure 11. Arrangements of Double-layer Shoring Systems with Top and
Bottom inclined Bracing Reinforcements

4.   TEST RESULTS AND DISCUSSION

4.1   Load Capacity of Isolated Wooden Shore

The wooden shores were stored at room temperature (roughly 28–30°C) for 3 days before tests. Since water content has a considerable influence on the mechanical properties of wooden shores, it is advisable to reach a steady state for water content to avoid the generation of inaccurate test results. Two tests were conducted for the 3-m wooden shores. In test I, load capacity is 28.2 kN, that in test II is 20.94 kN, and average load capacity is 24.57 kN. Although the two test capacities are insufficient to fully represent load capacity of isolated wooden shores due to the large variability of wood, test results are very close to the load capacity of Kapur when compared with results obtained by previous studies [18]. Thus, these tests can serve as a reference for follow-up tests.

4.2   Effects of Lateral Supports

Table 1 shows test results for load capacities of double-layer shoring systems with and without lateral supports. For the double-layer shoring system without lateral supports, the load capacity in test I is 1.36 kN, that in test II is 1.19 kN, and average load capacity is 1.28 kN. The failure model indicates that the joint layer of horizontal stringers tilts gradually on the in-plane direction, generating a continuous and slow lateral displacement. However, no displacement exists at the top and bottom ends, indicating that the horizontal stringer is the weak point in the shoring system. Figure 12(a) presents test results. Figure 13 shows the P-Δ curve of test II, where P is the vertical load, and Δ is the horizontal displacement of the horizontal stringer. The tested load capacity is approximately 1.19 kN.

(a) No supports   (b) Lateral supports on two sides   (c) Lateral supports on four sides
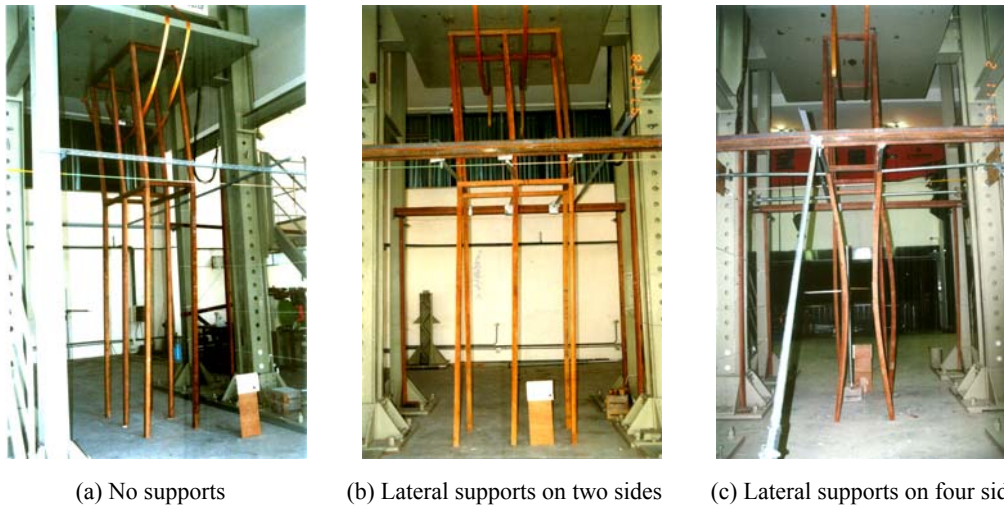
Figure 12. Test Results on Double-layer Shoring Systems with and without Lateral Supports
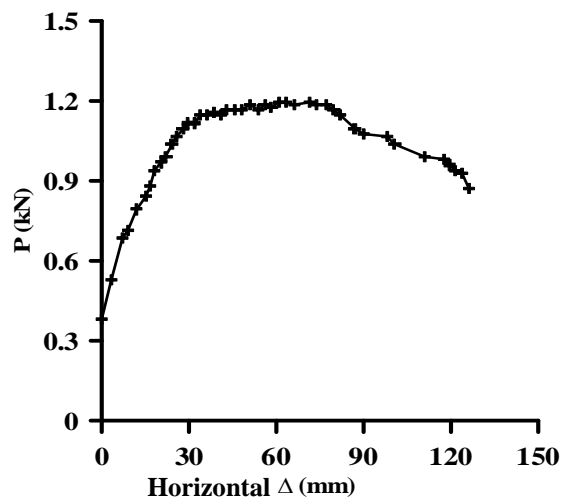
Figure 13. P-Δ Curve of Test II on Double-layer Shoring System without Lateral Supports
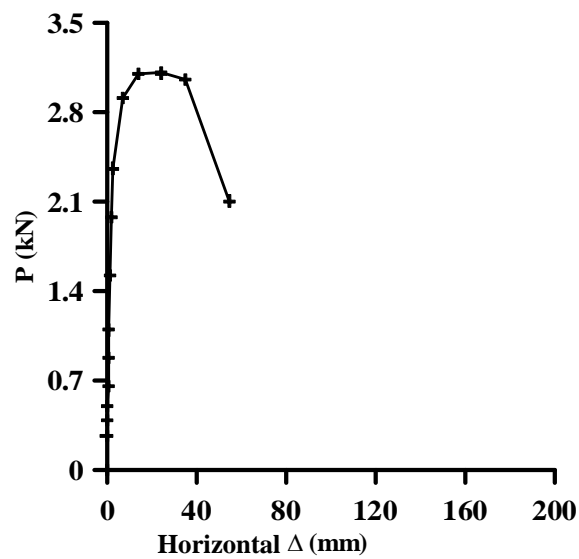
Figure 14. P-Δ Curve of Test I on Double-layer Shoring System with Lateral supports on Two Sides

For the double-layer shoring system with lateral supports on two sides, the supports were only set on the in-plane to force the failure of the shoring structure to occur on the out-of-plane. Figure 4 presents definitions for in-plane and out-of-plane. Figure 12(b) shows test results. The load capacity in test I is 3.23 kN, that in test II is 1.54 kN, and average load capacity is 2.38 kN. The P-Δ curve (Figure 14) for test I is close to a vertically straight line before the load reaches 1.74 kN, indicating that the initial imperfection of the shoring system is extremely small. The maximum load is 3.23 kN when the shoring system fails.

The 8-post double-layer shoring systems on the top and bottom with lateral supports on two sides were also tested. The load capacity in test I is 2.17 kN, that in test II is 5.94 kN, and that in test III is 2.88 kN (Table 1). Average load capacity is 3.66 kN. A comparison of test results for the 8-post double-layer shoring system with those for the 6-post double-layer shoring system indicates that the shoring system with lateral supports on one side only does not have sufficient load capacity, and the extension of the shoring system (i.e., adding wooden shores) does not necessarily increase the load capacity of these two double-layer shoring systems.

For the double-layer shoring system with lateral supports on four sides, the longitudinal and latitudinal directions were set with supports to make the shoring system bear lateral forces from two axial directions. In the test, the lateral deflections at the stringer, Δ2, and at the wooden shore (tube 1), Δ1, were measured. The lateral deflection Δ1 of wooden shores is lager than that of stringer Δ2 (Figure 15). The load capacity in test I is 81.78 kN, that in test II is 84.06 kN, that in test III is 101.26 kN, and the average load capacity is 89.03 kN (Table 1). Figure 12(c) presents test results.

Clearly, in the case of double-layer shoring systems with lateral supports on four sides, average load capacity of the 6-post shores at the top and bottom is 89.03 kN (Table 1), which is 40% less than total load capacity of the 3-m isolated wooden shore times 6 (24.57 × 6 = 147.42 kN). The load capacities of the double-layer shoring systems without lateral supports or with lateral supports on two sides are much lower than those of the shoring system with lateral supports along four sides. We infer that the main cause of collapse of the double-layer shoring system is due to insufficient lateral support. It means that unless a double-layer shoring system is sufficiently reinforced with lateral supports on four sides, system load capacity decreases substantially and the possibility of collapse is high.
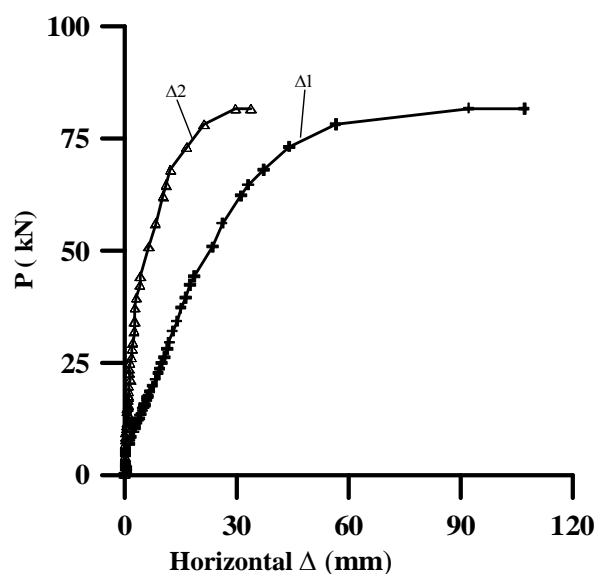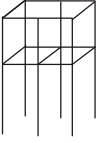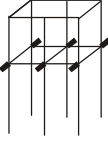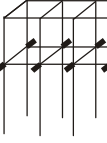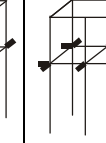
Figure 15. P-Δ Curve of Test I on Double-layer Shoring System with
Lateral supports on Four Sides

Table 1. Comparison of Load Capacities of Double-layer Shoring Systems with
Various Lateral Supports

Unit:kN

No of tests	Shoring models			
	No supported	Supported on two sides		Supported on four sides
I	1.36	3.23	2.17	81.78
II	1.19	1.54	5.94	84.06
III	---	---	2.88	101.26
Avg.	1.28	2.38	3.66	89.03
Note: --- denotes no test.				

4.3   Effect of Joint Forms of Horizontal Stringers

This study considers three connection forms: single butt, single overlap and double overlap. Table 2 shows test results for horizontal stringers with different connection forms in double-layer shoring systems with lateral supports along four sides.

(A)   Single butt

Two tests were conducted on this single butt. The load capacities in tests I and II are 77.21 kN and 76.34 kN, respectively. Average load capacity is 76.77 kN. This single butt connection on the horizontal stringers provides a good force transmission when lateral supports exist on the four sides. Failure is located on the bottom story of the double-layer shoring system as the bottom shores are longer than the top shores (Figure 16(a)). This is because the horizontal stringer is changed form a sideway case to a non-sideway case.

As shown by the P-Δ curve (Figure 17), minus-displacement does not occur in the initial stage of the test. This curve is close to a vertically straight line before the load reaches 39.23 kN. When the load exceeds 39.23 kN, lateral displacement of the bottom-story wooden shore occurs gradually. The shoring system failed when lateral displacement reached 4.8 cm.

(B)   Single overlap

Three tests were conducted for a horizontal stringers overlapping once in the double-layer shoring system. The load capacity in test I is 99.72 kN, 70.58 kN in test II, 20.83 kN in test III is, and average load capacity is 63.71 kN (Table 2).

When the single overlap was adopted at the joints of horizontal stringers, two failure models occurred due to the influence of the initial leaning direction of shoring members. This implies that the shores may be installed leaning toward or away from the overlap position. When the initial lean of all shoring members is away from the overlap position—mode 1—the load capacity of the shoring system is approximately 85.15 kN (= (99.72+70.58)/2). Conversely, when the initial lean of all shoring members is toward the overlap position—mode 2—the load capacity of the shoring system is roughly 20.83 kN. Figure 16(b) presents test results for failure mode 2. On construction sites, shores in a double-layer shoring system with a single overlap should be installed on the basis of mode 1.

(C)   Double overlaps

Two tests were performed for the case in which horizontal stringers overlap twice in the double-layer shoring system. The load capacity in test I is 51.50 kN, that in test II is 34.13 kN, and average load capacity is 42.82 kN (Table 2).

When the double overlap technique was adopted at the joints of horizontal stringers, two failure modes occurred due to the initial lean of shoring members, as in the case of a single overlap. When the initial lean of all shoring members is away from the overlap position (mode 1), load capacity of the shoring system is roughly 51.50 kN. Conversely, when the initial lean of all shoring members moves toward the overlap position (mode 2), load capacity of the shoring system is about 34.13 kN. Figure 16(c) shows test results for mode 1. When the double overlap scheme was adopted at the joints of horizontal stringers, average load capacity of the double-layer shoring system was approximately 30% less than the case when the single overlap technique was adopted ((63.71−42.82)/63.71×100%=32.8%).

(a) Single butt   (b) Single overlap   (c) Double overlap
Figure 16. Test Results on Double-layer Shoring Systems with
Varied Joint Forms of Horizontal Stringers
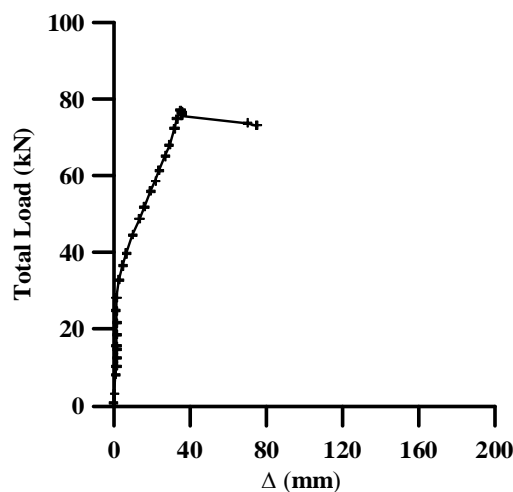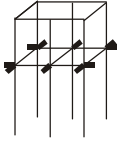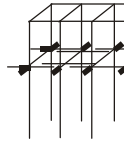
Figure 17. P-Δ Curve of Test I on Double-layer Shoring System with Single Butt for
Horizontal Stringers

The case of the single butt has the largest load capacity, followed by the single overlap (Table 2). The double overlap scheme has the lowest load capacity. The failure modes of the single overlap and double overlap schemes are very similar. In both cases, shoring members tend to displace toward the location of the overlap position after loading, resulting in systematic failure of the double-layer shoring system. We assume that regardless of whether the single overlap or double overlap scheme is adopted, as long as the initial lean of shoring members is toward the overlap position, the shoring system is likely to collapse as its load capacity is reduced. We recommend adopting the single butt technique, instead of single or double overlaps, when connecting horizontal stringers to a double-layer shoring system to facilitate a direct transfer of axial horizontal forces.

Table 2. Comparison of Load Capacities of Double-layer Shoring Systems with
Varied Joint Forms of Horizontal Stringers

Unit:kN

No. of tests	Joint forms of stringers		
	Single butt	Single overlap	Double overlap
I	77.21	99.72	51.50
II	76.34	70.58	34.13
III	---	20.83	---
Avg.	76.77	63.71	42.82
Note: --- denotes no test.			

4.4 Effect of Horizontal Braces

Figure 7 shows the setup of the rectangular hollow closed-form horizontal braces, which are commonly used in construction sites in Taiwan. The horizontal stringers move after loading (Figure 18). The overall structure displaces progressively toward the in-plane direction after loading. Figure 19 shows the P-Δ curve.

Test results (Table 3) indicate that load capacity of the shoring system with lateral supports on two sides and with the rectangular hollow closed-form horizontal braces is similar to that of the shoring system without closed-form horizontal braces (Figure 12(b)). This implies that on construction sites, setting up rectangular hollow closed-form horizontal braces on wooden shores does not increase significantly the load capacity of the double-layer shoring system.

The expected reinforcement effect does not occur after horizontal braces are installed in the double-layer shoring system. This may be because workers tie wires around the horizontal braces to resist bending moments and to resist lateral displacement. However, since wire strength is relatively small, when the wires become loose after loading, their anti-bending moment declines markedly. Therefore, when rectangular hollow closed-form horizontal braces are only tied up on the bottom story of the shoring system, they cannot increase system load capacity. However, further investigation is needed for such reinforcement.

Figure 18. Test Results on Double-layer Shoring System with Horizontal Braces

Figure 19. P-Δ Curve of Test I on Double-layer Shoring System with
Horizontal Brace Reinforcement

Figure 20. Test Results on Double-layer Shoring System with Axial Force Indirect Transfer

Table 3. Comparison of Load Capacities of Double-layer Shoring Systems with
and without Horizontal Braces

Unit:kN

No. of tests	Shoring models	
	Without horizontal braces	With horizontal braces
I	3.23	3.32
II	1.54	1.11
III	---	---
Avg.	2.38	2.22
Note: --- denotes no test.		

4.5 Effect of Eccentric Loads on Shores

Test results demonstrate that when vertical shores at the top and bottom stories do not contact directly, the load capacity in test I is 80.68 kN, that in test II is 89.87 kN, and the average load capacity is 85.27 kN, which is close to the average load capacity of 89.03 kN when the vertical shores at the top and bottom stories are symmetrical (Figure 5(c)).

Figure 8 shows the test setup with four lateral supports fastened on four sides respectively. Figure 20 shows the test results after loading. When loading starts, the bottom wooden shore buckles first, and then the horizontal stringers parallel to the in-plane and out-of-plane surfaces bend progressively. As soon as the shore, tube 4, at the bottom wooden shore broke, the overall structure collapsed instantly.

The P-Δ curve in Figure 21 shows an unstable increasing trend. It is likely because the force applied to the wooden shore is non-uniform and constantly changing, causing the wooden shores and horizontal stringers to deform. Test results demonstrate that the horizontal stringers provide considerable load capacity when they bear the bending moment caused by the asymmetrical top- and bottom-story wooden shores. In terms of construction-site safety, adopting a double-layer shoring system with asymmetrical top- and bottom-story wooden shores is inadvisable.

4.6 Effect of Inclined Boundaries

Table 4 lists the test results for the double-layer shoring system with a 20° inclination relative to the ground. The load capacity in test I is 124.74 kN, that in test II is 113.76 kN, and the average load capacity is 119.25 kN. Figure 9 shows the test setup of the shoring system with lateral supports on four sides. During the test, the wooden shores started deforming slightly toward the in-plane direction under loading. Notably, tubes 4 and 5 buckle; that is, as loading increases, the deformation of tubes 4 and 5 increases until they buckle successively. Figure 22 shows test results. Figure 23 shows the P-Δ curve for the double-layer shoring system with a 20° inclination relative to the ground.

The average load capacity of the double-layer shoring system with a non-inclined surface and lateral supports on four sides is 89.03 kN (Figure 12(c)). Load capacity, 119.25 kN, of the double-layer shoring system with a 20° inclination relative to the ground, is 25% higher than others in the double-layer shoring system with the flat ground ((119.25−89.03)/119.25 =25.3%). This is mainly because some wooden shores of the former system are shorter than those of the latter system. Thus, the short wooden shores have small effective length and provide higher critical loads for the system. Based on test results, we infer that for a double-layer shoring system with lateral supports on four sides, the effect of effective length on load capacity is larger than that of the system on an inclined ground.
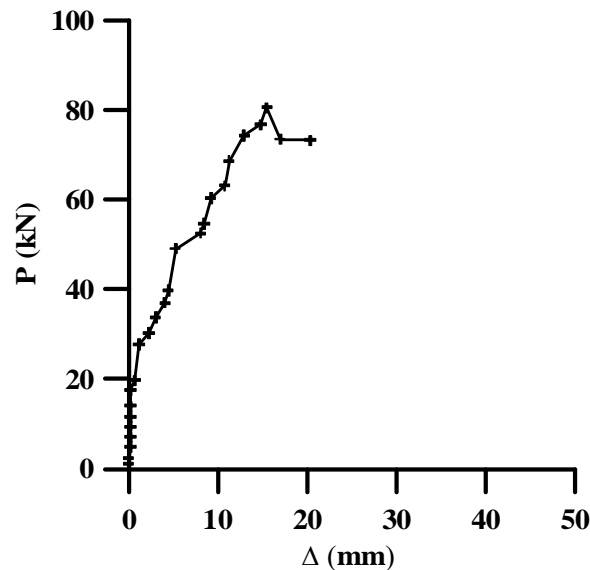
Figure 21. P-Δ Curve of Test I on Double-layer Shoring System with
Axial Force Non-direct Transfer

Figure 22. Test Results on Double-layer Shoring System with Inclined Boundary Condition

4.7 Combination of Wooden Shores and Steel-tube shores

Three tests were conducted for the double-layer shoring system with top wooden shores and bottom adjustable steel-tube shores with lateral supports on four sides. As the load capacity in test I is 168.36 kN, that in test II is 123.34 kN, and that in test III is 123.51 kN, the average load capacity is 138.40 kN (Table 4).

Figure 24 shows the test results for test I. This test shows the buckling failure of some adjustable steel-tube shores in the system. As loading increases, the top-story wooden shores and bottom-story adjustable steel-tube shores deform. When the shoring system collapsed, the bottom-story adjustable steel-tubes buckled (Figure 24), indicating that the load capacity of top-story wooden shores exceeds that of bottom adjustable steel-tube shores. Additionally, the load capacity (138.40 kN) of the double-layer shoring system with top-story wooden shores and bottom-story adjustable steel-tube shores is larger than that (89.03 kN) of the shoring system with wooden shores on both the top and bottom stories (Table 4).
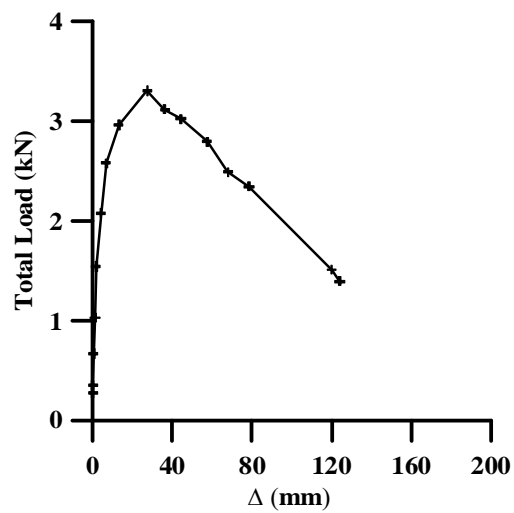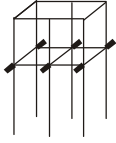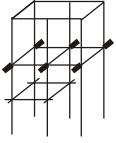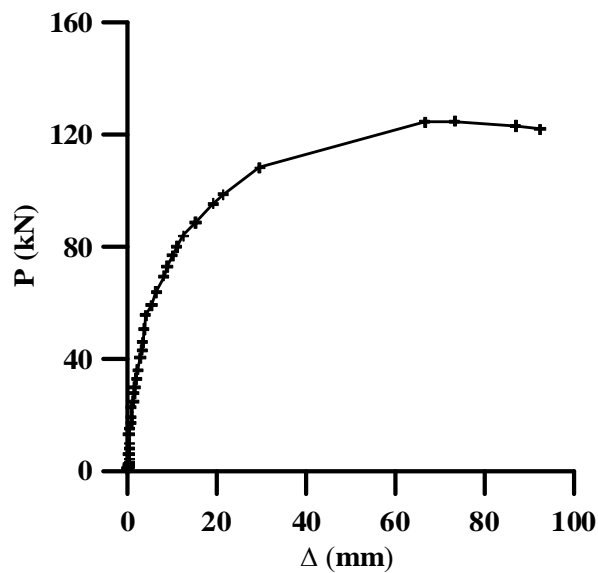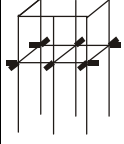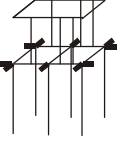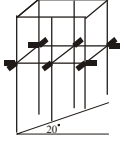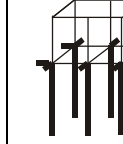

Figure 23. P-Δ Curve of Test I on Double-layer Shoring System with Inclined Boundary Condition

Figure 24. Test Results on Double-layer Shoring System with Combined Setup of Shores

Table 4. Comparison of Load Capacities of Double-layer Shoring Systems with Different Installations

Unit:kN

No. of tests	Shoring models			
	Supported on four sides	Axial force non-direct transfer	Inclined 20° to the gound	Combined use of wooden shore and adjustable steel tube shore
I	81.78	80.68	124.74	168.36
II	84.06	89.87	113.76	123.34
III	101.26	---	---	123.51
Avg	89.03	85.27	119.25	138.40

Note: --- denotes no test.

4.8   Effect of Different Reinforcements

4.8.1   *Large inclined reinforcement braces on the top and bottom stories*

The load capacities in tests I, II, and II for this reinforcement technique are 84.01 kN, 111.62 kN and 107.25 kN, respectively, and average load capacity is 100.96 kN. At the early stage in each of the three tests, the double-layer shoring system was only slightly displaced. This was followed by constant creaking noises, which we inferred to be the noise made by nails being gradually pulled out when resisting the lateral displacement of the overall shoring structure.

As shown in Table 1 and Table 5, the load capacity with this reinforcement technique increases to roughly 42 times (=100.96/2.38) that of the non-reinforced scheme. This is because the inclined reinforcement braces can make the horizontal stringers from the sideway case to the non-sideway case. Thus, the inclined reinforcement braces change the failure mode from system buckling to member buckling (Figure 25(a)).
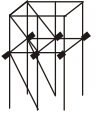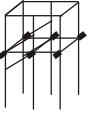
4.8.2   *Small inclined reinforcement braces on the top and bottom stories*

The load capacities in these two tests are 24.84 kN and 22.02 kN, and average load capacity is 23.43 kN (Table 5). At the start of this test, the horizontal stringers showed very minute displacements. Over time, the nails fastening the small inclined braces to the top and bottom stories gradually pulled out. As loading continued and reached the load capacity, the overall double-layer shoring system failed due to marked horizontal displacement (Figure 25(b)).

The load capacities illustrated in Table 1 and Table 5 indicate that this reinforcement case is roughly 10 times (=23.43/2.38) that of the non-reinforced case. Compared with the setup with large inclined braces, the two ends of the large inclined bracings are diagonally shored up the ground and horizontal stringers, respectively, which are considered more rigid. Thus, the large inclined braces strengthen to the overall double-layer shoring system. Conversely, because the two ends of the small inclined bracings shore up the wooden shores and horizontal stringers, respectively, and are pinned with nails, the ability of the nails is not sufficient to withstand the lateral displacement of the horizontal stringers. Although the load capacity of small inclined braces for both top and bottom stories is not comparable to that of large inclined braces, the required material for this reinforcement method is considerably reduced.

Table 5. Comparison of Load Capacity of Double-layer Shoring Systems with
Varied Reinforcement Configurations

Unit:kN

No. of tests	Shoring models			
	6-post reinforcements			8-post reinforcements
	Large inclined reinforcement on top & bottom stories	Small inclined reinforcement on top & bottom stories	Small & large inclined reinforcements	Lateral bracings on two sides & V-shaped reinforcement
I	84.01	24.84	35.65	166.31
II	111.62	22.02	---	112.82
III	107.25	---	---	168.56
Avg.	100.96	23.43	35.65	149.23
Note: --- denotes no test.				

4.8.3 *Small and large reinforcement braces with closed-form horizontal braces*

The tested load capacity of the small and large reinforced inclined braces with closed-form horizontal braces is 35.65 kN (Table 5). As the shoring materials required to complete this test were insufficient, only one test for this reinforcement case was considered in this study. This test is the final one.

In this test, minor lateral displacement of the overall system appeared first. However, the displacement was gradually replaced by the inclined reinforcement braces. The reinforced brace deformed toward the in-plane direction and finally buckles. Figure 25(c) shows the test result.

Comparison of the load capacities in Table 1 and Table 5 indicates that the load capacity of this reinforcement scheme is approximately 15 times (=35.65/2.38) that of the non-reinforced case. This implies that this reinforcement scheme can increase the load capacity of double-layer shoring systems. However, the final failure mode is still system buckling (Figure 25(c)).

4.8.4 *V-shaped large inclined reinforcement braces*

The load capacities in three tests for this reinforcement technique are 166.31 kN, 112.82 kN, and 168.56 kN, and average load capacity is 149.23 kN (Table 5). Figures 11(d) and 26(a) show the installation before loading. After loading, the double-layer shoring system displaced gradually in the in-plane direction. Subsequently, some inclined reinforcement braces shored on the horizontal stringers deformed. Finally, one inclined strengthening brace buckled. This causes other inclined reinforcement shores to fall and the double-layer shoring system then becomes considerably displaced and finally collapses (Figure 26(b)).

For the setup of a V-shaped large inclined reinforcement braces (Figures 11(d) and 26(a)), the load capacity of this reinforcement scheme is about 41 times (=149.23/3.66) that of the non-reinforced 8-post case (Table 1). The load capacity of this V-shaped reinforced installation is close to that of case (A) with inclined reinforcement braces on simpler top and bottom stories. However, installation of these reinforced shores in case (D) is easier than that in case (A) on construction sites since workers only need to install strengthening braces on the bottom story.

(a) Large inclined reinforcement   (b) Small inclined reinforcements   (c) Small & large reinforcements

Figure 25. Test Results on 6-post Double-layer Shoring Systems with Different Reinforcements

(a) V-shaped inclined braces before loading   (b) V-shaped inclined braces after loading

Figure 26. Test Results on V-shaped Reinforcement Braces in Double-layer Shoring System

5.   CONCLUSIONS

1.   The failure of the double-layer shoring systems shows that horizontal stringers tilt in the direction without lateral supports when no displacement is present at the top and the bottom. This indicates that the horizontal stringer is the weak point in the double-layer shoring system.

2. The collapse of a double-layer shoring system is mainly caused by insufficient lateral supports on the horizontal stringers. Therefore, the lateral supports on four sides at the positions of horizontal stringers must be setup to prevent shoring systems from collapsing.

3. Different joints for the horizontal stringers significantly change the load capacity. The single butt has the highest load capacity. The failure modes of single and double overlaps are very similar. For single or double overlaps, the shoring system collapses under a low load capacity when the initial leaning of shoring members is toward the overlap position. We recommend utilizing the single butt for connecting horizontal stringers in a double-layer shoring system.

4. Reinforcing the join between rectangular hollow closed-form horizontal braces and vertical wooden shores using steel wire only at the bottom story does not enhance the load capacity of double-layer shoring systems. Reinforcing these horizontal braces cannot replace reinforced lateral supports at horizontal stringers.

5. The horizontal stringers provide considerable load capacity, even when stringers bear the bending moment caused by asymmetrical top- and bottom-story wooden shores. However, failure is sudden and drastic. In consideration of construction site safety, we advise that the asymmetrical top- and bottom-story wooden shores in a double-layer shoring system should not be used.

6. For the lateral supports on four sides of a double-layer shoring system, the inclination ground of the double-layer shoring system does not apparently impair tested load capacities.

7. The load capacity of the double-layer shoring system with a setup combining wooden shores and adjustable steel-tube shores is higher than that of the shoring system using only wooden shores.

8. After comparing the large or small inclined reinforcements on both the top and bottom stories and reinforcement with V-shaped inclined bracings in double-layer shoring systems, we recommend that reinforcement with V-shaped inclined bracings should be utilized to reinforce double-layer shoring systems.

9. If a double-layer shoring system is not well reinforced with lateral supports, simply increasing the number of leaning-column wooden shores does not increase system load capacity significantly. However, falsework workers seldom realize this. This is one of the reasons for the collapse of double-layer shoring systems.

ACKNOWLEDGMENTS

REFERENCES

[1]   Institute of Occupational Safety and Health (IOSH); Occupational Accidents Report – Construction Industry, Library of IOSH, Council of Labor Affairs, Executive Yuan, 1994. (in Chinese)

[2]   Hadipriono, F.C. and Wang, H.C., "Analysis of Causes of Formwork Failures in Concrete Structures", Journal of Construction Engineering and Management, ASCE, 1986, Vol. 112, No. 1, pp. 112-121.

[3]   Kao, C.C., "An Investigation on Safety and Usage of Domestic Steel-tube Scaffolds", Taiwan Constructional Research Center, 1983, Report No.TR-7210. (in Chinese)

[4]   Leu, L.J., Kao, C.C., Yang, Y.B., Huang, W.H., Huang, M.Y., Tsou, C.H., Wu, S.H. and Lin, C.C., "A Study on the Capacity and Frequency Measurement of Steel Scaffolds", Institute of Occupational Safety and Health Council of Labor Affairs, Taiwan, 1996, Report IOSH85-S126. (in Chinese)

[5]   Chan, S.L., Chu, A.Y.T. and Albermani, F.G., "Stability and Simulation-Based Design of Steel Scaffolding without Using te Effective Length Method", Structural Stability and Dynamics, Dec. 2003, Vol. 3, No. 4, pp. 443-460.

[6]   Chan, S.L. and Cho, S.H., "Second-Order Analysis and Design of Angle Trusses Part 1: Elastic Analysis and Design", Engineering Structures, 2008a, No. 30, pp. 616-625.

[7]   Chan, S.L. and Cho, S.H., "Second-Order Analysis and Design of Angle Trusses Part 2: Plastic Analysis and Design", Engineering Structures, 2008b, No. 30, pp. 626-631.

[8]   Iu, C.K.J. and Chan, S.L., "A Simulation-based Large Deflection and Inelastic Analysis of Steel Frames under Fire", Journal of Constructional Steel Research, 2004, No. 60, pp.1495-1524.

[9]   Peng, J.L., Pan, A.D.E., Chen, W.F., Yen, T. and Chan, S.L., "Structural Modeling and Analysis of Modular Falsework Systems", Journal of Structural Engineering, ASCE, 1997, Vol. 123, No. 9, pp. 1245-1251.

[10]   Peng, J.L., Pan, A.D., Rosowsky, D.V., Chen, W.F., Yen, T. and Chan, S.L., "High Clearance Scaffold Systems during Construction – I. Structural Modelling and Modes of Failure", Engineering Structures, 1996a, Vol. 18, No. 3, pp. 247-257.

[11]   Peng, J.L., Rosowsky, D.V., Pan, A.D., Chen, W.F., Chan, S.L. and Yen, T., "High Clearance Scaffold Systems during Construction - II. Structural Analysis and Development of Design Guidelines", Engineering Structures, 1996b, Vol. 18, No. 3, pp. 258-267.

[12]   Mosallam, K. and Chen, W.F., "Design Consideration for Formwork in Multistory Concrete Buildings", Engineering Structures, 1990, Vol. 12, No. 7, pp. 163-172.

[13]   El-Shahhat, A.M., Rosowsky, D.V. and Chen, W.F., "Construction Safety of Multistory Concrete Building", ACI Structural Journal, 1994, Vol. 91, No. 4, pp. 475-485.

[14]   Peng, J.L., "Stability Analyses and Design Recommendations for Practical Shoring Systems during Construction", Journal of Construction Engineering and Management, ASCE, 2002, Vol. 128, No. 6, pp. 536-544.

[15]   Peng, J.L., "Structural Modeling and Design Considerations for Double-layer Shoring Systems", Journal of Construction Engineering and Management, ASCE, 2004, Vol. 130, No. 3, pp. 368-377.

[16]   Lemessurier, W. J., "A Practical Method of Second Order Analysis, Part 2 - Rigid Frames", AISC Engineering Journal, 1977, Vol. 14, No. 2, pp. 49-67.

[17]   Chinese National Standard, "Wood-Determination of Compression Properties", (In Chinese) CNS - 453, 2005, No. O2004.

[18]   Yen, T., Chen, W.F. and Lin, C.H., "Research of Wooden Shore Strength and Check Lists Using in Construction", (in Chinese) Council of Labor Affairs, Taipei, Taiwan, 1994.

DYNAMIC NUMERICAL SIMULATION OF STEEL FRAME-TYPED PIERS INSTALLED WITH SMA DAMPING DEVICES BASED ON MULTI-LINEAR ONE DIMENSIONAL CONSTITUTIVE MODEL

Xiao-Qun Luo[1,2] , Hanbin Ge[3,*] and Tsutomu Usami[4]

[1]*Post doctoral researcher, Advanced Research Center for Seismic Experiments and Computations, Meijo University Shiogamaguchi, Tempaku-ku, Nagoya, 468-8502, Japan*
[2]*Lecturer, Department of Building Engineering, Tongji University, No. 1239, Sipin Road, Shanghai, 200092, China.*
[3]*Professor, Dept. of Civil Engineering, Meijo University Shiogamaguchi, Tempaku-ku, Nagoya, 468-8502, Japan. Email: gehanbin@meijo-u.ac.jp*
[4]*Professor, Dept. of Civil Engineering, Meijo University Shiogamaguchi, Tempaku-ku, Nagoya, 468-8502, Japan. Email: usamit@meijo-u.ac.jp*
*(Corresponding author: E-mail: gehanbin@meijo-u.ac.jp)

ABSTRACT: In this paper, the effectiveness of seismic performance upgrading is studied by adoption of damping devices made of shape memory alloys (SMAs). An axial-type SMA damper is constructed and modeled on the basis of a modified multi-linear one dimensional constitutive model of SMAs. Time history analyses are carried out on typical steel frames with SMA damping devices. Performance parameters for seismic performance upgrading are investigated in consideration of four influence factors, i.e., strength ratio, martensite fraction, length ratio, and ground motion. Dynamic analyses of bare frames and frames with equivalent BRB dampers are also conducted for comparisons. Numerical investigations show that excellent re-centering ability and energy dissipation can be afforded by installing SMA damping devices in structures.

1. INTRODUCTION

Damping devices are usually applied for suppression of undesired structural vibrations under severe loadings such as strong earthquake motions. With development of new materials and new control techniques, many damping devices are developed such as viscous dampers, visco-elastic dampers, friction dampers, hysteretic metal dampers, shape memory alloy dampers and so on Weber et al. [1].

Due to their shape memory effect and super-elasticity, shape memory alloys (SMAs) can undergo large deformations over 10% and return to their original shape without residual deformations through heat process or removal of load. Recently, besides applications in biomedical field, aerospace field, etc., more attentions are also received for SMAs seismic applications in the field of civil and building engineering because of their intelligent characteristics such as re-centering, energy dissipating, damping and so on. Various damping devices and isolation devices were proposed by many researchers. For examples, two families of passive seismic control devices, i.e., special frame braces and isolation devices for buildings and bridges, were implemented within the MANSIDE project Dolce et al. [2]. A smart isolator combined by a laminated rubber bearing with a SMA device was proposed for bridge protection Wilde et al. [3]. Novel SMA-based devices were also present by Li et al. [4], Zhu and Zhang [5,6], Song et al. [7], McCormick et al. [8], etc., on which experiments, numerical models and applications were investigated but most of them were still in laboratory stage.

In the present paper, an axial-type SMA damper is developed for seismic performance upgrading of steel structures, and modeled on the basis of a simple multi-linear one dimensional constitutive law of SMAs. A seismic performance study of steel frame bridge piers with the SMA damper is performed with the help of time history analysis using several strong ground motions, and the effectiveness is verified under detailed comparisons.

2. CONSTITUTIVE MODELS OF SMAS

In order to simulate material behavior of SMAs numerically, microscopic methodology and macroscopic methodology are two approaches which focus on molecular level and phenomenological features of SMAs, respectively Paiva and Savi [9]. Phenomenological models are gotten more interests for their simplicity and suitability in seismic engineering application. Besides models generated from experiment results Delemont and DesRoches [10], many models were derived through different theoretical approaches. For examples, Graesser and Cozzarelli proposed a model based on one strain variable ε Graesser and Cozzarelli [11], which later modified by Wilde et al. [3] and Zhu and Zhang [5]. A class of thermo-mechanical models with assumed phase transformation kinetics was firstly proposed by Tanaka [12], in which an internal variable ξ was used to represent the martensite volumetric fraction. Extent researches were conducted by several authors Brinson [13]; Boyd and Lagoudas [14]; Tamai and Kitagawa [15] and Auricchio and Sacco [16].

In this study, a modified version of the constitutive model for SMA is proposed which initially developed by Motahari and Ghassemieh [17], where a kind of thermo-mechanical models was also presented.

2.1 The Motahari and Ghassemieh Model

A temperature-dependent multi-linear constitutive model was derived by Motahari and Ghassemieh [17] to simulate the behavior of SMAs, which originated from the special expression of Gibbs free energy of a material undergoing a solid-solid phase transformation shown below:

$$G(\sigma,\xi,T) = -\frac{1}{2\rho}\frac{\sigma^2}{E} - \frac{1}{\rho}\sigma[\alpha(T-T_0)+\xi\varepsilon_L] + c\left[(T-T_0)-T\ln\frac{T}{T_0}\right] - s_0 T + u_0 \tag{1}$$

where G represents the Gibbs free energy which is dependent on three variables, i.e., the axial stress σ, the martensite fraction ξ and the working temperature T; s_0 and u_0 are specific entropy and specific internal energy at the reference state of SMAs, respectively; ρ, α, T_0, E, ε_L and c are the density, effective thermal expansion, reference temperature, elastic modulus, maximum residual strain and thermal expansion factor, respectively.

Following standard thermodynamics formulations, the stress expression can be derived from Eq. 1:

$$\sigma = E\varepsilon = E(\xi)\left(-\frac{\partial G}{\partial \sigma}\right) = E(\xi)[\varepsilon - c(T-T_0) - \varepsilon_L\xi] \tag{2}$$

In Eq. 2, the elastic modulus of SMAs in the transformation process is a function of the martensite fraction ξ, and expressed by the following Eq. 3 in the Motahari and Ghassemieh model:

$$E(\xi) = E_A + \xi(E_M - E_A) \tag{3}$$

Dynamic Numerical Simulation of Steel Frame-Typed Piers Installed with
SMA Damping Devices Based on Multi-linear One Dimensional Constitutive Model

724

here, $E(\xi)$ is the elastic modulus of SMAs with the martensite fraction ξ, E_A and E_M are SMA elastic modules in the austenite state and martensite state, respectively.

Adoption of linearization assumption between transformation stresses and strains in the isothermal process (i.e., $T=T_0$) leads to such a relation by using Eqs. 2 and 3:

$$E(\xi)\varepsilon = \left(E_A + \xi(E_M - E_A)\right)\left[\varepsilon - \varepsilon_L\xi\right] = a\varepsilon + b \tag{4}$$

here, a and b are two undetermined coefficients.

Considering material properties of SMA, the multi-linear constitutive model is illustrated in Figure 1(a) in which the four transformation stresses, i.e., σ_{MS}, σ_{MF}, σ_{AS} and σ_{AF}, are determined by material constants C_A, C_M, transformation temperatures T_{MS}, T_{MF}, T_{AS}, T_{AF} and the reference temperature T_0. If unloading occurs before completion of forward transformation or reloading occurs before completion of reversal transformation, the inner hysteretic path is illustrated in Figure 1(b) that the forward transformation takes place when the stress reaches to σ_{MS} and the reversal transformation takes place when the stress reaches to σ_{AS} in the inner loop.
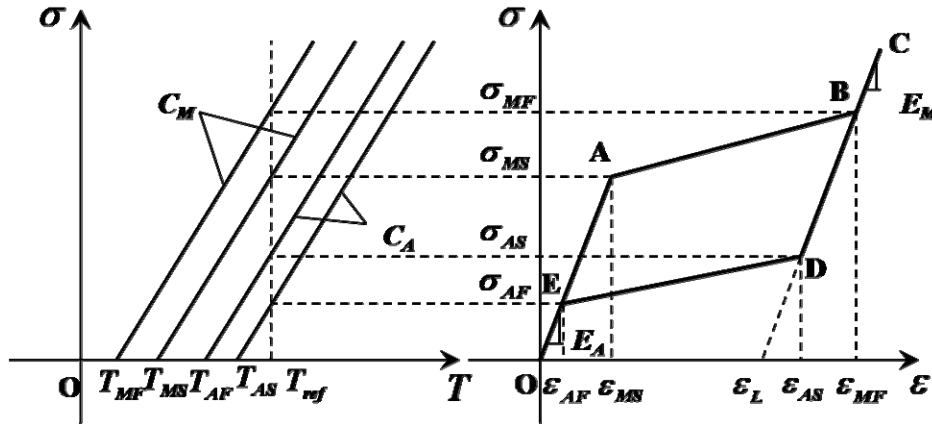
(a) Bone curve of the Motahari and Ghassemieh model
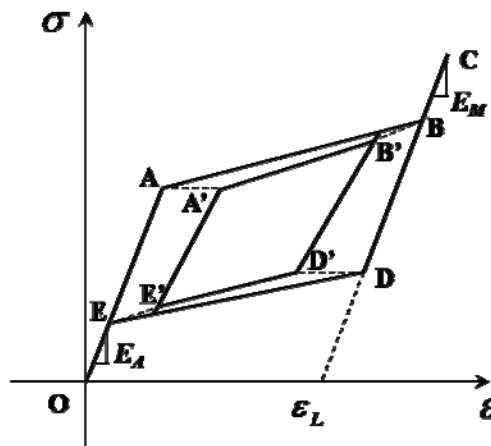
(b) Inner hysteretic loop adopted in the Motahari and Ghassemieh model

Figure 1. The Motahari and Ghassemieh Model for SMAs (Motahari and Ghassemieh [17])

2.2   Modifications to the M.-G. Model

In this study, a constitutive model for SMAs is proposed by modifying the Motahari and Ghassemieh model (i.e., the M.-G. model) to make it more applicable for engineering applications.

First, the modified model omits the relations between temperature and transformation stress. As we know, stress variation in SMAs during phase transformation precess is temperature dependent and strain rate dependent. However in such a simplified multi-linear model, the issue of considering the effect of temperature or strain rate is turned to determine the transformation stresses of SMAs during iso-thermal or adiabatic process. As shown in the left part of Figure 1(a), it is one of the effective methods to determine transformation stresses relation to temperature as originally developed by Brinson [13]. In authors' opinion, the key part of the constitutive model in Figure 1(a) in its right part can be extracted and the transformation stresses can be determined either by the thermo-stress coupling relations in the M.-G. model or by other approaches such as experimental tests, data from material suppliers and other researchers' methods mentioned in section 1.

Next, the relation of the elastic modulus in Eq. 3 represents an upper bound for all kinds of elastic modules summarized by Auricchio, but experimental evidence shows that the assumption is quite unrealistic (Auricchio and Sacco [16]). For this reason, the equivalent modulus is adopted in Reuss scheme as follows:

$$\frac{1}{E} = \frac{(1-\xi)}{E_A} + \frac{\xi}{E_M} \tag{5}$$

Replacing Eq. 3 with Eq. 5, and substituting it into Eq. 4, the varied martensite fraction ξ in the forward transformation process and the reversal transformation process can be explicitly expressed:

$$\xi = \frac{E_A E_M \varepsilon - (a\varepsilon + b)E_M}{(a\varepsilon + b)(E_A - E_M) - E_A E_M \varepsilon_L} \tag{6}$$

The proposed constitutive model can be easily illustrated in Figure 2. As shown in Figure 2(a), the bone curve of the multi-linear constitutive model is plotted when SMAs are assumed in the austenite state at the reference temperature, in which four transformation stresses, i.e., σ_{MS}, σ_{MF}, σ_{AS} and σ_{AF} are known and the elastic modules in the austenite state and martensite state are E_A and E_M, respectively. The controlled transformation strains can be easily obtained as follows:

$$\varepsilon_{MS} = \frac{\sigma_{MS}}{E_A} \quad ; \quad \varepsilon_{MF} = \frac{\sigma_{MF}}{E_M} + \varepsilon_L \quad ; \quad \varepsilon_{AS} = \frac{\sigma_{AS}}{E_M} + \varepsilon_L \quad ; \quad \varepsilon_{AF} = \frac{\sigma_{AF}}{E_A} \tag{7}$$

and then the undetermined coefficients a and b can be calculated from the known start transformation point and the finish transformation point.

Shown in Figure 2(b) is the model to solve detwinning process of SMAs in the martensite state, where the start and finish critical stresses are named σ_{MSCR}, σ_{MFCR}, and both the initial stiffness and stiffness after detwinning are taken as the same as E_M.

Different from the M.-G. model, a modified inner hysteretic strategy called diagonal rule is proposed as shown in Figure 2(c). Generally in the isothermal process, four transformation stresses, i.e., σ_{MS}, σ_{MF}, σ_{AS} and σ_{AF}, obey the inequalities, $\sigma_{AF} \leq \sigma_{AS} \leq \sigma_{MS} \leq \sigma_{MF}$ (Auricchio and Sacco [16]). But in high frequency earthquake loadings, transformation temperatures and stresses in SMAs rise because the SMAs don't have sufficient time to dissipate heat. Due to the rate-dependent

characteristic of SMAs, if the transformation stress σ_{AS} is greater than σ_{MS}, the inner loop suggested in the M.-G. model would get misleading results. The diagonal rule defines the diagonal line between σ_{MS} and σ_{AS} as a reference line for the phase transformation start point in the inner loop. If unloading occurs before completion of forward transformation, the loading path with a slope of $E(\xi)$ at the unloading point B' descends from B' to D' on the diagonal line, and then points to A (a point corresponding to σ_{AF}) which imitates the inner reversal transformation process. This rule is the same in the reloading process before completion of reversal transformation.
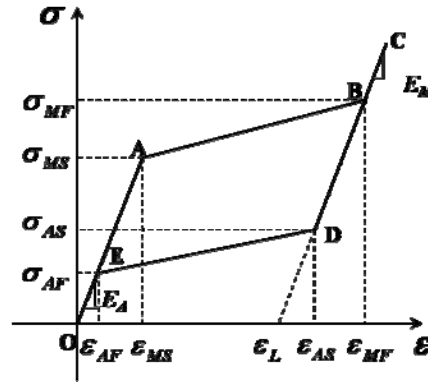
(a) Constitutive model of SMA transformation process between austenite and martensite states
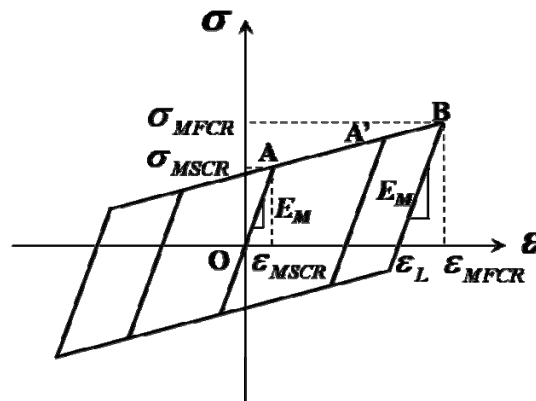
(b) Constitutive model of martensite SMA detwinning process
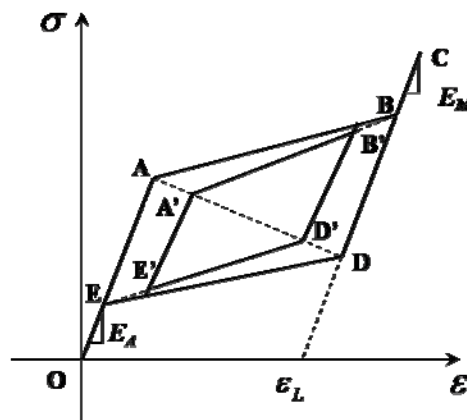
(c) Diagonal rule assumption of inner hysteretic loop

Figure 2. Modified Motahari and Ghassemieh Model for SMAs

3.   CONSTRUCTING AND MODELING OF AXIAL-TYPE SMA DAMPER

The axial-type SMA damper considered is shown in Figure 3(a), in which two blocks (i.e., Part A and Part B) made of steel can slide past each other, and two sets of austenite wire systems and one martensite sheet are kernel material in the damper. Lubricating material is placed at the contact interface of Part A and Part B to reduce friction. The whole SMA damper can be distinctly divided into two groups, i.e., recentering group and energy dissipation group. The recentering group consists of the two sets of austenite wires A and B, which are in tension only and react in reverse directions because the austenite wires A and B have excellent superelastic ability with relative small hysteretic loop, as shown in Figure 3(b)-(1) and Figure 3(b)-(2). And the energy dissipation group is made up of the martensite sheet that is restrained so that it can afford tension and compression without undergoing buckling and its good energy dissipation ability is as shown in Figure 3(b)-(3).

The working principle of the SMA damper is described here. While the damper is in tension, Austenite Wire B is in action like Figure 3(b)-(1) and Austenite Wire A doesn't work at this moment; while the damper is in compression, Austenite Wire A is in action like Figure 3(b)-(2) and Austenite Wire B doesn't work; whether in tension or in compression, the restrained Martensite Sheet is always in action with the same amplitude like Figure 3(b)-(3). Combined the three curves together as Figure 3(b)-(4), considering fraction distributions between austenite parts and martensite part, the corresponding analytical model of the damper is constructed shown as Figure 3(b)-(5). The discontinuous points A-G in Figure 3(b)-(5) are the martensite forward transformation start point A, austenite forward transformation start point B, martensite forward transformation finish point C, austenite forward transformation finish point D, austenite reversal transformation start point E, martensite reversal transformation start point F, austenite reversal transformation finish point G, respectively. It is noted that the point A is defined as the design stress σ_d.

Like SMA dampers developed by Dolce et al. [2] and Zhu and Zhang [6] mentioned above, two groups, i.e., recentering group and energy dissipation group, are designed in the axial-type SMA damper. Corresponding to a pair of pre-tensioned SMA wire systems in the damper by Dolce et al. and a friction sliding surface design in the damper by Zhu and Zhang, the restrained martensite sheet is the energy dissipation group in the proposed damper of this study. Moreover, two sets of austenite SMA wire systems are set as recentering group that is similar to both the dampers. The damper by Zhu and Zhang [6] is improved from the damper by Zhu and Zhang [5] that a friction design is added to increase energy dissipation. Compared to the damper by Dolce et al., a restrained marteniste sheet instead of pretensioned wire systems is adopted in the damper to dissipate energy. If no pretension is applied in the damper by Dolce et al., the energy dissipation ability shown in Figure 3(c) is lower than that in the axial-type damper as shown in Figure 3(b)-(3). However, more than 3% prestrain is a large load for support structures in the damper by Dolce et al. especially for bridge engineering.
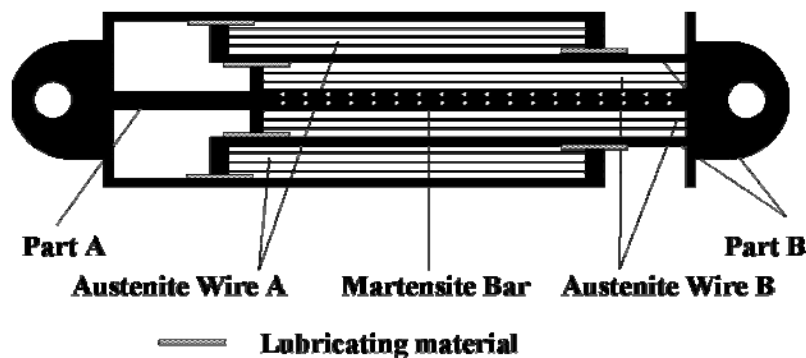
(a) SMA damper prototype
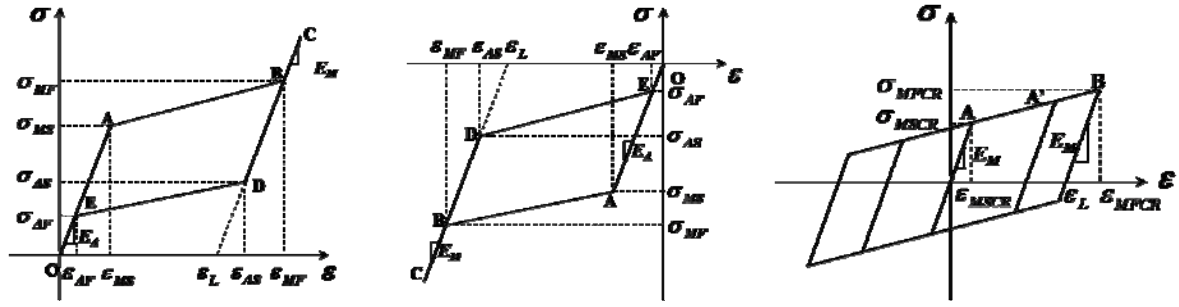
(b)-(1) Austenite Wire B   (b)-(2) Austenite Wire A   (b)-(3) Martensite Sheet
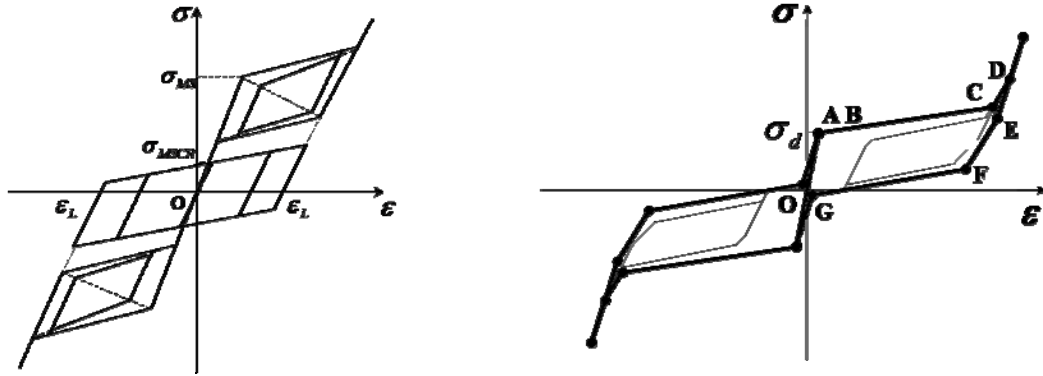
(b)-(4) Combined model of the three sets of SMA   (b)-(5) Constitutive law of the SMA damper
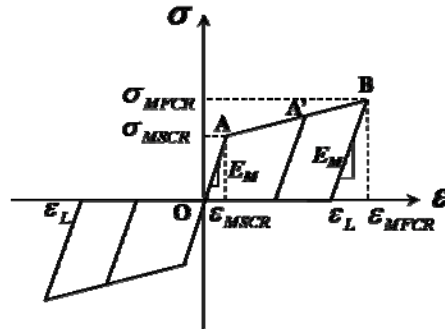
(c) Constitutive law of energy dissipation group in Dolce's damper

Figure 3. Prototype and Stress-strain Relationship of SMA Damper

4.   DESIGN AND MODELING OF SMA DAMPING DEVICES IN STEEL FRAME STRUCTURES

A benchmark frame FA is a 12×12m square-shaped plane frame as shown in Figure 4. The main frame is made of SM490 steel grade and details of the bare frame and BRB damped frame can be found in a previous study by Chen et al. [18]. The SMA damping device consists of two SMA dampers and two steel brace components, in which material constants of SMA given in the paper by Motahari and Ghasemieh [17] are employed as listed in Table 1. Steel brace components are assumed to be rigid for simplicity. The yield shear force and top displacement of the bare main frame given in Table 2 are determined from a pushover analysis.

(a) Bare frame bridge pier   (b) Frame with SMA damper   (c) Frame with equivalent BRB

(d) Sections of frame girders and piers
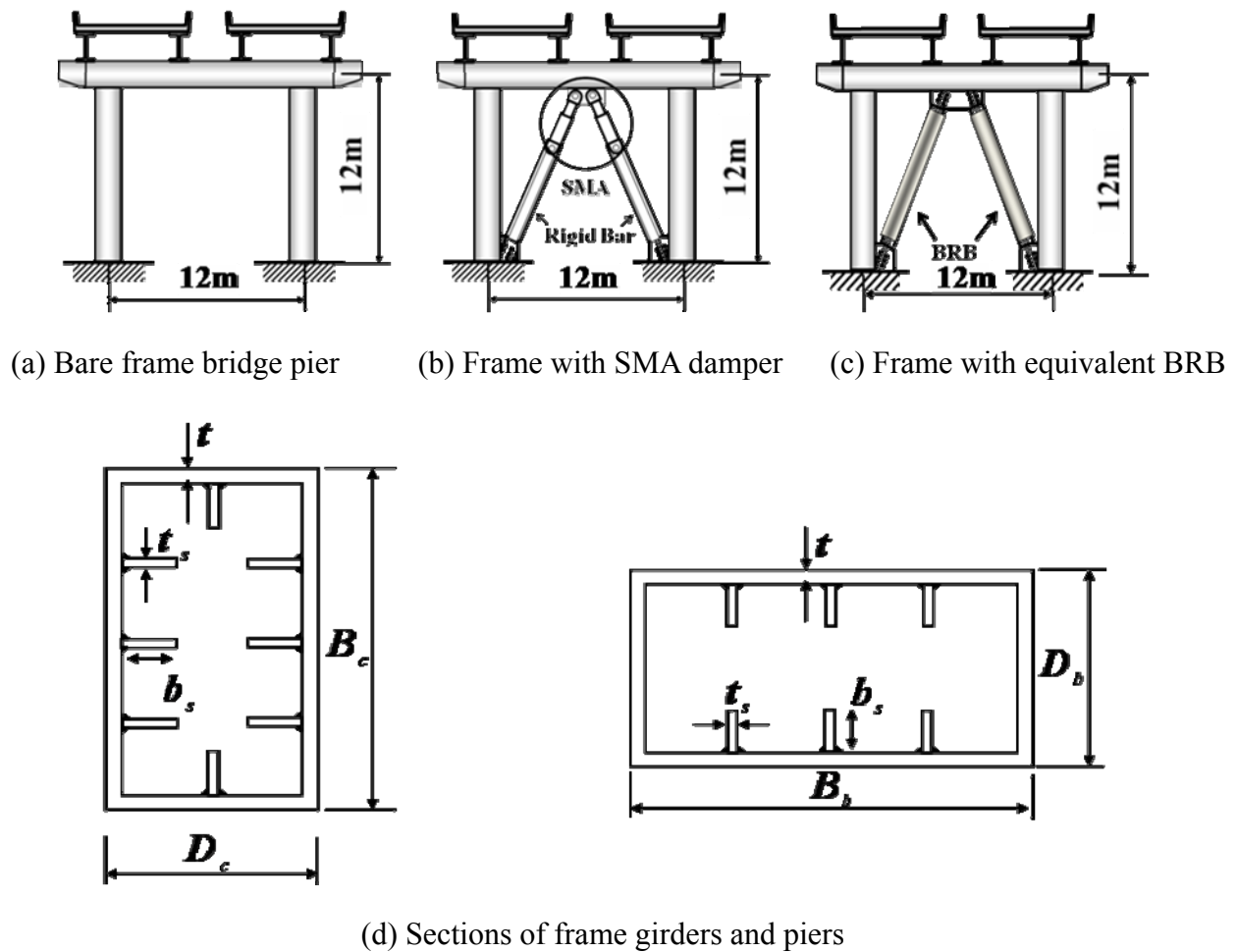
Figure 4. Benchmark Frame Bridge Pier

Table 1. SMA Material Constants (Motahari and Ghassemieh [17])

E_A(GPa)	E_M(GPa)	ε_L	T(°C)	σ_{MSCR}(MPa)
70	30	0.05	40	100
σ_{MS}(MPa)	σ_{MF}(MPa)	σ_{AS}(MPa)	σ_{AF}(MPa)	σ_{MFCR}(MPa)
235	325	210	100	170

Table 2. Basic Information of the Bare Frame

Name	M(kg)	V_y (kN)	$\delta_{y,top}$ (m)
FA	2042	6758	0.078

Four strong ground motions are considered in the analysis, three of which are recommended in the JRA code [19], i.e., JRT-EW-M, JRT-NS-M and FUKIAI-M, and the other is LA16 available in SAC [20].

As in a previous study of controlled structures Ye and Ouyang [21], three parameters, i.e., the strength ratio α_F, the stiffness ratio α_K and the displacement ratio α_δ, were proposed as design governing parameters shown below:

$$\alpha_F = \frac{F_{y,d}}{F_{y,f}} \qquad \alpha_k = \frac{K_{y,d}}{K_{y,f}} \qquad \alpha_\delta = \frac{\delta_{y,d}}{\delta_{y,f}} \tag{8}$$

here, $F_{y,d}$, $K_{y,d}$ and $\delta_{y,d}$ are yield strength, elastic stiffness and yield displacement of the damping device, respectively, while $F_{y,f}$, $K_{y,f}$ and $\delta_{y,f}$ are those of the main structure.

Geometric parameters and basic properties of the SMA damping device are illustrated in Figure 5, where $(EA)_{SMA}$ and l_{SMA} are stiffness and length of the SMA damper, respectively, $(EA)_b$ and l_b are stiffness and length of the steel brace, respectively, F_{SMA}, K_{SMA} and δ_{SMA} are lateral yield force, elastic stiffness and displacement of the SMA damping device, respectively. α_L and β_L are taken as two scale factors on the length ratio and stiffness ratio between the steel brace component and SMA damper listed below:

$$\alpha_L = l_b / l_{SMA} \tag{9}$$

$$\beta_L = (EA)_b / (EA)_{SMA} \tag{10}$$

Moreover, l is the whole length of the damping device.

$$l = l_{SMA} + l_b \tag{11}$$

Relationships between F_{SMA}, K_{SMA} and δ_{SMA} are expressed by:

$$F_{SMA} = K_{SMA}\delta_{SMA} \tag{12}$$

and K_{SMA} and δ_{SMA} can be obtained as follow:

$$K_{SMA} = A_{SMA} \cdot \frac{1}{C_1} \frac{E_{SMA}L^2}{l^3} \tag{13}$$

$$\delta_{SMA} = \frac{\sigma_{SMA}}{E_{SMA}} \frac{l^2}{L} C_1 \tag{14}$$

in which,

$$C_1 = \frac{2}{(1+\alpha_L)}\left(1+\frac{\alpha_L}{\beta_L}\right) \tag{15}$$

As a result, Eq. 12 can be rewritten as:

$$F_{SMA} = \sigma_{SMA} A_{SMA} \frac{L}{l} \tag{16}$$

In particular, α_L=0 means that the damper is designed by full SMA component and β_L=∞ means that the stiffness of the steel brace is assumed to be rigid.
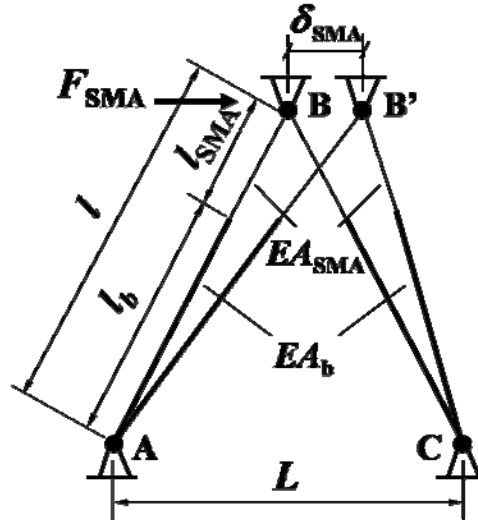
Figure 5. Schematic diagram for SMA damping device

5.   RESULTS AND COMMENTS

In order to investigate the upgrading effectiveness of the seismic performance of frames with SMA damping devices, performance parameters to be investigated include:

1) maximum top displacement, δ_{max};
2) residual top displacement, δ_{res};
3) maximum base shear, V_{max};
4) normalized axial strain of SMA dampers, $\varepsilon_{max}/\varepsilon_{y)SMA}$; and
5) normalized average compressive strain at the base of the pier, $\varepsilon_{a,max}/\varepsilon_{y)Steel}$.

These five performance parameters are evaluated under considerations of four influence factors listed as follows:
1) strength ratio, α_F;
2) martensite fraction of SMA dampers, ξ;
3) length ratio, α_L; and
4) ground motion.

5.1   Effects of Strength Ratio α_F

Only JRT-EW-M accelerogram is used for the time-history analysis presented in this subsection. For comparison, equivalent frames with BRB dampers are designed with the same strength ratio α_F and stiffness ratio α_K as frames with austenite SMA damping devices, and the basic information of SMA models and BRB models are shown in Table 3. The response results are illustrated in Figure 6 and maximum seismic responses are listed in Table 4.

Shown in Figure 6(a) are the time history responses of the top displacement for the SMA and BRB models together with the bare frame. Compared to the bare frame, it can be seen that the displacement demands are greatly reduced in both the damped models. With the same strength ratio, comparisons bewteen the SMA and BRB models indicate that the maximum top displacement in the SMA models is a little larger, but the residual top displacement is far less than those in the BRB models. Stress-strain responses of the SMA and BRB dampers with the same α_F are also investigated as shown in Figure 6(b), the hysteretic loops of SMAs are shallower than those of

BRBs. Relationships between the total base shear and top displacement of damped frames are shown in Figure 6(c) that the maximum base shear and maximum top displacement in the SMA models are larger than those in the BRB models.

Table 4 represents normalized maximum responses obtained from the time-history analysis. Compared to the bare frame, significant reductions can be seen in nearly all the performance parameters except for the maximum base shear. From comparisons between the SMA and BRB models with the same α_F and α_K, it is found that the efficiency of the BRB models is better than the SMA models except for the ability of re-centering. For example, in the case of α_F=1.0, the residual top displacement in the SMA models reaches to $0.002\delta_y$ while $0.151\delta_y$ in the BRB models, and the maximum average strain at the base of the pier in the BRB models is nearly $0.9\varepsilon_y$, while $1.4\varepsilon_y$ in the SMA models which is still less than $2.0\varepsilon_y$, which is required for the performance level 2 as in Usami et al. [22].

The facts revealed in Figure 6 and Table 4 suggest that excellent superelastic recovery mechanism restrains full development of energy dissipation ability in austenite SMA dampers, so in generally the energy dissipating ability of the BRB dampers is better than the SMA's, but the seismic demands of frames with SMA damping devices can still be effectively controlled in light damage (i.e., $\varepsilon_{a,max}\leq2.0\varepsilon_y$). Moreover, the re-centering ability in the SMA models is far better than those in the BRB models so that it is useful for reducing permanent deformation in structures under strong earthquakes.

Table 3. Basic Information of BRB and SMA Models

Case	α_F	α_K	σ_y(MPa)	A (m^2)	α_L
B-F05	0.5	6.32	59.3	0.092	--
B-F10	1.0	6.41	118	0.093	--
B-F15	1.5	6.42	172	0.093	--
S-F05	0.5	6.32	235	0.023	10.3
S-F10	1.0	6.41	235	0.047	4.69
S-F15	1.5	6.42	235	0.068	2.90
Note: B-F and S-F represent BRB models and SMA models, respectively, and numbers after F stand for the value of the strength ratio α_F.					

Table 4. Effects of α_F

Case	Time history analysis results				
	$\dfrac{\varepsilon_{a)max}}{\varepsilon_y}$	$\dfrac{\delta_{max}}{\delta_{y,f}}$	$\dfrac{\delta_{res}}{\delta_{y,f}}$	$\dfrac{V_{b,max}}{F_{y,f}}$	$\left.\dfrac{\varepsilon_{max}}{\varepsilon_y}\right)_{SMA}$
Bare	20.4	3.33	0.981	1.19	--
B-F05	2.01	1.69	0.138	1.10	14.5
S-F05	3.77	2.15	0.023	1.65	18.8
B-F10	0.889	0.995	0.151	1.28	4.36
S-F10	1.43	1.91	0.002	1.70	8.38
B-F15	0.653	0.945	0.046	1.57	2.84
S-F15	0.731	1.00	0.008	1.65	3.06
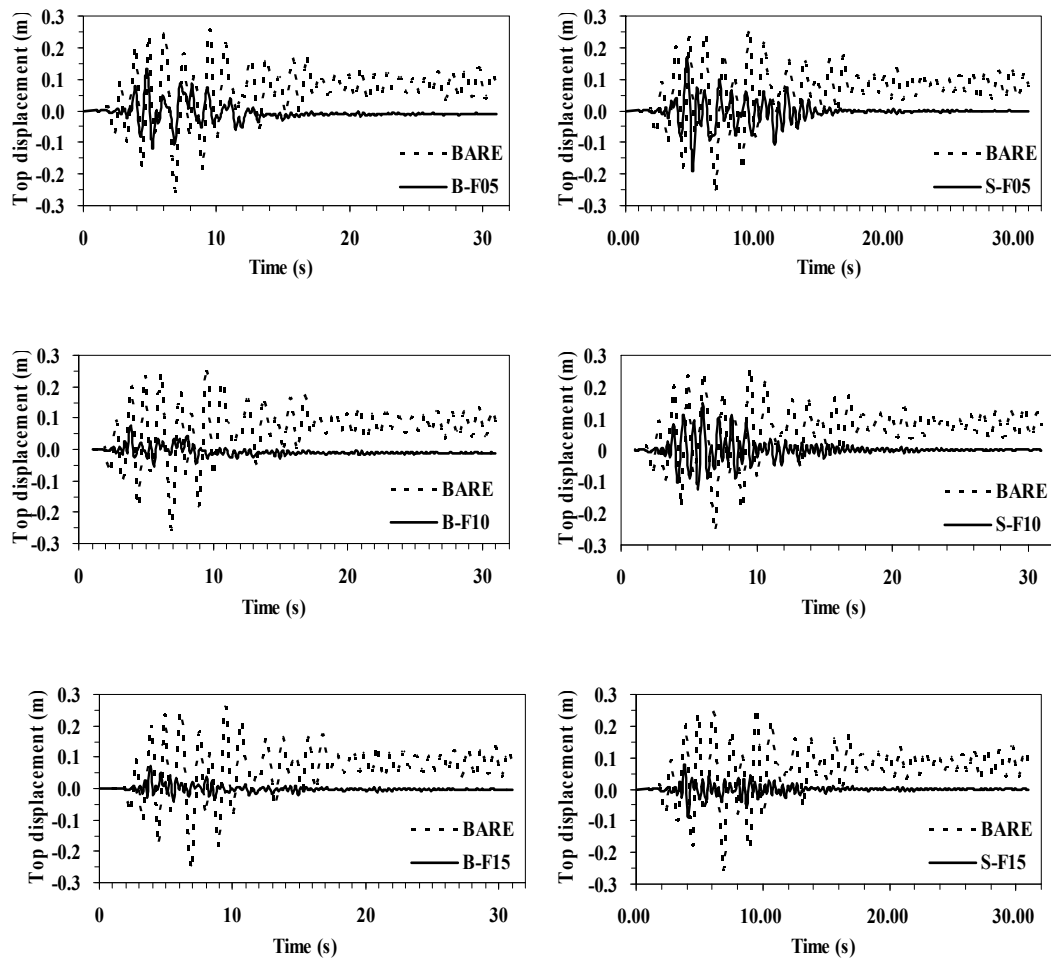
(a) Top displacement response
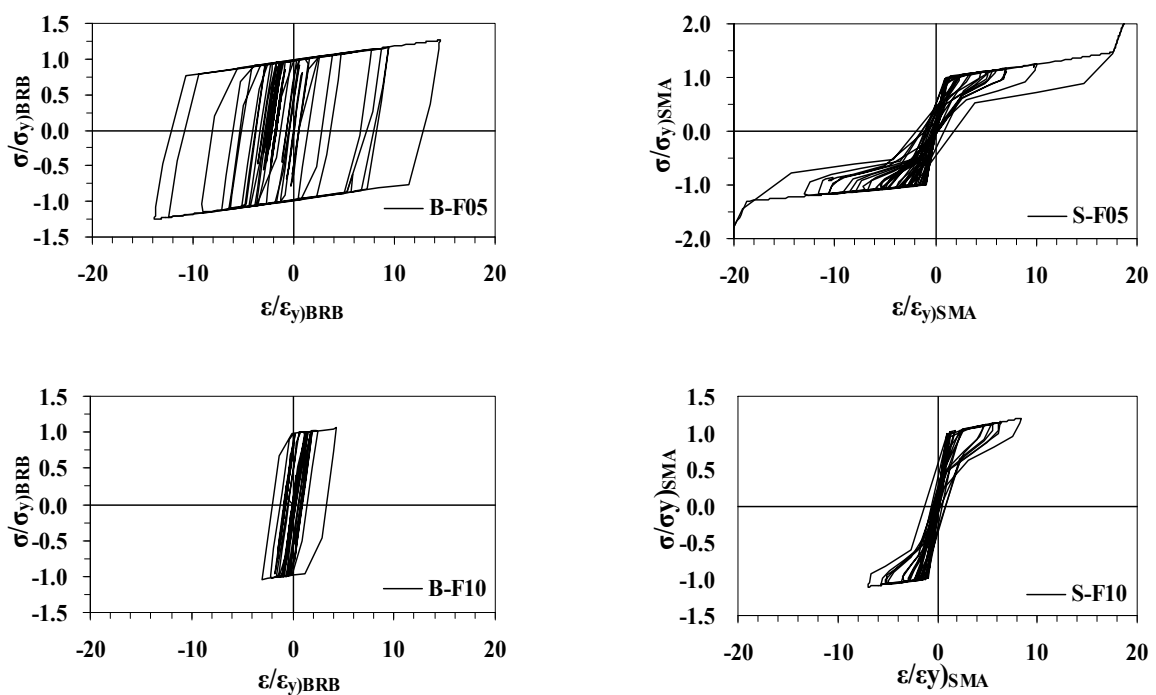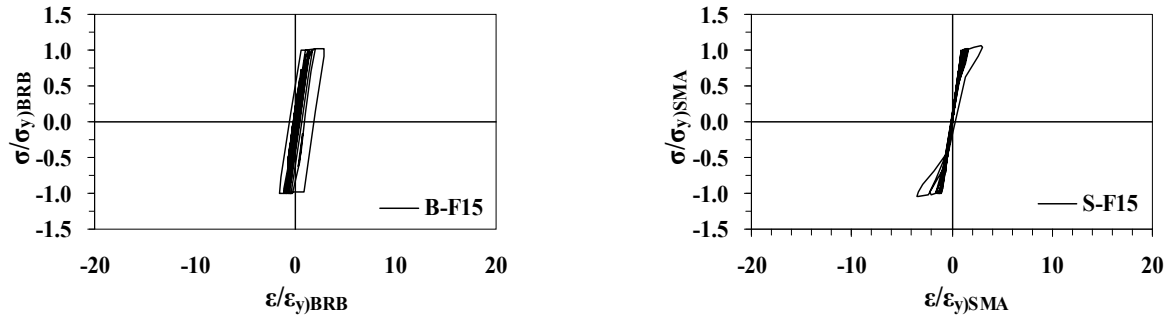
(b) Stress-strain response of dampers
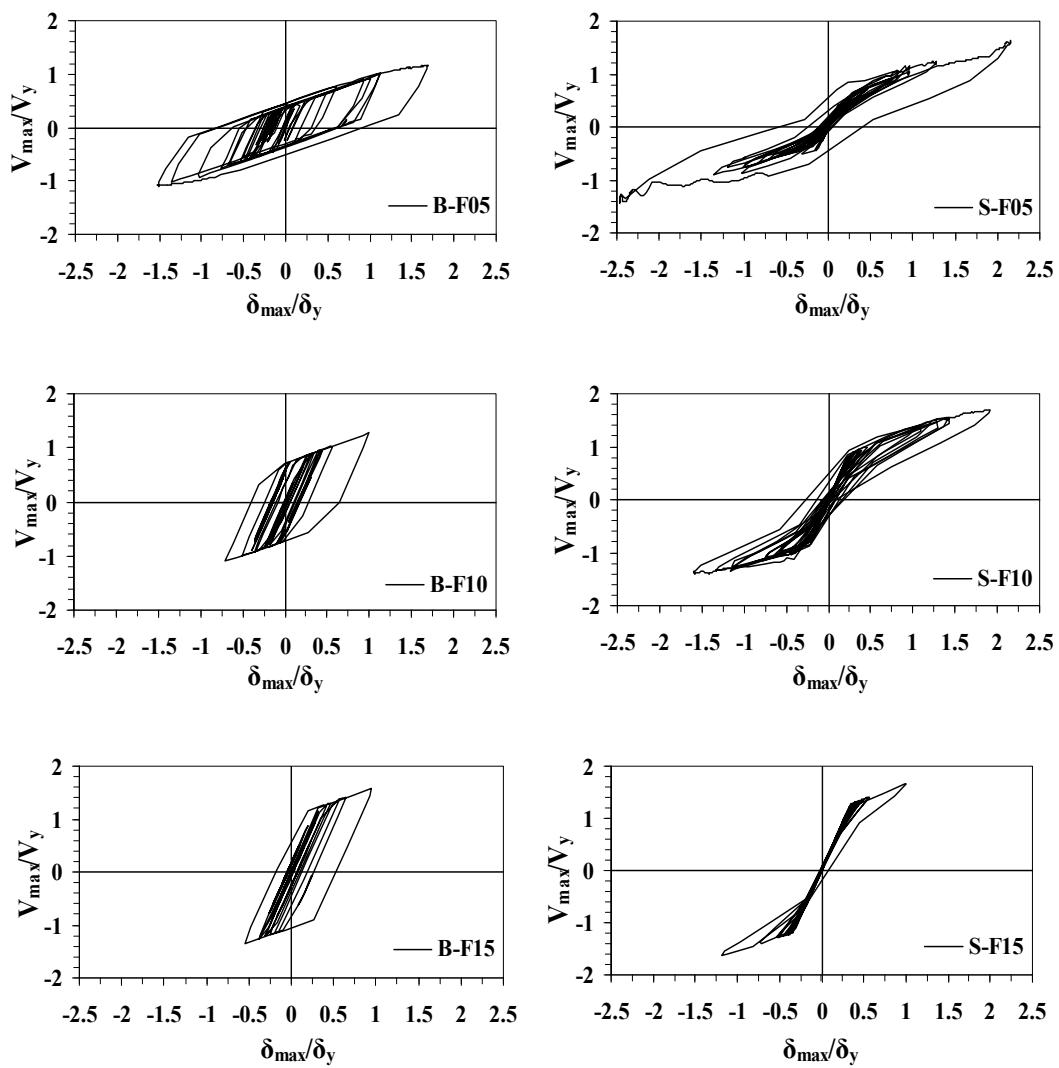
(c) Base shear-top displacement responses

Figure 6. Comparisons between the BRB and SMA Models
with Different Strength Ratios α_F

5.2   Effects of Martensite Fraction ξ in SMA Dampers

Only JRT-EW-M accelerogram, the strength ratio α_F=1.0 and the length ratio α_L=4.69 are used here. Five different cases are investigated with five different martensite fractions, i.e., 0%, 25%, 50%, 75% and 100%, which mentioned as M00, M25, M50, M75 and M100. It is noted that the case of M00 is the same as the case S-F10. Because of different start transformation stresses in the austenite and martensite states, areas of SMA are calculated based on Eq. 16 and listed in Table 5.

Table 5. Effects of ξ

Case	Time history analysis results					
	A (m^2)	$\dfrac{\varepsilon_{a)max}}{\varepsilon_y}$	$\dfrac{\delta_{max}}{\delta_{y,f}}$	$\dfrac{\delta_{res}}{\delta_{y,f}}$	$\dfrac{V_{b,max}}{F_{y,f}}$	$\left.\dfrac{\varepsilon_{max}}{\varepsilon_y}\right)_{SMA}$
M00	0.0465	1.43	1.91	0.002	1.70	8.38
M25	0.0543	1.40	1.68	0.008	1.64	7.48
M50	0.0653	1.35	1.29	0.028	1.52	5.77
M75	0.0817	0.856	0.932	0.040	1.43	4.26
M100	0.1093	0.706	0.829	0.034	1.40	4.11

Shown in Figure 7(a) are the time history responses of the top displacement for the SMA models with different martensite fractions. Compared to the case of M00, it can be seen that with the increase of the martensite fraction, the residual top displacements increase and the maximum displacement demands are reduced. Shown in Figure 7(b) are the stress-strain responses of dampers, and the same tendency also appears in the relationships between the total base shear versus top displacement shown in Figure 7(c) that the hysteretic loop turns more and more stable and full as the content of martensite SMA increases.

The normalized maximum responses from the time history analysis are shown in Table 5. As we can see, investigated performances of δ_{max}, V_{max} and $\varepsilon_{a,max}$ are improved with increasing content of martensite SMA, but the performance of δ_{res} decreases because of lack of super-elasticity in martensite SMAs. For example, the maximum base shear decreases from nearly $1.7V_y$ in the case of M00 to below $1.4V_y$ in the case of M100, while the corresponding residual top displacement increases from $0.002\delta_{y,f}$ to $0.034\delta_{y,f}$.

5.3   Effects of Length Ratio α_L in Damping Devices

Only JRT-EW-M accelerogram, the strength ratio α_F=1.0 and the martensite fraction ratio ξ=0 are used here. Five different length ratios, i.e., 1, 2, 4, 6 and 4.69, are considered.   The case of 4.69 is the same as the cases of S-F10 and M00 in the above subsections.

Under the conditions of the same SMA area and martensite fractions, from Eqs. 13 and 15, it can be found that the bigger the length ratio, the larger the stiffness of the damping device. From the normalized maximum responses shown in Table 6, it is noted that with the length ratio increasing, all investigated performances of δ_{max}, V_{max}, $\varepsilon_{a,max}/\varepsilon_{y)Steel}$ and δ_{res} are improved, and $\varepsilon_{max}/\varepsilon_{y)SMA}$ increases rapidly mainly because the length of SMA damper is shorten with the increased length ratio.
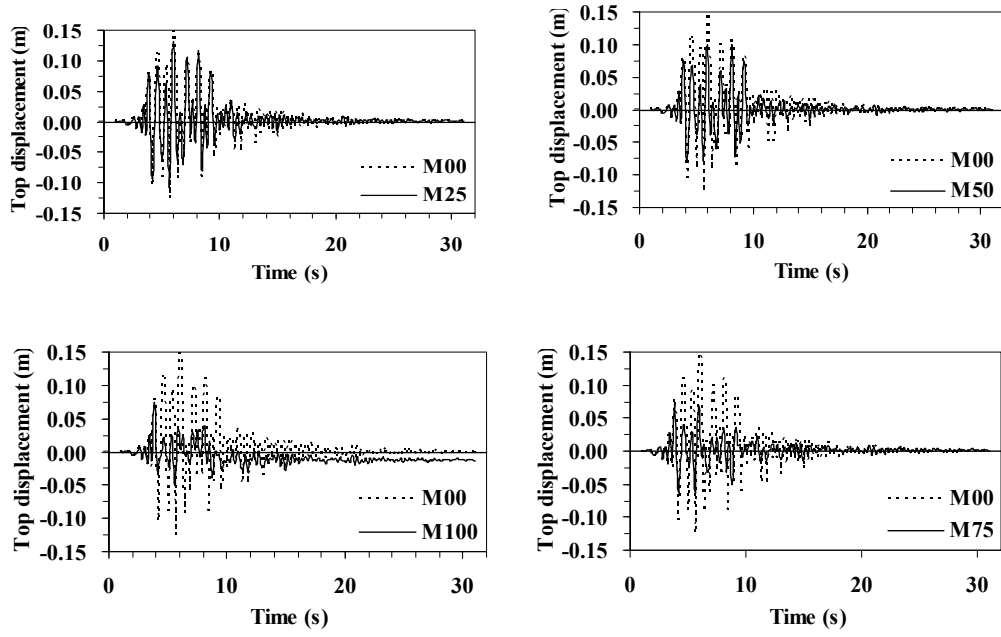
(a) Top displacement response
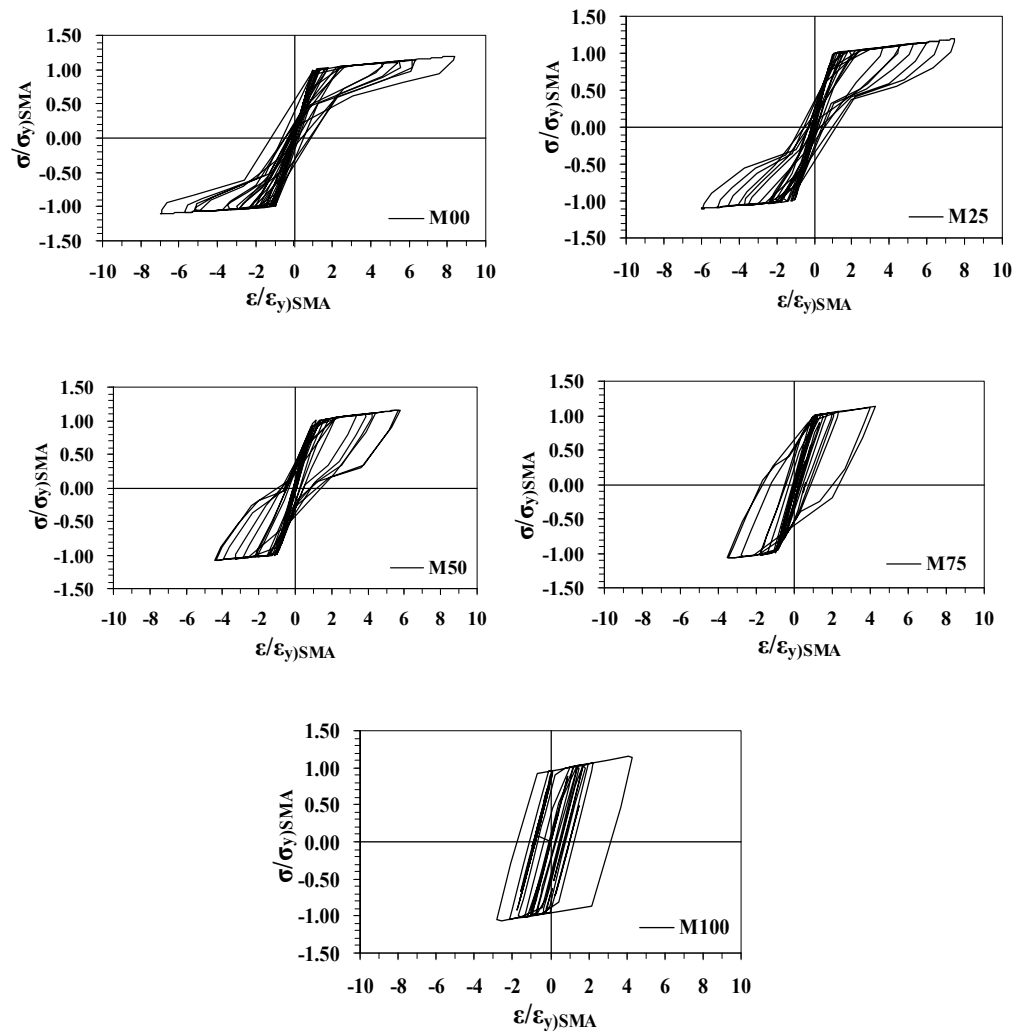
(b) Stress-strain Response of Dampers
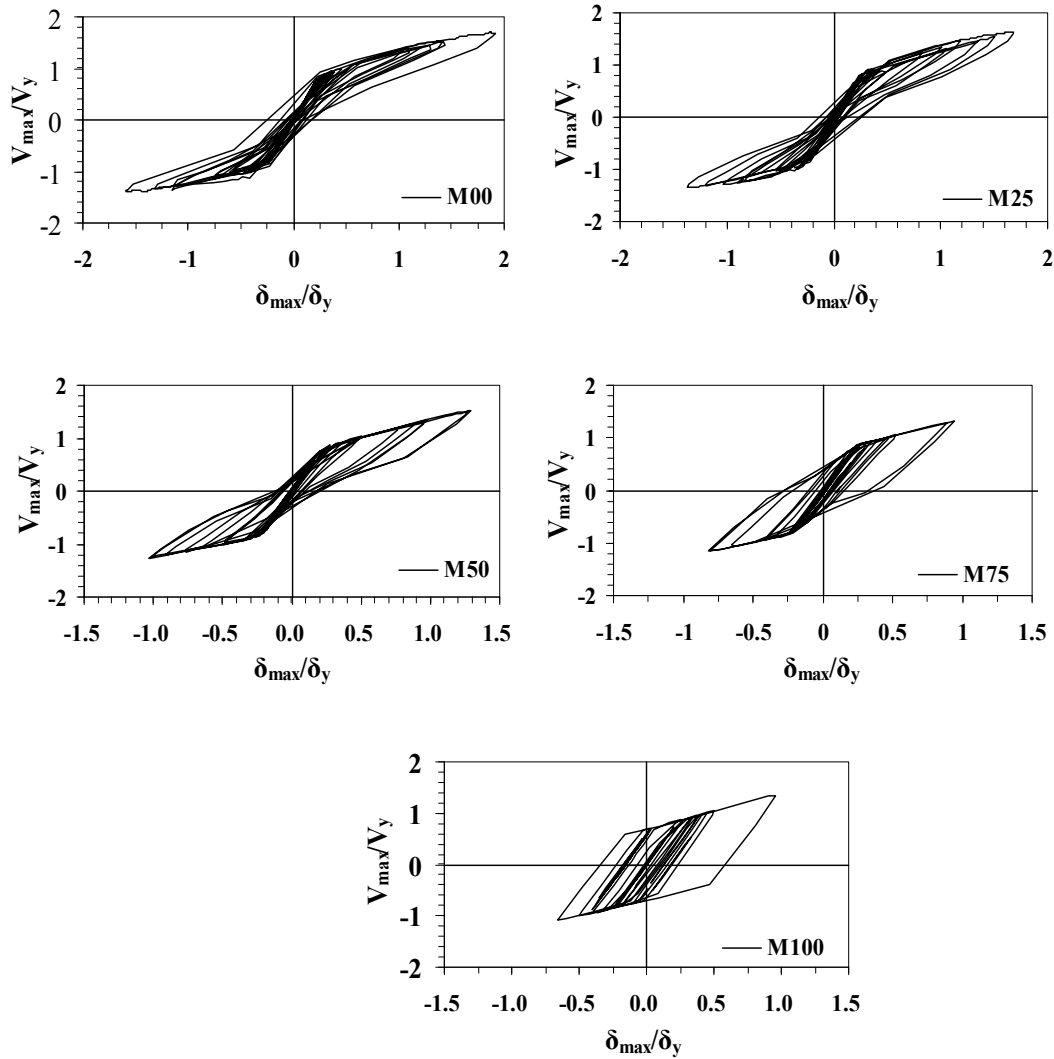
(c) Base Shear-top Displacement Responses

Figure 7. Comparisons of SMA Models with Different Martensite Fraction Ratios ξ

Table 6. Effects of α_L

Case	Time history analysis results				
	$\dfrac{\varepsilon_{a)max}}{\varepsilon_y}$	$\dfrac{\delta_{max}}{\delta_{y,f}}$	$\dfrac{\delta_{res}}{\delta_{y,f}}$	$\dfrac{V_{b,max}}{F_{y,f}}$	$\left.\dfrac{\varepsilon_{max}}{\varepsilon_y}\right)_{SMA}$
L4.69	1.43	1.91	0.002	1.70	8.38
L1	1.92	2.05	0.070	1.57	3.06
L2	1.83	1.90	0.049	1.57	4.34
L4	1.51	1.93	0.013	1.69	7.39
L6	1.59	1.86	0.013	1.74	10.2

5.4   Effects of Various Strong Ground Motions

To further investigate efficiency of dampers under various ground motions, except for aforementioned JRT-EW-M, three other ground motions JRT-NS-M, FUKIAI-M and LA16 are employed. The bare frame, frames with SMA damping devices and equivalent frames with BRB dampers under α_F=0.5 are considered.

The result comparisons are illustrated in Figure 8. Compared to the bare frame, it is clear as mentioned before that each performance demand in the damped frames has a large reduction except for the base shear force. Comparing between the SMA and BRB models, it can be found that most performance indices of the SMA models are larger than the BRB models, particularly in JRT-NS-M and FUKIAI-M cases. The residual top displacements of the SMA models are far less than those of the BRB models under the ground motions of JRT-EW-M and LA16 but almost equal under the ground motions of JRT-NS-M and FUKIAI-M. Therefore, it can be concluded that the performance of the SMA model is much more sensitive to earthquake inputs, and attentions are needed in practical design.

(a) Normalized max top disp.   (b) Normalized residual top disp.

(c) Normalized max shear force   (d) Normalized average strain at piers
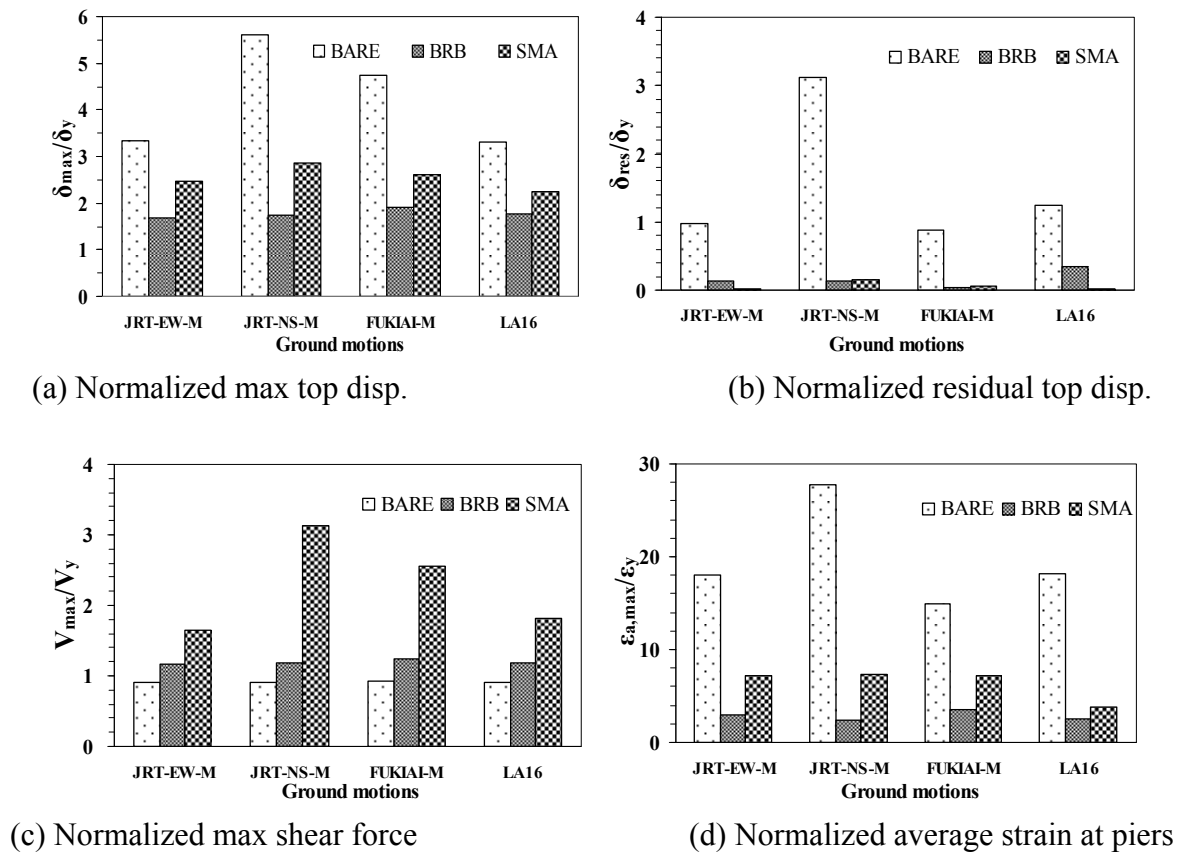
Figure 8. Comparison of SMA Models with Various Strong Earthquake Motions

6.   CONCLUSIONS

This paper is dealt with applications of superelastic SMAs for seismic performance upgrading of civil engineering structures. Initially, a modified multi-linear model with diagonal rule which accounts for inner hysteretic loops is developed for SMA material. Then, an axial-type SMA damper is proposed and the corresponding modeling is presented based on the material model.

Dynamic numerical simulations have been implemented to evaluate the seismic behavior of a benchmark steel portal frame using SMA damping devices. Comparisons with the bare frame and the equivalent frame with BRB dampers are carried out and four influence factors are considered. Following conclusions can be drawn:

1) Compared to the bare frame, use of the SMA damper is effective to improve seismic performance of the main structure.

2) If designed with the same α_F and α_K, a SMA damper is superior to BRBs on re-centering ability. However, the energy dissipation ability in SMA dampers is less than in BRB dampers. Thus, selection of SMA dampers should be attractive to control the residual displacement for special structures after strong earthquake.

3) The more the martensite content include in the SMA damper, the more the re-centering ability loses and the more the energy dissipating ability has in the frame.

4) When the length ratio increases, the stiffness of the brace system increases and the energy dissipating ability increases.

5) The performance of structures with the SMA damper is sensitive to earthquake inputs, and attentions are needed in practical design.

ACKNOWLEDGEMENT

REFERENCES

[1]   Weber, F., Feltrin, G., Huth, O., "Guidelines for Structural Control", SAMCO Final Report by Structural Engineering Research Laboratory, Swiss Federal Laboratories for Materials Testing and Research, Dübendorf, Switzerland, 2006.

[2]   Dolce, M., Cardone, D. and Marnetto, R., "Implementation and Testing of Passive Control Devices Based on Shape Memory Alloys", Earthquake Engng Struct. Dyn., 2000, Vol. 29, pp. 945-968.

[3]   Wilde, K., Gardoni, P. and Fujino, Y., "Base Isolation System with Shape Memory Alloy Device for Elevated Highway Bridges", Engineering Structures, 2000, Vol. 22, pp. 222-229.

[4]   Li, H., Mao, C.X., and Ou, J.P., "Experimental and Theoretical Study on Two Types of Shape Memory Alloy Devices", Earthquake Engng Struct. Dyn., 2007, Vol. 37, pp. 407-426.

[5]   Zhu, S.Y. and Zhang, Y.F., "Seismic Behavior of Self-centring Braced Frame Buildings with Reusable Hysteretic Damping Brace", Earthquake Engng Struct. Dyn., 2007, Vol. 36, pp. 1329-1346.

[6]   Zhu, S.Y. and Zhang, Y.F., "Seismic Analysis of Concentrically Braced Frame Systems with Self-Centering Friction Damping Braces", Journal of Structural Engineering, ASCE, 2008, Vol. 134, No. 1, pp. 121-131.

[7]   Song, G., Ma, N., Li, H.N., "Applications of Shape Memory Alloys in Civil Structures", Engineering Structures, 2006, Vol. 28, pp. 1266-1274.

[8]   McCormick, J., DesRoches, R., Fugazza, D. and Auricchio, F., "Seismic Assessment of Concentrically Braced Steel Frames with Shape Memory Alloy Braces", Journal of Structural Engineering, ASCE, 2007, Vol. 133, No. 6, pp. 862-870.

[9]   Paiva, A. and Savi, M.A., "An Overview of Constitutive Models for Shape Memory Alloys", Mathematical Problems in Engineering, 2006, pp. 1-30.

[10] Delemont, M. and DesRoches, R., "Seismic Retrofit of Simply Supported Bridges Using Shape Memory Alloys", Engineering Structures, 2002, Vol. 24, pp. 325-332.

[11] Graesser, E.J. and Cozzarelli, F.A., "Shape-memory Alloys as New Materials for Aseismic Isolation", Journal of Engineering Mechanics, ASCE, Vol. 117, No. 11, pp. 2590-2608.

[12] Tanaka, K., "A Thermomechanical Sketch of Shape Memory Effect: One-dimensional Tensile Behavior", Materials Science Research International, 1985, Vol. 18, pp. 251-263.

[13] Brinson, L.C., "One Dimensional Constitutive Behavior of Shape Memory Alloys: Thermomechanical Derivation with Non-constant Material Functions and Redefined Martensite Internal Variable", Journal of Intelligent Material Systems and Structures, 1993, Vol. 4, pp. 229-242.

[14] Boyd, J.G. and Lagoudas, D.C., "A Thermodynamic Constitutive Model for the Shape Memory Materials. Part I: the Monolithic Shape Memory Alloys", Int. J. of Plasticity, 1996, Vol. 12, No. 6, pp. 805-842.

[15] Tamai, H. and Kitagawa, Y., "Pseudoelastic Behavior of Shape Memory Alloy Wire and its Application to Seismic Resistance Member for Building", Computational Material Science, 2002, Vol. 25, pp. 218-227.

[16] Auricchio, F. and Sacco, E., "A One-dimensional Model for Superelastic Shape-memory Alloys with Different Elastic Properties between Austenite and Martensite", Int. J. Nonlinear Mechanics, 1997, Vol. 32, No. 6, pp. 1101-1114.

[17] Motahari, S.A. and Ghassemieh, M., "Multilinear One-dimensional Shape Memory Material Model for Use in Structural Engineering Applications", Engineering Structures, 2007, Vol. 29, pp. 904-913.

[18] Chen, Z.Y., Ge, H.B., Kasai, A. and Usami, T., "Simplified Seismic Design Approach for Steel Portal Frame Piers with Hysteretic Dampers", Earthquake Engineering and Structural Dynamics, 2007, Vol. 36, No. 4, pp. 541-562.

[19] JRA, "Design Specification of Highway Bridges. Part V: Seismic design", Japan Road Association, Tokyo, Japan, 2002, (in Japanese).

[20] SAC., "Develop Suites of Time Histories, SAC Joint Venture Steel Project Phase2: Project Task 5.4.1", Draft Report prepared by Woodward-Clyde Federal Services, Pasadena, CA, 1997.

[21] Ye, L.P., and Ouyang, Y.F., "Dual Seismic Structure System and its Parametric Analysis", Engineering Mechanics, 2000, Vol. 17, No. 2, pp. 23-29.

[22] Usami, T. ed., "Guidelines for Seismic and Damage Control Design of Steel Bridges", Japanese Society of Steel Construction, Gihodo Shuppan, Tokyo, Japan, 2006 (in Japanese).

Appendix A

In the simplified model, temperature effect should be considered in transformation stress determination. In the text, SMA material constants at $T_0 = 40^oC$ is cited from Ref. [17]. According to the formualtions in Ref. [17], considering the SMA tranformation constant of 5.6 MPa/^oC, if $T_0 = 25^oC$, the four transformation stresses would decrease nearly 84MPa, as listed in Table A-1.

Take the case of S-F10 under JRT-EW-M accelerogram as example, the SMA damper was redesigned by Eqs. 8-16 in the paper with the same strength ratio and stiffness ratio, new dimensions of SMA damper are listed in Table A-2.

The performance investigation is illustrated as shown in Figure A-1. At the same level of strength ratio and stiffness ratio, it is found that similar structural responses existed in the structures with SMA dampers at $T_0 = 40^oC$ and at $T_0 = 25^oC$. It might be concluded that the conclusion of the paper would not have much difference by using the material constants at $T_0 = 40^oC$.

Table A-1. Material constants of SMAs at $T_0 = 40^oC$ and $T_0 = 25^oC$

$T_0(^oC)$	σ_{MS}(MPa)	σ_{MF}(MPa)	σ_{AS}(MPa)	σ_{AF}(MPa)
40	235	325	210	100
25	151	241	126	16

Table A-2. Design parameters and dimensions of SMAs at $T_0 = 40^oC$ and $T_0 = 25^oC$

$T_0(^oC)$	A(mm^2)	l_{SMA}(mm)	α_F	α_K
40	4651	2358	1.0	6.41
25	7238	3664	1.0	6.41
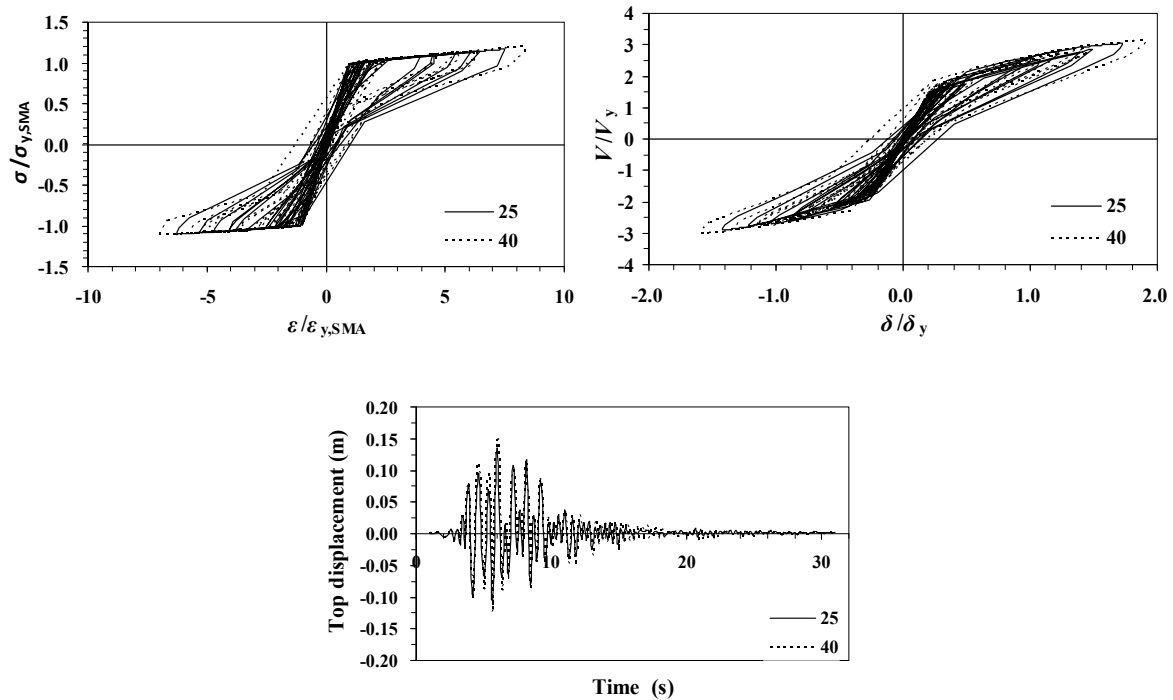
Figure A-1. Comparison of SMA Models with Material Constants at Different Reference Temperature

INFLUENCE OF THERMAL INSULATION ON THE ENERGY BALANCE FOR COLD-FORMED BUILDINGS

H. Gervásio [1], P. Santos [2,*], L. Simões da Silva [3] and A.M.G. Lopes [4]

[1] *ISISE, GIPAC Lda, Coimbra, Portugal*
[2] *CICC, Civil Engineering Department, University of Coimbra, Coimbra, Portugal*
[3] *ISISE, Civil Engineering Department, University of Coimbra, Coimbra, Portugal*
[4] *ADAI, Mechanical Engineering Department, University of Coimbra, Coimbra, Portugal*
*(Corresponding author: E-mail: pfsantos@dec.uc.pt)

ABSTRACT: Two major factors contribute to the sustainability of buildings: material efficiency and energy efficiency. Material efficiency relates to the use of environmental-friendly materials and to the minimization of construction waste materials, either during construction and at the end-of-life stage of the building. Energy efficiency is currently understood as the optimization of the energy used during the operation stage of the building. This entails the energy needed for heating, cooling, lighting, etc. Often in order to improve the energy needs of a building, more insulation material is used, thus leading to a trade-off between embodied energy and operational energy. It is the aim of this paper to analyse and discuss the balance between the embodied energy and the operational energy for various levels of insulation, over its life cycle. The operational energy is estimated based on the simplified approach provided by the Portuguese Code of practice. The estimated operational energy is then balanced against the life cycle embodied energy of the system. Finally, the simplified approach for the calculation of the operational energy is confronted to more sophisticated dynamic simulations using the software EnergyPlus.

Keywords: Energy efficiency, Light steel residential buildings, Thermal insulation, Life-cycle energy analysis, Embodied energy, Operational energy

1. INTRODUCTION

Buildings are one of the major concerns regarding the sustainability of our habitat. The construction industry consumes materials and energy and is one of the main causes of pollution and resource depletion. According to the EU Communication ''Towards a thematic strategy on the urban environment'' [1], ''(…)*Heating and lighting of buildings accounts for the largest single share of energy use (42%, of which 70% is for heating) and produces 35% of all greenhouse gas emissions. Buildings and the built environment use half of the material taken from the Earth's crust and are the source of 450 MT construction and demolition waste per year (over a quarter of all waste produced)(…) In Europe, people spend almost 90% of their time inside buildings. Poor design and construction methods can have a significant effect on the health of the building's occupiers and can produce buildings that are expensive to maintain, heat and cool, disproportionately affecting the elderly and less affluent social groups. Badly designed buildings such as housing estates can facilitate criminal behaviour.*(…)''

The construction sector is of vital importance in our society and is a major contributor to socio-economic development in every country.

As the largest and most fragmented industry, the construction sector faces huge challenges in the pursuit of sustainability. Sustainable construction is a way for the industry to move towards achieving sustainable development, taking into account environmental, socio-economic and cultural issues. Sustainable construction ensures more economical use of finite raw materials and reduces and above all prevents the accumulation of pollutants and waste over the complete cycle of the building. Therefore, the use of environmentally friendly materials, cleaner construction

methodologies, minimization and optimization of energy use, etc, are a major step towards the well being of the environment and foster sustainable development.

Several researchers have addressed the evaluation of the environmental impact of buildings over the entire life-cycle. Debnath et al. [2] presented a comparison of the embodied energy required for single and double storey residential buildings with load bearing walls, and four storey residential buildings with a reinforced concrete structure in India. They concluded that in India the embodied energy of construction materials in residential buildings is about 3-5 GJ/m^2.

In Sweden, Adalberth [3] suggested a methodology for a life-cycle energy analyses and applied it to three prefabricated single-unit dwellings [4]. He found that 85 % of total energy usage is required during the management phase leading to conclude that is essential to produce dwellings that requires small amounts of energy during this phase. A Canadian research [5] examined the embodied energy and greenhouse gas emissions associated with the on-site construction of alternative structural building assemblies based in different materials: wood, steel and concrete. Significant differences were found between the energy and greenhouse gas emissions associated with the construction of these structural assemblies, with concrete typically involving higher quantities.

In the UK, Eaton and Amato [6] performed a comparative life-cycle analysis of steel and concrete framed office buildings and concluded that there is no operational energy benefit in the passive thermal performance of modern concrete framed office buildings as compared with modern steel ones. Yohanis and Norton [7] studied the variation of life-cycle operational and embodied energy for a generic single-storey office building in the UK. They used a early design model to determine operational energy, capital cost and embodied energy and verify that capital and embodied energy costs as functions of glazing ratio do not vary significantly. More recently, Hacker et al. [8] investigated the effects of thermal mass and climate change on embodied and operational carbon dioxide emissions from a residential house in south-east England. The results presented there were indicative of the lifecycle CO_2 savings and other performance benefits that can potentially be achieved by using heavyweight structural elements to provide thermal mass in housing. However these results are related to a particular dwelling with specific assumptions for several variables.

A recent study by Utama and Gheewala [9] focused on life-cycle energy of single storey houses, particularly on the effect of enclosure materials associated with air-conditioning, trying to identify the best practice of common construction materials used in Indonesia. They verify that materials having low initial embodied energy do not automatically have low life cycle energy and concluded that the best option for reducing life-cycle energy would be having lightweight enclosure materials (medium density and less thickness) leading to less time lag and also having low U-value.

In Israel, Huberman and Pearlmutter [10] performed a life-cycle energy analysis of building materials in the Negev desert region. They concluded that traditional local building materials (well-insulated stabilized soil blocks) may optimize the building's energy requirements over its entire life cycle, by analyzing both embodied and operational energy consumption comparing several possible alternatives. The cumulative energy saved over a 50-year life cycle by this material substitution was around 20%.

All these studies were carried out for a relatively small number of specific climatic regions. According to the subdivision of climatic regions presented by IPCC [11] for the various continents, only a few are represented in these studies. In addition, for the UK, contradictory conclusions are obtained, namely with respect to the benefits of the use of heavyweight structural elements to provide thermal mass in residential buildings. In the coastal region of Portugal there is a void in

respect to life-cycle energy analysis of buildings. This work intends to partially fill this void, analysing a real residential lightweight steel building located in Portugal and making use of typical local climatic conditions to compute the operational energy needed in order to secure the thermal comfort of occupants (heating and cooling). It is well known that in the quantification of the life-cycle energy use by buildings, the operational energy needs to be considered along with the embodied energy of the building materials. The improvement of the thermal behaviour of a building usually requires the utilisation of more insulation materials, which, in turn, increase the embodied energy of the system. The analysis of the trade-off between the operational energy and the embodied energy of a building is one of the main purposes of this paper. This should provide directives for the improvement of the thermal efficiency of modern Portuguese residential buildings in order to minimize the total life cycle building energy.

The structure of this paper is presented next. Firstly, a brief description of the major steps in life cycle analysis and an outline of the methodology for the evaluation of the energy efficiency of residential buildings is presented. Subsequently, using a real lightweight residential building in Portugal, a reference case is analysed. Finally, a parametric study is carried out, whereby increasing levels of insulation are used to assess the trade-off between energy efficiency and life cycle embodied energy.

2.   LIFE CYCLE ANALYSIS

2.1   Introduction

A Life Cycle approach entails the analysis of one or more criteria through the complete life cycle of a building. The complete life cycle of a building, represented in Figure 1, includes all the stages from raw material acquisition, through material production, construction and operation, to demolition and management of construction waste. A life cycle analysis should also include the intermediate phases, such as the transportation of materials and equipment from one place to the other.

In this paper, the criterion for the life cycle analysis is the energy requirement of a building. Two types of energy are going to be quantified: the embodied energy of the building and the operational energy.

The embodied energy of a material refers to the energy used to extract and process the raw materials in order to produce it. A building is usually composed of several types of materials, each of which contributes to the building's total embodied energy. In this analysis, and considering the building's life, the life cycle embodied energy refers to the energy needed to produce the materials, the energy required to construct and repair the building during its use stage, and the energy related to the end-of-life of the building. The energy due to the transportation of materials and equipment is also included in the life cycle analysis. The building's embodied and operational energy are represented in Figure 1.

The operational energy is hereby referred to the energy required to operate the building during its use phase. Thus, the operational energy entails the energy needed to condition the building (to heat, cool and/or ventilate), the energy needed for illumination and power equipment, and the energy needed for other services. In Figure 1, the operational energy refers only to the use phase in the building's cycle.

The embodied energy content of a building is usually considered to be small when compared with the energy required for operating the building over its cycle, although in some cases the embodied energy can be equivalent to many years of operational energy [12]. In fact, as developments in the energy efficiency of the building envelope become more effective, the embodied energy becomes more and more important.
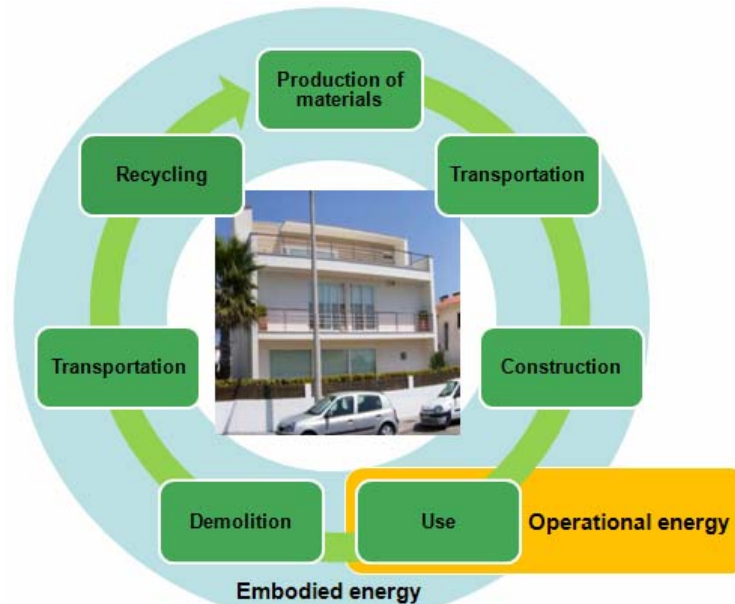
Figure 1. Life Cycle Analysis of the Building

2.2   Life Cycle Assumptions

A life cycle analysis implies a long time period for the analysis. Regarding buildings, assuming a service life of 50 years, the time period of the analysis should include these 50 years, plus the time needed for the production of the materials and the assemblage of the building, and the time needed for the demolition of the structure. However, for the sake of simplification, it is assumed that the time period of the analysis is 50 years. It is further considered that the production of materials and the construction of the building take place in year 0, and that the demolition of the building occurs 50 years later.

The use stage relates to the interval of years between the construction and the demolition of the structure, and includes the maintenance and repair operations, which are necessary over to maintain the building in the required condition. These operations are usually estimated based on common practice. In the following case study, and according to information provided by a manufacturer, it is assumed that the Exterior Insulation Finishing System (EIFS) of the building needs to be repaired every 25 years.

The end-of-life stage is probably the phase more difficult to analyse, particularly in construction facilities with a long life span. Steel is 100% recyclable and scrap can be converted to the same quality steel depending upon the recycling process. Thus, in this paper it is assumed that, at the end-of-life stage, the structure will be demolished and steel is going to be recycled with a recycling rate of 80%. The recovery of steel scrap for recycling allows allocating a credit to the arising scrap. The credit, or benefit, is due to the fact that the production of secondary steel from scrap (in the Electric Arc Furnace route) avoids the production of primary steel from the Blast Furnace route. The approach followed in this case study is the closed material loop recycling methodology proposed by the International Iron and Steel Institute [13]. All the remaining materials are assumed to be sent to landfill.

3. ENERGY EFFICIENCY OF RESIDENTIAL BUILDINGS

3.1 Introduction

The European Directive on the Energy Performance of Buildings (EPBD) [14] is one of the main legislative instruments affecting the building sector in Europe. The directive is designed to promote the energy performance of buildings in member states by introducing a framework for an integrated methodology for measuring energy performance; application of minimum standards in new buildings and certain renovated buildings, and regular updating of these; energy certification and advice for new and existing buildings; and inspection and assessment of boilers and heating/cooling systems. The directive entered into force on the 4th of January, 2003.

To support the implementation of the EPBD in European Member States, the European standards body, CEN, has been developing a series of standards. Among these, the standard for the calculation of energy use for space heating and cooling is EN ISO 13790 [15]. This standard provides calculation methods for the assessment of the energy used for space heating and cooling of residential and non-residential buildings. Calculation procedures are included for the quantification of: (i) heat transfer by transmission and ventilation of the building; (ii) solar gains and its contribution to the building heat balance; and (iii) annual energy needs for heating and cooling. Two main types of calculation methods are available in ISO 13790: quasi-steady state methods, calculating the heat balance over a sufficiently long period of time in order to ignore heat stored and released; and, dynamic methods, calculating the heat balance with short periods (e.g. hourly) and considering the heat stored and released from the mass of the building. In the category of quasi-steady state methods the standard provides a monthly and a seasonal method. In the category of dynamic methods, the standard provides a simplified approach based on a hourly dynamic procedure, and calculation procedures for a more detailed approach based on simulation methods. Consistency in the application of the methods provided in the standard is ensured by a maximum of common procedures and descriptions, boundary conditions and input data.

The adoption of the EPBD in Portugal led to the reformulation of previous codes and to the publication in 2006 of a new Code of Practice for the thermal behavior of residential and small commercial buildings [16], and a new Code of Practice for buildings with HVAC power higher than 25 kW [17]. Both codes have been developed according to the specifications of the European Standard EN ISO 13790 [15].

3.2 Simplified Quasi Steady-State Analysis

The methodology adopted in this paper for the calculation of the energy needs for heating and the energy needs for cooling, is provided by the Portuguese code of practice *"Regulamento das Características de Comportamento Térmico dos Edifícios* (RCCTE)"* [16], hereafter referred to as RCCTE. The methodology was developed according to the European Standard EN ISO 13790 [15] with the adaptations needed to comply with the reality of construction and current operation of buildings in Portugal.

The RCCTE methodology follows a quasi-steady approach and energy needs are calculated per year, considering a heating season and a cooling season. In the following paragraphs the RCCTE methodology is described, but before that, a brief overview of ISO 13790 is given in order to introduce the general framework for the calculation procedures. The seasonal ("quasi-steady state") approach of ISO 13790 is considered, in which dynamic effects are taken into account by introducing correlation factors. Therefore, considering the heating season, the energy needs for space heating, $(Q_{H,nd})$, in *MJ*, is given by

$$Q_{H,nd} = Q_{H,ht} - \eta_{H,gn} Q_{H,gn} \tag{1}$$

where $Q_{H,ht}$ is the total heat transfer for the heating mode, $Q_{H,gn}$ are the total heat gains for the heating mode, and $\eta_{H,gn}$ is the utilization factor for the internal and solar heat gains. The gain utilization factor ($\eta_{H,gn}$) takes into account that only part of the gains are utilized to decrease the energy need for heating, the rest leading to an undesired increase of the internal temperature. This factor is a function of the gain/loss ratio ($\gamma = Q_{gn}/Q_{ht}$) and a numerical parameter (τ) that depends on the time constant of the building (building inertia), and is illustrated in Figure 2.
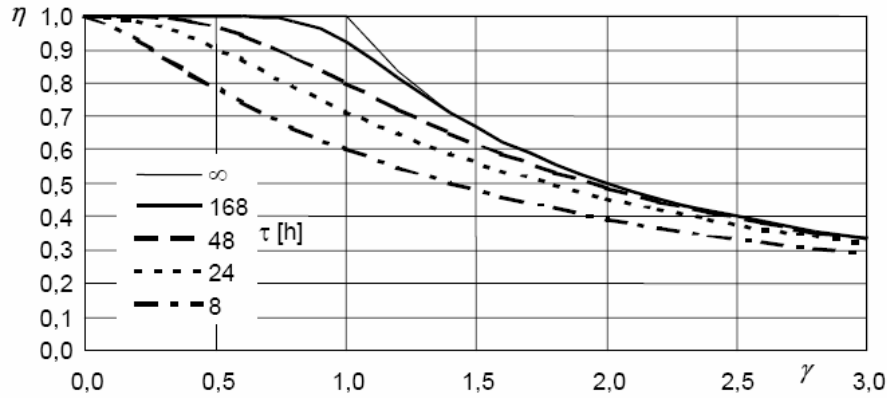
Figure 2. Gain Utilization Factor for Heating [15]

For the cooling season, the energy needs for cooling ($Q_{C,nd}$), in *MJ*, may be obtained by two different ways, corresponding to the same method and leading to the same result:

    i)   by the use of a utilisation factor for losses (mirror image of the approach for heating)

$$Q_{C,nd} = Q_{C,gn} - \eta_{C,ls} Q_{C,ht} \tag{2}$$

where $Q_{C,gn}$ are the total heat gains for the cooling mode, $Q_{C,ht}$ is the total heat transfer for the cooling mode, and $\eta_{C,ls}$ is the loss utilization factor, which takes into account that only part of the transmission and ventilation heat transfer is used to decrease the cooling needs;

    ii)   by the use of a utilisation factor for gains (similar to the heating utilization factor)

$$Q_{C,nd} = (1 - \eta_{C,gn}) Q_{C,gn} \tag{3}$$

where $\eta_{C,gn}$ is the gain utilization factor, which takes into account the fact that only part of the gains is compensated by thermal heat transfer by transmission and ventilation assuming a certain maximum internal temperature. The curves for $\eta_{C,gn}$ are the same as for $\eta_{H,gn}$ (see Figure 2).

For each mode, heating mode (H) or cooling mode (C), the total heat transfer (Q_{ht}) of a space zone and for a given calculation period is given by the sum of the heat transfer by transmission through the wrapped components (Q_{tr}) and the total heat transfer by ventilation (Q_{ve}), given by, in *MJ*,

$$Q_{ht} = Q_{tr} + Q_{ve} \tag{4}$$

The total heat gains (Q_{gn}), over the given period, are given by the sum of the internal heat sources (Q_{int}), and the sum of the solar heat gains (Q_{sol}), in *MJ*,

$$Q_{gn} = Q_{int} + Q_{sol} \tag{5}$$

The same procedure was adopted in RCCTE. Two main parameters are quantified: the annual nominal energy needs for heating (N_{ic}) and the annual nominal energy needs for cooling (N_{vc}). The code also provides maximum allowable annual values for heating (N_i) and for cooling (N_v). The requirement regarding the maximum values should be verified taking into consideration the limit values of thermal quality, which are given in terms of maximum allowable values of the thermal transmittance (U) of the different elements. The limit values of N_i and N_v depend on the climatic characteristics of the location of the building and its geometrical shape. For the quantification of this and other parameters, the country is divided into three climatic zones for the heating season and three climatic zones for the cooling season, represented in Figure 3.

For the quantification of annual energy needs, the criteria for thermal comfort in RCCTE specify a set-point temperature for the heating season of 20ºC and a set-point temperature for the cooling season of 25ºC, independently of the climatic zone of the country.

In RCCTE, the length of the heating season depends on the location of the building in the country, according to Figure 3. It may vary from 4.3 months, for the least severe zone, to 6 months, in the most severe one. Similarly to Eq. 1, the quantification of the annual energy needs for heating (N_{ic}) is given, per net area of the floor, in *kWh/m²*, as

$$N_{ic} = (Q_{ht} - \eta . Q_{gn})/A_p \qquad \text{and} \qquad N_{ic} < N_i \tag{6}$$

where Q_{ht} and Q_{gn} have the same meaning as in Eq. 1 and η is the gain factor, defined later in Eq. 14.

(a) Heating season   (b) Cooling season
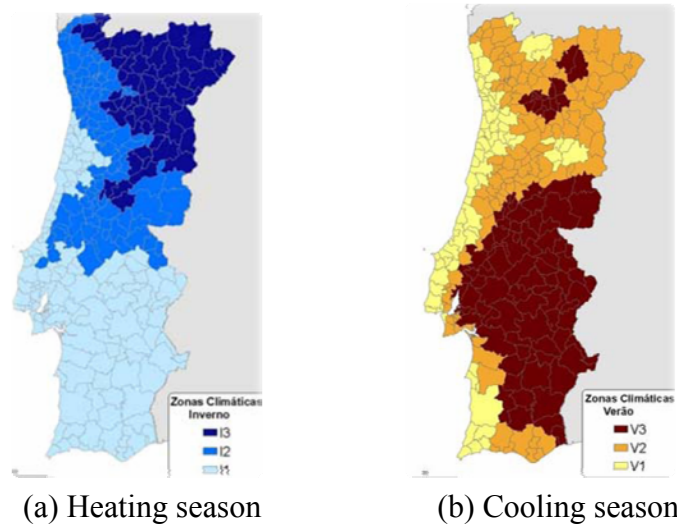
Figure 3. Portuguese Climatic Zones (according to RCCTE)

The heat transfer by transmission (Q_{tr}), in *kWh*, is given by the sum of: (i) the heat transfer from the conditioned space to the exterior (Q_{ext}); (ii) the heat transfer from the conditioned space to an adjacent unconditioned space (Q_{lna}); (iii) the heat transfer through the ground floor (Q_{pe}); and (iv) the heat transfer by thermal bridges (Q_{pt}), given by

$$Q_{tr} = Q_{ext} + Q_{lna} + Q_{pe} + Q_{pt} \tag{7}$$

For the calculation of heat transfer rate through the envelope of the building (Q_{ext}) (e.g. walls, roof, floor, windows), the following expression, in W, may be used,

$$Q_{ext} = U \cdot A \cdot (\theta_i - \theta_{atm}) \tag{8}$$

or, considering the degree-days (in °C·days), the heat transfer, in kWh, is given by

$$Q_{ext} = 0.024 \cdot U \cdot A \cdot GD \tag{9}$$

where, U is the thermal transmittance of the element of the building envelope (in $W/m^2 \cdot °C$), A is the corresponding area (in m^2), θ_i is the set-point temperature of the building for heating (in °C), and θ_{atm} is the outside air temperature (in °C). Similar expressions are used for the calculation of the remaining components in Eq. 7.

The heat transfer rate due to the ventilation (Q_{ra}), in W, is given by

$$Q_{ra} = \rho \cdot C_p \cdot R_{ph} \cdot V \cdot (\theta_i - \theta_{atm})/3600 \tag{10}$$

where ρ is the air density (in kg/m^3), C_p is the air specific heat capacity (in $J/kg \cdot °C$), R_{ph} is the air exchange rate in the conditioned space (in h^{-1}), V is the interior volume of the building (in m^3), and θ_i and θ_{atm} are the set-point temperature of the building for heating and the outside air temperature (in °C), respectively. Considering the volumetric heat capacity of air,

$$\rho \cdot C_p = 1200 \ J/(m^3 K)$$

and the degree-days, GD (in °C·days), the energy needed to compensate these losses during the heating season, Q_{ve} (= Q_{ra}), is given by, in kWh,

$$Q_{ve} = 0.024 \cdot [0.34 \cdot (R_{ph} \ V \cdot GD)] \tag{11}$$

Eq. 11 is only valid for natural ventilation, without any mechanical equipment.

For the heating season, the heat gains are obtained from internal sources and from solar heat, as indicated in Eq. 4. Internal heat gains (Q_{int}) include metabolic heat from occupants and dissipated heat from appliances, lighting devices and other equipments. According to RCCTE, the internal heat gains are given by (in kWh),

$$Q_{int} = q_i \cdot M \cdot A_p \cdot 0.72 \tag{12}$$

where M is the length of the heating season (in months); A_p is the net area of the floor (in m^2); and q_i is average internal heat gains per unit of the net area of the floor (in W/m^2). The internal heat gains may vary considerable; however, for certain types of buildings, RCCTE provides tabulated values. For instance, for residential buildings, it may be assumed that $q_i = 4 \ W/m^2$.

The solar heat gains in RCCTE are given by the gains through glazed elements, according to the following expression, in kWh:

$$Q_{sol} = G_{sul} \sum_j \left[X_j \sum_n A_{snj} \right] \cdot M \tag{13}$$

where G_{sul} is the monthly average of the solar energy irradiation in a vertical surface facing south, per unit of area, during the heating season (in kWh/m^2); X_j is a factor depending on the orientation of the surface; A_{snj} is the effective collecting area of surface n with orientation j (in m^2); and M is the length of the heating season (in months). The value of G_{sul} is given in RCCTE for each region in Portugal. The effective collecting area (A_{snj}) may be affected by factors taking into account the shading reduction due to external obstacles, the window characteristics and the properties of the glazing.

To take into account dynamic effects, the gain utilisation factor is given by,

$$\begin{cases} \eta = \dfrac{1-\gamma^a}{1-\gamma^{a+1}} & if \quad \gamma \neq 1 \\[4mm] \eta = \dfrac{a}{a+1} & if \quad \gamma = 1 \end{cases} \tag{14}$$

This factor is dependent on the thermal inertia of the building and on the heat balance ratio, given by $\gamma = Q_{gn}/Q_{ht}$. RCCTE provides values for the parameter a according to the inertia of the building. Thus, for buildings with weak thermal inertia, $a = 1.8$; for buildings with medium thermal inertia, $a = 2.6$; and for buildings with strong thermal inertia, $a = 4.2$.

For the cooling season, RCCTE follows a similar approach as for the heating season. In this case, the length of the cooling season is assumed to be four months, from June to September, for all zones of the country. RCCTE adopts the 2nd approach of the ISO standard 13790. Thus, from (3), the energy needed to keep the building at the set-point temperature, during these four months, in kWh/m^2, is given by,

$$N_{vc} = Q_{gn} (1 - \eta) / A_p \qquad and \qquad N_{vc} < N_c \tag{15}$$

The heat gains of the building, in this case, are given by the sum of internal gains (Q_{int}), solar gains (Q_{sol}), gains through ventilation (Q_{vent}) and gains by transmission (Q_{tr}) through the envelope of the building.

3.3   Advanced Simulation Analysis

The advanced simulation analysis is performed using the DesignBuilder software [18], which uses the EnergyPlus software [19] as the engine for the dynamic thermal simulation. EnergyPlus is an energy analysis and thermal load simulation program, with several important computational features such as, integrated simultaneous solution; sub-hourly, user-definable time steps; heat balance based solution; transient heat conduction; improved ground heat transfer modelling; combined heat and mass transfer; thermal comfort models; anisotropic sky model; advanced fenestration calculations; day lighting controls; loop based configurable HVAC systems and atmospheric pollution calculations, etc. These features, although not representing a fully dynamic simulation such as would be obtained using CFD technique, allow obtaining reasonably precise and realistic simulation results. EnergyPlus has been extensively tested and validated since 1999 [20] and is now rated as a reference simulation tool for sub-dynamic thermal simulation [21, 22]. EnergyPlus was also recently rated as the best energy simulation program for the evaluation of the energy flows through windows [23].

4.   REFERENCE EXAMPLE: LIGHT STEEL RESIDENTIAL BUILDING

4.1   General Description

The case study focuses on a single-family dwelling with 2 main floors, with an area of 165 m^2 each, and a smaller top floor with an area of 115 m^2, located in central Portugal and illustrated in Figure 4.

Southern and Eastern Views   Northern and Western Vviews
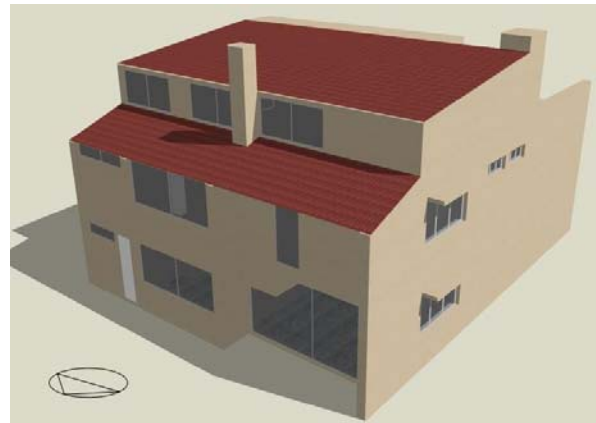
Figure 4. Elevation Views of the Building

The building frame consists of a steel structure formed by cold formed steel profiles, designed for a service life of 50 years according to the Structural Eurocodes [24]. The total internal net space is 361 m2. The ground floor is composed of a living-dining room, a small office, a kitchen, a small pantry, two bathrooms and stairs (see Figure 5). The first floor has 4 bedrooms, 4 bathrooms and stairs. The top floor has one master bedroom and one bathroom. The main facade of the house faces south.

1 - Kitchen
2 - Dining / Living room
3 - Office room
4 - WC
5 - Corridor / Stairs
6 - Bedroom

Ground floor   1st floor   2nd floor
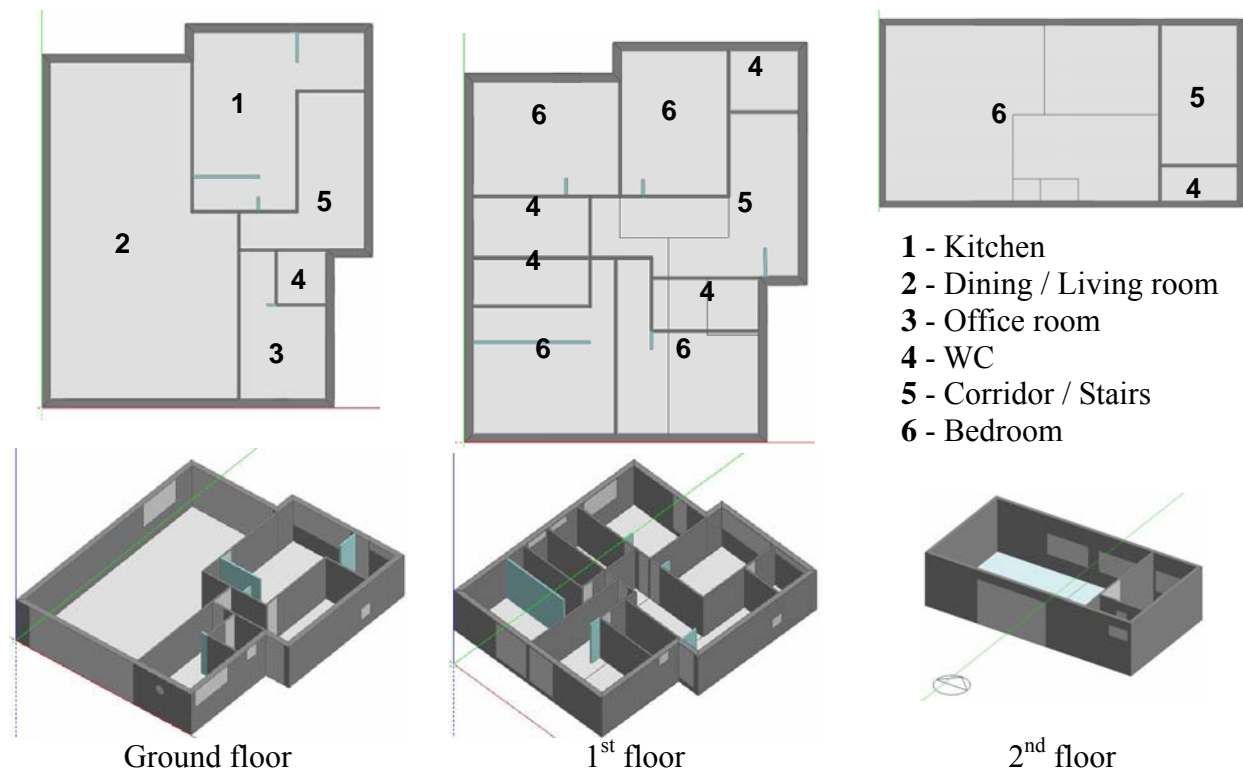
Figure 5. Layout of the Floors

The characteristics of the building components are described in the following paragraphs. The external walls are made of an outside layer of Oriented Strand Board (OSB) panels, 11 mm thick, and an inside layer of gypsum boards with a thickness of 15 mm. The gap between the two panels is filled with rock wool 140 mm thick. The internal walls are made of gypsum boards with a thickness of 15 mm and a layer of rock wool with a thickness of 70 mm. The slabs are made of composite panels with a top layer of OSB panels (15 mm), an intermediate layer of rock wool 70 mm thick, and a bottom layer of gypsum boards 13 mm thick. The ground floor is made of a light-concrete slab over a layer of gravel. The terrace floor is made of a top layer of OSB panels 18 mm thick, covered by 40 mm of cast concrete and a ceramic finish, an intermediate layer of rock wool 140 mm thick, and a bottom layer of gypsum boards 13 mm thick. The rock wool insulation panels completely clad the steel frame ensuring that the house achieves high thermal and acoustic behaviour according to regulatory requirements. The envelope of the house is covered by an Exterior Insulation and Finish System (EIFS). The quantities of the main materials estimated for the construction are indicated in Table 1.

Table 1. Bill of Materials

Material	Quantities	Unit
Concrete C25/30	70680	kg
Cold formed steel	19494	kg
Rock wool (50 kg/m^3)	6167	kg
Gypsum plasterboard (600 kg/m^3)	6340	kg
Oriented strand board (650 kg/m^3)	7016	kg
Steel reinforcement	1307	kg
Exterior Insulation and Finish System (EIFS):		
Polystyrene board (30 kg/m^3)	297	kg
Finish Coat (acrylic)	330	m^2

4.2   Climatic Data

Geographically, continental Portugal is located between latitudes 37° and 42° N and longitudes of 9.5° and 6.5° W. The maximum altitude is 2000 m. The country has a diverse climate from north to south and from east to the west coast. The north part of the country has an Atlantic climate with cold and wet winters. The central regions have a mixture of Atlantic and Mediterranean climates, with mild winters and hot and dry summers, particularly in the inner regions. The southern part of the country has a very dry climate with mild winters.

According to the Portuguese *Instituto de Meteorologia* [25], the annual average of the air temperature varies regularly over the year, reaching the highest values in August and the minimum values in January. In the summer, the values of the average maximal temperature vary between 16°C in the highest mountain (inner central-northern region) and from 32°C to 34°C in the inner central-southern part of the country. The values of the average minimal temperature, during winter, vary between 2°C in the inner high lands and 12°C in the south. The rain values vary from the northern part to the southern part of the country. On average, about 42% of the annual rainfall occurs during the winter (December-February), while the lowest values happen during summer (July and August) with a share of 6% of the annual rainfall.
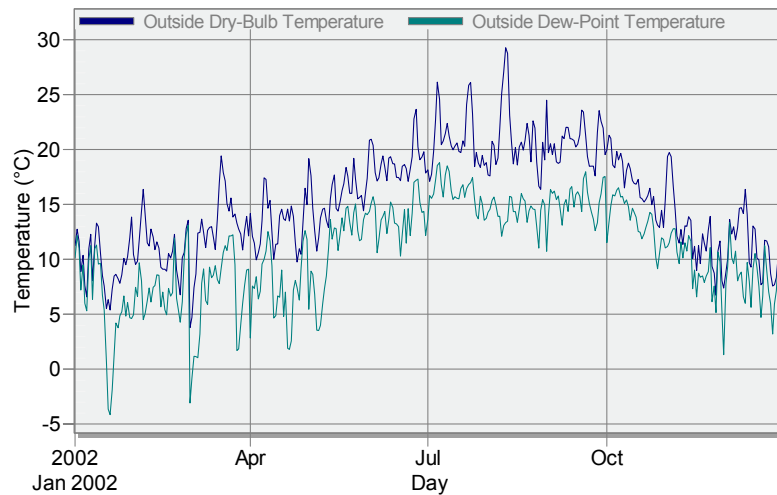
Figure 6. Annual Outside Air Temperature for Coimbra (Reference Year 2002)

Coimbra is located in central Portugal. According to Figure 2, Coimbra is located in heating zone I1 and cooling zone V2. The annual variation of the outside temperature, according to data from EnergyPlus, is shown in Figure 6. The length of the heating season is 6 months and the corresponding degree-days are 1834 (base 20 ºC).

4.3 Life Cycle Energy Analysis

4.3.1 *Thermal characteristics of the building components*

Table 2 indicates the geometric characteristics of the different elements of the building and the corresponding thermal properties.

Table 2. Thermal Transmittances of the Building Components

	Material	Thickness	U (W/m^2.°C)
External walls	Gypsum board	15 mm	0.218
	Rock wool	140 mm	
	OSB	11 mm	
	Exterior Insulation and Finish System (EIFS)	33 mm	
Internal walls	Gypsum board	15 mm	0.479
	Rock wool	70 mm	
	Gypsum board	15 mm	
Roof	Gypsum board	15 mm	0.262
	Rock wool	140 mm	
	OSB	11 mm	
	Ceramic tiles	15 mm	
Terrace	Gypsum board	15 mm	0.253
	Rock wool	140 mm	
	OSB	18 mm	
	Cast concrete	40 mm	
	Ceramic	10 mm	
Internal floor	Gypsum board	15 mm	0.252
	Rock wool	140 mm	
	OSB	18 mm	
Windows	Double pane clear glass	6/14/4 mm	2.733

4.3.2   Operational Energy

The operational energy, in this case study, is the energy needed for heating and cooling the building, according to the requirements of RCCTE, during the use stage of the building (see Figure 1). The quantification of the operational energy considers a time period for the analysis of 50 years. According to RCCTE, the whole building may be considered a unique thermal zone, which is kept continuously at a constant set-point temperature of 20°C and 25°C, respectively, for the heating season and for the cooling season. The annual energy need for heating, given from (1), is summarized in Table 3.

Table 3. Annual Energy Need for Heating ($Q_{H,nd}$)

Heat losses (kWh/year)	Exterior walls	2137.86
	Roof and Terrace	1578.85
	Windows/Doors	10562.96
	Ventilation	6989.74
	Total	**21269.41**
Heat gains (kWh/year)	Internal	5468.08
	Solar	12334.20
	Total	**17802.28**
η		0.70
Heating energy (kWh/year)		**8835.67**

Given a total net floor area of 316.44 m^2, the annual energy need for heating, per m^2, is obtained from Eq. 6, and its value should be less than the limit value of N_i:

$$N_{ic} = 27.92 \ kWh/m^2.year < N_i = 81.08 \ kWh/m^2.year$$

The energy need for heating, per year, is represented in Figure 7.
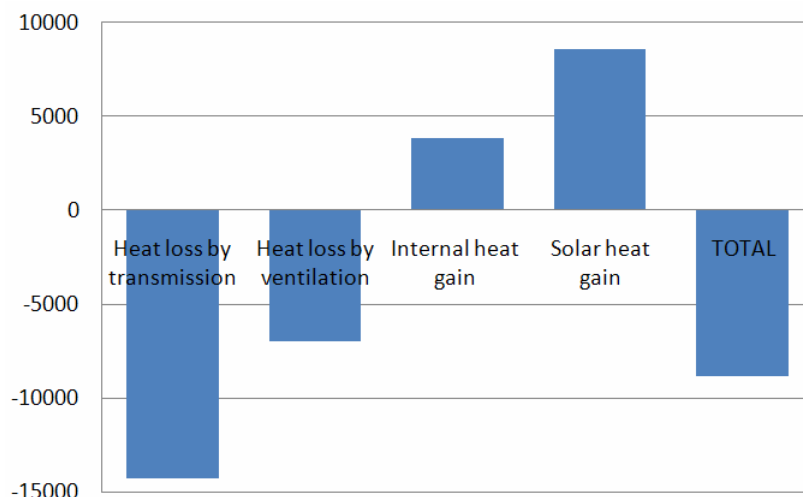
Figure 7. Annual Energy Need for Heating *(kWh/year)*

Regarding the cooling season, the annual energy need for cooling, given by Eq. 3, is summarized in Table 4.

Table 4. Annual Energy Need for Cooling ($Q_{C,nd}$)

Heat losses (kWh/year)	Exterior walls	853.28
	Roof and Terrace	630.16
	Windows/Doors	4215.97
	Ventilation	2789.80
	Total	**8489.21**
Heat gains (kWh/year)	Walls	876.64
	Windows	5840.38
	Internal	3706.15
	Total	**10423.17**
η		0.58
Cooling energy (kWh/year)		**4424.50**

The annual energy need for cooling per m^2, is given from (15), $N_{vc} = 13.98\ kWh/m^2$. Its value is less than the limit value of $N_v = 18.00\ kWh/m^2$. The net annual energy need for cooling is represented in Figure 8.
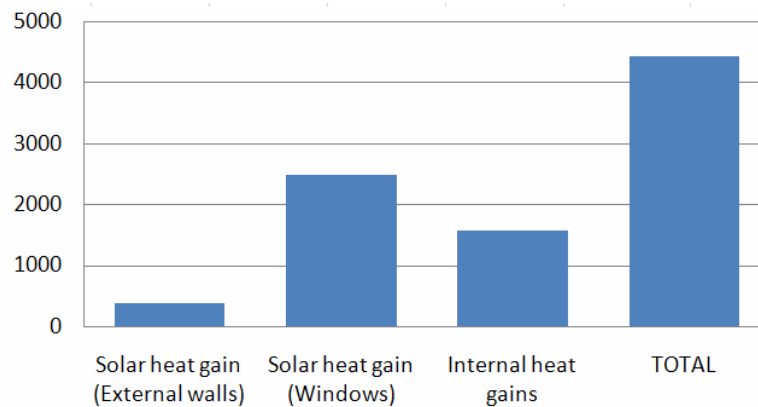
Figure 8. Annual Energy Need for Cooling (*kWh/year*)

4.3.3 Embodied energy

The quantification of the embodied energy of the building, considering the time period of 50 years, is performed by the Cumulative Energy Demand method and the computer program SimaPro v7.0 [26]. All the inventory data needed for the analysis was supplied by the Ecoinvent database [27]. Similar procedure has been used in other studies comparing the life cycle embodied energy and the operational energy of buildings [28, 29].

The life cycle embodied energy is represented as a tree in Figure 9. The first branch of the tree represents the construction stage, the second the end-of-life stage, and the third brace the operation stage. The thickness of the lines represents the relative importance of each stage to the overall result. Thus, the construction stage contributes with a share of 122%, the use stage with a share of less than 2%, and finally the last stage with a share of -23%. The minus at the end-of-life stage is the credit given to the recycling of the steel structure.
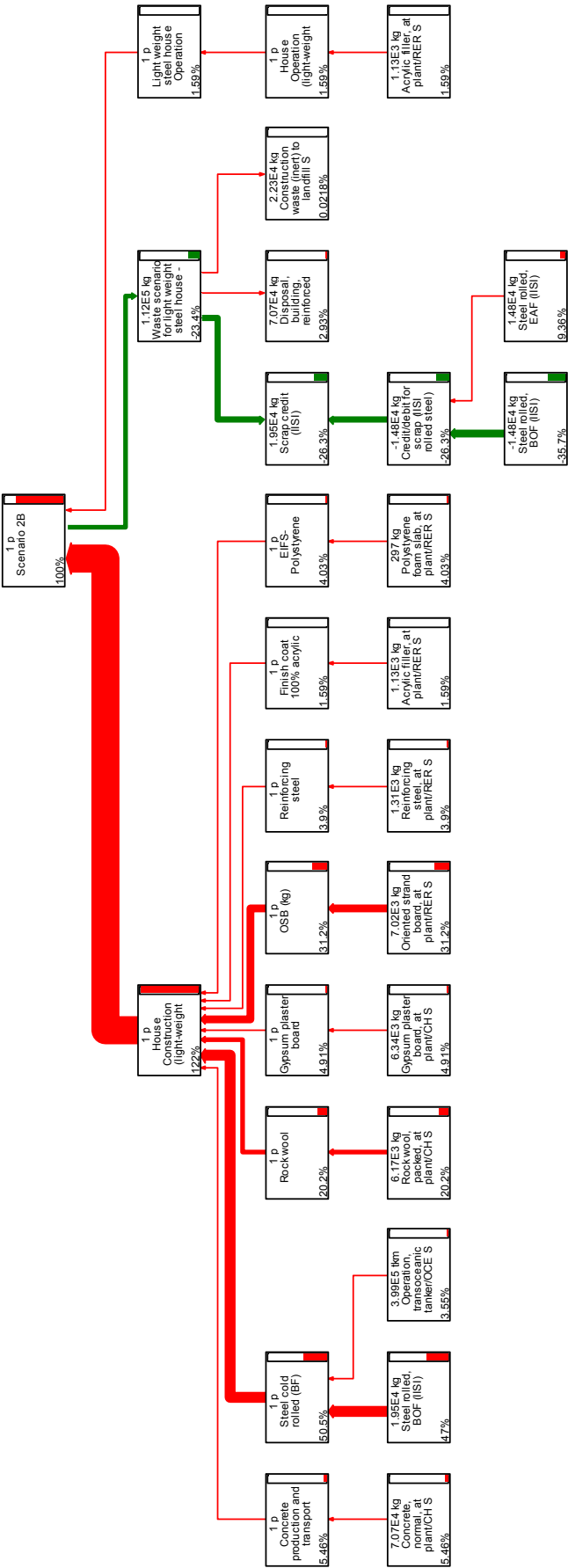
Figure 9. Tree Representation of the Life Cycle Embodied Energy of the Building

4.3.4   *Comparison between embodied energy and operational energy*

Comparing the energy needed during the operation stage of the building (operational energy) and the embodied energy of the building over the 50 years period, the results are presented in Figure 10.
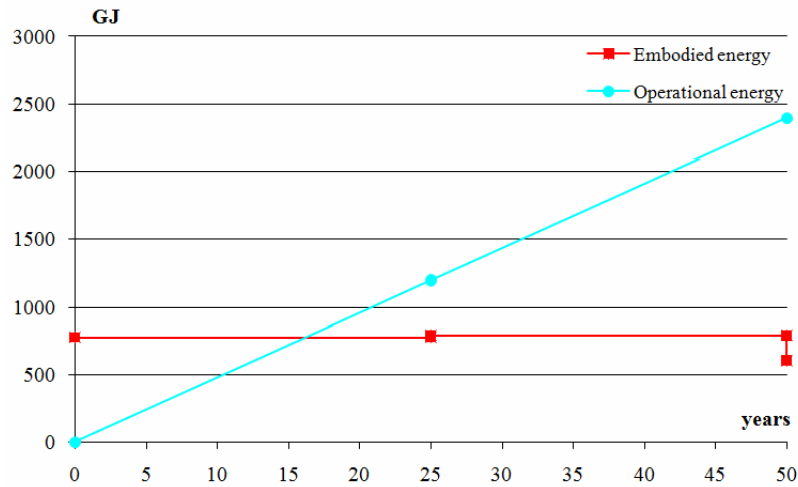
Figure 10. Life Cycle Operational and Embodied Energy

The total life cycle operational energy represents about 80% of the total life cycle energy. It should be noted that the operational energy, in this case study, includes only the energy needs for heating and cooling. The time period needed for the operational energy to overcome the embodied energy is 16 years.

5.   PARAMETRIC STUDY: INFLUENCE OF LEVEL OF INSULATION

5.1   Scenarios

In order to assess the influence of the level of insulation, several alternative solutions are analysed. The first scenario corresponds to the original solution, where only the external walls have an outside layer of polystyrene with 3 cm, and represents the reference scenario. Scenario 2 corresponds to a lower level of insulation. Scenario 3 corresponds to an increased level of insulation, with the thickness of the layer in the external walls increased to 10 cm, and a layer of polystyrene added to the roof and to the terrace slab, as shown in Figure 11.
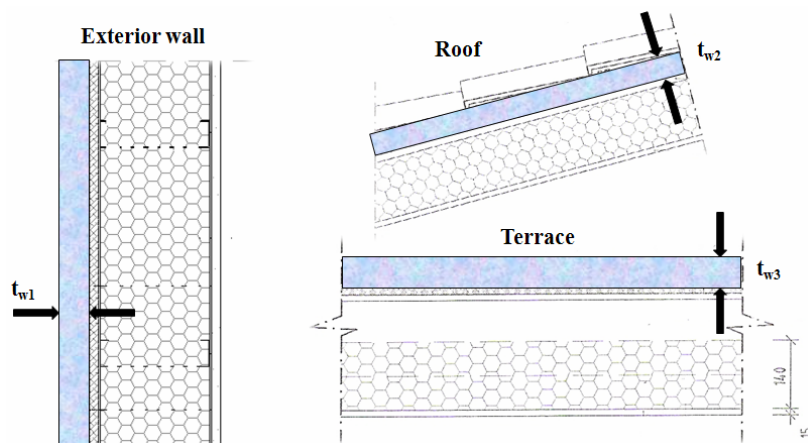
Figure 11. Schemes of the Alternative Scenario 3: t_{w1} = 100 mm, t_{w2} = t_{w3} = 60 mm

Table 5. Level of Insulation for the Various Scenarios and Relative Thermal Transmittances

		Scenario 1	Scenario 2	Scenario 3	Scenario 4	Scenario 5
Ext. Wall	Polystyrene (mm)	30	0	100	100	30
	Rock wool (mm)	140	70	140	140	140
	U (W/m^2.°C)	0.218	0.478	0.158	0.158	0.218
Roof	Polystyrene (mm)	-	-	60	60	-
	Rock wool (mm)	140	70	140	140	140
	U (W/m^2.°C)	0.262	0.482	0.188	0.188	0.262
Terrace	Polystyrene (mm)	-	-	60	60	-
	Rock wool (mm)	140	70	140	140	140
	U (W/m^2.°C)	0.253	0.456	0.184	0.184	0.253
Windows	U (W/m^2.°C)	2.733	2.733	2.733	1.900	2.733
	Glass solar factor	0.78	0.78	0.78	0.50	0.78
	Shading effect	yes	yes	yes	yes	no

Scenario 4 is identical to scenario 3 but with an improvement in the thermal behaviour of the windows. Finally, scenario 5 is similar to scenario 1 but without the shading effect from horizontal overhangs above the windows. The various scenarios are summarized in Table 5. These scenarios will change the amount of the material needed for each solution, which will be taken into consideration for the calculation of the embodied energy for each case. In the following paragraphs, the results obtained for each scenario are presented.

5.2   Simplified Approach

The total annual energy need, for the five scenarios defined above, is indicated in Table 6. The relative values are referred to scenario 1. It is seen that although the amount of external insulation was more than doubled in scenario 3, the total energy needs are only reduced by 6%. By comparison, scenario 4 decreases the total energy needs by about 19%, the only difference being the improvement of the thermal properties of the windows. Scenario 2 corresponds to a reduction of the global insulation of the building and results in an increase of 23% of the total energy needs. Finally, scenario 5, which ignores the shading effect of overhangs above the windows, increases by about 4% the energy needs.

Table 6. Annual Energy Needs, Per Year, for the Different Scenarios

	$Q_{H,n}$		$Q_{C,n}$		TOTAL/Year	
	(kWh/year)	Δ (%)	(kWh/year)	Δ (%)	(kWh/year)	Δ (%)
Scenario 1	8835.67	-	4424.49	-	13260.16	-
Scenario 2	11829.46	33.9%	4447.28	0.5%	16276.73	22.7%
Scenario 3	8076.21	-8.6%	4409.20	-0.3%	12485.41	-5.8%
Scenario 4	7428.75	-15.9%	3346.86	-24.4%	10775.61	-18.7%
Scenario 5	7824.54	-11.4%	5897.60	33.3%	13722.14	3.5%

Table 7 and Figure 12 summarize the balance between life cycle embodied energy and life cycle operational energy for the five scenarios. The influence of the degree of insulation results in variations of + 22.7% and −18.7% of the operational energy, with corresponding variations of the embodied energy of -15.4% and +18.3%. Globally, the solution with the best insulation minimizes the total energy (-11%). Finally, the operational energy becomes dominant for a service life in excess of 11.7 to 22.9 years and represents, over the service life of 50 years, 73.2% to 85.2% of the total life cycle energy, depending on the scenario.

Table 7. Total Life Cycle Operational and Embodied Energies

	Operational energy		Embodied energy		TOTAL	Operational/Total	Balanced year
	(GJ)	Δ	(GJ)	Δ	(GJ)		
Scenario 1	2393.53	-	601.09	-	2994.63	79.9%	16.3
Scenario 2	2938.04	22.7%	508.51	-15.4%	3446.55	85.2%	11.7
Scenario 3	2253.68	-5.8%	711.30	18.3%	2964.99	76.0%	19.8
Scenario 4	1945.06	-18.7%	711.30	18.3%	2656.36	73.2%	22.9
Scenario 5	2476.92	3.5%	601.09	0%	3078.02	80.5%	15.7
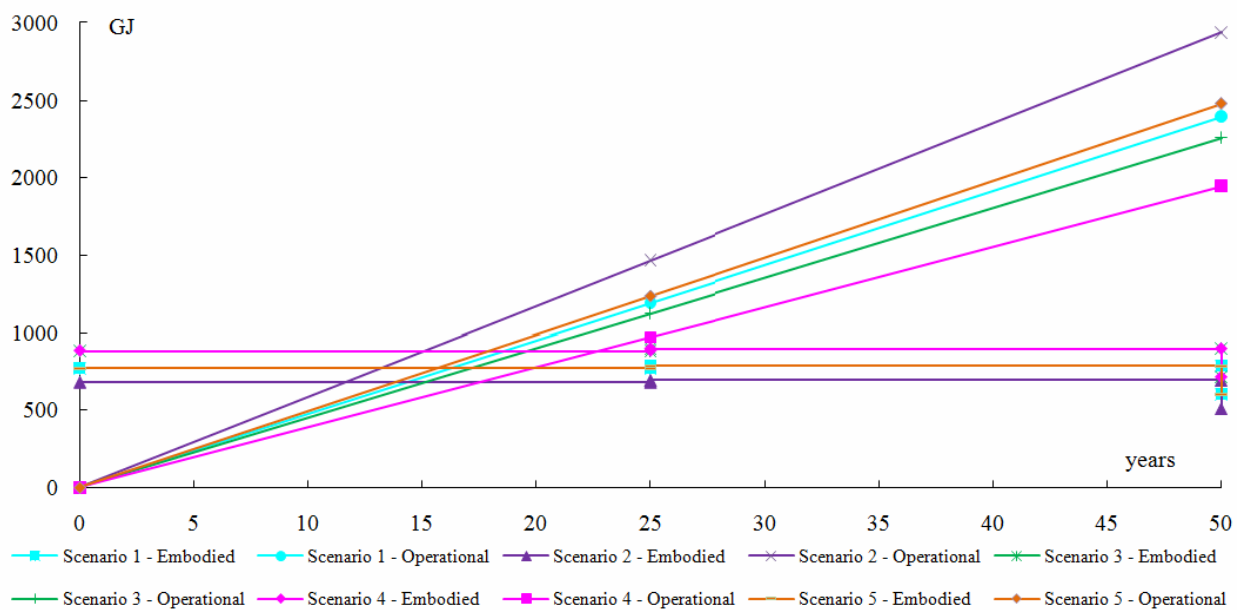
Figure 12. Balance of Life Cycle Embodied Energy and Life Cycle Operational Energy

The parametric study shows that for a standard service life of residential buildings of 50 years, reducing the operating energy is more important than reducing the embodied energy. Furthermore, the solution that minimizes the operating energy also minimizes total lifecycle energy.
It is also well-known that a simplified quasi steady-state approach can be used for a comparative analysis but does not simulate real daily conditions (namely thermal inertia of the building and ventilation are not properly considered in the analysis). Additionally, examination of Table 6 shows a consistent trend for the heating period, but reveals some discrepancies for the cooling period. In order to validate the results obtained with the simplified approach and to overcome some of the limitations indicated, a dynamic simulation analysis is performed for the 5 scenarios indicated in Table 5, and is described in the next paragraphs.

5.3   Dynamic Simulation Approach

5.3.1   Modelling and analysis options

The model of the building used for the simulation analysis was presented in Figure 4. The model was assembled using 15 thermal zones, corresponding to the main internal partitions of the building. The ground floor has four thermal zones; the first floor has eight thermal zones, and finally the top floor has two zones (see Figure 5). The stairways and corridors is a thermal zone common to the three floors.

The boundaries of the model were defined in order to consider the same conditions as for the simplified approach. Thus, the thermal transmittance of the elements of the building is indicated in Table 2. The internal heat gains were modelled assuming a value of 4 W/m^2 and the natural ventilation infiltration is considered to be 0.6 air changes per hour. Also, no thermal bridges were considered in the analysis and no losses were considered through the ground floor of the building.

The exterior climatic conditions were simulated using the DesignBuilder weather data for Coimbra (PRT_COIMBRA_IWEC.epw), as illustrated in Figure 6. The simulations were performed on a hourly basis. The results obtained for each scenario are presented in the following paragraphs.

5.3.2   Simulation under passive thermal conditions

Figure 13 presents the average temperature inside the building for the 5 scenarios, calculated without the specification of any heating or cooling equipment (passive thermal conditions), summarized in Table 8.

Table 8. Average Operational Temperatures

Average Operational Temperature (ºC)	Scenario 1	Scenario 2	Scenario 3	Scenario 4	Scenario 5
Annual	24.17	23.19	24.51	24.77	27.06
Summer (maximum)	29.57 (36.71)	28.75 (36.07)	29.84 (36.88)	30.09 (36.91)	33.03 (41.01)
Winter (minimum)	20.85 (15.00)	19.72 (13.64)	21.26 (15.47)	21.53 (15.67)	23.20 (16.23)
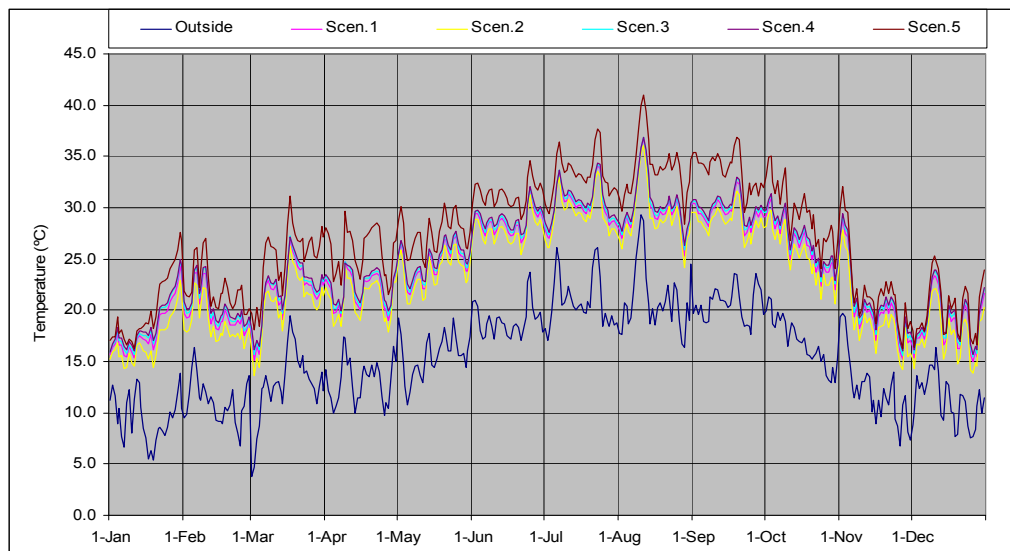
Figure 13. Temperatures Variation Inside and Outside the Building
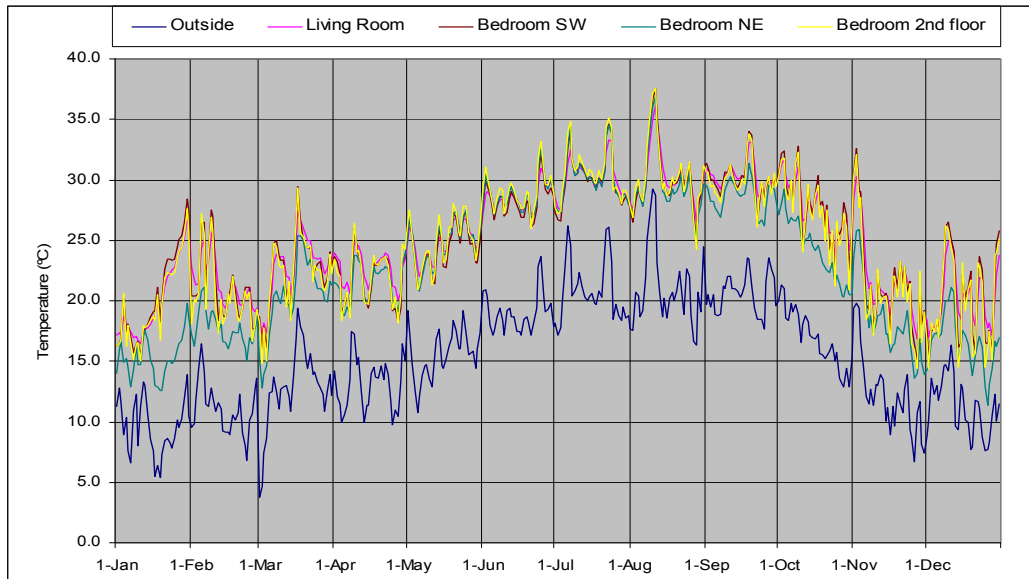
Figure 14. Temperatures Variation Inside and Outside the Building

The variation of the average daily temperatures of Figure 13 shows that for most of the winter period the average temperature is below the set-point temperature of 20ºC. The same conclusion is noted for the summer period, many days having average temperatures above the set-point temperature of 25ºC. Figure 14 illustrates the annual temperature variation for scenario 1 in several compartments. Significant differences are clearly noted (differences of 1.52ºC and 3.58ºC for the average summer and winter temperatures, respectively (Table 9).

Table 9. Average Operational Temperatures

Average Operational Temperature (ºC)	Living Room (ground floor)	Bedroom SE/SW (1st floor)	Bedroom NW/NE (1st floor)	Bedroom (2nd floor)
Annual	25.05	24.33 / 24.89	24.05 / 23.01	24.80
Summer (maximum)	29.80 (36.10)	29.17 / 29.70 (36.99) (37.53)	30.69 / 29.34 (38.98) / (36.83)	29.96 (37.61)
Winter (minimum)	22.33 (16.44)	21.65 / 22.26 (14.74) (15.02)	19.59 / 18.75 (11.88) / (11.04)	21.81 (14.43)

5.3.3 *Heating season*

In order to compare with the RCCTE simulations, Figure 15 presents the results of a simulation for the heating period (1st October to 31st March) assuming that the heating equipment is turned on and off automatically in order to ensure an inside temperature not lower than 20ºC. Tables 10 and 11 allow the comparison of the results of RCCTE with the results from the dynamic simulation.
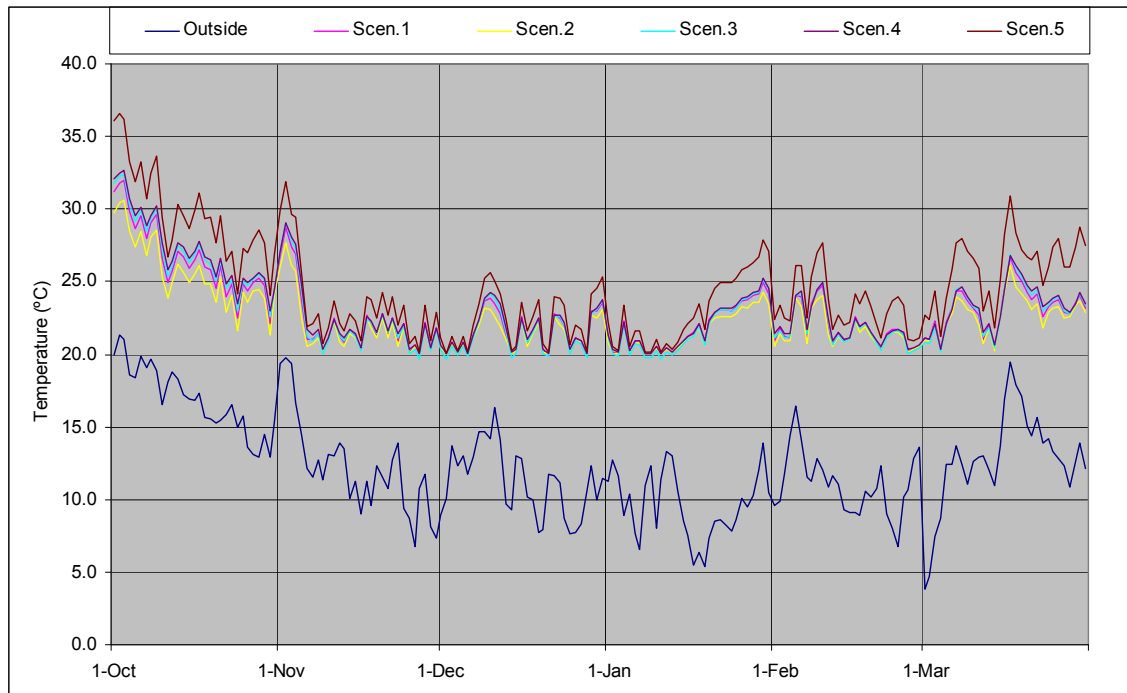
Figure 15. Temperatures Variation Inside and Outside the Building (Winter Season)

Table 10. Annual Heating Energy According to RCCTE

kWh/year	RCCTE				
	Scenario 1	Scenario 2	Scenario 3	Scenario 4	Scenario 5
Exterior walls	2137.86	4687.70	1549.36	1549.36	2137.86
Roof and Terrace	1578.85	2881.73	1138.69	1138.69	1578.85
Windows/Doors	10562.96	10562.96	10562.96	7343.63	10562.96
Ventilation	6989.74	6989.74	6989.74	6989.74	6989.74
Total heat loss	**21269.41**	**25122.13**	**20240.76**	**17021.43**	**21269.41**
Internal	5468.08	5468.08	5468.08	5468.08	5468.08
Solar	12334.20	12334.20	12334.20	7906.54	15105.65
Total heat gains	**17802.28**	**17802.28**	**17802.28**	**13374.62**	**20573.73**
η	0.70	0.75	0.68	0.72	0.65
Heating energy	**8835.67**	**11829.46**	**8076.21**	**7428.75**	**7824.53**

Table 11. Annual Heating Energy According to EnergyPlus

kWh/year	DsB (E+)				
	Scenario 1	Scenario 2	Scenario 3	Scenario 4	Scenario 5
Exterior walls	2087.46	4245.81	1528.05	1548.50	2438.26
Roof and Terrace	1685.96	2828.09	1231.63	1240.57	2059.67
Windows/Doors	8865.79	8457.01	8889.36	5625.42	10474.45
Ventilation	8079.469	7870.963	8065.089	8201.21	9323.051
Total heat loss	**20718.68**	**23401.88**	**19714.14**	**16615.70**	**24295.44**
Internal	5715.439	5715.439	5715.439	5715.439	5715.439
Solar	11175.87	11175.87	11175.87	8518.763	16097.5
Total heat gains	**16891.31**	**16891.31**	**16891.31**	**14234.2**	**21812.94**
Heating energy	**3827.37**	**6510.57**	**2822.83**	**2381.50**	**2482.50**
Other	389.22	425.08	384.23	359.07	549.33
Total HE	**4216.60**	**6935.65**	**3207.06**	**2740.57**	**3031.83**

Reasonable agreement (same trend) is noted for the heat losses for the exterior walls, roof and terrace (except scenario 5 and heat gains (internal and solar), while windows/doors losses and ventilation losses do not correlate so well). Global results present the same trend but the numerical results are over-estimated by RCCTE by a two to one ratio.

5.3.4 *Cooling season*

Similarly, in order to compare with the RCCTE simulations, Figure 16 presents the results of a simulation for the cooling period (1st June to 30st September) assuming that the cooling equipment is turned on and off automatically in order to ensure an inside temperature not higher than 25ºC.
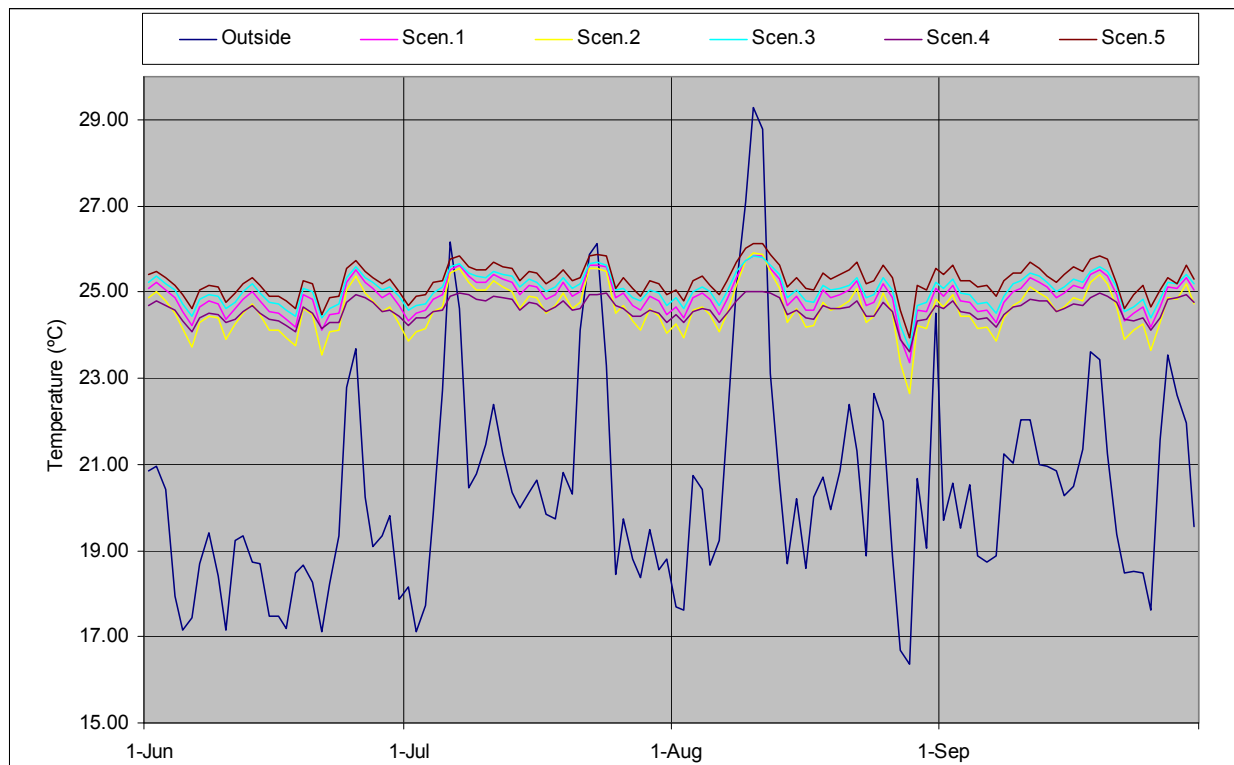
Figure 16. Temperatures Variation Inside and Outside the Building (Summer Season)

Table 12. Annual Cooling Energy According to RCCTE

kWh/year	RCCTE				
	Scenario 1	Scenario 2	Scenario 3	Scenario 4	Scenario 5
Exterior walls	853.28	1870.99	618.39	618.39	853.28
Roof and Terrace	630.16	1150.18	454.48	454.48	630.16
Windows/Doors	4215.97	4215.97	4215.97	2931.05	4215.97
Ventilation	2789.80	2789.80	2789.80	2789.80	2789.80
Total heat loss	**8489.21**	**10026.94**	**8078.65**	**6793.72**	**8489.21**
Walls	876.64	1714.09	633.37	633.37	876.64
Windows	5840.38	5840.38	5840.38	3743.83	7714.59
Internal	3706.15	3706.15	3706.15	3706.15	3706.15
Total heat gains	**10423.17**	**11260.62**	**10179.90**	**8083.35**	**12297.38**
η	0.58	0.61	0.57	0.59	0.52
Cooling energy	**4424.50**	**4447.28**	**4409.20**	**3346.86**	**5897.60**

The results of RCCTE and the results from the dynamic simulation are indicated in Tables 12 and 13, respectively. In this case, the comparison is not so straightforward since RCCTE considers both heat losses and heat gains through the walls. Global results indicate higher cooling energy needs (about 100% higher) according to the dynamic simulation. In addition, scenario 4 (the best insulated solution) does not present the best performance.

Table 13. Annual Cooling Energy According to EnergyPlus

kWh/year	DsB (E+)				
	Scenario 1	Scenario 2	Scenario 3	Scenario 4	Scenario 5
Exterior walls	170.54	238.15	149.35	91.32	109.78
Roof and	38.79	166.72	5.39	42.03	-10.26
Windows/Doors	2198.98	2035.43	2284.29	509.19	1917.92
Ventilation	2066.55	1920.75	2138.18	1917.19	2115.62
Total heat loss	**4474.86**	**4361.05**	**4577.21**	**2559.73**	**4133.06**
Windows	7510.87	7510.87	7510.87	5643.84	12063.65
Internal	3895.44	3895.44	3895.44	3895.44	3895.44
Total heat	**11406.31**	**11406.31**	**11406.31**	**9539.28**	**15959.09**
Cooling energy	**6931.45**	**7045.26**	**6829.10**	**6979.55**	**11826.03**
Other	-414.37	-148.28	-488.09	-388.70	-671.17
Total CE	**6517.078**	**6896.977**	**6341.01**	**6590.853**	**11154.86**

6. CONCLUSIONS

In this work the life cycle energy analysis (LCEA) for a light steel residential building constructed in Portugal was performed in order to assess the influence of thermal insulation on the balance between embodied and operational energy. Besides the real thermal insulation adopted on this building, other scenarios were simulated including lower and higher insulation of opaque and transparent building components. Two different approaches were used to compute the building operational energy: RCCTE (Portuguese code of practice, that corresponds to the transposition of the simplified quasi-steady-state analysis procedures specified in ISO 13790) and advanced dynamic simulation analysis using the EnergyPlus software.

The RCCTE Portuguese methodology is based on the EN ISO 13790 standard and uses a quasi-steady approach, where thermal inertia effects are neglected. Results are provided for annual averages. EnergyPlus adopts a sub-dynamic approach, in a sub-hourly basis. Both these models were applied to a single-family dwelling building with a quite complex layout. Thermal loads for the heating and the cooling season were computed using the two approaches. The heat gains component showed a good agreement between the two, but the prediction values for the heat losses with RCCTE are significantly higher than those obtained with EnergyPlus, specially the component due to losses through the walls. These differences are certainly due to the complexity of the adopted geometry. Interaction effects between building regions are certainly not fully taken into account when using integral approaches such as those adopted by these models. Future research will include the study of simpler buildings and compartments, to better establish the differences between predictions and their relation to the characteristics of the geometry. CFD (computational fluid dynamics) simulations are also planned, to provide reference values.

The LCEA indicate that operational energy (only heating and cooling) represents a very significant share (80%) of the building total life cycle energy, 16 years being the time needed for the operational energy to overcome the embodied energy. As expected, when improving the insulation, there is a longer delay for the operational energy to overcome the embodied energy (up to 23 years) and the operational energy share decreases to about 73% of total life cycle energy.

The different thermal insulating scenarios studied show the importance of improving the thermal performance of "weaker components", i.e., insulation improvement should be preferably directed towards the less performing components, such as windows, potentially leading to operational energy savings of about 20% for the same occupant's thermal comfort. Over the entire LCEA this reduction represents a decrease of about 11.5% of total energy (embodied and operational).

These findings show, even with only one case study, that for climatic conditions typical of southern Europe it is possible to improve significantly the thermal efficiency of residential buildings optimizing the insulation materials distribution along the building envelop, paying particularly attention to transparent building components (e.g. windows and doors). This optimization can be accomplished without increasing significantly the embodied energy of the building that takes a bigger share (with the potential to achieve a share of 50%) in the total life-cycle building energy.

ACKNOWLEDGEMENTS

REFERENCES

[1]   COM(2004)60, "Communication from the Commission to the Council, the European Parliament", The European Economic and Social Committee and the Committee of the Regions: Towards a Thematic Strategy on the Urban Environment, Brussels, 2004.

[2]   Debnath, A., Singh, S.V. and Singh, Y.P., "Comparative Assessment of Energy Requirements for Different Types of Residential Buildings in India, Energy and Buildings", 1995, Vol. 23, pp. 141–146.

[3]   Adalberth, K., "Energy Use During the Life Cycle of Buildings: A Method, Building and Environment, 1997, Vol. 32, No. 4, pp. 317–320.

[4]   Adalberth, K., "Energy Use During the Life Cycle of Single-unit Dwellings: Examples", Building and Environment, 1997, Vol. 32, No. 4, pp. 321–329.

[5]   Cole, R.J., "Energy and Greenhouse Gas Emissions Associated with the Construction of Alternative Structural Systems", Building and Environment, 1999, Vol. 34, No. 3, pp.335–348.

[6]   Eaton, K.J. and Amato, A., "A Comparative Life Cycle Assessment of Steel and Concrete Framed Office Buildings", J. Construct. Steel Res., 1998, Vol. 46, No. 1-3, pp. 286-287.

[7]   Yohanis, Y.G. and Norton, B., "Life-cycle Operational and Embodied Energy for a Generic Single-storey Office Building in the UK", Energy, 2002, Vol. 27, pp. 77–92.

[8]   Hacker, J.N., De Saulles, T.P., Minson, A.J., Holmes, M.J., "Embodied and Operational Carbon Dioxide Emissions from Housing: A Case Study on the Effects of Thermal Mass and Climate Change, Energy and Buildings, 2008, Vol. 40, pp. 375–384.

[9]   Utama, A. and Gheewala, S.H., "Life Cycle Energy of Single Landed Houses in Indonesia, Energy and Buildings, 2008, Vol. 40, pp. 1911–1916.

[10]   Huberman, N. and Pearlmutter, D., "A Life-cycle Energy Analysis of Building Materials in the Negev Desert, Energy and Buildings", 2008, Vol. 40, pp. 837–848.

[11] IPCC. 2007, "Climate change 2007: The physical science basis. Contribution of Working Group I to the Fourth Assessment Report of the IPCC", Cambridge University Press. Cambridge, United Kingdom and New York, NY, USA, 2007.

[12] http://www.greenhouse.gov.au/yourhome/technical/fs31.htm. Last accessed in 07/09/18.

[13] IISI. 2002, "World Steel Life Cycle Inventory. Methodology report 1999/2000", Committee on Environmental Affairs, Brussels, 2002.

[14] European Directive 2002/91/CE. 2002, "Directive 2002/91/CE of the European Parliament and of the Council of 16 December 2002 on the Energy Performance of Buildings".

[15] EN ISO 13790, 2008, "Energy Performance of Buildings – Calculation of Energy Use for Space Heating and Cooling", International Organization for Standardization, Geneva, Switzerland.

[16] Decreto-Lei nº80/2006, "Regulamento das Características Térmicas dos Edifícios (RCCTE)" (in Portuguese).

[17] Decreto-Lei nº79/2006, "Regulamento dos Sistemas Energéticos e de Climatização dos Edifícios (RSECE) (in Portuguese).

[18] Website Software DesignBuilder: http://www.designbuilder.co.uk/.

[19] Website Software Energy Plus: http://www.energyplus.gov.

[20] Crawley, D., et al., "EnergyPlus: Creating a New-generation Building Energy Simulation Program, Energy and Buildings, 2001, Vol. 33, pp. 319–331.

[21] Crawley, D., Hand, J., Kummert, M. and Griffith, B., "Contrasting the Capabilities of Building Energy Performance Simulation Programs", Building and Environment, 2008, Vol. 43, pp. 661-673.

[22] Tronchin, L. and Fabbri, K., "Energy Performance Building Evaluation in Mediterranean Countries: Comparison between Software Simulations and Operating Rating Simulation", Energy and Buildings, 2008, Vol. 40, pp. 1176–1187.

[23] Loutzenhiser, P., Manz, H., Moosberger, S. and Maxwell, G., "An Empirical Validation of Window Solar Gain Models and the Associated Interactions", International Journal of Thermal Sciences, 2009, Vol. 48, pp. 85–95.

[24] EN 1993-1-3, Eurocode 3, "Design of Steel Structures – Part 1.3: General Rules – Supplementary Rules for Cold-formed Members and Sheeting", European Committee for Standardization, Brussels, 2006.

[25] Instituto de Meteorologia, Portugal, http://www.meteo.pt/pt/oclima/normais/

[26] SimaPro 7, "Software and Database Manual", PRé Consultants, Amersfoort, The Netherlands, 2008.

[27] Frischknecht, R., Jungbluth, N., Althaus, H.-J., Doka, G., Dones, R., Hellweg, S., Hischier, R., Nemecek, T., Rebitzer, G. and Spielmann, M., "Code of Practice", Ecoinvent Report No. 2, Swiss Center for Life Cycle Inventories, Dübendorf, 2004.

[28] Bribián, I., Usón, A., Scarpellini, S. 2009, "Life Cycle Assessment in Buildings: State-of-the-art and Simplified LCA Methodology as a Complement for Building Certification", Building and Environment, Vol. 44, pp. 2510–2520.

[29] Thormark, C. 2002, "A Low Energy Building in a Life Cycle – Its Embodied Energy, Energy need for Operation and Recycling Potential", Building and Environment, Vol. 37, pp. 429–435.

A MIXED CO-ROTATIONAL 3D BEAM ELEMENT FORMULATION FOR ARBITRARILY LARGE ROTATIONS

Z.X. Li [1,*] and L. Vu-Quoc [2]

[1]*Associate professor, Department of Civil Engineering, Zhejiang University, Hangzhou 310058, China*
[2]*Professor, Department of Mechanical and Aerospace Engineering, University of Florida, Gainesville FL 32611, USA*
*(Corresponding author: E-mail: lizx19993@zju.edu.cn)

ABSTRACT: A new 3-node co-rotational element formulation for 3D beam is presented. The present formulation differs from existing co-rotational formulations as follows: 1) vectorial rotational variables are used to replace traditional angular rotational variables, thus all nodal variables are additive in incremental solution procedure; 2) the Hellinger-Reissner functional is introduced to eliminate membrane and shear locking phenomena, with assumed membrane strains and shear strains employed to replace part of conforming strains; 3) all nodal variables are commutative in differentiating Hellinger-Reissner functional with respect to these variables, resulting in a symmetric element tangent stiffness matrix; 4) the total values of nodal variables are used to update the element tangent stiffness matrix, making it advantageous in solving dynamic problems. Several examples of elastic beams with large displacements and large rotations are analysed to verify the computational efficiency and reliability of the present beam element formulation.

Keywords: Co-rotational method; vectorial rotational variable; 3D beam element; locking-free; Hellinger-Reissner functional; assumed strain.

1.   INTRODUCTION

Developing an efficient beam element formulation for large displacement analysis of framed structures has been an issue for many researchers. There already exist various formulations to address this issue. These formulations had been separated into three categories: Total Lagrangian formulation, updated Lagrangian formulation, and co-rotational formulation. The main ideas of the co-rotational approach (Rankin and Brogan [1], Crisfield [2], Yang et. al.[3]) can be summarized as follows: 1) define an element reference frame that translates and rotates with the element's overall rigid-body motion, but does not deform with the element; 2) calculate the nodal variables with respect to this reference frame; the element's overall rigid-body motion is thus excluded in computing the local internal force vector and the element tangent stiffness matrix, resulting an element-independent formulation; 3) the geometric nonlinearity induced by the large element rigid-body motion is incorporated in the transformation matrix relating the local and global internal force vector and tangent stiffness matrix.

Many co-rotational beam and shell element formulations have been proposed. The pioneer work can be traced to Wempner [4], Belytschko et al.[5,6], Argyris et al.[7] and Oran [8,9]. Surveys of the existing co-rotational finite element formulations were presented respectively by Stolarski et al.[10], Crisfield and Moita [11], Yang et al.[3], and Felippa and Haugen [12]. Recently, Urthaler and Reddy [13] developed three locking-free co-rotational planar beam element formulations by adopting respectively the Euler–Bernoulli, Timoshenko, and simplified Reddy theories in modelling of the element kinematic behaviour. Galvaneito and Crisfield [14] proposed an energy-conserving procedure for the implicit non-linear dynamic analysis of planar beam structures by using a form of co-rotational technique. Iura et al.[15] investigated the accuracy of the co-rotational formulation for 3-D Timoshenko beam undergoing finite strains and finite rotations. Pajot and Maute [16] studied the sensitivies of a co-rotational element formulation to element shape and material parameters, and the effect of the unsymmetric terms in a consistent tangent

stiffness on element computational accuracy; see also Simo and Vu-Quoc [17] on the effect of tangent stiffness symmetrization on rate of convergence.

Due to the non-commutativity of spatial finite rotations, nodal rotations are always updated by using a complicated transformation matrix [18,19] in an incremental solution procedure; such non-commutativity renders both the local and global element tangent stiffness matrices asymmetric in most existing co-rotational formulations. Thus more computer storage is needed to store all necessary coefficients, while the computational efficiency decreases. Simo and Vu-Quoc [17] proved that in a conservative system, although their tangent stiffness matrix is asymmetric away from equilibrium, this matrix becomes symmetric at equilibrium. Crisfield and his co-workers [2,20] also encountered this phenomenon, and artificially symmetrized the element tangent stiffness matrix by excluding the non-symmetric term. This treatment can greatly improve the computational efficiency. Crisfield [2] and Simo [21] also predicted that a symmetric tangent stiffness matrix could be achieved if a certain set of additive rotational variables were employed in a co-rotational element formulation. In the present co-rotational beam element formulation, such additive rotational variables are used, and the versatile vectorial rotational variables had also been employed in a co-rotational 2D beam element formulation [22], a co-rotational 3D beam conforming element formulation [23], a co-rotational curved triangular shell element formulation [24], and a co-rotational curved quadrilateral shell element formulation [25], respectively.

2.   DESCRIPTION OF THE CO-ROTATIONAL FRAMEWORK

In the present beam element formulation, several basic assumptions were adopted: 1) the element is straight at the initial configuration; 2) the shape of the cross-section does not distort with element deforming; 3) the element cross-section is bisymmetric; 4) restrained warping effect is ignored.
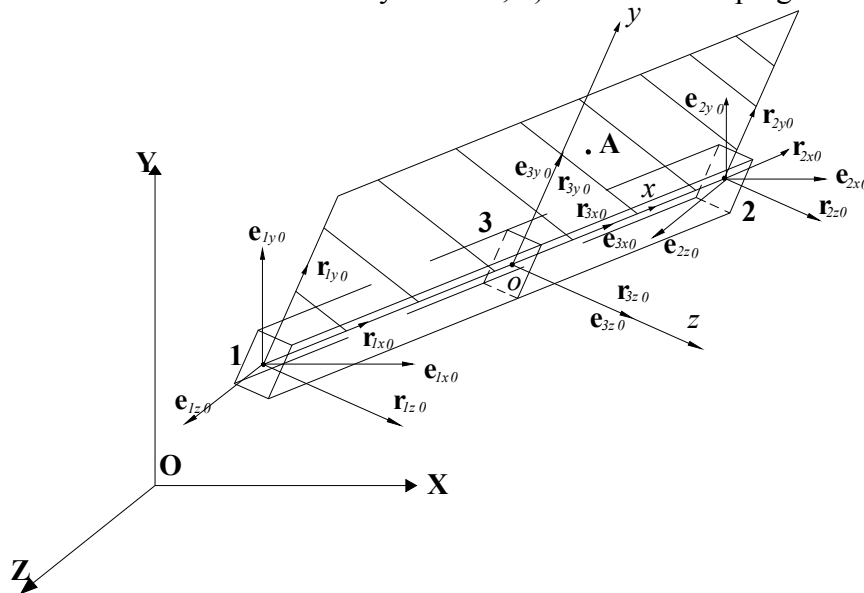
Figure 1. Definition of Local and Global Coordinate Systems

The local and global coordinate systems of the beam element are illustrated in Figure 1, where three local coordinate axes run along two principal axes of the cross-section at the internal node and their cross-product, and translate and rotate with the element rigid-body translations and rotations, but do not deform with the element.

An auxiliary point in one of the symmetry plane of the beam element is employed in defining the local coordinate axes (see Point A in Figure 1). $\mathbf{e}_{x0}$, $\mathbf{e}_{y0}$, $\mathbf{e}_{z0}$ are the normalized orientation vectors of x-axis, y-axis and z-axis, respectively. They are calculated from

$$\left.\begin{aligned}
\mathbf{e}_{x0} &= \frac{\mathbf{v}_{120}}{|\mathbf{v}_{120}|} \\
\mathbf{e}_{z0} &= \frac{\mathbf{v}_{120} \times \mathbf{v}_{3A0}}{|\mathbf{v}_{120} \times \mathbf{v}_{3A0}|} \\
\mathbf{e}_{y0} &= \mathbf{e}_{z0} \times \mathbf{e}_{x0}
\end{aligned}\right\} \tag{1}$$

where,

$$\left.\begin{aligned}
\mathbf{v}_{120} &= \mathbf{X}_{20} - \mathbf{X}_{10} \\
\mathbf{v}_{3A0} &= \mathbf{X}_{A0} - \mathbf{X}_{30}
\end{aligned}\right\} \tag{2}$$

and $\mathbf{X}_{i0}$ ($i=1,2,3,A$) is the global coordinates of Node i.

The orientation vectors $\mathbf{e}_{ix}$, $\mathbf{e}_{iy}$, $\mathbf{e}_{iz}$ of Node i at the deformed configuration are calculated from the rotational variables directly in an incremental solution procedure. In particular, at Node 3 (the internal node of the beam element), $\mathbf{e}_{3x}$, $\mathbf{e}_{3y}$, $\mathbf{e}_{3z}$ are coincident with the orientation of local coordinate axes,

$$\left.\begin{aligned}
\mathbf{e}_{3x} &= \mathbf{e}_x \\
\mathbf{e}_{3y} &= \mathbf{e}_y \\
\mathbf{e}_{3z} &= \mathbf{e}_z
\end{aligned}\right\} \tag{3}$$

and at the initial configuration,

$$\left.\begin{aligned}
\mathbf{e}_{3x0} &= \mathbf{e}_{x0} \\
\mathbf{e}_{3y0} &= \mathbf{e}_{y0} \\
\mathbf{e}_{3z0} &= \mathbf{e}_{z0}
\end{aligned}\right\} \tag{4}$$

however, the initial orientation vectors of two end nodes are defined as

$$\left.\begin{aligned}
\mathbf{e}_{ix0}^{\mathrm{T}} &= \langle 1 \quad 0 \quad 0 \rangle \\
\mathbf{e}_{iy0}^{\mathrm{T}} &= \langle 0 \quad 1 \quad 0 \rangle \\
\mathbf{e}_{iz0}^{\mathrm{T}} &= \langle 0 \quad 0 \quad 1 \rangle
\end{aligned}\right\} \quad i = 1,2 \tag{5}$$

In the global coordinate system, each element employs 18 degrees of freedom,

$$\mathbf{u}_G^{\mathrm{T}} = \left\langle U_1 \quad V_1 \quad W_1 \quad e_{1y,n_1} \quad e_{1y,m_1} \quad e_{1z,n_1} \quad \cdots \quad U_3 \quad V_3 \quad W_3 \quad e_{3y,n_3} \quad e_{3y,m_3} \quad e_{3z,n_3} \right\rangle \tag{6}$$

where, $\mathbf{d}_i^{\mathrm{T}} = \langle U_i \quad V_i \quad W_i \rangle$ is the vector of global translational displacements at Node i;

$\mathbf{n}_{gi}^{\mathrm{T}} = \left\langle e_{iy,n_i} \quad e_{iy,m_i} \quad e_{iz,n_i} \right\rangle$ ($n_i, m_i = X, Y$ or Z) is the vector of vectorial rotational variables at Node i, it consists of three independent components of $\mathbf{e}_{iy}$ and $\mathbf{e}_{iz}$ in the global coordinate system.

In the local coordinate system, each element has 12 degrees of freedom, and each end node 6 freedoms,

$$\mathbf{u}_{\mathrm{L}}^{\mathrm{T}} = \left\langle u_1 \quad v_1 \quad w_1 \quad r_{1y,n_1} \quad r_{1y,m_1} \quad r_{1z,n_1} \quad u_2 \quad v_2 \quad w_2 \quad r_{2y,n_2} \quad r_{2y,m_2} \quad r_{2z,n_2} \right\rangle \tag{7}$$

where, $\mathbf{t}_i^{\mathrm{T}} = \left\langle u_i \quad v_i \quad w_i \right\rangle$ are the vector of local translational displacements at Node i, and $\boldsymbol{\theta}_i^{\mathrm{T}} = \left\langle r_{iy,n_i} \quad r_{iy,m_i} \quad r_{iz,n_i} \right\rangle$ ($n_i, m_i = x, y$ or z) are the vector of vectorial rotational variables at Node i, it consists of three independent components of $\mathbf{e}_{iy}$ and $\mathbf{e}_{iz}$ in the local coordinate system.

The rotational variables e_{iy,n_i}, e_{iy,m_i} and e_{iz,n_i} are defined according to the following procedure.

Firstly, assumed that $\left| e_{iy,l_i} \right| \geq \left| e_{iy,m_i} \right|$, $\left| e_{iy,l_i} \right| \geq \left| e_{iy,n_i} \right|$ ($l_i, m_i, n_i \in \{X, Y, Z\}$, and $l_i \neq m_i \neq n_i$) at the preceding incremental loading step:

Case 1: if $\left| e_{iz,l_i} \right| \geq \left| e_{iz,m_i} \right|$ and $\left| e_{iz,l_i} \right| \geq \left| e_{iz,n_i} \right|$, then three rotational variables at the next incremental loading step are $\mathbf{n}_{gi}^{\mathrm{T}} = \left\langle e_{iy,n_i} \quad e_{iy,m_i} \quad e_{iz,n_i} \right\rangle$, where $\{n_i, m_i, l_i\}$ is a circular permutation of $\{X, Y, Z\}$, other components of $\mathbf{e}_{iy}$ and $\mathbf{e}_{iz}$ can be calculated from them,

$$e_{iy,l_i} = s_1 \sqrt{1 - e_{iy,n_i}^2 - e_{iy,m_i}^2} \tag{8a}$$

$$e_{iz,m_i} = \frac{- e_{iy,m_i} e_{iy,n_i} e_{iz,n_i} + s_2 e_{iy,l_i} \sqrt{1 - e_{iy,n_i}^2 - e_{iz,n_i}^2}}{1 - e_{iy,n_i}^2} \tag{8b}$$

$$e_{iz,l_i} = s_3 \sqrt{1 - e_{iz,m_i}^2 - e_{iz,n_i}^2} \tag{8c}$$

where, s_1, s_3 take a numeric value of 1 or -1, they have the same signs as e_{iy,l_i} or e_{iz,l_i} at last incremental step; s_2 is also such a constant, and it is conditioned on $\mathbf{e}_{iy}^{\mathrm{T}} \mathbf{e}_{iz} = 0$.

Case 2: if $\left| e_{iz,m_i} \right| \geq \left| e_{iz,l_i} \right|$ and $\left| e_{iz,m_i} \right| \geq \left| e_{iz,n_i} \right|$ at the end of the current incremental step, then three rotational variables are defined as $\mathbf{n}_{gi}^{\mathrm{T}} = \left\langle e_{iy,n_i} \quad e_{iy,m_i} \quad e_{iz,n_i} \right\rangle$, and other components of $\mathbf{e}_{iy}$ and $\mathbf{e}_{iz}$ can be calculated as,

$$e_{iy,l_i} = s_1 \sqrt{1 - e_{iy,n_i}^2 - e_{iy,m_i}^2} \tag{9a}$$

$$e_{iz,l_i} = \frac{- s_1 \sqrt{1 - e_{iy,m_i}^2 - e_{iy,n_i}^2} e_{iy,n_i} e_{iz,n_i} + s_2 e_{iy,m_i} \sqrt{1 - e_{iy,n_i}^2 - e_{iz,n_i}^2}}{1 - e_{iy,n_i}^2} \tag{9b}$$

$$e_{iz,m_i} = s_3 \sqrt{1 - e_{iz,n_i}^2 - e_{iz,l_i}^2} \tag{9c}$$

where, s_1, s_2, s_3 are the same kind of constants as those in Case 1.

Vector $\mathbf{e}_{ix}$ is the cross-product of Vectors $\mathbf{e}_{iy}$ and $\mathbf{e}_{iz}$,

$$\mathbf{e}_{ix} = \mathbf{e}_{iy} \times \mathbf{e}_{iz} \tag{10}$$
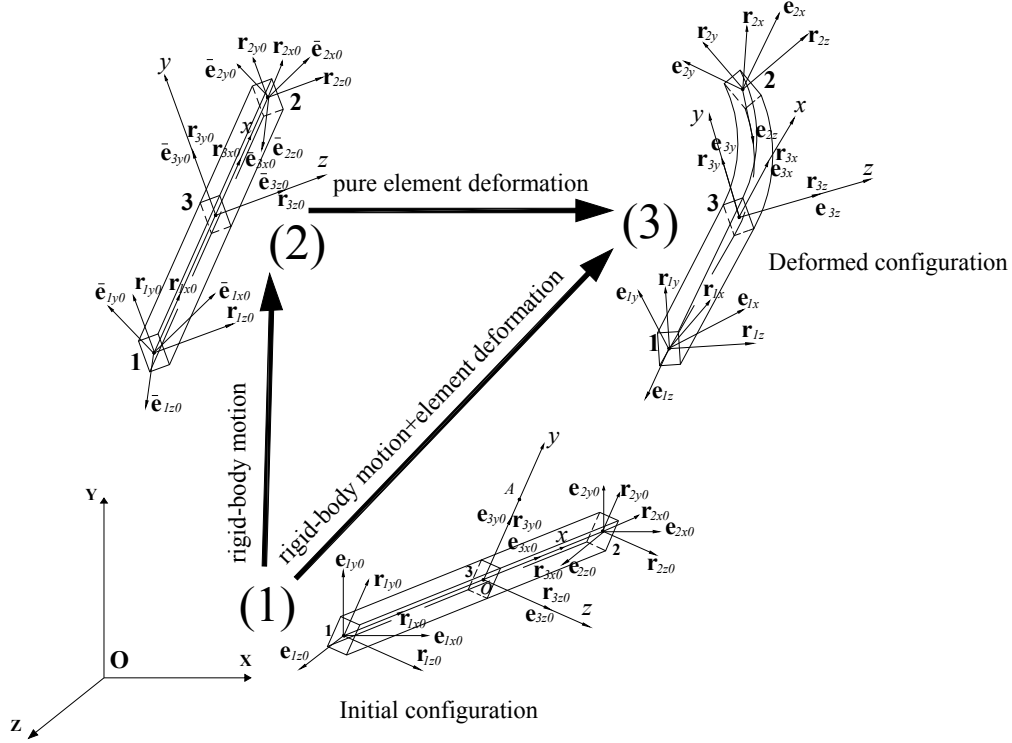
Figure 2. Illumination of the Co-rotational Framework

The definition of local vectorial rotational variables $\boldsymbol{\theta}_i^{\mathrm{T}} = \left\langle r_{iy,n_i} \quad r_{iy,m_i} \quad r_{iz,n_i} \right\rangle$ follows the same route as that of $\mathbf{n}_{gi}^{\mathrm{T}} = \left\langle e_{iy,n_i} \quad e_{iy,m_i} \quad e_{iz,n_i} \right\rangle$.

Rigid-body motion contributes nothing to element strains, so it can be excluded in advance to achieve an element-independent formulation. This procedure is illuminated in Figure 2, where (1) represents an element at its initial configuration, (3) is at the deformed configuration, from (1) to (3) the element experiences both rigid-body motion and pure deformation. (2) is an intermediate configuration between (1) and (3), from (1) to (2), the element has only rigid-body motion, while, from (2) to (3), the element experiences pure deformation. In the present co-rotational formulation, the rigid-body motion from (1) to (2) is excluded, and only pure element deformation from (2) to (3) is considered in calculating the local internal force vector and element tangent stiffness matrix. Thus, the relationships between local and global nodal variables are given as,

$$\left. \begin{aligned} \mathbf{t}_i &= \mathbf{R}(\mathbf{d}_i - \mathbf{d}_3) + (\mathbf{R} - \mathbf{R}_0)\mathbf{v}_{i0} \\ \mathbf{r}_{iy} &= \mathbf{R}\mathbf{R}_i^{\mathrm{T}}\mathbf{e}_{y0} \\ \mathbf{r}_{iz} &= \mathbf{R}\mathbf{R}_i^{\mathrm{T}}\mathbf{e}_{z0} \end{aligned} \right\} \qquad i=1,2 \tag{11}$$

where,

$$\mathbf{R}_0 = \begin{bmatrix} \mathbf{e}_{x0}^{\mathrm{T}} \\ \mathbf{e}_{y0}^{\mathrm{T}} \\ \mathbf{e}_{z0}^{\mathrm{T}} \end{bmatrix} \tag{12a}$$

$$\mathbf{R} = \begin{bmatrix} \mathbf{e}_x^{\mathrm{T}} \\ \mathbf{e}_y^{\mathrm{T}} \\ \mathbf{e}_z^{\mathrm{T}} \end{bmatrix} \tag{12b}$$

$$\mathbf{R}_i = \begin{bmatrix} \mathbf{e}_{ix}^{\mathrm{T}} \\ \mathbf{e}_{iy}^{\mathrm{T}} \\ \mathbf{e}_{iz}^{\mathrm{T}} \end{bmatrix} \qquad i=1,2 \tag{12c}$$

Especially, at the internal node,

$$\left. \begin{aligned} \mathbf{t}_3^{\mathrm{T}} &= \langle 0 \quad 0 \quad 0 \rangle \\ \mathbf{r}_{3y}^{\mathrm{T}} &= \langle 0 \quad 1 \quad 0 \rangle \\ \mathbf{r}_{3z}^{\mathrm{T}} &= \langle 0 \quad 0 \quad 1 \rangle \end{aligned} \right\} \tag{13}$$

$\mathbf{v}_{i0}$ is the relative vector oriented from Node 3 to Node i,

$$\mathbf{v}_{i0} = \mathbf{X}_{i0} - \mathbf{X}_{30} \qquad i=1,2 \tag{14}$$

3.   KINEMATICS OF A 3-NODE ISO-PARAMETRIC BEAM ELEMENT

In the present 3-node iso-parametric beam element, the local coordinates, displacements and vectorial rotations at any point of the element central line are interpolated by using Lagrangian shape functions. The initial and current local coordinates at any point of the element can be depicted as

$${}^0\mathbf{g} = \sum_{i=1}^{3} N_i(\xi)\mathbf{x}_{i0} + y_l \sum_{i=1}^{3} N_i(\xi)\mathbf{r}_{iy0} + z_l \sum_{i=1}^{3} N_i(\xi)\mathbf{r}_{iz0} \tag{15a}$$

$$\mathbf{g} = \sum_{i=1}^{3} N_i(\xi)(\mathbf{t}_i + \mathbf{x}_{i0}) + y_l \sum_{i=1}^{3} N_i(\xi)\mathbf{r}_{iy} + z_l \sum_{i=1}^{3} N_i(\xi)\mathbf{r}_{iz} \tag{15b}$$

where, $N_i(\xi)$ is the Lagrangian shape function at Node i; ξ is the natural coordinate of a point in the element along its central line; $\mathbf{x}_{i0}$ is the initial local coordinates of Node i; y_l and z_l are the relative coordinates of any point in the element to its central line.

Considering the possibility of large displacements and large rotations, Green strain measure is introduced to describe the strain-displacement relationship. For a beam element, the strain-displacement relationship is given as

$$\boldsymbol{\varepsilon} = \left\{ \begin{array}{c} \varepsilon_{xx} \\ \gamma_{xy} \\ \gamma_{xz} \end{array} \right\} = \left\{ \begin{array}{c} \dfrac{1}{2}\left(\mathbf{g}_x^{\mathrm{T}}\mathbf{g}_x - {}^0\mathbf{g}_x^{\mathrm{T}\,0}\mathbf{g}_x\right) \\ \mathbf{g}_x^{\mathrm{T}}\mathbf{g}_y - {}^0\mathbf{g}_x^{\mathrm{T}\,0}\mathbf{g}_y \\ \mathbf{g}_x^{\mathrm{T}}\mathbf{g}_z - {}^0\mathbf{g}_x^{\mathrm{T}\,0}\mathbf{g}_z \end{array} \right\} \tag{16}$$

where,

$$\left. \begin{array}{l} {}^0\mathbf{g}_x = \dfrac{\partial {}^0\mathbf{g}}{\partial x} \\[3mm] \mathbf{g}_x = \dfrac{\partial \mathbf{g}}{\partial x} \end{array} \right\} \tag{17}$$

For convenience, Eq. 16 can be rewritten as

$$\boldsymbol{\varepsilon} = \boldsymbol{\varepsilon}^{(0)} + y_l \boldsymbol{\varepsilon}^{(1)} + z_l \boldsymbol{\varepsilon}^{(2)} + y_l z_l \boldsymbol{\varepsilon}^{(3)} + y_l^2 \boldsymbol{\varepsilon}^{(4)} + z_l^2 \boldsymbol{\varepsilon}^{(5)} \tag{18}$$

where,

$$\boldsymbol{\varepsilon}^{(0)} = \left\{ \begin{array}{c} \varepsilon_{xx}^{(0)} \\ \gamma_{xy}^{(0)} \\ \gamma_{xz}^{(0)} \end{array} \right\} = \left\{ \begin{array}{c} \dfrac{1}{2}\dfrac{\partial \mathbf{u}_0^{\mathrm{T}}}{\partial x}\dfrac{\partial \mathbf{u}_0}{\partial x} + \dfrac{\partial \mathbf{u}_0^{\mathrm{T}}}{\partial x}\dfrac{\partial \mathbf{x}}{\partial x} \\ \dfrac{\partial \mathbf{u}_0^{\mathrm{T}}}{\partial x}\mathbf{r}_y + \dfrac{\partial \mathbf{x}^{\mathrm{T}}}{\partial x}\left(\mathbf{r}_y - \mathbf{r}_{y0}\right) \\ \dfrac{\partial \mathbf{u}_0^{\mathrm{T}}}{\partial x}\mathbf{r}_z + \dfrac{\partial \mathbf{x}^{\mathrm{T}}}{\partial x}\left(\mathbf{r}_z - \mathbf{r}_{z0}\right) \end{array} \right\} \tag{19a}$$

$$\boldsymbol{\varepsilon}^{(1)} = \left\{ \begin{array}{c} \varepsilon_{xx}^{(1)} \\ \gamma_{xy}^{(1)} \\ \gamma_{xz}^{(1)} \end{array} \right\} = \left\{ \begin{array}{c} \dfrac{\partial \mathbf{u}_0^{\mathrm{T}}}{\partial x}\dfrac{\partial \mathbf{r}_y}{\partial x} + \dfrac{\partial \mathbf{x}^{\mathrm{T}}}{\partial x}\dfrac{\partial\left(\mathbf{r}_y - \mathbf{r}_{y0}\right)}{\partial x} \\ \dfrac{\partial \mathbf{r}_y^{\mathrm{T}}}{\partial x}\mathbf{r}_y - \dfrac{\partial \mathbf{r}_{y0}^{\mathrm{T}}}{\partial x}\mathbf{r}_{y0} \\ \dfrac{\partial \mathbf{r}_y^{\mathrm{T}}}{\partial x}\mathbf{r}_z - \dfrac{\partial \mathbf{r}_{y0}^{\mathrm{T}}}{\partial x}\mathbf{r}_{z0} \end{array} \right\} \tag{19b}$$

$$\boldsymbol{\varepsilon}^{(2)} = \left\{ \begin{array}{c} \varepsilon_{xx}^{(2)} \\ \gamma_{xy}^{(2)} \\ \gamma_{xz}^{(2)} \end{array} \right\} = \left\{ \begin{array}{c} \dfrac{\partial \mathbf{u}_0^{\mathrm{T}}}{\partial x}\dfrac{\partial \mathbf{r}_z}{\partial x} + \dfrac{\partial \mathbf{x}^{\mathrm{T}}}{\partial x}\dfrac{\partial\left(\mathbf{r}_z - \mathbf{r}_{z0}\right)}{\partial x} \\ \dfrac{\partial \mathbf{r}_z^{\mathrm{T}}}{\partial x}\mathbf{r}_y - \dfrac{\partial \mathbf{r}_{z0}^{\mathrm{T}}}{\partial x}\mathbf{r}_{y0} \\ \dfrac{\partial \mathbf{r}_z^{\mathrm{T}}}{\partial x}\mathbf{r}_z - \dfrac{\partial \mathbf{r}_{z0}^{\mathrm{T}}}{\partial x}\mathbf{r}_{z0} \end{array} \right\} \tag{19c}$$

$$\boldsymbol{\varepsilon}^{(3)} = \left\{ \begin{array}{c} \varepsilon_{xx}^{(3)} \\ \gamma_{xy}^{(3)} \\ \gamma_{xz}^{(3)} \end{array} \right\} = \left\{ \begin{array}{c} \dfrac{\partial \mathbf{r}_y^{\mathrm{T}}}{\partial x}\dfrac{\partial \mathbf{r}_z}{\partial x} - \dfrac{\partial \mathbf{r}_{y0}^{\mathrm{T}}}{\partial x}\dfrac{\partial \mathbf{r}_{z0}}{\partial x} \\ 0 \\ 0 \end{array} \right\} \tag{19d}$$

$$\mathbf{\varepsilon}^{(4)} = \begin{Bmatrix} \varepsilon_{xx}^{(4)} \\ \gamma_{xy}^{(4)} \\ \gamma_{xz}^{(4)} \end{Bmatrix} = \begin{Bmatrix} \frac{1}{2}\left(\frac{\partial \mathbf{r}_y}{\partial x} \frac{\partial \mathbf{r}_y}{\partial x} - \frac{\partial \mathbf{r}_{y0}}{\partial x} \frac{\partial \mathbf{r}_{y0}}{\partial x} \right) \\ 0 \\ 0 \end{Bmatrix} \tag{19e}$$

$$\mathbf{\varepsilon}^{(5)} = \begin{Bmatrix} \varepsilon_{xx}^{(5)} \\ \gamma_{xy}^{(5)} \\ \gamma_{xz}^{(5)} \end{Bmatrix} = \begin{Bmatrix} \frac{1}{2}\left(\frac{\partial \mathbf{r}_z^{\mathrm{T}}}{\partial x} \frac{\partial \mathbf{r}_z}{\partial x} - \frac{\partial \mathbf{r}_{z0}^{\mathrm{T}}}{\partial x} \frac{\partial \mathbf{r}_{z0}}{\partial x} \right) \\ 0 \\ 0 \end{Bmatrix} \tag{19f}$$

in Eqs. 19a~f,

$$\mathbf{u}_0 = \sum_{i=1}^{3} N_i(\xi)\mathbf{t}_i \tag{20a}$$

$$\mathbf{r}_y = \sum_{i=1}^{3} N_i(\xi)\mathbf{r}_{iy} \tag{20b}$$

$$\mathbf{r}_{y0} = \sum_{i=1}^{3} N_i(\xi)\mathbf{r}_{iy0} \tag{20c}$$

$$\mathbf{r}_z = \sum_{i=1}^{3} N_i(\xi)\mathbf{r}_{iz} \tag{20d}$$

$$\mathbf{r}_{z0} = \sum_{i=1}^{3} N_i(\xi)\mathbf{r}_{iz0} \tag{20e}$$

$$\frac{\partial}{\partial x} = \frac{\dfrac{\partial}{\partial \xi}}{\displaystyle\sum_{i=1}^{3}\left(N_{i,\xi} x_{i0}\right)} \tag{20f}$$

in Eq. 20f, $N_{i,\xi}$ represents the first derivative of $N_i(\xi)$ with respect to ξ.

4.   ELEMENT FORMULATION

To eliminate membrane and shear locking phenomena in beam elements, Hellinger–Reissner mixed functional are employed, where part of conforming strains are replaced by assumed strains,

$$\pi_{\mathrm{HR}} = \mathrm{E}\int_V \varepsilon_{xx}^a \varepsilon_{xx}\, \mathrm{d}V - \frac{1}{2}\mathrm{E}\int_V \left(\varepsilon_{xx}^a\right)^2 \mathrm{d}V + \mathrm{k}_0\mathrm{G}\int_V \gamma_{xy}^a \gamma_{xy}\, \mathrm{d}V$$

$$- \frac{1}{2}\mathrm{k}_0\mathrm{G}\int_V \left(\gamma_{xy}^a\right)^2 \mathrm{d}V + \mathrm{k}_0\mathrm{G}\int_V \gamma_{xz}^a \gamma_{xz}\, \mathrm{d}V - \frac{1}{2}\mathrm{k}_0\mathrm{G}\int_V \left(\gamma_{xz}^a\right)^2 \mathrm{d}V - \mathrm{W}_e \tag{21}$$

where, E and G are the Young's modulus and the shear modulus, respectively; k_0 is the shear factor of the cross-section; V is the element volume; W_e is the work done by external forces; and

$$\varepsilon_{xx}^a = \mathbf{P}\boldsymbol{\alpha} + y_l \varepsilon_{xx}^{(1)} + z_l \varepsilon_{xx}^{(2)} + y_l z_l \varepsilon_{xx}^{(3)} + y_l^2 \varepsilon_{xx}^{(4)} + z_l^2 \varepsilon_{xx}^{(5)} \tag{22a}$$

$$\gamma_{xy}^a = \mathbf{P}\boldsymbol{\beta} + y_l \gamma_{xy}^{(1)} + z_l \gamma_{xy}^{(2)} \tag{22b}$$

$$\gamma_{xz}^a = \mathbf{P}\boldsymbol{\chi} + y_l \gamma_{xz}^{(1)} + z_l \gamma_{xz}^{(2)} \tag{22c}$$

$$\mathbf{P} = \langle 1, \xi \rangle \tag{22d}$$

$$\boldsymbol{\alpha} = \langle \alpha_1, \alpha_2 \rangle^{\mathrm{T}} \tag{22e}$$

$$\boldsymbol{\beta} = \langle \beta_1, \beta_2 \rangle^{\mathrm{T}} \tag{22f}$$

$$\boldsymbol{\chi} = \langle \chi_1, \chi_2 \rangle^{\mathrm{T}} \tag{22g}$$

$\alpha_1, \alpha_2, \beta_1, \beta_2, \chi_1, \chi_2$ are independent variables employed in defining assumed strains.

By enforcing the variation of the Hellinger–Reissner functional π_{HR} with respect to $\mathbf{u}_{\mathbf{L}}, \boldsymbol{\alpha}, \boldsymbol{\beta}$ and $\boldsymbol{\chi}$,

$$\begin{aligned}
\delta \pi_{\mathrm{HR}} = {}& \mathrm{E} \int_V \varepsilon_{xx}^a \delta\varepsilon_{xx} \, \mathrm{dV} + \mathrm{E} \int_V \varepsilon_{xx} \delta\varepsilon_{xx}^a \, \mathrm{dV} - \mathrm{E} \int_V \varepsilon_{xx}^a \delta\varepsilon_{xx}^a \, \mathrm{dV} \\
&+ k_0 \mathrm{G} \int_V \gamma_{xy}^a \delta\gamma_{xy} \, \mathrm{dV} + k_0 \mathrm{G} \int_V \gamma_{xy} \delta\gamma_{xy}^a \, \mathrm{dV} \\
&- k_0 \mathrm{G} \int_V \gamma_{xy}^a \delta\gamma_{xy}^a \, \mathrm{dV} + k_0 \mathrm{G} \int_V \gamma_{xz}^a \delta\gamma_{xz} d \, \mathrm{V} \\
&+ k_0 \mathrm{G} \int_V \gamma_{xz} \delta\gamma_{xz}^a \, \mathrm{dV} - k_0 \mathrm{G} \int_V \gamma_{xz}^a \delta\gamma_{xz}^a \, \mathrm{dV} - \delta \mathrm{W}_e
\end{aligned} \tag{23}$$

where,

$$\delta\varepsilon_{xx}^a = \mathbf{P}\delta\boldsymbol{\alpha} + \left(y_l \mathbf{B}_{xx}^{(1)} + z_l \mathbf{B}_{xx}^{(2)} + y_l z_l \mathbf{B}_{xx}^{(3)} + y_l^2 \mathbf{B}_{xx}^{(4)} + z_l^2 \mathbf{B}_{xx}^{(5)} \right)\delta\mathbf{u}_{\mathrm{L}} \tag{24a}$$

$$\delta\varepsilon_{xx} = \left(\mathbf{B}_{xx}^{(0)} + y_l \mathbf{B}_{xx}^{(1)} + z_l \mathbf{B}_{xx}^{(2)} + y_l z_l \mathbf{B}_{xx}^{(3)} + y_l^2 \mathbf{B}_{xx}^{(4)} + z_l^2 \mathbf{B}_{xx}^{(5)} \right)\delta\mathbf{u}_{\mathrm{L}} \tag{24b}$$

$$\delta\gamma_{xy}^a = \mathbf{P}\delta\boldsymbol{\beta} + \left(y_l \mathbf{B}_{xy}^{(1)} + z_l \mathbf{B}_{xy}^{(2)} \right)\delta\mathbf{u}_{\mathrm{L}} \tag{24c}$$

$$\delta\gamma_{xy} = \left(\mathbf{B}_{xy}^{(0)} + y_l \mathbf{B}_{xy}^{(1)} + z_l \mathbf{B}_{xy}^{(2)} \right)\delta\mathbf{u}_{\mathrm{L}} \tag{24d}$$

$$\delta\gamma_{xz}^a = \mathbf{P}\delta\boldsymbol{\chi} + \left(y_l \mathbf{B}_{xz}^{(1)} + z_l \mathbf{B}_{xz}^{(2)} \right)\delta\mathbf{u}_{\mathrm{L}} \tag{24e}$$

$$\delta\gamma_{xz} = \left(\mathbf{B}_{xz}^{(0)} + y_l \mathbf{B}_{xz}^{(1)} + z_l \mathbf{B}_{xz}^{(2)} \right)\delta\mathbf{u}_{\mathrm{L}} \tag{24f}$$

$$\delta \mathrm{W}_e = \mathbf{f}_{\mathrm{ext}}^{\mathrm{T}} \delta\mathbf{u}_{\mathrm{L}} \tag{24g}$$

considering the independence of $\delta\boldsymbol{\alpha}, \delta\boldsymbol{\beta}, \delta\boldsymbol{\chi}$ and $\delta\mathbf{u}_L, \mathbf{f} = \mathbf{f}_{ext}$ at the equilibrium state, and assumed that the cross-section of the beam element is bisymmetric, meanwhile, let

$$\mathbf{H} = A\int_L \mathbf{P}^T\mathbf{P}\,\mathrm{d}x \tag{25a}$$

$$\mathbf{F}_1 = A\int_L \mathbf{P}^T\varepsilon_{xx}^{(0)}\,\mathrm{d}x \tag{25b}$$

$$\mathbf{F}_2 = A\int_L \mathbf{P}^T\gamma_{xy}^{(0)}\,\mathrm{d}x \tag{25c}$$

$$\mathbf{F}_3 = A\int_L \mathbf{P}^T\gamma_{xz}^{(0)}\,\mathrm{d}x \tag{25d}$$

then,

$$\boldsymbol{\alpha} = \mathbf{H}^{-1}\mathbf{F}_1 \tag{26a}$$

$$\boldsymbol{\beta} = \mathbf{H}^{-1}\mathbf{F}_2 \tag{26b}$$

$$\boldsymbol{\chi} = \mathbf{H}^{-1}\mathbf{F}_3 \tag{26c}$$

and the local internal force vector $\mathbf{f}$ of the element can be calculated by

$$
\begin{aligned}
\mathbf{f} = &\; E\int_L\left[I_y\left(\mathbf{B}_{xx}^{(0)^T}\varepsilon_{xx}^{(5)} + \mathbf{B}_{xx}^{(2)^T}\varepsilon_{xx}^{(2)} + \mathbf{B}_{xx}^{(5)^T}\varepsilon_{xx}^{(0)}\right) + I_{\omega y}\mathbf{B}_{xx}^{(5)^T}\varepsilon_{xx}^{(5)}\right]\mathrm{d}x + EA\int_L\mathbf{B}_{xx}^{(0)^T}\mathbf{P}\,\mathrm{d}x\boldsymbol{\alpha} \\
&+ E\int_L\left[I_z\left(\mathbf{B}_{xx}^{(0)^T}\varepsilon_{xx}^{(4)} + \mathbf{B}_{xx}^{(1)^T}\varepsilon_{xx}^{(1)} + \mathbf{B}_{xx}^{(4)^T}\varepsilon_{xx}^{(0)}\right) + I_{\omega z}\mathbf{B}_{xx}^{(4)^T}\varepsilon_{xx}^{(4)}\right]\mathrm{d}x \\
&+ EI_{\omega yz}\int_L\left(\mathbf{B}_{xx}^{(4)^T}\varepsilon_{xx}^{(5)} + \mathbf{B}_{xx}^{(5)^T}\varepsilon_{xx}^{(4)} + \mathbf{B}_{xx}^{(3)^T}\varepsilon_{xx}^{(3)}\right)\mathrm{d}x \\
&+ k_0 G\left[\int_L\left(I_y\mathbf{B}_{xy}^{(2)^T}\gamma_{xy}^{(2)} + I_z\mathbf{B}_{xy}^{(1)^T}\gamma_{xy}^{(1)}\right)\mathrm{d}x + A\int_L\mathbf{B}_{xy}^{(0)^T}\mathbf{P}\,\mathrm{d}x\boldsymbol{\beta}\right] \\
&+ k_0 G\left[\int_L\left(I_y\mathbf{B}_{xz}^{(2)^T}\gamma_{xz}^{(2)} + I_z\mathbf{B}_{xz}^{(1)^T}\gamma_{xz}^{(1)}\right)\mathrm{d}x + A\int_L\mathbf{B}_{xz}^{(0)^T}\mathbf{P}\,\mathrm{d}x\boldsymbol{\chi}\right]
\end{aligned} \tag{27}
$$

where, A is the cross-sectional area of the element, $I_y = \int_A z_l^2\,\mathrm{d}A$, $I_z = \int_A y_l^2\,\mathrm{d}A$, $I_{\omega y} = \int_A z_l^4\,\mathrm{d}A$, $I_{\omega z} = \int_A y_l^4\,\mathrm{d}A$, $I_{\omega yz} = \int_A y_l^2 z_l^2\,\mathrm{d}A$.

The element tangent stiffness matrix in the local coordinate system can be calculated from differentiating the local internal force vector of the element with respect to $\mathbf{u}_L$,

$$
\begin{aligned}
\mathbf{k}_{\mathrm{T}} = \mathrm{E} \int_{\mathrm{L}} &\left[\mathrm{I}_y \left(\mathbf{B}_{xx}^{(2)\mathrm{T}} \mathbf{B}_{xx}^{(2)} + \mathbf{B}_{xx}^{(5)\mathrm{T}} \mathbf{B}_{xx}^{(0)} + \mathbf{B}_{xx}^{(0)\mathrm{T}} \mathbf{B}_{xx}^{(5)} \right) + \mathrm{I}_{\omega y} \mathbf{B}_{xx}^{(5)\mathrm{T}} \mathbf{B}_{xx}^{(5)} \right] \mathrm{d}x \\
&+ \mathrm{E} \int_{\mathrm{L}} \left[\mathrm{I}_z \left(\mathbf{B}_{xx}^{(1)\mathrm{T}} \mathbf{B}_{xx}^{(1)} + \mathbf{B}_{xx}^{(4)\mathrm{T}} \mathbf{B}_{xx}^{(0)} + \mathbf{B}_{xx}^{(0)\mathrm{T}} \mathbf{B}_{xx}^{(4)} \right) + \mathrm{I}_{\omega z} \mathbf{B}_{xx}^{(4)\mathrm{T}} \mathbf{B}_{xx}^{(4)} \right] \mathrm{d}x \\
&+ \mathrm{I}_{\omega yz} \mathrm{E} \int_{\mathrm{L}} \left(\mathbf{B}_{xx}^{(3)\mathrm{T}} \mathbf{B}_{xx}^{(3)} + \mathbf{B}_{xx}^{(4)\mathrm{T}} \mathbf{B}_{xx}^{(5)} + \mathbf{B}_{xx}^{(5)\mathrm{T}} \mathbf{B}_{xx}^{(4)} \right) \mathrm{d}x \\
&+ \mathrm{E} \int_{\mathrm{L}} \left[\mathrm{I}_y \left(\frac{\partial \mathbf{B}_{xx}^{(2)\mathrm{T}}}{\partial \mathbf{u}_{\mathrm{L}}^{\mathrm{T}}} \varepsilon_{xx}^{(2)} + \frac{\partial \mathbf{B}_{xx}^{(5)\mathrm{T}}}{\partial \mathbf{u}_{\mathrm{L}}^{\mathrm{T}}} \varepsilon_{xx}^{(0)} + \frac{\partial \mathbf{B}_{xx}^{(0)\mathrm{T}}}{\partial \mathbf{u}_{\mathrm{L}}^{\mathrm{T}}} \varepsilon_{xx}^{(5)} \right) + \mathrm{I}_{\omega y} \frac{\partial \mathbf{B}_{xx}^{(5)\mathrm{T}}}{\partial \mathbf{u}_{\mathrm{L}}^{\mathrm{T}}} \varepsilon_{xx}^{(5)} \right] \mathrm{d}x \\
&+ \mathrm{E} \int_{\mathrm{L}} \left[\mathrm{I}_z \left(\frac{\partial \mathbf{B}_{xx}^{(1)\mathrm{T}}}{\partial \mathbf{u}_{\mathrm{L}}^{\mathrm{T}}} \varepsilon_{xx}^{(1)} + \frac{\partial \mathbf{B}_{xx}^{(4)\mathrm{T}}}{\partial \mathbf{u}_{\mathrm{L}}^{\mathrm{T}}} \varepsilon_{xx}^{(0)} + \frac{\partial \mathbf{B}_{xx}^{(0)\mathrm{T}}}{\partial \mathbf{u}_{\mathrm{L}}^{\mathrm{T}}} \varepsilon_{xx}^{(4)} \right) + \mathrm{I}_{\omega z} \frac{\partial \mathbf{B}_{xx}^{(4)\mathrm{T}}}{\partial \mathbf{u}_{\mathrm{L}}^{\mathrm{T}}} \varepsilon_{xx}^{(4)} \right] \mathrm{d}x \\
&+ \mathrm{EI}_{\omega yz} \int_{\mathrm{L}} \left(\frac{\partial \mathbf{B}_{xx}^{(3)\mathrm{T}}}{\partial \mathbf{u}_{\mathrm{L}}^{\mathrm{T}}} \varepsilon_{xx}^{(3)} + \frac{\partial \mathbf{B}_{xx}^{(4)\mathrm{T}}}{\partial \mathbf{u}_{\mathrm{L}}^{\mathrm{T}}} \varepsilon_{xx}^{(5)} + \frac{\partial \mathbf{B}_{xx}^{(5)\mathrm{T}}}{\partial \mathbf{u}_{\mathrm{L}}^{\mathrm{T}}} \varepsilon_{xx}^{(4)} \right) \mathrm{d}x \\
&+ \mathrm{EA} \int_{\mathrm{L}} \frac{\partial \mathbf{B}_{xx}^{(0)\mathrm{T}}}{\partial \mathbf{u}_{\mathrm{L}}^{\mathrm{T}}} \mathbf{P} \, \mathrm{d}x \boldsymbol{\alpha} + \mathrm{EA}^2 \left(\int_{\mathrm{L}} \mathbf{B}_{xx}^{(0)\mathrm{T}} \mathbf{P} \, \mathrm{d}x \right) \mathbf{H}^{-1} \left(\int_{\mathrm{L}} \mathbf{P}^{\mathrm{T}} \mathbf{B}_{xx}^{(0)} \, \mathrm{d}x \right) \\
&+ \mathrm{k}_0 \mathrm{G} \left[\mathrm{I}_y \int_{\mathrm{L}} \left(\mathbf{B}_{xy}^{(2)\mathrm{T}} \mathbf{B}_{xy}^{(2)} + \frac{\partial \mathbf{B}_{xy}^{(2)\mathrm{T}}}{\partial \mathbf{u}_{\mathrm{L}}^{\mathrm{T}}} \gamma_{xy}^{(2)} \right) \mathrm{d}x + \mathrm{A}^2 \left(\int_{\mathrm{L}} \mathbf{B}_{xy}^{(0)\mathrm{T}} \mathbf{P} \, \mathrm{d}x \right) \mathbf{H}^{-1} \int_{\mathrm{L}} \mathbf{P}^{\mathrm{T}} \mathbf{B}_{xy}^{(0)} \, \mathrm{d}x \right] \\
&+ \mathrm{k}_0 \mathrm{G} \left[\mathrm{I}_z \int_{\mathrm{L}} \left(\mathbf{B}_{xy}^{(1)\mathrm{T}} \mathbf{B}_{xy}^{(1)} + \frac{\partial \mathbf{B}_{xy}^{(1)\mathrm{T}}}{\partial \mathbf{u}_{\mathrm{L}}^{\mathrm{T}}} \gamma_{xy}^{(1)} + \mathbf{B}_{xz}^{(1)\mathrm{T}} \mathbf{B}_{xz}^{(1)} + \frac{\partial \mathbf{B}_{xz}^{(1)\mathrm{T}}}{\partial \mathbf{u}_{\mathrm{L}}^{\mathrm{T}}} \gamma_{xz}^{(1)} \right) \mathrm{d}x \right] \\
&+ \mathrm{k}_0 \mathrm{GA} \left(\int_{\mathrm{L}} \frac{\partial \mathbf{B}_{xy}^{(0)\mathrm{T}}}{\partial \mathbf{u}_{\mathrm{L}}^{\mathrm{T}}} \mathbf{P} \, \mathrm{d}x \boldsymbol{\beta} + \int_{\mathrm{L}} \frac{\partial \mathbf{B}_{xz}^{(0)\mathrm{T}}}{\partial \mathbf{u}_{\mathrm{L}}^{\mathrm{T}}} \mathbf{P} \, \mathrm{d}x \boldsymbol{\chi} \right) \\
&+ \mathrm{k}_0 \mathrm{G} \left[\mathrm{I}_y \int_{\mathrm{L}} \left(\mathbf{B}_{xz}^{(2)\mathrm{T}} \mathbf{B}_{xz}^{(2)} + \frac{\partial \mathbf{B}_{xz}^{(2)\mathrm{T}}}{\partial \mathbf{u}_{\mathrm{L}}^{\mathrm{T}}} \gamma_{xz}^{(2)} \right) \mathrm{d}x + \mathrm{A}^2 \left(\int_{\mathrm{L}} \mathbf{B}_{xz}^{(0)\mathrm{T}} \mathbf{P} \, \mathrm{d}x \right) \mathbf{H}^{-1} \int_{\mathrm{L}} \mathbf{P}^{\mathrm{T}} \mathbf{B}_{xz}^{(0)} \, \mathrm{d}x \right] \quad (28)
\end{aligned}
$$

where, $\mathbf{k}_{\mathrm{T}}$ is the sum of symmetric matrices, and some general matrices plus their transposes, thus $\mathbf{k}_{\mathrm{T}}$ is symmetric.

Gaussian integral procedure is adopted to calculate the internal force vector and tangent stiffness matrix,

$$
\begin{aligned}
\mathbf{f} = \mathrm{E} \sum_{i=1}^{n_0} &\left\{ \mathrm{I}_y \left(\mathbf{B}_{xx}^{(0)\mathrm{T}} \varepsilon_{xx}^{(5)} + \mathbf{B}_{xx}^{(2)\mathrm{T}} \varepsilon_{xx}^{(2)} + \mathbf{B}_{xx}^{(5)\mathrm{T}} \varepsilon_{xx}^{(0)} \right) + \mathrm{I}_{\omega y} \mathbf{B}_{xx}^{(5)\mathrm{T}} \varepsilon_{xx}^{(5)} \right\} w_{\mathrm{T}}(i) \mathrm{J} \Big|_{\xi_i} + \mathrm{EA} \sum_{i=1}^{n_0} \left[\left(\mathbf{B}_{xx}^{(0)\mathrm{T}} \mathbf{P} \right) w_{\mathrm{T}}(i) \mathrm{J} \right]_{\xi_i} \boldsymbol{\alpha} \\
&+ \mathrm{E} \sum_{i=1}^{n_0} \left\{ \mathrm{I}_z \left(\mathbf{B}_{xx}^{(0)\mathrm{T}} \varepsilon_{xx}^{(4)} + \mathbf{B}_{xx}^{(1)\mathrm{T}} \varepsilon_{xx}^{(1)} + \mathbf{B}_{xx}^{(4)\mathrm{T}} \varepsilon_{xx}^{(0)} \right) + \mathrm{I}_{\omega z} \mathbf{B}_{xx}^{(4)\mathrm{T}} \varepsilon_{xx}^{(4)} \right\} w_{\mathrm{T}}(i) \mathrm{J} \Big|_{\xi_i} \\
&+ \mathrm{EI}_{\omega yz} \sum_{i=1}^{n_0} \left[\left(\mathbf{B}_{xx}^{(4)\mathrm{T}} \varepsilon_{xx}^{(5)} + \mathbf{B}_{xx}^{(5)\mathrm{T}} \varepsilon_{xx}^{(4)} + \mathbf{B}_{xx}^{(3)\mathrm{T}} \varepsilon_{xx}^{(3)} \right) w_{\mathrm{T}}(i) \mathrm{J} \right]_{\xi_i} \\
&+ \mathrm{k}_0 \mathrm{G} \left\{ \sum_{i=1}^{n_0} \left[\left(\mathrm{I}_y \mathbf{B}_{xy}^{(2)\mathrm{T}} \gamma_{xy}^{(2)} + \mathrm{I}_z \mathbf{B}_{xy}^{(1)\mathrm{T}} \gamma_{xy}^{(1)} \right) w_{\mathrm{T}}(i) \mathrm{J} \right]_{\xi_i} + \mathrm{A} \sum_{i=1}^{n_0} \left(\mathbf{B}_{xy}^{(0)\mathrm{T}} \mathbf{P} w_{\mathrm{T}}(i) \mathrm{J} \right)_{\xi_i} \boldsymbol{\beta} \right\} \\
&+ \mathrm{k}_0 \mathrm{G} \left\{ \sum_{i=1}^{n_0} \left[\left(\mathrm{I}_y \mathbf{B}_{xz}^{(2)\mathrm{T}} \gamma_{xz}^{(2)} + \mathrm{I}_z \mathbf{B}_{xz}^{(1)\mathrm{T}} \gamma_{xz}^{(1)} \right) w_{\mathrm{T}}(i) \mathrm{J} \right]_{\xi_i} + \mathrm{A} \sum_{i=1}^{n_0} \left(\mathbf{B}_{xz}^{(0)\mathrm{T}} \mathbf{P} w_{\mathrm{T}}(i) \mathrm{J} \right)_{\xi_i} \boldsymbol{\chi} \right\} \quad (29)
\end{aligned}
$$

$$\mathbf{k}_T = E \sum_{i=1}^{n_0} \left\{ \left[I_y \left(\mathbf{B}_{xx}^{(2)^T} \mathbf{B}_{xx}^{(2)} + \mathbf{B}_{xx}^{(5)^T} \mathbf{B}_{xx}^{(0)} + \mathbf{B}_{xx}^{(0)^T} \mathbf{B}_{xx}^{(5)} \right) + I_{\omega y} \mathbf{B}_{xx}^{(5)^T} \mathbf{B}_{xx}^{(5)} \right] w_T(i) J \right\}_{\xi_i}$$

$$+ E \sum_{i=1}^{n_0} \left\{ \left[I_z \left(\mathbf{B}_{xx}^{(1)^T} \mathbf{B}_{xx}^{(1)} + \mathbf{B}_{xx}^{(4)^T} \mathbf{B}_{xx}^{(0)} + \mathbf{B}_{xx}^{(0)^T} \mathbf{B}_{xx}^{(4)} \right) + I_{\omega z} \mathbf{B}_{xx}^{(4)^T} \mathbf{B}_{xx}^{(4)} \right] w_T(i) J \right\}_{\xi_i}$$

$$+ E I_{\omega yz} \sum_{i=1}^{n_0} \left[\left(\mathbf{B}_{xx}^{(3)^T} \mathbf{B}_{xx}^{(3)} + \mathbf{B}_{xx}^{(4)^T} \mathbf{B}_{xx}^{(5)} + \mathbf{B}_{xx}^{(5)^T} \mathbf{B}_{xx}^{(4)} \right) w_T(i) J \right]_{\xi_i}$$

$$+ E \sum_{i=1}^{n_0} \left\{ \left[I_y \left(\frac{\partial \mathbf{B}_{xx}^{(2)^T}}{\partial \mathbf{u}_L^T} \varepsilon_{xx}^{(2)} + \frac{\partial \mathbf{B}_{xx}^{(5)^T}}{\partial \mathbf{u}_L^T} \varepsilon_{xx}^{(0)} + \frac{\partial \mathbf{B}_{xx}^{(0)^T}}{\partial \mathbf{u}_L^T} \varepsilon_{xx}^{(5)} \right) + I_{\omega y} \frac{\partial \mathbf{B}_{xx}^{(5)^T}}{\partial \mathbf{u}_L^T} \varepsilon_{xx}^{(5)} \right] w_T(i) J \right\}_{\xi_i}$$

$$+ E \sum_{i=1}^{n_0} \left\{ \left[I_z \left(\frac{\partial \mathbf{B}_{xx}^{(1)^T}}{\partial \mathbf{u}_L^T} \varepsilon_{xx}^{(1)} + \frac{\partial \mathbf{B}_{xx}^{(4)^T}}{\partial \mathbf{u}_L^T} \varepsilon_{xx}^{(0)} + \frac{\partial \mathbf{B}_{xx}^{(0)^T}}{\partial \mathbf{u}_L^T} \varepsilon_{xx}^{(4)} \right) + I_{\omega z} \frac{\partial \mathbf{B}_{xx}^{(4)^T}}{\partial \mathbf{u}_L^T} \varepsilon_{xx}^{(4)} \right] w_T(i) J \right\}_{\xi_i}$$

$$+ E I_{\omega yz} \sum_{i=1}^{n_0} \left[\left(\frac{\partial \mathbf{B}_{xx}^{(3)^T}}{\partial \mathbf{u}_L^T} \varepsilon_{xx}^{(3)} + \frac{\partial \mathbf{B}_{xx}^{(4)^T}}{\partial \mathbf{u}_L^T} \varepsilon_{xx}^{(5)} + \frac{\partial \mathbf{B}_{xx}^{(5)^T}}{\partial \mathbf{u}_L^T} \varepsilon_{xx}^{(4)} \right) w_T(i) J \right]_{\xi_i}$$

$$+ E A \sum_{i=1}^{n_0} \left(\frac{\partial \mathbf{B}_{xx}^{(0)^T}}{\partial \mathbf{u}_L^T} P w_T(i) J \right)_{\xi_i} \boldsymbol{\alpha} + E A^2 \sum_{i=1}^{n_0} \left(\mathbf{B}_{xx}^{(0)^T} P w_T(i) J \right)_{\xi_i} \mathbf{H}^{-1} \sum_{i=1}^{n_0} \left(\mathbf{P}^T \mathbf{B}_{xx}^{(0)} w_T(i) J \right)_{\xi_i}$$

$$+ k_0 G \left\{ I_y \sum_{i=1}^{n_0} \left[\left(\mathbf{B}_{xy}^{(2)^T} \mathbf{B}_{xy}^{(2)} + \frac{\partial \mathbf{B}_{xy}^{(2)^T}}{\partial \mathbf{u}_L^T} \gamma_{xy}^{(2)} \right) w_T(i) J \right]_{\xi_i} + A^2 \sum_{i=1}^{n_0} \left(\mathbf{B}_{xy}^{(0)^T} P w_T(i) J \right)_{\xi_i} \mathbf{H}^{-1} \sum_{i=1}^{n_0} \left(\mathbf{P}^T \mathbf{B}_{xy}^{(0)} w_T(i) J \right)_{\xi_i} \right\}$$

$$+ k_0 G I_z \sum_{i=1}^{n_0} \left[\left(\mathbf{B}_{xy}^{(1)^T} \mathbf{B}_{xy}^{(1)} + \frac{\partial \mathbf{B}_{xy}^{(1)^T}}{\partial \mathbf{u}_L^T} \gamma_{xy}^{(1)} + \mathbf{B}_{xz}^{(1)^T} \mathbf{B}_{xz}^{(1)} + \frac{\partial \mathbf{B}_{xz}^{(1)^T}}{\partial \mathbf{u}_L^T} \gamma_{xz}^{(1)} \right) w_T(i) J \right]_{\xi_i}$$

$$+ k_0 G A \left[\sum_{i=1}^{n_0} \left(\frac{\partial \mathbf{B}_{xy}^{(0)^T}}{\partial \mathbf{u}_L^T} P w_T(i) J \right)_{\xi_i} \boldsymbol{\beta} + \sum_{i=1}^{n_0} \left(\frac{\partial \mathbf{B}_{xz}^{(0)^T}}{\partial \mathbf{u}_L^T} P w_T(i) J \right)_{\xi_i} \boldsymbol{\chi} \right]$$

$$+ k_0 G \left\{ I_y \sum_{i=1}^{n_0} \left[\left(\mathbf{B}_{xz}^{(2)^T} \mathbf{B}_{xz}^{(2)} + \frac{\partial \mathbf{B}_{xz}^{(2)^T}}{\partial \mathbf{u}_L^T} \gamma_{xz}^{(2)} \right) w_T(i) J \right]_{\xi_i} + A^2 \sum_{i=1}^{n_0} \left(\mathbf{B}_{xz}^{(0)^T} P w_T(i) J \right)_{\xi_i} \mathbf{H}^{-1} \sum_{i=1}^{n_0} \left(\mathbf{P}^T \mathbf{B}_{xz}^{(0)} w_T(i) J \right)_{\xi_i} \right\} \quad (30)$$

where, n_0 is the number of Gaussian integral points along the central axis ξ of element, $n_0=3$ in solving the examples below; ξ_i and $w_T(i)$ are the natural coordinate and weight factor at Gaussian point i, respectively; J is the Jacobian, $J = \sum_{i=1}^{3} N_{i,\xi} x_{i0}$; $\boldsymbol{\alpha}, \boldsymbol{\beta}, \boldsymbol{\chi}$ can be calculated from Eqs. 26a~c, and

$$\mathbf{H} = A \sum_{i=1}^{n_0} \left[\mathbf{P}^T P w_T(i) J \right]_{\xi_i} \tag{31}$$

$$\mathbf{F}_1 = A \sum_{i=1}^{n_0} \left[\mathbf{P}^T \varepsilon_{xx}^{(0)} w_T(i) J \right]_{\xi_i} \tag{32}$$

$$\mathbf{F}_2 = \mathbf{A} \sum_{i=1}^{n_0} \left[\mathbf{P}^\mathrm{T} \gamma_{xy}^{(0)} w_\mathrm{T}(i) \, \mathbf{J} \right]_{\xi_i} \tag{33}$$

$$\mathbf{F}_3 = \mathbf{A} \sum_{i=1}^{n_0} \left[\mathbf{P}^\mathrm{T} \gamma_{xz}^{(0)} w_\mathrm{T}(i) \, \mathbf{J} \right]_{\xi_i} \tag{34}$$

The global internal force vector $\mathbf{f}_\mathrm{G}$ can be calculated from the local internal force vector $\mathbf{f}$,

$$\mathbf{f}_\mathrm{G} = \mathbf{T}^\mathrm{T} \mathbf{f} \tag{35}$$

where, $\mathbf{T}$ is the transformation matrix from the global coordinate system to the local coordinate system, it is calculated from

$$\mathbf{T} = \frac{\partial \mathbf{u}_\mathrm{L}}{\partial \mathbf{u}_\mathrm{G}^\mathrm{T}} \tag{36}$$

The global tangent stiffness matrix is derived from $\mathbf{f}_\mathrm{G}$ as below,

$$\mathbf{k}_\mathrm{TG} = \frac{\partial \mathbf{f}_\mathrm{G}}{\partial \mathbf{u}_\mathrm{G}^\mathrm{T}} = \mathbf{T}^\mathrm{T} \frac{\partial \mathbf{f}}{\partial \mathbf{u}_\mathrm{G}^\mathrm{T}} + \frac{\partial \mathbf{T}^\mathrm{T}}{\partial \mathbf{u}_\mathrm{G}^\mathrm{T}} \mathbf{f} = \mathbf{T}^\mathrm{T} \mathbf{k}_\mathrm{T} \mathbf{T} + \frac{\partial \mathbf{T}^\mathrm{T}}{\partial \mathbf{u}_\mathrm{G}^\mathrm{T}} \mathbf{f} \tag{37}$$

It is obvious that the first term in the right side of Eq. 37 is symmetric. The second term includes the second derivatives of local nodal variables with respect to global nodal variables, where the global nodal variables are commutative, thus the second term is also symmetric, resulting in a symmetric element tangent stiffness matrix $\mathbf{k}_\mathrm{TG}$ in the global coordinate system.

5.   CALCULATION OF EQUIVALENT EXTERNAL FORCE VECTOR

In the present element formulation, vectorial rotational variables are employed to replace traditional angular rotational variables, thus the components of the internal force vector with respect to vectorial rotational variables are not moment and torque, and an equivalent external force vector must be adopted.

Firstly, assumed that Vector $\mathbf{e}_n$ is rotated through infinitesimal rotations of $\boldsymbol{\theta}^\mathrm{T} = \langle \delta\theta_X \quad \delta\theta_Y \quad \delta\theta_Z \rangle$ to become Vector $\mathbf{e}_{n+1}$, then an approximate relationship of $\mathbf{e}_n$ and $\mathbf{e}_{n+1}$ can be given as

$$\mathbf{e}_{n+1} = [\mathbf{I} + \mathbf{S}(\delta\boldsymbol{\theta})] \mathbf{e}_n \tag{38}$$

where, $\mathbf{I}$ is a 3×3 unit matrix, and

$$\mathbf{S}(\delta\boldsymbol{\theta}) = \begin{bmatrix} 0 & -\delta\theta_Z & \delta\theta_Y \\ \delta\theta_Z & 0 & -\delta\theta_X \\ -\delta\theta_Y & \delta\theta_X & 0 \end{bmatrix} \tag{39}$$

Eq. 38 can be rewritten as

$$\mathbf{e}_{n+1} - \mathbf{e}_n = \mathbf{S}(\delta\boldsymbol{\theta})\mathbf{e}_n = -\mathbf{S}(\mathbf{e}_n)\delta\boldsymbol{\theta} \tag{40}$$

or

$$\delta\mathbf{e}_n = -\mathbf{S}(\mathbf{e}_n)\delta\boldsymbol{\theta} \tag{41}$$

thus the relationship between the principal vectors of the cross-section of the element at Node i and the nodal angular rotations can be written as

$$\left.\begin{aligned}\delta\mathbf{e}_{iy} &= -\mathbf{S}(\mathbf{e}_{iy})\delta\boldsymbol{\theta}\\ \delta\mathbf{e}_{iz} &= -\mathbf{S}(\mathbf{e}_{iz})\delta\boldsymbol{\theta}\end{aligned}\right\} \tag{42}$$

furthermore, the relationship between the incremental vectorial rotational variables and the nodal angular rotational variables can be given as

$$\begin{Bmatrix}\delta e_{iy,n_i}\\ \delta e_{iy,m_i}\\ \delta e_{iz,n_i}\end{Bmatrix} = -\begin{bmatrix}S_{n_i,1}(\mathbf{e}_{iy}) & S_{n_i,2}(\mathbf{e}_{iy}) & S_{n_i,3}(\mathbf{e}_{iy})\\ S_{m_i,1}(\mathbf{e}_{iy}) & S_{m_i,2}(\mathbf{e}_{iy}) & S_{m_i,3}(\mathbf{e}_{iy})\\ S_{n_i,1}(\mathbf{e}_{iz}) & S_{n_i,2}(\mathbf{e}_{iz}) & S_{n_i,3}(\mathbf{e}_{iz})\end{bmatrix}\begin{Bmatrix}\delta\theta_{iX}\\ \delta\theta_{iY}\\ \delta\theta_{iZ}\end{Bmatrix} \tag{43}$$

where, $S_{j,k}(\mathbf{e}_{iy})$ and $S_{j,k}(\mathbf{e}_{iz})$ are respectively the components of $\mathbf{S}(\mathbf{e}_{iy})$ and $\mathbf{S}(\mathbf{e}_{iz})$ at j^{th} row and k^{th} column.

In calculating the equivalent components of the external force vector with respect to vectorial rotational variables, the work done by the equivalent components must be equal to that done by the corresponding moment and torque at Node i,

$$\begin{Bmatrix}M_{eq1}\\ M_{eq2}\\ M_{eq3}\end{Bmatrix}^{T}\begin{Bmatrix}\delta e_{iy,n_i}\\ \delta e_{iy,m_i}\\ \delta e_{iz,n_i}\end{Bmatrix} = \begin{Bmatrix}M_{iX}\\ M_{iY}\\ M_{iZ}\end{Bmatrix}^{T}\begin{Bmatrix}\delta\theta_{iX}\\ \delta\theta_{iY}\\ \delta\theta_{iZ}\end{Bmatrix} \tag{44}$$

where, M_{eqj} (j=1,2,3) is the equivalent component of the external force vector with respect to vectorial rotational variable, and $M_{i\alpha}$ ($\alpha = X,Y,Z$) is moment or torque loaded at Node i.
Substitute Eq. 43 into Eq. 44, the equivalent components of the external force vector with respect to vectorial rotational variables can be calculated as

$$\begin{Bmatrix}M_{eq1}\\ M_{eq2}\\ M_{eq3}\end{Bmatrix} = -\begin{bmatrix}S_{n_i,1}(\mathbf{e}_{iy}) & S_{n_i,2}(\mathbf{e}_{iy}) & S_{n_i,3}(\mathbf{e}_{iy})\\ S_{m_i,1}(\mathbf{e}_{iy}) & S_{m_i,2}(\mathbf{e}_{iy}) & S_{m_i,3}(\mathbf{e}_{iy})\\ S_{n_i,1}(\mathbf{e}_{iz}) & S_{n_i,2}(\mathbf{e}_{iz}) & S_{n_i,3}(\mathbf{e}_{iz})\end{bmatrix}^{-T}\begin{Bmatrix}M_{iX}\\ M_{iY}\\ M_{iZ}\end{Bmatrix} \tag{45}$$

6.   EXAMPLES

6.1   Locking Problem

6.1.1   Membrane locking problem

An initially straight cantilever beam is subjected to an end bending moment (Figure 3). Its width and thickness are b and h, respectively, the cross-sectional shear factor is 5/6, and its length is L=100; The material properties of the beam are E=2.1×10^7 and μ=0.3, respectively.
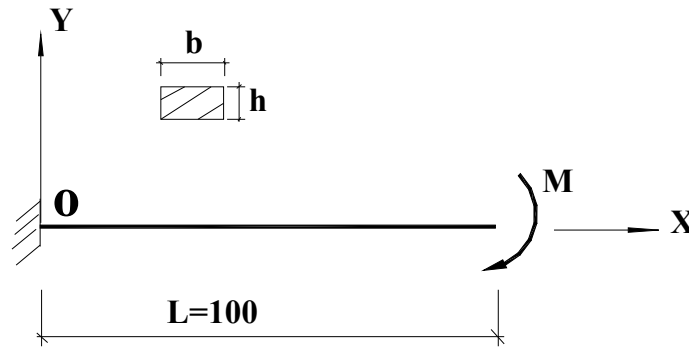

Figure 3. A Cantilever Beam subject to an End Bending Moment

Firstly, assumed that b=0.5 and h=0.1. The cantilever beam is divided into 7 elements equally. The deformed shapes of the cantilever at different end moment levels are depicted in Figure 4. It is shown that the beam experiences large displacement and large rotation, and its end rotation arrives at 2π under $M = \dfrac{2\pi\, E\, I}{L}$, the proposed beam element formulation demonstrates satisfying efficiency and reliability. Urthaler & Reddy [13] and Lee [26] had also solved a similar problem, but they did not present the geometry and material properties of the cantilever beam.
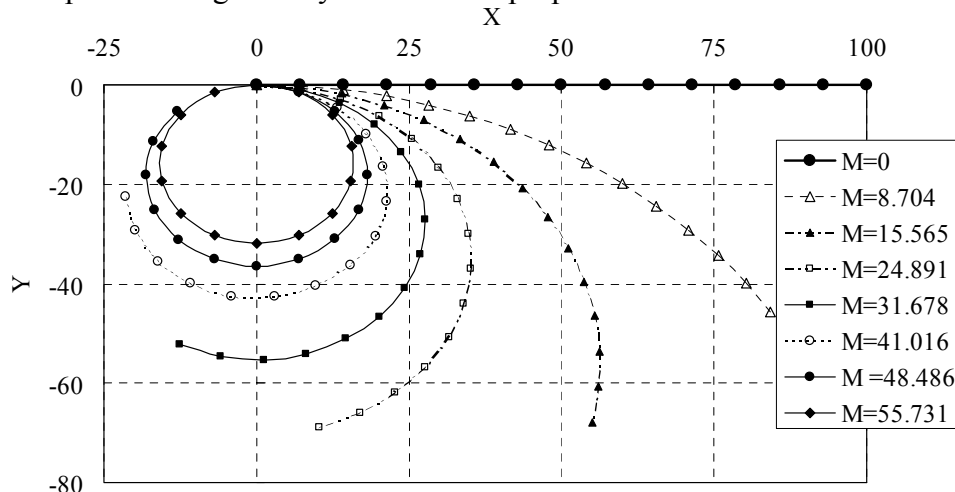
Figure 4. Deformed Shapes of the Cantilever Beam under Different End Moment Levels

To illuminate the computational efficiency and accuracy of the present beam element using assumed membrane strains and shear strains (for convenience, it is abbreviated as AM+AS element), 4 cantilever beams with the same width (b=0.5) and different thickness values (h=0.2, 0.1, 0.05, 0.01) are solved respectively. For comparison, the theoretic solutions and the results from beam elements using conforming membrane strains and shear strains (CM+CS), conforming membrane strains and assumed shear strains (CM+AS), assumed membrane strains and conforming shear strains (AM+CS) are also given in Table 1. It is shown that numerical locking will become more serious in the CM+CS and CM+AS elements with the cantilever beam thickness decrease,

and employing assumed shear strains or not has little effect on the computational efficiency and accuracy of these elements, however, adopting assumed membrane strains can eliminate numerical locking in the AM+CS and AM+AS elements effectively even if the cantilever beam thickness decreases greatly.

Table 1. End Moment Bending a Cantilever Beam into an Exact Complete Circle

Thickness h	0.2	0.1	0.05	0.01
CM+CS-40e	495.820 (12.73%)	82.988 (50.95%)	20.878 (203.81%)	2.856 (--)
CM+AS-40e	495.820 (12.73%)	82.982 (50.94)	20.878 (203.81%)	2.856 (--)
AM+CS-7e	445.913 (1.38%)	55.735 (1.38)	6.961(1.30%)	5.574×10^{-2} (1.38%)
AM+AS-7e	445.909 (1.38%)	55.731 (1.37%)	6.968 (1.40%)	5.574×10^{-2} (1.38%)
Exact values	439.823	54.978	6.872	5.498×10^{-2}

Note: "-40e" and "-7e" denote the element meshes employed; Values in the parentheses are the relative errors between the simulation results and the theoretical solutions.

6.1.2   Shear locking problem

A beam is clamped at both ends and loaded with a concentrated load at the central point (Figure 5a). It has a length of 2L=20, width b=0.5 and thickness h, and its material properties are $E=2.1 \times 10^7$ and μ =0.3, respectively. Considering the symmetry of its geometry and loading case, only one half of the beam is studied (Figure 5b).
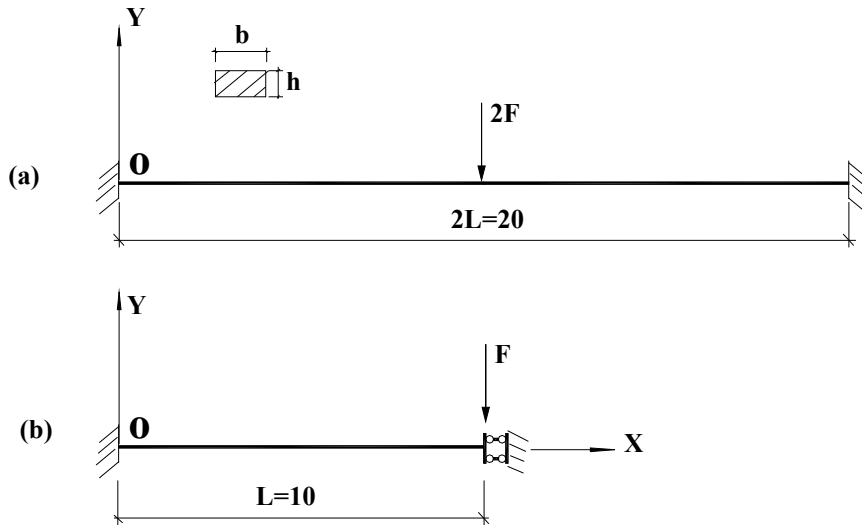
Figure 5. A Clamped Beam subject to a Concentrated Load at Central Point

Table 2. Deflection at the Loading Point of an End-Clamped Beam

Thickness h	0.5	0.2	0.05	0.01
Load	328.126	21.000	3.281×10^{-1}	2.625×10^{-3}
CM+CS -2e	0.1812	0.1407	0.0740	0.0283
-5e	0.2173	0.1639	0.0829	0.0316
-10e	0.2204	0.1667	0.0842	0.0323
CM+AS-2e	0.2208	0.1673	0.0846	0.0326
-5e	0.2208	0.1673	0.0846	0.0325
-10e	0.2208	0.1673	0.0847	0.0325
AM+CS-2e	0.1817	0.1418	0.0750	0.0288
-5e	0.2173	0.1639	0.0829	0.0316
-10e	0.2205	0.1667	0.0842	0.0323
AM+AS-2e	0.2212	0.1678	0.0849	0.0326
-10e	0.2208	0.1673	0.0847	0.0325

Different beam thickness values (h=0.5,0.2,0.05 and 0.01) are considered. For comparison, the deflections at the loading point calculated by using AS+AM, CS+CM, AS+CM and CS+AM elements using different element meshes are presented in Table 2. It demonstrates that the convergence of the CM+CS and AM+CS elements become deteriorated with the beam thickness decrease, even assumed membrane strains are introduced in AM+CS element, thus fine element mesh must be employed to get accurate solutions; while the thickness variation has little effect on the computational accuracy and convergence of the AM+AS and CM+AS elements, satisfying solutions can be achieved by using very coarse element meshes of them.

6.1.3 *Membrane and shear locking problems*

A cantilever beam is subjected to a concentrated load at the free end (Figure 6). It has a length L=5, width b=0.5 and thickness h; its material properties are E=2.1$\times 10^7$ and μ =0.3, respectively.
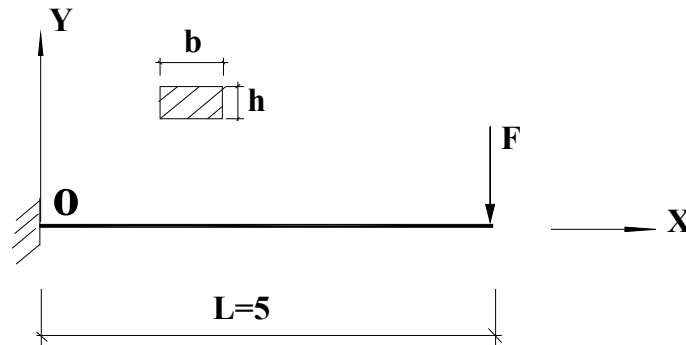

Figure 6. A Cantilever Beam subject to a Concentrated Load at Free End

Different thickness values of the cantilever beam are considered, and the results calculated by using CM+CS, CM+AS, AM+CS and AM+AS elements are presented in Table 3. It is shown that numerical locking occurs in CM+CS, CM+AS and AM+CS elements, it becomes more serious with beam thickness decrease, and this tendency is even more obvious in CM+CS, CM+AS elements, while the AM+AS element is free of locking.

Table. 3 Deflection at the Free End of a Cantilever Beam

Thickness h	0.5	0.2	0.05	0.01
Load	656.250	42.000	6.563×10^{-1}	5.250×10^{-3}
CM+CS-1e	0.1942	0.1725	0.1123	0.0472
-2e	0.2412	0.2322	0.2003	0.1097
-10e	0.2513	0.2495	0.2487	0.2461
CM+AS-1e	0.2480	0.2332	0.1746	0.1097
-2e	0.2508	0.2464	0.2158	0.1253
-10e	0.2513	0.2497	0.2493	0.2467
AM+CS-1e	0.1975	0.1890	0.1872	0.1872
-2e	0.2417	0. 2355	0.2339	0.2338
-10e	0.2513	0.2495	0.2488	0.2487
AM+AS-1e	0.2513	0.2496	0.2494	0.2493
-10e	0.2513	0.2497	0.2494	0.2494

Based on the three examples above, several conclusions can be drawn: 1) membrane locking exists in the first example, it becomes even more serious in a thin beam element, introducing assumed membrane strains in a Hellinger-Reissner functional can exclude membrane locking effectively; 2) shear locking occurs in the second example, and assumed shear strains in a Hellinger-Reissner functional can eliminate it successfully; 3) both membrane locking and shear locking are observed

in the third example, and employing assumed membrane strains and shear strains simultaneously can avoid them; 4) locking phenomena are closely related to element thickness, loading cases and boundary conditions, etc., and they may even occur in thick beam problems.

1.1   A Cantilever 45^0- bend subject to End Loading

A cantilever 45^0- bend lies in X-Y plane (see Figure 7), it has an average radius of 100in, and a square cross-section of 1×1 in^2, its elastic modulus E and Poisson's ratio μ are 10^7psi and 0.0, respectively. A concentrated load in Z-direction is applied at the free end.
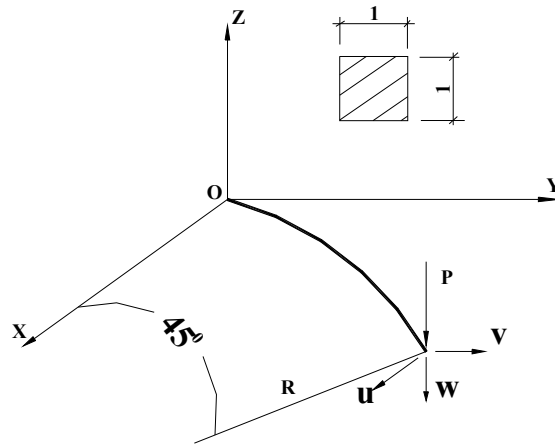

Figure 7. A Cantilever 45^0-bend with a Concentrated Tip Load

This bend is divided into 8 beam elements equally, and these elements are idealized as straight beams. The tip displacements under different load levels are given in Table 4. To verify the reliability and accuracy of the procedure, the results from Bathe & Bolourchi [27] and Simo & Vu-Quoc [17] are also presented in Table 4, it is shown that the results from present studies can fit in well with them.

Table 4. Tip Displacements under Different Load Levels

Load level (lb)	Tip displacement (in)								
	Present study			Bathe and Bolourchi [27]			Simo and Vu-Quoc [17]		
	u	v	w	u	v	w	u	v	w
300	-7.20	-12.21	-40.53	-6.8	-11.5	-39.5	-6.97	-11.86	-40.08
450	-10.94	-18.78	-48.75	--	--	--	-10.68	-18.38	-48.39
600	-13.75	-23.86	-53.64	-13.4	-23.5	-53.4	-13.51	-23.47	-53.37

6.3   A Space Arc Frame Subject to Concentrated Loading

This arc frame consists of two groups of members (Figure 8). The cross-section properties of the members in the arc frame planes are A_1=0.5, I_{y1}=0.4 and I_{z1}=0.133, respectively, and for the rib members, A_2=0.1, I_{y2}=0.05 and I_{z2}=0.05, respectively. The material properties are E=4.32×10^5 and G=1.66×10^5. This frame is pinned at four boundary nodes. In addition to four vertical concentrated loads P, the structure is also subjected to two lateral concentrated loads 0.001P (Figure 8).
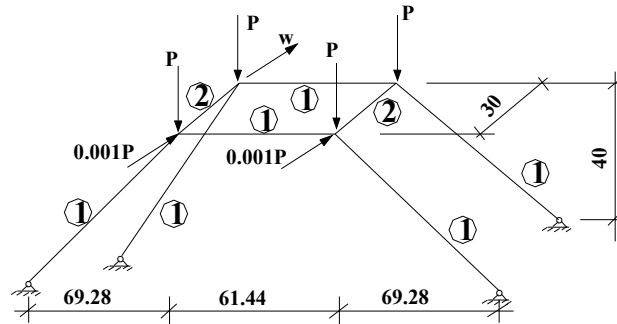
Figure 8. Space Arc Frame

In numerical analysis, each member is treated as one element. The deflection curve at Point A of the arc frame is presented in Figure 9, it is in close agreement with the solution from Wen and Rahimzadeh [28].
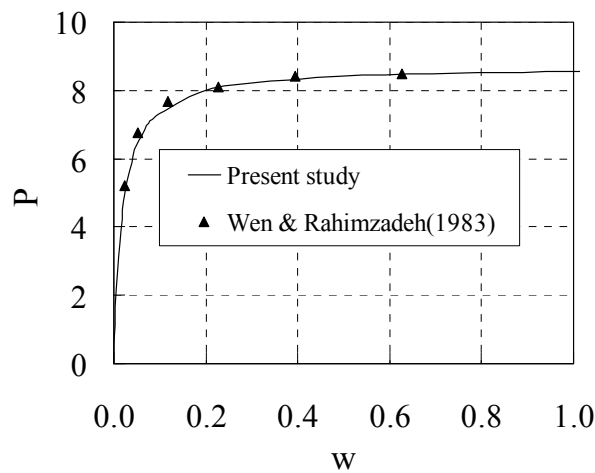

Figure 9. Response of Space Arc Frame under Ultimate Concentrated Loading

7.   CONCLUSIONS

A mixed co-rotational 3D beam element formulation is proposed by using the Hellinger-Reissner functional, where vectorial rotational variables are employed to replace traditional angular rotational variables, taking advantages in calculating the element tangent stiffness matrix. The equivalent components of the external force vector with respect to vectorial rotational variables can be calculated directly from corresponding end moment and torque, thus this element can also be used in modelling of beams subject to end moment and torque. Through three patch tests of locking problems, the present beam element demonstrates its locking-free behaviours, and its computational accuracy and efficiency are verified by multiple elastic examples of large displacement and large rotation problems.

ACKNOWLEDGEMENTS

REFERENCES

[1] Rankin, C.C. and Brogan, F.A., "An Element Independent Corotational Procedure for the Treatment of Large Rotation", Journal of Pressure Vessel Technology-Transactions of The ASME, 1986, Vol. 108, No. 2, pp. 165-174.

[2] Crisfield, M.A., "Nonlinear Finite Element Analysis of Solid and Structures", John Wiley & Sons, Chichester, 1996, Vol. 2.

[3] Yang, H.T.Y., Saigal, S., Masud, A. and Kapania, R.K., "Survey of Recent Shell Finite Elements", International Journal for Numerical Methods in Engineering, 2000, Vol. 47, No.1, pp. 101-127.

[4] Wempner, G., "Finite Elements, Finite Rotations and Small Strains of Flexible Shells", International Journal of Solids and Structures, 1969, Vol. 5, No. 2, pp. 117-153.

[5] Belytschko, T. and Hseih, B.J., "Non-linear Transient Finite Element Analysis with Convected Co-ordinates", International Journal for Numerical Methods in Engineering, 1973, Vol. 7, No. 3, pp. 255-271.

[6] Belytschko, T. and Glaum, L.W., "Application of Higher Order Corotational Stretch Theories to Nonlinear Finite Element Analysis", Computers & Structures, 1979, Vol. 10, No. 1-2, pp. 175-182.

[7] Argyris, J.H., Bahner, H., Doltsnis, J., et al., "Finite Element Method - the Natural Approach", Computer Methods in Applied Mechanics and Engineering, 1978, Vol.17/18, Part 1, pp. l-106.

[8] Oran, C., "Tangent Stiffness in Plane Frames", Journal of the Structural Division, ASCE, 1973, Vol. 99, ST6, pp. 973-985.

[9] Oran, C., "Tangent Stiffness in Space Frames", Journal of the Structural Division, ASCE, 1973, Vol. 99, ST6, pp. 987-1001.

[10] Stolarski, H., Belytschko, T. and Lee, S.H., "Review of Shell Finite Elements and Corotational Theories", Computational Mechanics Advances, 1995, Vol. 2, No. 2, pp. 125-212.

[11] Crisfield, M.A. and Moita, G.F., "A Unified Co-rotational Framework for Solids, Shells and Beams", International Journal of Solids and Structures, 1996, Vol. 33, No. 20-22, pp. 2969-2992.

[12] Felippa, C.A. and Haugen, B., "A Unified Formulation of Small-strain Corotational Finite Elements, I. Theory", Computer Methods in Applied Mechanics and Engineering, 2005, Vol. 194, No. 21-24, pp. 2285-2335.

[13] Urthaler, Y. and Reddy, J.N., "A Corotational Finite Element Formulation for the Analysis of Planar Beams", Communications in Numerical Methods in Engineering, 2005, Vol. 21, No. 10, pp. 553–570.

[14] Galvanetto, U. and Crisfield, M.A., "An Energy-conserving Co-rotational Procedure for the Dynamics of Planar Beam Structures", International Journal for Numerical Methods in Engineering, 1996, Vol. 39, No. 13, pp. 2265-2282.

[15] Iura, M., Suetake, Y. and Atluri, S.N., "Accuracy of Co-rotational Formulation for 3-D Timoshenko's Beam", CMES-Computer Modeling In Engineering & Sciences, 2003, Vol. 4, No. 2, pp. 249-258.

[16] Pajot, J.M. and Maute, K., "Analytical Sensitivity Analysis of Geometrically Nonlinear Structures Based on the Co-rotational Finite Element Method", Finite Elements in Analysis and Design, 2006, Vol. 42, No. 10, pp. 900-913.

[17] Simo, J.C. and Vu-Quoc, L., "A Three-dimensional Finite-strain Rod Model. Part II, Computational Aspects", Computer Methods in Applied Mechanics and Engineering, 1986, Vol. 58, No. 1, pp. 79-116.

[18]   Jelenic, G. and Crisfield, M.A., "Problems Associated with the Use of Cayley Transform and Tangent Scaling for Conserving Energy and Momenta in the Reissner–Simo Beam Theory", Communications in Numerical Methods in Engineering, 2002, Vol. 18, No. 10, pp.711-720.

[19]   McRobie, F.A. and Lasenby, J., "Simo-Vu Quoc rods using Clifford algebra", International Journal for Numerical Methods in Engineering, 1999, Vol. 45, No. 4, pp. 377-398.

[20]   Crisfield, M.A., "Consistent Co-rotational Formulation for Non-linear, Three-dimensional, Beam-elements", Computer Methods in Applied Mechanics and Engineering, 1990, Vol. 81, No. 2, pp. 131-150.

[21]   Simo, J.C., "(Symmetric) Hessian for Geometrically Nonlinear Models in Solid Mechanics, Intrinsic Definition and Geometric Interpretation", Computer Methods in Applied Mechanics and Engineering, 1992, Vol. 96, No. 2, pp. 189-200.

[22]   Li, Z.X., "A Mixed Co-rotational Formulation of 2D Beam Element Using Vectorial Rotational Variables", Communications in Numerical Methods in Engineering, 2007, Vol. 23, No. 1, pp. 45-69.

[23]   Li, Z.X., "A Co-rotational Formulation for 3D Beam Element Using Vectorial Rotational Variables", Computational Mechanics, 2007, Vol. 39, No. 3, pp. 293-308.

[24]   Li, Z.X. and Vu-Quoc, L., "An Efficient Co-rotational Formulation for Curved Triangular Shell Element", International Journal for Numerical Methods in Engineering, 2007, Vol.72, No. 9, pp. 1029-1062.

[25]   Li, Z.X., Izzuddin, B.A. and Vu-Quoc, L., "A 9-node Co-rotational Quadrilateral Shell Element", Computational Mechanics, 2008, Vol. 42, No. 6, pp. 873-884.

[26]   Lee, K., "Analysis of Large Displacements and Large Rotations of Three-dimensional Beams by Using Small Strains and Unit Vectors", Communications in Numerical Methods in Engineering, 1997, Vol. 13, No. 12, pp. 987-997.

[27]   Bathe, K.J. and Bolourchi, S., "Large Displacement Analysis of Three-dimensional Beam Structures", International Journal for Numerical Methods in Engineering, 1979, Vol. 14, No.7, pp. 961-986.

[28]   Wen, R.K. and Rahimzadeh, J., "Nonlinear Elastic Frame Analysis by Finite Element", Journal of the Structural Division, ASCE, 1983, Vol. 109, No. 8, pp. 1951-1971.

THERMAL RESPONSE TO FIRE OF UNIFORMLY INSULATED STEEL MEMBERS: BACKGROUND AND VERIFICATION OF THE FORMULATION RECOMMENDED BY CHINESE CODE CECS200

Guo-qiang Li[1,2] and Chao Zhang[2,*]

[1]Sate Key Laboratory for Disaster Reduction in Civil Engineering, 1239 Siping Road, Shanghai, China
[2]College of Civil Engineering, Tongji University, 1239 Siping Road, Shanghai 200092, China
*(Corresponding author: E-mail: 08_chao_zhang@tongji.edu.cn)

ABSTRACT: Currently, Chinese technical code for fire safety of steel structures in buildings (CECS200) is being revised. This paper intends to give the background of the recommended formulation in CECS200 for temperature calculation of uniformly insulated steel members. Analytical formulations recommended by other codes including EC3, ECCS, SFPE handbook, etc.., and FE method are used for comparison and verification. Theoretical derivation of the exact analytical formulations is also given. Two boundary conditions at the fire-insulation interface have been discussed in the derivation. By investigating the steel temperature of three insulated sections with different section factors which are protected by typical fire protection materials, the formulation recommended by CECS200 is proved to be reasonable and simple for engineering usage.

Keywords: Fire resistance, uniformly insulated steel members, 1D model, temperature calculation, analytical formulations, FEM

1.   INTRODUCTION

Bare Steel is frangible to fire by its high conductivity and low specific heat capacity. As a result, insulation is always required for steel members to ensure the stability of the building in fire condition. Historically, the most common methods of insulation have included concrete encasement, envelopment in gypsum plaster or gypsum board and spray application of light weight cementitous or mineral fiber spray-applied fire resistive materials (SFRMs). In recent years, intumescent coatings have been widely used in fire protection engineering. Unlike the traditional fire protection materials like concrete, gypsum, SFRMs, etc.., the intumescent coatings are reactive materials that they are 'inert' at low temperatures but swell to provide a charred layer of low conductivity materials at temperatures of approximately 200-250°C[1].

Traditionally, the thickness of insulation needed on steel members is determined by standard fire tests [2-3]. In standard fire tests, after a specified period of time, if the insulated member withstands the fire exposure without exceeding any of the endpoint failure criteria, the insulation is sufficient and the thickness of the insulation is considered to be the limit value of the protection. The standard fire conditions in the tests are represented in terms of the standard gas temperature history specified in different standards like ASTM E119 [2], ISO834 [3], etc... The widely used endpoint failure criteria in fire resistance test standard is that the maximum mean steel temperature must be lower than the critical temperature which is the temperature that causes structure collapse in a fire situation.

As an alternative to standard fire testing, analytical methods have been developed to evaluate the fire protection materials [4-7]. Analytical methods require solution of 2D (ignoring temperature gradient along the length of the member) transient heat transfer diffusion equation [8], which is usually complicated. In practice, a simplified 1D condensed heat transfer model, as shown in Figure 1, based on lumped capacitance concept has been adopted by different codes [4-7]. This

concept assumes that the temperature distribution is uniform inside the entire steel section. Using this 1D model, various mathematical techniques including separation of variables [9], Laplace transform [10] and Green's function approach [11] have been developed to give analytical formulations for uniformly insulated steel members in fire. There are two boundary conditions, which are Dirichlet and Neumann boundary conditions, at the fire-insulation interface for the solution of the 1D diffusion equation. In reference [9], Dirichlet boundary condition has been assumed and the derived formulation has been adopted by Eurocode 3[4]. In references [10] and [11], both Dirichlet and Neumann boundary conditions can be considered. Assuming Dirichlet boundary condition, Silva [12] derives a simple formulation of the problem which has been recommended for the revision of the Brazilian Standard 14323 [13].
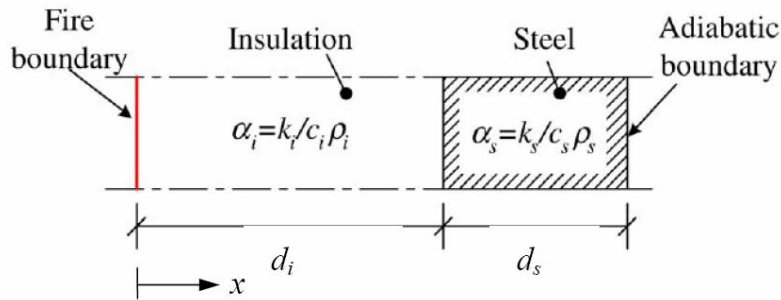

Figure 1. 1D Heat Transfer Model

Currently, Chinese technical code for fire safety of steel structure in buildings (CECS200) [7] is being revised. This paper intends to give the background of the formulation given by CECS200 [7] for temperature calculation of uniformly insulated steel members. The exact analytical derivations of the problem are also presented. Three steel I sections with different section factors insulated by typical nonreactive fire protection materials which are normal weight concrete (NWC), gypsum board and SFRMs are investigated. The mean steel temperature calculated by CECS200 [7], EC3 [4], ECCS [5], SFPE handbook [6] and Silva [12] are compared with the numerical results from the popular FEM program ANSYS [14]. ANSYS is power to solve transient, non-linear heat transfer problems. Its capacity of application in fire condition has been verified by experiments [15]. The same thermal elements used in reference [15] are adopted in this paper. In Appendix, the FEM model is further verified. Detail information about the FEM model is also given in the Appendix.

2.   THEORETICAL BACKGROUND

2.1   Governing Equation and Boundary Conditions

The governing heat transfer equation for the 1D model in Figure 1 is given by

$$\alpha_i \frac{\partial^2 T(x,t)}{\partial x^2} - \frac{\partial T(x,t)}{\partial t} = 0 \tag{1}$$

where $\alpha_i = k_i/\rho_i c_i$ is the thermal diffusivity; k_i is the thermal conductivity; and $\rho_i c_i$ is the thermal capacity, in which ρ_i, c_i are the density and specific heat of the insulation material, respectively.

By lumped capacitance concept, the boundary condition at the steel-insulation interface is given by

$$-k_i \frac{\partial T(d_i,t)}{\partial x} = \frac{c_s \rho_s}{A_p/V} \frac{\partial T(d_i,t)}{\partial t} \tag{2}$$

$$T_s(t) = T(d_i,t) \tag{3}$$

At the fire-insulation interface, the Neumann boundary condition is

$$-k_i \frac{\partial T(0,t)}{\partial x} = (h_c + h_r)[T_g(t) - T(0,t)] \tag{4}$$

where, h_c = 25 W/(m^{2}K) is the convective heat transfer coefficient; h_r is the radiative heat transfer coefficient, given by

$$h_r = \sigma \varepsilon_{res}[(T_g(t)+273)^2 + (T(0,t)+273)^2] \times [T_g(t)+273+T(0,t)+273] \tag{5}$$

where, σ = 5.67×10^{-8} W/(m^{2}K^4) is the Stefan-Boltzmann constant; and ε_{res} is the resultant emissivity for radiation heat transfer, given by

$$\varepsilon_{res} = \frac{1}{1/\varepsilon_g + 1/\varepsilon_m - 1} \approx \varepsilon_g \varepsilon_m \tag{6}$$

where ε_g and ε_m are the emissivity of the fire and insulation surface respectively. The emissivity of a real surface is a function of the surface temperature [8, 16-17], but in present codes [4-7], constant values of emissivity are adopted. In this paper, constant values with ε_g=1.0 and ε_g=0.7 recommended in EC4 [18] are used.

The Neumann boundary condition at the fire-insulation interface is complex. In practice, Dirichlet boundary condition has been widely adopted in deriving temperature formulations for uniformly insulated steel members [4, 7, 9, 12], which is given by

$$T(0,t) = T_g(t) \tag{7}$$

Eq. 7 assumes that there is no heat loss through surface convection and radiation, thus the insulation can effectively 'block' the thermal energy at the fire-insulation interface [19]. This assumption gives good prediction of steel temperature for insulation with low density and low conductivity but yields conservative results for insulation with high density and high conductivity [16]. In reference [16], two insulation materials, ceramic fibre blanket and concrete, have been studied, and temperature-dependent emissivity has been used. Using Green's function, Wang et al. [11] shows that for steel sections insulated by gypsum and concrete, the Dirichlet boundary condition will yield higher steel temperature than the real ones using Neumann boundary condition.

2.2   Exact Analytical Derivations

2.2.1   Separation of Variables

Introducing a state variable defined by

$$\theta(x,t) = T(x,t) - T_0 \tag{8}$$

Then, the governing equation Eq. 1 and the boundary conditions Eqs. 2 and 7 are expressed as

$$\alpha_i \frac{\partial^2 \theta(x,t)}{\partial x^2} - \frac{\partial \theta(x,t)}{\partial t} = 0 \tag{9}$$

$$-k_i \frac{\partial \theta(d_i,t)}{\partial x} = \frac{c_s \rho_s}{A_p / V} \frac{\partial \theta(d_i,t)}{\partial t} \tag{10}$$

$$\theta(0,t) = 0 \tag{11}$$

Solving the correlated Eqs. 9 to 12 with the following initial condition

$$\theta(x,0) = \theta_0 \quad , \quad t = 0 \tag{12}$$

we get

$$\theta(x,t)/\theta_0 = \sum_{n=1}^{\infty} C_n \exp(-\frac{\alpha_i \xi_n^2}{d_i^2} t) \sin(\xi_n \frac{x}{d_i}) \tag{13}$$

From Eq. 3, we get $\theta_s(t) = \theta(d_i,t)$, then

$$\theta_s(t)/\theta_0 = \sum_{n=1}^{\infty} C_n \exp(-\frac{\alpha_i \xi_n^2}{d_i^2} t) \sin(\xi_n) \tag{14}$$

In which, ξ_n is obtained by solving the following transcendental equation

$$\xi_n \tan \xi_n = \mu \tag{15}$$

where,

$$\mu = \frac{c_i \rho_i}{c_s \rho_s} d_i (A_p / V) \tag{16}$$

The coefficients C_n in Eq. 14 are obtained by

$$C_n = \frac{2(\xi_n^2 + \mu^2)}{\xi_n(\xi_n^2 + \mu^2 + \mu)} \tag{17}$$

In the case that μ is small, Eq. 14 can be approximated as

$$\theta_s(t)/\theta_0 = \begin{cases} 0 & t \le t_d \\ \exp(-\dfrac{t-t_d}{\tau}) & t > t_d \end{cases} \tag{18}$$

where,

$$t_d = \mu\tau/8 \,, \quad \tau = \frac{c_s\rho_s d_i}{(A_p/V)k_i}(1+\frac{\mu}{3}) \tag{19}$$

Assuming the thermal properties are constant, temperature response can be calculated for the insulated steel member subject to a time-varying boundary condition, using the principle of superposition (Duhamel's theorem), as

$$T_s(t) = \int_0^t T(t-\zeta)d(1-\theta_s(\zeta)/\theta_0) \tag{20}$$

where T is the time-varying heating curve. The ISO834 standard fire curve can be approximated by a sum of exponential terms as

$$T = \sum_{j=0}^{3} B_j \exp(-\beta_j t) \tag{21}$$

where B_j and β_j are as given in Table 1.

Table 1. B_j, β_j for ISO834 Standard Curve

j	0	1	2	3
$B(^oC)$	1325	-430	-270	-625
$\beta(h^{-1})$	0	0.2	1.7	19

Substituting Eqs. 14 and 21 into Eq. 20 we get the steel temperature

$$T_s = \sum_{n=1}^{\infty}\sum_{j=0}^{3} \frac{B_j C_n \sin(\xi_n)}{1-\beta_j d_i^2/(\alpha_i\xi_n^2)} \times [\exp(-\beta_j t)-\exp(-\frac{\alpha_i\xi_n^2}{d_i^2}t)] \tag{22}$$

Substituting Eqs. 18 and 21 into Eq. 20, we get the approximate steel temperature, for $t > t_d$,

$$T_s = \sum_{j=0}^{3} \frac{B_j}{1-\beta_j\tau} \times \left[\exp(-\beta_j(t-t_d))-\exp(-\frac{t-t_d}{\tau})\right] \tag{23}$$

To consider time-varying material properties, an approximate temperature time derivative is derived by Wickström[9] from Eq. 23 as

$$\frac{dT_s}{dt} = \frac{T-T_s}{\tau} - (e^{\mu/10}-1)\frac{dT}{dt} \tag{24}$$

Eq. 24 is adopted by EC3 [4], and the increment of steel temperature ΔT_s within a time interval Δt is given by

$$\Delta T_s = \frac{k_i A_p / V}{c_s \rho_s d_i} \frac{T_g - T_s}{(1 + \mu/3)} \Delta t - (e^{\mu/10} - 1)\Delta T_g \qquad (\Delta T_s \geq 0,\ \text{if } \Delta T_g > 0) \tag{25}$$

where, $\Delta t \leq 30s$ for insulated steel members.

2.2.2 Laplace Transform

An alternative solution of the problem using Laplace transfer is given by ECCS [5] as

$$\frac{dT_s}{dt} = A'(T_g - T_s) - B'\frac{dT_g}{dt} \tag{26}$$

where

$$A' = \frac{1}{(\dfrac{c_s \rho_s}{A_p/V})(\dfrac{d_i}{k_i} + \dfrac{1}{h_c + h_r})(1 + \dfrac{\mu}{N})} \tag{27}$$

$$B' = b/(1 + N/\mu) \tag{28}$$

with N and b as weighting factors. Certainly, for limiting case $(h_c + h_r) \rightarrow \infty$ Neumann boundary is equivalent to Dirichlet boundary. At this case,

$$b = \frac{1 + \mu/4}{2(1 + 5\mu/8)} \tag{29}$$

$$N = 2(b + 1) \tag{30}$$

2.3   Simple Derivation in CECS200

In Chinese Code CECS200 [7], the following assumptions are made in deriving the formulation for temperature calculation of insulated steel members,
   (1)   Dirichlet boundary is safely assumed at fire-insulation interface;
   (2)   The temperature distribution within the insulation is linear; and
   (3)   The temperature distribution within the steel is uniform.

At time increment Δt, the total energy transferred to the steel is

$$\Delta Q = \frac{k_i}{d_i}[T(t) - T_s(t)]A_p \Delta t \tag{31}$$

The energy absorbed by the steel is

$$\Delta Q_s = c_s \rho_s V[T_s(t + \Delta t) - T_s(t)] \tag{32}$$

Thermal Response to Fire of Uniformly Insulated Steel Members: Background and
Verification of the Formulation Recommended by Chinese Code CECS200

794

The energy absorbed by the insulation is

$$\Delta Q_i = \frac{T_s(t+\Delta t) - T_s(t) + \Delta T_g}{2} c_i \rho_i A_p d_i \tag{33}$$

By energy balance, we have

$$\Delta Q = \Delta Q_s + \Delta Q_i \tag{34}$$

Substituting Eqs. 31, 32 and 33 into Eq. 34 and ignoring the secondary term, we get the formulation given by CECS200 [7] as

$$\Delta T_s = \frac{k_i A_p / V}{c_s \rho_s d_i} \frac{T_g - T_s}{(1 + \mu/2)} \Delta t \tag{35}$$

3. COMPARISON OF DIFFERENT FORMULATIONS

3.1 Different Formulations

Eq. 25, Eq. 26 and Eq. 35 give the formulations recommended by EC3 [4], ECCS [5] and CECS200 [7] respectively. In SFPE handbook [6] different formulations are recommended based on the value of μ. For $\mu > 1/2$, the same formulation in CECS200 or Eq. 35 is recommended; and for $\mu \leq 1/2$,

$$\Delta T_s = \frac{k_i A_p / V}{c_s \rho_s d_i} (T_g - T_s) \Delta t \tag{36}$$

The formulation recommended by Silva [13] is

$$\Delta T_s = \frac{k_i A_p / V}{c_s \rho_s d_i} \frac{T_g - T_s}{(1 + \mu/4)} \Delta t - \frac{\Delta T_g}{4/\mu + 1} \tag{37}$$

The formulation recommend by Pettersson et al. [20] is

$$\Delta T_s = \frac{A_p / V}{c_s \rho_s} \frac{1}{(\dfrac{d_i}{k_i} + \dfrac{1}{h_c + h_r})} \frac{T_g - T_s}{(1 + \dfrac{\mu}{2})} \Delta t - \frac{\Delta T_g}{\dfrac{2}{\mu} + 1} \tag{38}$$

3.2 Material and Geometric Properties

Figure 2 shows the schematics of the analyzed section. Totally 3 typical steel I section with different section factors are investigated. The geometric properties of the sections are given in Table 2. The thickness of all sections is 50mm.

Table 3 gives the thermal properties of fire protection materials [21] which are NWC, gypsum board and SFRMs. Temperature-independent properties are investigated. The thermal properties of the steel are ρ_s=7850 kg/m^3 and c_s=600 J/(kg^{o}C).
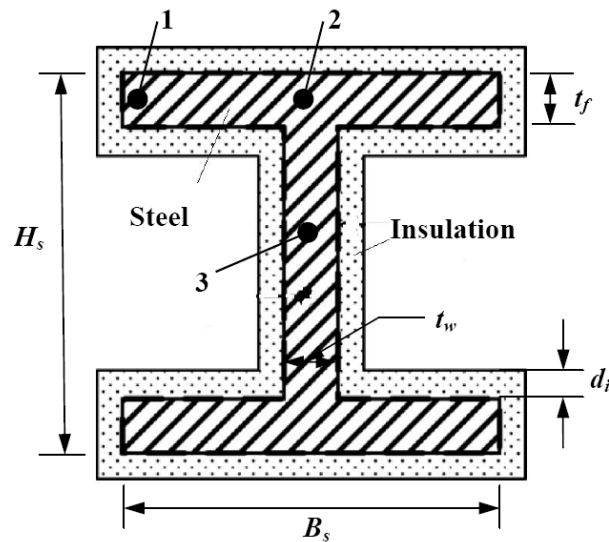
Figure 2. Schematics of Analyzed Section

Table 2. Geometric Properties of Analyzed Sections

Section name	B_s (mm)	H_s (mm)	t_w (mm)	t_f (mm)	A_p/V (m^{-1})	d_i (mm)
#1	200	200	8	12	190.72	50
#2	300	300	10	15	152.14	50
#3	400	400	15	25	93.86	50

Table 3. Thermal Properties of Insulation Materials

	ρ_i (kg/m^3)	c_i J/(kg ^{o}C)	k_i W/(m ^{o}C)
SFRM	250	800	0.12
gypsum board	800	1700	0.2
NWC	2300	1200	1.6

3.3   Results and Discussions

Figure 3 to Figure 5 show the steel temperature-time curves of insulated sections resulting from different methods. The steel temperatures obtained with FEM are taken as the average value of the temperatures measured at the location of points 1, 2 and 3, as shown in Figure. 2.

When calculating by Eqs. 25, 26, 37 and 38, the increments of the steel temperature are negative at early heating process, which is illegal to physics law. To avoid this, in practice we assume the steel temperature increments as zero if the values calculated by those equations are negative.

Thermal Response to Fire of Uniformly Insulated Steel Members: Background and
Verification of the Formulation Recommended by Chinese Code CECS200

796

When calculating by Eqs. 26 and 38, the values of h_r are required. From Eq. 5 we know in order to get h_r, the value of the surface temperature of the insulation, $T(0, t)$ should be known beforehand. However, $T(0, t)$ is an unknowable variable. In practice when calculating h_r we safely take fire temperature as the surface temperature that $T(0,t) \approx T_g(t)$. This treatment has been used by Wong and Ghojel [16] in their analysis.

As shown in Figure 3, when insulated by SFRMs, for all sections steel temperature – time curves given by EC3 [4], ECCS [5], CECS200 [7] and Silva [12] fit very well. Curves given by SFPE handbook [6] and Pettersson et al. [20] deviate from curves given by other four formulations. Comparatively, SFPE handbook [6] over-predicts the steel temperature and Pettersson et al. [20] under-predicts the steel temperature.

As shown in Figure 4, when insulated by gypsum board, for all sections temperature – time curves given by EC3 [4], ECCS [5] and Silva [12] fit well. CECS200 [7] and SFPE handbook [6] give the same results which fit well with the results given by EC3, ECCS and Silva at late heating stage but safely deviate from those results at early and mid heating stage. Comparing with other formulations, Perttersson et al. [20] under-predicts the steel temperature during the whole heating period.

As shown in Figure 5, when insulated by NWC, for all sections temperature – time curves given by EC3 [4], ECCS [5] and CECS200 [7] and SFPE handbook [6] fit very well. Silva [12] gives similar but slightly conservative results. Perttersson et al. [20] gives unsafe results.

As shown in Figures. 3-5, comparing with the 'exact' FEM results, except Pettersson et al. [20] under-predicts the steel temperature all other analytical methods will over-predict the steel temperature. Results also show section factors have little effect on the relationship between different curves.


4.   CONCLUSIONS

Based on the results of this study, the following conclusions can be drawn:
- Comparing with the 'exact' FEM method, except formulation recommended by Pettersson et al. [20] other formulations will yield conservative results. This is because in the derivation of those formulations, Dirichlet boundary has been assumed at the fire-insulation interface.
- Formulations recommended by EC3 [4] and ECCS [5] nearly give the same results. Results given by formulations recommended by CECS200 [7] fit well with the results given by formulations recommended by EC3 [4], ECCS [5] and Silva [12].
- When calculating by formulation recommended by CECS200 [7], there will not occur unreasonable situation that steel temperature increment is negative in early heating state. Considering its simple form, formulation recommended by CECS200 [7] is preferable for engineering usage.
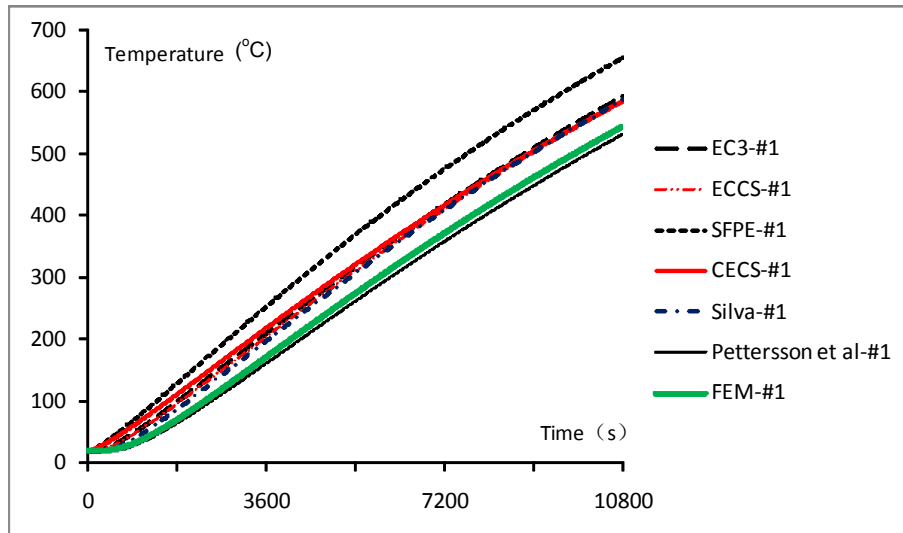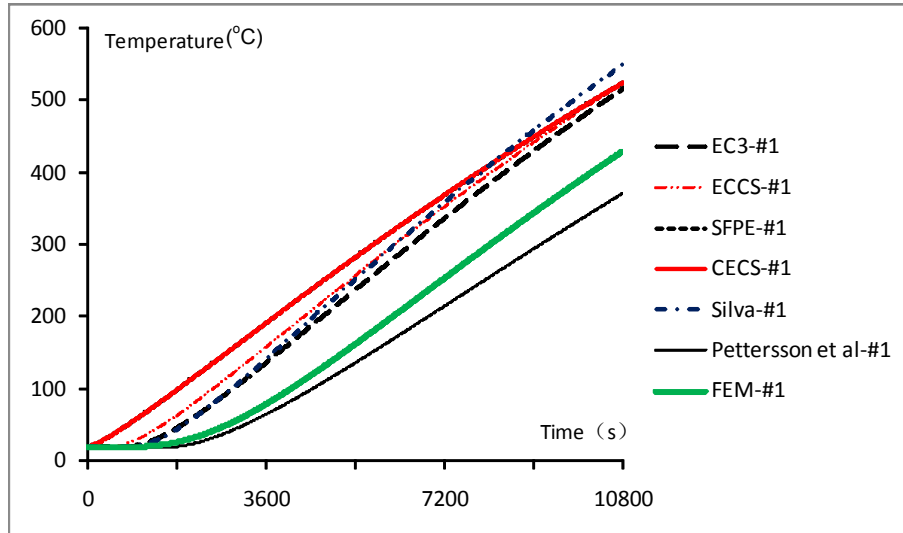
(a) 1# section
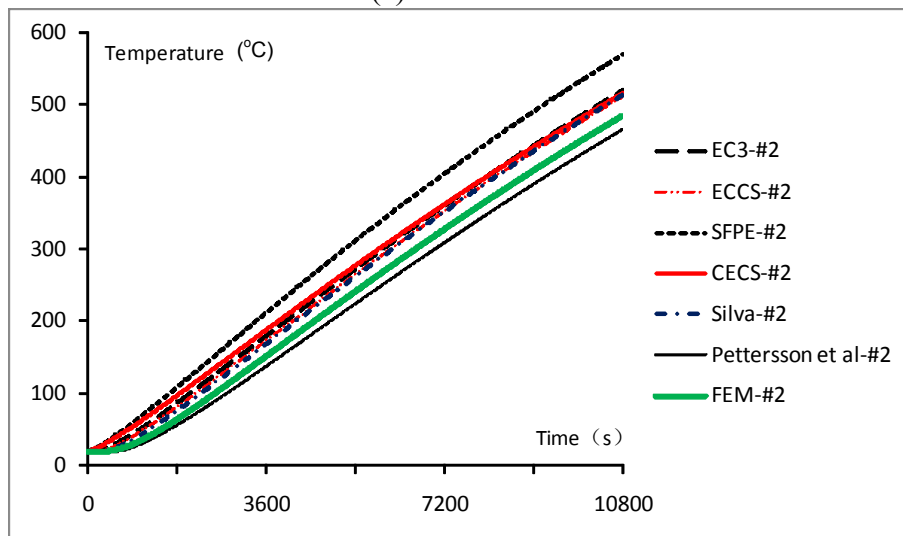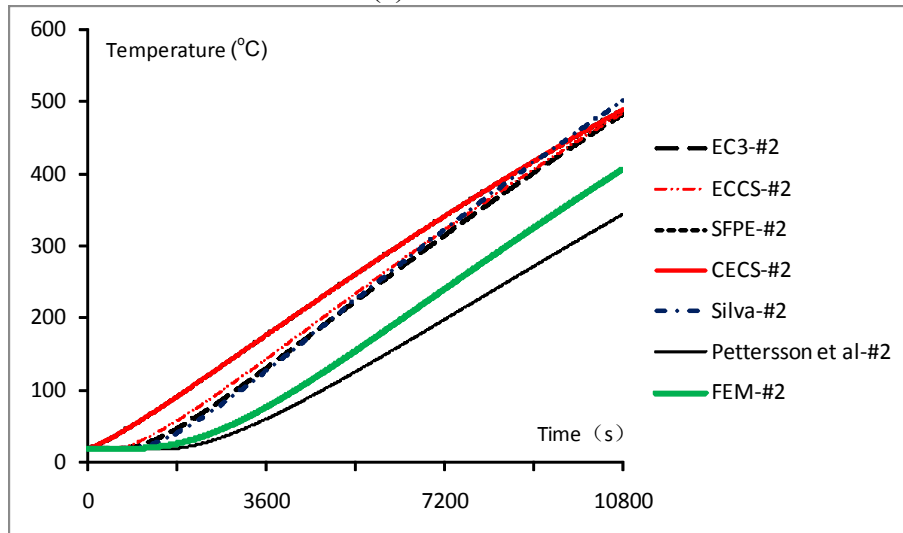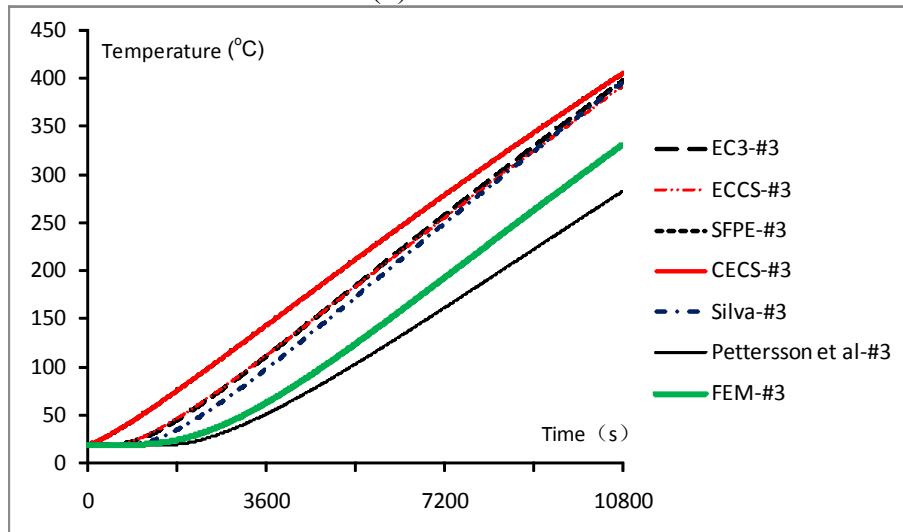
(b) 2# section
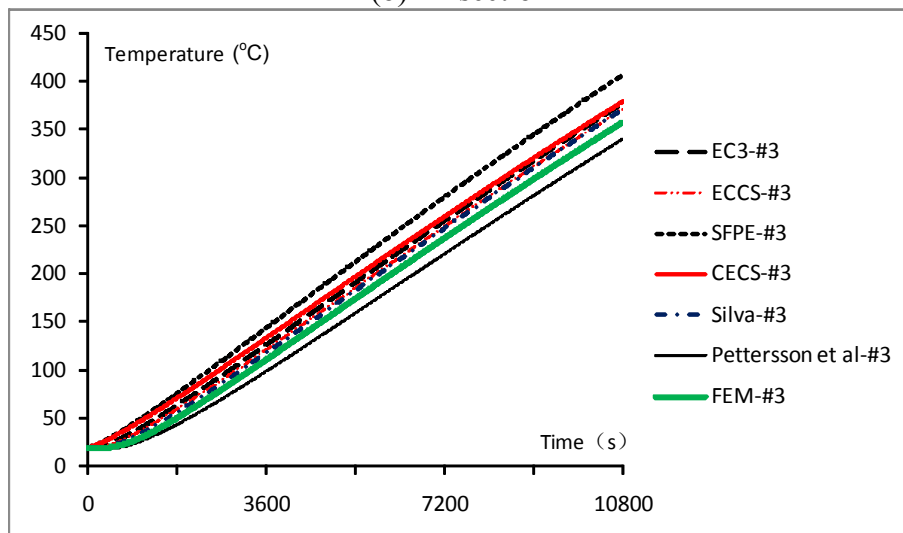
(c) 3# section

Figure 3. Results of Steel Temperature when Insulated by SFRMs
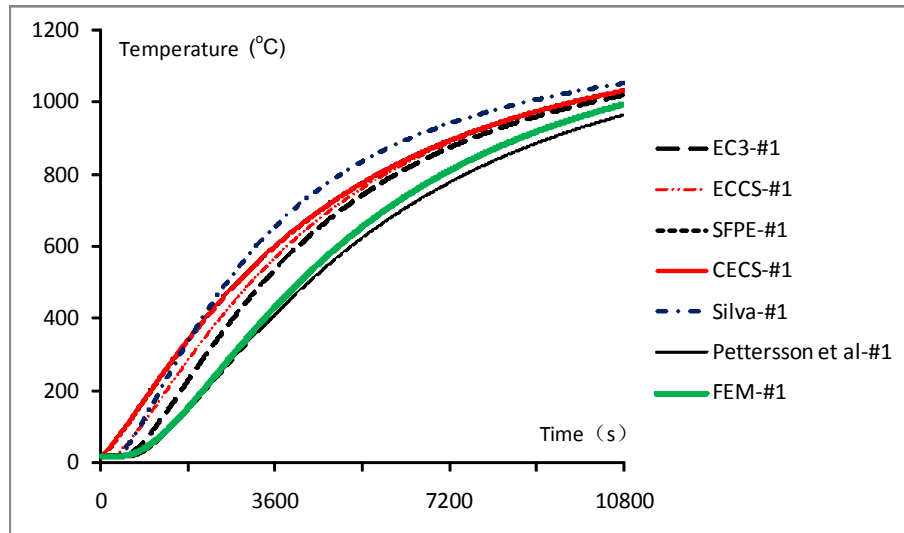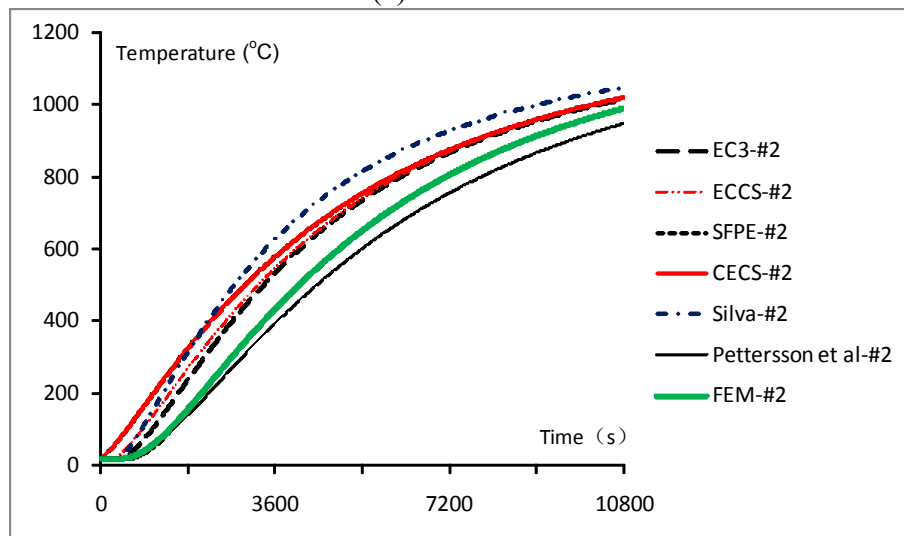
(a) 1# section
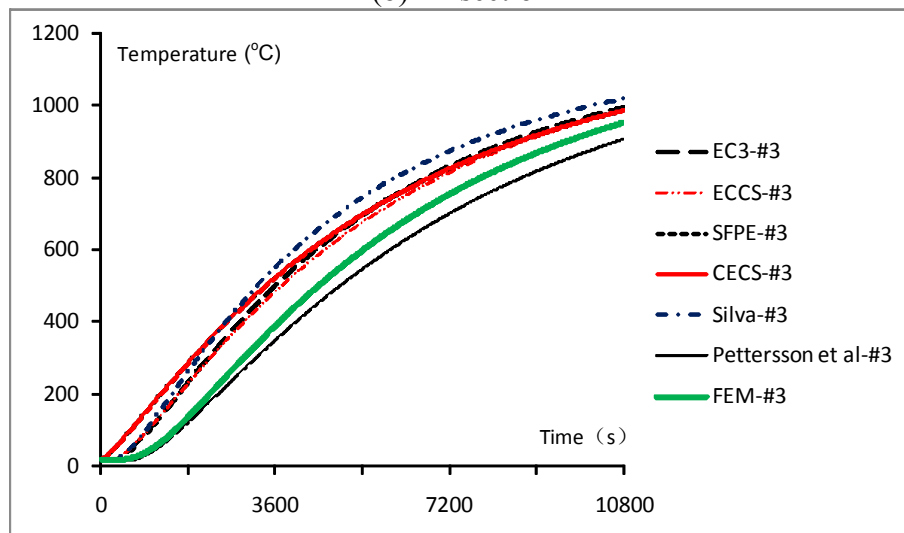
(b) 2# section

(c) 3# section

Figure 4. Results of Steel Temperature when Insulated by Gypsum Board

(a) 1# section

(b) 2# section

(c) 3# section

Figure 5. Results of Steel Temperature when Insulated by NWC

Thermal Response to Fire of Uniformly Insulated Steel Members: Background and
Verification of the Formulation Recommended by Chinese Code CECS200

800

APPENDIX

In numerical simulation by ANSYS, 2D thermal solid element PLANE55 and thermal surface effect element SURF151 are adopted.

PLANE55 can be used as a plane element or as an axisymmetric ring element with a two-dimensional thermal conduction capacity. The element has four nodes with a single degree of freedom, temperature, at each node. The element is applicable to a two-dimensional, steady-state or transient thermal analysis. It can also compensate for mass transport heat flow from a constant velocity field.

SURF151 may be used for various load and surface effect applications. It may be overlaid onto a face of any 2D thermal solid element (except axisymmetric harmonic elements). The element is applicable to two-dimensional thermal analysis. Various loads and surface effects may exist simultaneously. For example, SURF151 can be overlaid onto the surface of PLANE55 to simulate the effect of thermal radiation from ambient air to steel section.

Problem: A ceramic wall is initially uniform in temperature at 20 $^{\circ}$C and has a thickness of 30mm. It is suddenly exposed to a radiation source on the right side at 1000°C. The left side is exposed to room air at 20 $^{\circ}$C with a radiation surrounding temperature of 20 $^{\circ}$C. Properties of the ceramic are k =3.0 W/(m $^{\circ}$C), ρ = 1600 kg/m^3, and c = 800 J/(kg $^{\circ}$C). Radiation heat transfer with the surroundings at T_r (in $^{\circ}$C)may be calculated from

$$q_r = 0.8\sigma A[(T+273)^2 - (T_r+273)^2]$$

The convection heat transfer coefficient from the left side of the plate is given by

$$h = 1.92\Delta T^{1/4}$$

Determine the temperature distribution in the plate after 15,30,45,60,90,120, and 150 s.

Holman[8] solves the above problem by finite difference method (FDM). Here we solve the same problem by FEM using ANSYS. Figure. 6 shows the results from FDM and FEM. It finds the results from FEM fit well with the results given by Holman using FDM, which verify the validation of the FEM in this paper.
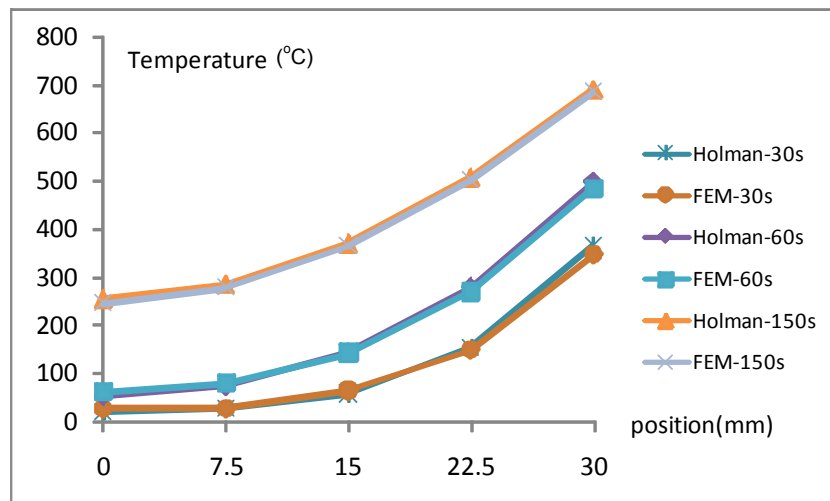

Figure 6. Comparison of Results by FEM and Holman [8]

ACKNOWLEGEMENT

REFERENCES

[1]   Fire Resistance of Steel-framed Buildings 2006 Edition, Corus Construction & Industrial, 2006.

[2]   Standard Test Methods for Fire Tests of Building Construction and Materials, ASTM E119-00a, ASTM International, West Conshohocken, PA, 2000.

[3]   BS 476-20, British Standard BS 476, Part 20: Method for Determination of the Fire Resistance of Load Bearing Elements of Construction (General Principles), British Standard Institution. London, 1987.

[4]   EN 1993-1-2, Eurocode 3: Design of Steel Structures – Part 1-2: General Rules – Structural Fire Design, British Standard Institution, London, 2005.

[5]   ECCS Technical Committee 3, European Recommendations for the Fire Safety of Steel Structures. Amsterdam: Elsevier Scientific Publishing Company, 1983.

[6]   Milke, J.A., Analytical Methods for Determining Fire Resistance of Steel Members, The SFPE Handbook of Fire Protection Engineering, 3rd ed. National Fire Protection Association, MA, 2002.

[7]   China Association for Engineering Construction Standardization (CECS200), Technical Code for Fire Safety of Steel Structure in Buildings (in Chinese), Beijing, China Planning Press, 2006.

[8]   Holman, J.P., Heat Transfer, 9th ed. McGraw-Hill Inc., 2002.

[9]   Wickstrőm, U., "Temperature Analysis of Heavily-insulated Steel Structures Exposed to Fire," Fire Safety Journal. 1985, Vol. 9, No. 3, pp. 281-5.

[10]   Melinek, S.J., Thomas, P.H., "Heat Flow to Insulated Steel," Fire Safety Journal, 1987, Vol. 12, pp. 1-8.

[11]   Wang, Z.H., Au, S.K., Tan, K.H., "Heat Transfer Analysis Using a Green's Function Approach for Uniformly Insulated Steel Members Subjected to Fire", Engineering Structures, 2005, Vol. 27, pp. 1551-62.

[12]   Valdir Pignatta e Silva, "Determination of the Steel Fire Protection Material Thickness by An Analytical Process – A Simple Derivation", Engineering Structures, 2005, Vol. 27, pp. 2036-43.

[13]   Valdir Pignatta e Silva and Ricardo Hallal Fakury, "Brazilian Standard for Steel Structures Fire Design", Fire Safety Journal, 2002, Vol. 37, No. 2, pp. 217-27.

[14]   ANSYS, User's Manual.

[15]   Ding, J., Li, G.Q. and Sakumoto, Y., "Parametric Studies on Fire Resistance of Fire-resistant Steel Members", Journal of Constructional Steel Research, 2004, Vol. 60, pp. 1007-27.

[16]   Wong, M.B. and Ghojel, J.I., "Sensitivity Analysis of Heat Transfer Formulations for Insulated Structural Steel Components", Fire Safety Journal, 2003, Vol. 38, pp. 187-201.

[17]   Staggs, J.E.J. and Phylaktou, H.N., "The Effects of Emissivity on the Performance of Steel in Furnace Tests," Fire Safety Journal, 2008, Vol. 43, pp. 1-10.

[18]   EN 1994-1-2, Eurocode 4: Design of Composite Steel and Concrete Structures – Part 1-2: General Rules – Structural Fire Design, British Standard Institution, London, 2005.

Thermal Response to Fire of Uniformly Insulated Steel Members: Background and
Verification of the Formulation Recommended by Chinese Code CECS200

802

[19]   Wang, Z.H. and Tan, K.H., "Sensitivity Study of Time Delay Coefficient of Heat Transfer
        Formulations for Insulated Steel Members Exposed to Fire", Fire Safety Journal, 2006, Vol.
        41, pp. 31-8.
[20]   Pettersson, O., Magnussen, S. and Thor, J., "Fire Engineering Design of Steel Structures,"
        Stockholm: Swedish Institute of Steel Construction, 1976.
[21]   Li, G.Q., Han, L.H., Lou, G.B. and Jiang, S.C., "Fire Resistance Design of Steel and
        Steel-concrete Structures (in Chinese)", China Architecture & Building Press, Beijing,
        China, 2006.

EVALUATION OF THE REMAINING SHEAR CAPACITY IN CORRODED STEEL I-BEAMS

Y. Sharifi[1,*] and R. Rahgozar[1]

[1]Civil Engineering Department, Kerman University, Kerman, Iran
*(Corresponding author: E-mail: yasser_sharifi@yahoo.com)

ABSTRACT: There are a large number of steel structures subjected to corrosion due to environmental exposure; which results in reduction of its load carrying capacity. In this paper, thickness loss data were compiled from three samples of corrosion damaged I-beams, removed from a petrochemical industry. Common examples of corrosion that were found included damage loss of section in flanges and holes in the web which is likely to reduce the shear capacity significantly. The collected data was used to calculate the percentage of remaining shear capacity. Corrosion damaged model was developed for steel I-beams based on average measured thicknesses of corroded beams. Formulas were developed to relate the percentage of remaining shear capacity to percentage thickness loss of the corrosion damaged I-beam. It will be shown that very few approximations were needed to derive these analytical relations. The effects of corrosion on steel beams are analyzed by evaluating the remaining capacity with regard to shear failure. Hence, the results of this study can be used for better prediction of the service life for deteriorating steel beams.

Keywords: Corrosion; steel beams; damaged model; remaining shear capacity

1.   INTRODUCTION

Steel structures such as ships, offshore platforms and land-based structures are prone to various types of damage as they get older. Corrosion and fatigue cracking may be the two most important types of damage in aging structures (Paik et al. [1-2]).

Nakai et al. [3] studied that corrosion is an unavoidable phenomenon in steel structures and thickness loss of the structural members due to corrosion is a great concern when the integrity of structures is considered. Concepts of 'corrosion margin' and 'allowable corrosion level' have been introduced conventionally to cope with this problem. The corrosion margin is an additional thickness at the design stage and the allowable corrosion level is used as a guide to determine when to renew worn members at the maintenance stage.

Corrosion is the major cause of deterioration in steel structures. Results of this deterioration can range from progressive weakening of the steel structure over a long period of time to sudden collapse of the structure. The effects of corrosion damage vary with the type of structure, the location and extent of deterioration. Corrosion damage must be carefully appraised and evaluated. In some cases, immediate repair or closure is necessary while in other cases, the conditions created by corrosion can be tolerated. In all cases, however, the likely progression of corrosion must be considered (Kulicki et al. [4]).

The main effects of corrosion on steel structures can be loss of material from the surface which leads to thinner sections (Figure 1). The section properties of a member, such as, area, second moment of area, radius of gyration, etc., would be reduced due to loss of material, thus causing a reduction in carrying capacity of the structure. Corrosion can lead to cracking (fracture), yielding or bucking of members. This can result in stress concentration, changes in geometric parameters, and a build-up of the corrosion products. These parameters are critical for the member's ability to resist load effects (Czarnecki and Nowak [5]). It has been pointed out by Kayser and Nowak [6] that the stiffness of members may also be reduced from loss of material, which may cause excessive deflections.

The most important form of corrosion is a general loss of surface material; this condition will lead to the gradual thinning of members. General corrosion accounts for the largest percentage of corrosion damage (Kayser [7]). The corrosion of metal has been intensively studied since the 1940's. A large amount of data has been collected on the rate of material loss in metal specimens under different environmental conditions. Corrosion test results on loss of materials for various environments (urban, rural and marine) have been summarized by Albrecht and Naeemi [8]. Loss of material may affect any one of the three modes of resistance in a steel I-beam i. e. bending, shear and bearing. Loss of flange material causes a reduction in the net area available to resist bending. Furthermore, the moment of inertia will be reduced, causing an increase in deflection. Also, the ultimate bending strength will be reduced, causing a reduction in maximum carrying capacity (Rahgozar [9]).

It is possible to establish a relationship between the remaining capacities of various failure modes (moment, shear, bearing …) and the loss of thickness for a given member. This approach can form the basis for establishing a quantitative relationship between the magnitude of corrosion defects and the corresponding remaining capacity. The corrosion decay model, namely uniform thickness loss model is developed in this study and will be used for the development of assessment method. For a particular failure mode of a beam, if the percentage remaining capacity is plotted against the percentage loss of thickness, we will obtain a curve that gives the relationship between them (Rahgozar [10]; Sharifi and Rahgozar [11]).

The effect of corrosion on structural strength is not yet clear. Further investigation is necessary to clarify how the corrosion affects strength of hold frames as beams. When beam strength is considered, (1) collapse strength (no buckling), (2) lateral-distortional buckling strength, (3) local buckling strength, (4) shear strength of web plates and (5) web crippling strength under concentrated loading etc. are important factors (Nethercot [12]). Furthermore, in this paper universal I-beams with uniform corrosion were used to calculate their remaining shear capacities. The results of this study can be used for a better prediction of the service life (remaining shear capacity) of deteriorating I-beams.


Figure 1. Loss of Material from the Surface of a Steel Beam Due to Corrosion

2.   ANALYSIS OF THE EFFECT OF CORROSION DAMAGE IN STEEL BEAMS

Development of corrosion decay models requires the information on locations where corrosion normally occurs and the types of corrosion damage in steel members. The most common form of corrosion damage in steel is the general surface corrosion. Uniform corrosion is the formation of oxide distributed uniformly over an exposed surface (Figure 1). This is the most common form of the corrosion, which leads to gradual thinning of members; and accounts for the greatest amount destruction in metals (Fontana [13]). General corrosion is the most serious form of corrosion observed on steel bridges (Kayser and Nowak [14]). Here a corrosion decay model was considered by reducing thickness of the sections. The model which is shown in Figure 2 is the uniform thickness loss in both flanges and web (Rahgozar [9]).

The corrosion decay model developed for the uniform thickness loss model sections with some modifications is as follows:

Loss of Material

| Flanges | μT_N |
| Web | μt_N |
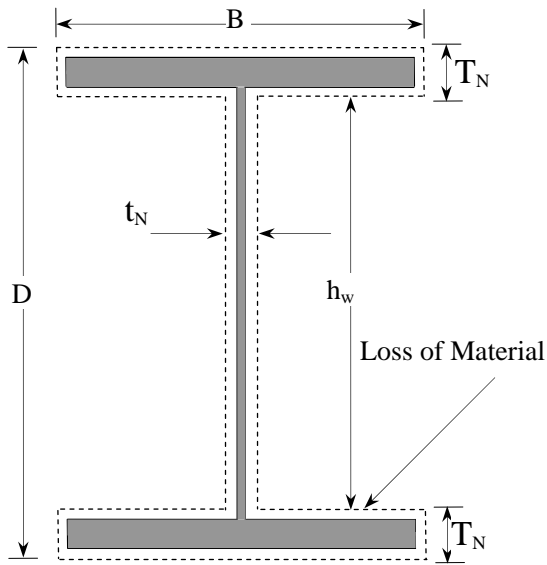
Where

T_N Thickness of the flange of as new section

t_N Thickness of the web of as new section

$\mu = \%LFT/100 = \%LWT/100$

$\%LFT$ = Percentage loss of flange thickness

$\%LWT$ = Percentage loss of web thickness

Figure 2. Uniform Thickness Loss Model

Thickness of the top flange = $T_N (1-\mu)$ (1a)
Thickness of the bottom flange= $T_N (1- \mu)$ (1b)
Average thickness of the flanges, $T_C = T_N (1- \mu)$ (1c)
Thickness of the web, $t_c = t_N (1- \mu)$ (1d)
Where
$\mu = \mu_F = \mu_W$,
$\mu_F = \% LFT/100$,
$\mu_W = \%LWT/100$,

3.   SHEAR CAPACITY

The web panel shown in Figure 3(a) is loaded in shear and the web is stiffened using stiffeners of length a_s. The thin flat plate of length, a_s, depth d, and thickness t shown in Figure 3(b) is simply supported along all four edges. The plate is loaded in shear, distributed uniformly along its edges. When these stresses are equal to the elastic buckling value, τ_{cr}, then the plate will buckle laterally out of its original plane into an adjacent position (Trahair et al. [15]). The elastic critical shear stress τ_{cr}, at which the web buckles can be predicated from plate buckling theory and is given by Timoshenko and Gere [16] as:

$$\tau_{cr} = k \frac{\pi^2 E}{12\left(1 - v^2\right)\left(d / t\right)^2} \tag{2}$$
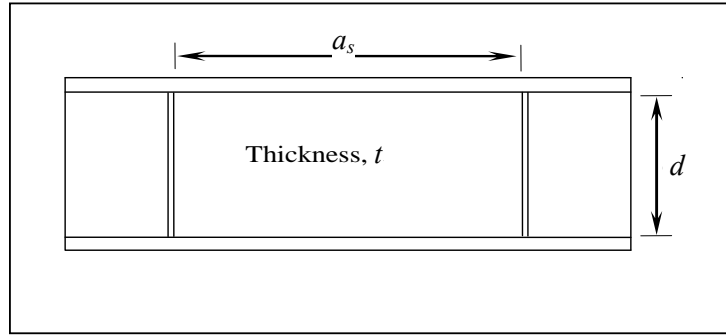
(a) Geometry of Web Panel
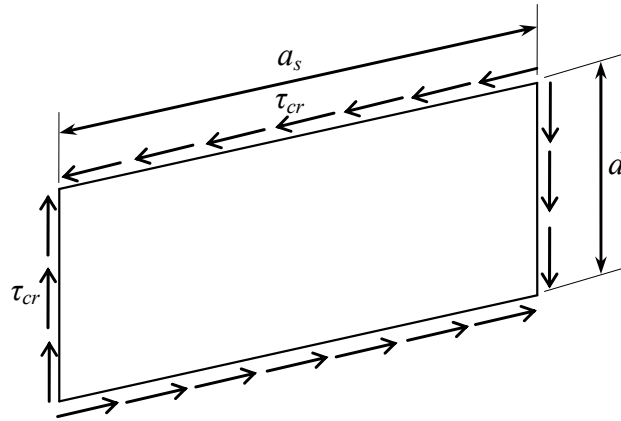
(b) Buckled Pattern of a Simply Supported Plate in Shear

Figure 3. Web Buckling Due to Pure Shear

In which the buckling coefficient, k is determined by a theoretical critical load analysis (Timoshenko and Gere [16]; Stowell et al. [17]). It is a function of plate geometry and boundary conditions and is given by Johnston [18] as:

$$k = 4.00 + \frac{5.34}{\left(a_s / d\right)^2} \qquad \text{for } a_s / d \leq 1 \tag{3a}$$

$$k = 5.34 + \frac{4.00}{\left(a_s / d\right)^2} \qquad \text{for } a_s / d \geq 1 \tag{3b}$$

If the numerical values for $v = 0.3$ and $E = 205000 \ N/mm^2$ are substituted in to Eq. 2, and further combined with Eqs. 3a and 3b, then,

$$\tau_{cr} = \left(0.75 + \frac{1.00}{\left(a_s / d\right)^2}\right)\left(\frac{995}{d / t}\right)^2 \qquad \text{for } a_s / d \leq 1 \tag{4a}$$

$$\tau_{cr} = \left(1.00 + \frac{0.75}{\left(a_s/d\right)^2}\right)\left(\frac{995}{d/t}\right)^2 \qquad \text{for } a_s/d \geq 1 \tag{4b}$$

The shear stresses in many structural members are transmitted by unstiffened webs, for which the aspect ratio, a/d, is large and assumed infinity. Therefore, for unstiffened webs, using Eq. 4b, τ_{cr} can be given as:

$$\tau_{cr} = \left(\frac{995}{d/t}\right)^2 \tag{5}$$

Using maximum distortion strain energy theory (Von-Mises yield criterion); it can be shown that the yield stress in shear, τ_y, is equal to $p_{yw}/\sqrt{3}\left(\approx 0.6 p_{yw}\right)$, where p_{yw} is the design strength of the web (Trahair et al. [15]). Stocky unstiffened webs in steel beam yield in shear before they buckle elastically. When a web panel yields, the critical shear stress is equal to the yield stress in shear.

i.e. $\quad \tau_{cr} = \dfrac{p_{yw}}{\sqrt{3}} \tag{6}$

Using Eqs. 5 and 6, the limiting ratio of d/t for web yielding in shear can be given as:

$$d/t = 79\varepsilon \tag{7}$$

where

$$\varepsilon = \sqrt{275/p_{yw}} \tag{8}$$

A stocky unstiffened web in an I-section beam subjected to pure shear loading is shown in Figure 4(a). The web behaves elastically in shear until yielding starts at $\tau_y = p_{yw}/\sqrt{3}$, yielding continues as the section undergoes increasing plastification until the web has yielded fully in shear (Figure 4(b)). Because the shear stress distribution at first yield is nearly uniform, the nominal first yield and fully plastic loads are nearly equal, and the shear shape factor is usually very close to 1.0. Stocky unstiffened webs in steel beams reach first yield before they buckle elastically, hence their strengths are determined by the shear stress τ_y, as indicated in Figure 4.

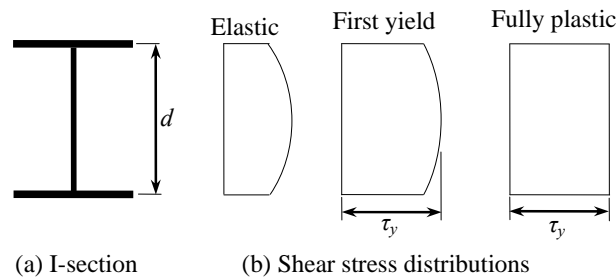
(a) I-section   (b) Shear stress distributions

Figure 4. Plastification of an I-Section Web in Shear

Thus the resistance of a stocky web in a flanged section for which the shear shape factor is near unity is closely approximated by the web plastic shear resistance:

$$V_w = dt\,\tau_y \tag{9}$$

When the depth to thickness ratio d/t of a long unstiffened steel web exceeds $79\sqrt{275/p_{yw}}$, its elastic buckling shear stress τ_{cr}, is less than the shear yield stress.

The design shear force F_v on a web for which the shear stress is approximately uniform must satisfy $F_v \le P_v$, in which P_v is the uniform shear capacity. The uniform shear capacity of a stocky web of area A_v is given by:

$$P_v = 0.6p_y A_v \tag{10}$$

Which is very close to $dt\,\tau_y \left(\approx 0.58A_v p_y\right)$ given for the fully plastic shear capacity. I-section web is classified by BS 5950 as stocky when its depth to thickness ratio satisfies $d/(t\varepsilon) \le 70$ for a hot-rolled beam (the web of all British universal sections of S275 or S355 steel are stocky), and when $d/(t\varepsilon) \le 62$ for a welded plate girder, otherwise it is classified as slender. Note that the value 62 is less than the value of 79 used in previous section on limiting slenderness when elastic buckling τ_{cr} is equal to shear yield stress τ_y (Trahair et al. [15]).

BS 5950 recommends that when d/t exceeds 62ε the web should be checked for signs of shear buckling. This limiting value of d/t is based on the experimental work by Horne [20]. The code uses notation q_e instead of τ_{cr} for the elastic critical shear stress. It also identifies three modes of behavior for webs.

The first mode is where the web strength is governed by its ultimate yield strength, i.e. $p_{yw}/\sqrt{3}$, the third is where the capacity is solely governed by the elastic critical shear stress, q_{cr}, and the intermediate stage is where an interaction occurs between the first and third modes. The divisions between the three modes are quantified by equivalent web slenderness factor, λ_w, which is given by (Trahair et al. [15]):

$$\lambda_w = \left(p_v/q_e\right)^{0.5} \tag{11}$$

where

$$p_v = 0.6p_{yw} \tag{12}$$

Code (BS 5950) gives the critical shear strength, q_w, of a web panel as follows:

For $\lambda_w \le 0.8$, $q_w = p_v$ $\tag{13a}$
For $0.8 < \lambda_w < 1.25$, $q_w = [(13.48 - 5.6\lambda_w)/9]\,p_v$ $\tag{13b}$
For $\lambda_w \ge 1.25$, $q_w = (0.9/\lambda_w)\,p_v$ $\tag{13c}$

when no stiffener is provided, using Eqs. 5 and 11 it can be shown that,

For $\lambda_w = 0.8$,   *then* $d/t = 62\varepsilon$ $\tag{14a}$
For $\lambda_w = 1.25$,   *then* $d/t = 97\varepsilon$ $\tag{14b}$

When an I-beam is subjected to bending, most of the applied shear force is resisted by the web. Web thickness of a corroded beam can remain uniform at initial stages of corrosion. In sections, where web thickness does not vary significantly due to corrosion, average web thickness may be used for evaluating the shear capacity. Under these circumstances shear capacity can be evaluated in accordance with BS 5950 [19]. When depth to thickness ratio, *d/t*, exceeds *62ε* the web should be checked for shear buckling in accordance with BS 5950 [19].

4.   ASSESSMENT METHOD FOR ESTIMATING THE REMAINING SHEAR CAPACITY IN CORRODED STEEL I-BEAMS

Corrosion in web and flanges leads to reduction in shear capacity. In addition, class of a section may be changed from one into another. This may change this failure mode from plastic yielding to shear buckling. If the web of a corrosion damaged beam varies in thickness significantly, the shear capacity should be calculated from first principles assuming elastic behavior. In sections where the variation in web thickness due to corrosion is small, average web thickness may be used for evaluating the shear capacity. The theory given in Section 3 was used in evaluation of remaining shear capacity in corrosion damaged beams.

Taking into account that corrosion may change the class of a section, three categories of sections in terms of *d/t* ratio are considered for the development of assessment methods for remaining shear capacity. The three categories are given below.

1. Category 1
$$d/t \leq 62\varepsilon \rightarrow q_w = p_v \tag{15a}$$
2. Category 2
$$62\varepsilon < d/t < 98\varepsilon \rightarrow q_w = [(13.48 - 5.6\lambda_w)/9] p_v \tag{15b}$$
3. Category 3
$$d/t \geq 98\varepsilon \rightarrow q_w = (0.9/\lambda_w) p_v \tag{15c}$$

Now the objective is to generate minimum curves for estimating the percentage remaining shear capacity *(%RSC)* of corrosion damaged beams. These minimum curves can be obtained by identifying the worst case scenario.

4.1   Categories of Sections Unchanged By Corrosion

4.1.1   *Category 1:* $d/t \leq 62\varepsilon$

Although corrosion reduces thickness of a web, some sections of this category that have the lowest *d/t* ratio in their as-new condition may remain in the same category even after being damaged by corrosion. For Category 1 sections, the shear capacity, P_v, is given by:

$$P_{vC} = p_v A_{vC} \quad \text{for corrosion damaged sections} \tag{16a}$$
$$P_{vN} = p_v A_{vN} \quad \text{for as-new sections} \tag{16b}$$

where A_v is the shear area taken as follows:

$$A_V = Dt \quad \text{for rolled I-sections} \tag{17a}$$
$$A_v = dt \quad \text{for welded I-sections.} \tag{17b}$$

In which, D is beam's depth and d is the clearing distance between flanges

The percentage remaining shear capacity (*%RSC*) of any corrosion damaged beam, which is the ratio of the capacity of corrosion damaged beam (P_{vC}) to the capacity of as- new beam (P_{vN}) may be expressed as:

$$\%RSC = 100\left(P_{vC} / P_{vN}\right) \tag{18}$$

$$\%RSC = 100\left(\frac{t_C}{t_N}\right) \tag{19}$$

where

t_N is web thickness of the beam in its as-new condition and

t_C is web thickness of the corrosion damaged beam

It should be noted from Eq. 19 that design strength of the material has no effect on *%RSC* in Category 1 sections. The relation for *%RSC* (Eq. 19) may be written as follows.

$$\%RSC = 100\left(1 - \frac{t_N - t_C}{t_N}\right) \tag{20}$$

$$\%RSC = 100\left(1 - \mu_w\right) \tag{21}$$

where

$\mu_W = \%LWT / 100$, and

%LWT is the percentage loss in web thickness.

The *%RSC* (Eq. 21) is a function of μ_w alone. Therefore, Eq. 21 may be used as the minimum curve for estimating the *%RSC* of any corrosion damaged sections that are category 1 in both as-new and corrosion damaged conditions. The estimates from the above equation will be almost exact for all the available I-sections.

4.1.2 Category 2: $62\varepsilon < d / t < 98\varepsilon$

Although corrosion reduces the thickness of a web, some sections that fall into Category 2 in their as new- condition may remain unchanging in part or their entire service life. For such sections, the shear capacity, P_v, is given by:

$$P_{vC} = p_v \phi_C A_{vC} \quad \text{for corrosion damaged sections} \tag{22a}$$
$$P_{vN} = p_v \phi_N A_{vN} \quad \text{for as-new sections} \tag{22b}$$

where

$$\phi = \left[1.5 - 0.62\lambda_w\right] \tag{23}$$

and A_v is as described in Section 4. 1.1

If it is assumed that the depths, D and d, of the corrosion damaged sections remain constant throughout their service life and the Eqs. 22a and 22b are combined with Eq. 18, then the *%RSC* of Category 2 sections is:

$$\%RSC = 100\left(\frac{\phi_C}{\phi_N}\right)\left(\frac{t_C}{t_N}\right) \tag{24}$$

Alternatively, using Eq. 21, the above equation can be modified to give,

$$\%RSC = 100\left(\frac{\phi_C}{\phi_N}\right)(1-\mu_w) \tag{25}$$

In this case the *%RSC* depends on both μ_w and the ratio ϕ_C/ϕ_N. In order to obtain the minimum of *%RSC* given by Eq. 25, the minimum of the ratio ϕ_C/ϕ_N must be obtained. Using Eq. 23, the ratio ϕ_C/ϕ_N may be written as:

$$\frac{\phi_C}{\phi_N} = \frac{1.5 - 0.62\lambda_{wC}}{1.5 - 0.62\lambda_{wN}} \tag{26}$$

where, λ_w is the web slenderness factor (see Section 4) and is given by:

$$\lambda_w = \left(\frac{p_v}{q_e}\right)^{0.5} = \frac{p_v^{0.5}}{995.0}\frac{d}{t} = \frac{(0.6p_{yw})^{0.5}}{995.0}\frac{d}{t} \tag{27a}$$

Assuming that *d* is constant, substituting Eq. 1b into Eq. 27a gives,

$$\lambda_{wC} = \frac{p_v^{0.5}}{995.0}\frac{d}{t_C} = \frac{p_v^{0.5}}{995.0}\frac{d}{t_N(1-\mu_w)} = \frac{\lambda_{wN}}{1-\mu_w} \tag{27b}$$

Now, substituting Eq. 27b into Eq. 26, gives the following expression for the ratio ϕ_C/ϕ_N:

$$\frac{\phi_C}{\phi_N} = \frac{\dfrac{2.42}{\lambda_{wN}} - \dfrac{1}{1-\mu_w}}{\dfrac{2.42}{\lambda_{wN}} - 1} \tag{28}$$

Eq. 28 demonstrates that for a given value of μ_w, when the value of λ_{wN} increases, the value of ϕ_C/ϕ_N decreases. Hence, for the minimum value of ϕ_C/ϕ_N, λ_{wN} must be the maximum obtainable from the maximum values of p_y and d/t_N (see Eq. 27a). The possible maximum values of p_y and d/t_N of Category 2 sections are:

Max $(p_y) = 450$ *N/mm²* and
Max $(d/t_N) = 60.33$ for section *UB44* (406×140*UB39*)

If the above maximum values are substituted into Eq. 27a, then the maximum value of λ_{wN} is:

Max $(\lambda_{wN}) = 0.996$ $\tag{29}$

Combining 28 and 29 gives the minimum of ϕ_C / ϕ_N as:

$$Min\left(\frac{\phi_C}{\phi_N}\right) = 1.7 - \frac{0.7}{1 - \mu_w} \tag{30}$$

Now, if Eqs. 25 and 30 are combined, the following relation is obtained for the minimum *%RSC* for Category 2 sections,

$$Min\left(\%RSC\right) = 100\left(1 - 1.7\mu_w\right) \tag{31}$$

Therefore, Eq. 31 may be used as the minimum curve to estimate the *%RSC* of any corrosion damaged sections that are Category 2 in their as-new condition and remain in this category even in their corroded states. The estimates will be conservative for some sections since Eq. 31 was derived for the worst combinations of p_y and d/t.

4.1.3   Category 3: $d/t \geq 98\varepsilon$

Plate girders that have the highest value of d/t may fall into Category 3 in their as-new condition. For Category 3 beams, the shear buckling capacity, P_v, is given by:

$$P_{vC} = \left(0.9 / \lambda_{wC}\right) p_v A_{vC} \quad \text{for corrosion damaged section} \tag{32a}$$

$$P_{vN} = \left(0.9 / \lambda_{wN}\right) p_v A_{vN} \quad \text{for as-new sections} \tag{32b}$$

If Eqs. 32a and 32b are combined with Eq. 18, and then the *%RSC* of Category 2 sections is obtained as:

$$\%RSC = 100\left(\frac{\lambda_{wN}}{\lambda_{wC}}\right)\left(\frac{t_C}{t_N}\right) = 100\left(\frac{\lambda_{wN}}{\lambda_{wC}}\right)\left(1 - \mu_w\right) \tag{33}$$

Assuming that the beam depth, d, remains constant for all of its service life, combining Eq. 27b with Eq. 33 gives the *%RSC* of Category 3 beams as:

$$\%RSC = 100\left(1 - \mu_w\right)^2 \tag{34}$$

The *%RSC* of Category 3 sections are a function of μ_w alone. Therefore, Eq. 34 may be used as the minimum curve for estimating the *%RSC* of any corrosion damaged section that is Category 3 in both as-new and corrosion damaged conditions. The above equation will give almost exact estimates of the *%RSC* for all such sections.

4.2   Category of Section Changed By Corrosion

4.2.1   Category 1 to Category 2 to Category 3

Some sections that are of Category 1 in their as-new condition may become Category 2 and then Category 3 during their service life due to loss of thickness in the web. When sections are of Category 1, Eq. 21 may be used as the minimum curve for estimating the *%RSC* as suggested before. Let us first consider the case in which the sections become Category 2 due to corrosion. When a section's category is changed from 1 to 2 the *%RSC* of such section may be obtained by combining Eqs. 13, 16b and 22a to yield:

$$\% RSC = 100\, \phi_C \left(1 - \mu_w\right) \tag{35}$$

where

$$\phi_C = \left[1.5 - 0.62\lambda_{wC}\right] \tag{36}$$

To obtain the minimum of *%RSC* in Eq. 35, the minimum of ϕ_C must be found first. Combining Eq. 27b and 36 yields,

$$\phi_C = 1.5 - \frac{0.62\lambda_{wN}}{1 - \mu_w} \tag{37}$$

For a given μ_w the minimum value of ϕ_C can be obtained for the maximum value of λ_{wN}. As in Section 4.1.2, the maximum value of λ_{wN} is obtained from the maximum values of p_y and d/t_N for a section that is of Category 1 in as-new condition; i. e.

$$Max\left(p_y\right) = 344\ N\ /mm^2 \qquad \text{and}$$

$$Max\left(d\ /t_N\right) = 60.33\ \ for\ section\ UB\ 44$$

Note: If $p_y > 344\ N\ /mm^2$, then section *UB44*, is of Category 2 in its as new condition

Using this data, maximum value of λ_{wN} is obtained as:

$$Max\left(\lambda_{wN}\right) = 0.82 \tag{38}$$

Substituting Eq. 38 into Eq. 37 gives the minimum of ϕ_C as:

$$Min(\phi_C) = 1.5 - \frac{0.511}{1 - \mu_w} \tag{39}$$

Now, if Eqs. 35 and 39 are combined, then the following relation is obtained for the minimum of *%RSC* for sections of category 2 that were originally of Category 1 in their as-new condition,

$$Min\left(\% RSC\right) = 100\left(1 - 1.5\mu_w\right) \tag{40}$$

Hence, when a corrosion damaged section is of Category 1 in its as-new condition and becomes of Category 2, Eq. 40 may be used for estimating the *%RSC*. This equation will give conservative estimates for some sections since it was derived for the worst combinations of p_y and *d/t* ratio.

Now, let us consider the case in which the sections become Category 3 due to corrosion. When they become Category3, using Eqs. 16b and 32a together with Eq. 18, the *%RSC* may be given as:

$$\% RSC = \frac{90}{\lambda_{wN}}(1 - \mu_w)^2 \tag{41}$$

For the minimum value of *%RSC* in Eq. 41, λ_{wN} must be maximum. The maximum value of λ_{wN} was obtained as 0.82 (see Eq. 38). Hence, the minimum *%RSC* in sections of Category 3 that were of Category 1 in their as-new condition is obtained as:

$$Min\left(\%RSC\right)=110\left(1-\mu_w\right)^2 \tag{42}$$

Therefore, when a corrosion damaged section is of Category 1 in its as-new condition becomes Category 3, Eq. 42 may be used as the minimum curve for estimating the *%RSC*. As Eq. 42 was derived for the worst combinations of P_y and *d/t*, the estimates will be conservative for some sections.

4.2.2   Category 2 to Category 3

Some sections that are of Category 2 in their as-new condition may become Category 3 due to loss of thickness in the web. When corrosion damaged sections are Category 2, Eq. 31 may be used as the minimum curve for estimating the *%RSC* as before. When they become Category 3, substituting Eqs. 22b and 32a into Eq. 18, gives the *%RSC* as:

$$\%RSC=\frac{90}{\lambda_{wN}\phi_N}\left(1-\mu_w\right)^2 \tag{43}$$

where the term $\lambda_{wN}\phi_N$ may be given by:

$$\lambda_{wN}\phi_N=\lambda_{wN}\left[1.5-0.62\lambda_{wN}\right] \tag{44}$$

In order to obtain the minimum *%RSC* from Eq. 43, maximum value of $\lambda_{wN}\phi_N$ must be used. Eq. 44 shows that when value of λ_{wN} increases, value of $\lambda_{wN}\phi_N$ also increases. For sections of category 2 in their as-new condition, maximum value of $\lambda_{wN}=0.996$ (see Eq. 29), hence, maximum value of $\lambda_{wN}\phi_N$ is:

$$Max\left(\lambda_{wN}\phi_N\right)=0.879 \tag{45}$$

Now, substituting Eq. 45 into Eq. 43 yields the minimum *%RSC* in sections of Category 3 that was originally of Category 2 in their as new condition i. e.:

$$Min\left(\%RSC\right)=102.4\left(1-\mu_w\right)^2 \tag{46}$$

Therefore, when corrosion damaged section that is of Category 2 in its as-new condition becomes Category 3; Eq. 46 can be used as the minimum curve for estimating the *%RSC*. Estimates will be conservative for some sections, as Eq. 46 was obtained for the worst possible case.

5.   MINIMUM CURVES FOR
THE UNIFORM THICKNESS LOSS MODEL SECTIONS

Corrosion discovered model for the uniform thickness loss model is developed for steel I-beams. It was found that a relationship between the remaining shear capacity and the loss of thickness for an I-beam section can be established and for a given category, if the percentage remaining shear capacity is plotted against the percentage loss of thickness; and the resulting curve establishes their relationship. Since these curves are obtained by identifying the worst case scenarios, they yield

conservative estimates and hence can be taken as minimum curves. The suggested minimum curves can be compared with the failure loads of three samples of corrosion damaged beams. The beams were tested individually for their ultimate failure (shear capacity) load in the laboratory (Rahgozar [9]).

Based on analytical findings, minimum curves were established and are given in Figure 5 for the following cases:

A. Sections that are of Category 2 in both their as-new and corrosion damaged conditions (C1)
B. Sections that are of Category 2 in both their as-new and corrosion damaged conditions (C2)
C. Sections that are of Category 2 in both their as-new and corrosion damaged conditions (C3)
D. Sections that are Category 1 in their as-new condition and become Category 2 and then Category 3 due to corrosion (C1 to C3)
E. Sections that are Category 1 in their as-new condition and become Category 2 during their service life (C1 to C2)
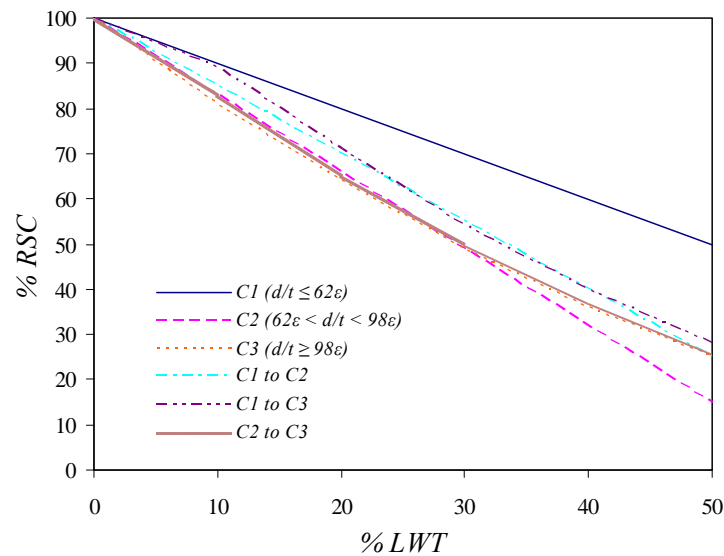F. Sections that are Category 2 in their as-new condition and become Category 3 during their service life (C2 to C3).

Figure 5. Minimum Curves for Estimating the *%RSC* of
Corrosion Damaged Beams with Uniform Thickness Loss

6.   CONCLUSIONS

In this paper a method has been proposed to asses the remaining shear capacity of corrosion damaged I-beams. The proposed methodology yields a quantitative relationship between the magnitude of structural defects and the corresponding remaining shear capacity in corrosion damaged beams. Here, it was discovered that estimates of the remaining shear capacity of corrosion damaged beams are almost exact. Furthermore, this methodology is easy to use and does not require lengthy calculations. In particular, equations obtained in this assessment method will be more effective in assessing the capacity of corrosion damaged I-beams. Realistic appraisal of the capacity of corrosion damaged beams by this method will avoid premature plant closures. In addition, this method may be used to identify the weaker members whose capacities are closer to the service loads. This assessment method will help practicing engineers to make a fast and reliable decision regarding the future of their corrosion damaged I-beam. For all practical purposes, the proposed minimum curves can be used along with the information on the material loss to estimate the percentage remaining shear capacity of corrosion damaged beams.

REFERENCES

[1]   Paik, J.K., Lee, J.M. and Ko, M.J., "Ultimate Compressive Strength of Plate Elements with Pit Corrosion Wastage", Journal of Engineering Maritime Environmental, 2003, Vol. 217, No. M4, pp. 185–200.

[2]   Paik, J.K., Lee, J.M. and Ko, M.J., "Ultimate Shear Strength of Plate Elements with Pit Corrosion Wastage", Thin-Walled Structures, 2004, Vol. 42, pp. 1161–76.

[3]   Nakai, T., Matsushita, H. and Yamamoto, N., "Effect of Pitting Corrosion on Strength of Web Plates Subjected to Patch Loading", Thin-Walled Structures, 2006, 44, pp. 10-19.

[4]   Kulicki, J.M., Prucs, Z., Sorgenfrei, D.F. and Mertz, D.R., "Guidelines for Evaluating Corrosion Effects in Existing Steel Bridges", National Cooperative Highway Research Program, Report 333, Transportation Research Board, National Research Council, Washington, D.C; 1990.

[5]   Czarnecki, A.A. and Nowak, A.S., "Time-Variant Reliability Profiles for Steel Girder Bridges", Structural Safety, Elsevier, 2008, Vol. 30, pp. 49-64.

[6]   Kayser, J.R. and Nowak, A.S., "Capacity Loss Due to Corrosion in Steel-Girder Bridges", Journal of Structural Engineering, ASCE, 1989, Vol. 115, pp. 1525-1537.

[7]   Kayser, J.R., "The Effects of Corrosion on the Reliability of Steel Girder Bridges", PhD thesis, Department of Civil Engineering, University of Michigan, USA, 1988.

[8]   Albrecht, P. and Naeemi, A.H., "Performance of Weathering Steel in Bridges", National Cooperative Highway Research Program, Report 272, Transportation Research Board, National Research Council, Washington, D. C., 1984.

[9]   Rahgozar, R., "Remaining Capacity Assessment of Corrosion Damaged Beams using Minimum Curves", Journal of Constructional Steel Research, Elsevier, 2009, Vol. 65, pp. 299-307.

[10]   Rahgozar, R., "Fatigue Endurance of Steel Structures Subjected to Corrosion", PhD. Thesis, Department of Civil Engineering, University of Bristol, UK, 1998.

[11]   Sharifi, Y. and Rahgozar, R., "Simple Model to Estimate the Remaining Moment Capacity of Corroded Varying Thickness Loss of I-Beam Sections", Proceeding of the 11th National Corrosion Congress, Kerman, Iran, 2009, pp. 1237-1244.

[12]   Nethercot, D.A., "Limit States Design of Structural Steelwork", Third Edition, Spon Press, London, UK, 2001.

[13]   Fontana, M.G., "Corrosion Engineering", McGraw Hill Book Company, New York, Third Edition, 1987.

[14]   Kayser, J.R. and Nowak, A.S., "Evaluation of Corroded Steel Bridges", Proceedings of Structures Congress Related to Bridge and Transmission Line Structures, American Society of Civil Engineers, Orlando, Florida; 1987, pp. 35-47.

[15]   Trahair, N.S., Bradford, M.A. and Nethercot D.A, "The Behavior and Design of Steel Structures to BS5950", Third Edition, British, London, Spon Press, Taylor & Francis Group, 2001.

[16]   Timoshenko, S.P. and Gere, J.M., "Theory of Elastic Stability", McGraw-Hill Book Company, 1961.

[17]   Stowell, E.Z., Heimerl, G.J., Libove, C. and Lundquist E.E., "Buckling Stresses for Flat Plates and Sections", Transaction of ASCE, 1952, Vol. 117, pp. 545-578.

[18]   Johnston, B.G., "Guide to Stability Design Criteria for Metal Structures", Third Edition, John Wiley & Sons, 1976.

[19]   BS 5950, "Structural use of Steel Work in Building: Part 1, Code of Practice for Design in Simple and Continuous Construction, Hot Rolled Sections", British Standard Institution, London, 1985.

[20]   Horne, M.R., "Plastic Theory of Structure", Thomas Melson and Sons, Ltd, 1971.